



# Kinetics of particle deposition at heterogeneous surfaces

D.Lj. Stojiljković, S.B. Vrhovac\*

Scientific Computing Laboratory, Center for the Study of Complex Systems, Institute of Physics Belgrade, University of Belgrade, Pregrevica 118, Zemun 11080, Belgrade, Serbia



## HIGHLIGHTS

- Kinetics of spherical particle deposition on a patterned substrates is studied.
- Patterns consist of square cells centered at the vertices of a square lattice.
- Cell size  $\alpha$  and cell–cell separation  $\beta$  have a striking influence on the kinetics.
- When  $\beta + \alpha/2 < 1$ , asymptotic approach of the coverage to the jamming limit is algebraic.
- Spatial distribution of particles inside the cell at the jammed state is studied.

## ARTICLE INFO

### Article history:

Received 26 January 2017  
Received in revised form 11 June 2017  
Available online 10 July 2017

### Keywords:

Random sequential adsorption  
Heterogeneous substrate

## ABSTRACT

The random sequential adsorption (RSA) approach is used to analyze adsorption of spherical particles of fixed diameter  $d_0$  on nonuniform surfaces covered by square cells arranged in a square lattice pattern. To characterize such pattern two dimensionless parameters are used: the cell size  $\alpha$  and the cell–cell separation  $\beta$ , measured in terms of the particle diameter  $d_0$ . Adsorption is assumed to occur if the particle (projected) center lies within a cell area. We focus on the kinetics of deposition process in the case when no more than a single disk can be placed onto any square cell ( $\alpha < 1/\sqrt{2} \approx 0.707$ ). We find that the asymptotic approach of the coverage fraction  $\theta(t)$  to the jamming limit  $\theta_j$  is algebraic if the parameters  $\alpha$  and  $\beta$  satisfy the simple condition,  $\beta + \alpha/2 < 1$ . If this condition is not satisfied, the late time kinetics of deposition process is not consistent with the power law behavior. However, if the geometry of the pattern approaches towards “noninteracting conditions” ( $\beta > 1$ ), when adsorption on each cell can be decoupled, approach of the coverage fraction  $\theta(t)$  to  $\theta_j$  becomes closer to the exponential law. Consequently, changing the pattern parameters in the present model allows to interpolate the deposition kinetics between the continuum limit and the lattice-like behavior. Structural properties of the jammed-state coverings are studied in terms of the radial distribution function  $g(r)$  and spatial distribution of particles inside the cell. Various, non-trivial spatial distributions are observed depending on the geometry of the pattern.

© 2017 Elsevier B.V. All rights reserved.

## 1. Introduction

The adsorption of particles on a flat substrate is a common phenomenon which has a great scientific and industrial importance as it has been linked to a wide range of applications in biology [1–4], nanotechnology [5,6], device physics [7–9],

\* Corresponding author.

E-mail addresses: [danica@ipb.ac.rs](mailto:danica@ipb.ac.rs) (D.Lj. Stojiljković), [vrhovac@ipb.ac.rs](mailto:vrhovac@ipb.ac.rs) (S.B. Vrhovac).

URLs: <http://www.scl.rs/danica/> (D.Lj. Stojiljković), <http://www.ipb.ac.rs/~vrhovac/> (S.B. Vrhovac).

physical chemistry [10,11], and materials science [12]. Depending on the application in question, the depositing objects could be colloidal particles, polymer chains, globular proteins, nanotubes, DNA segments, or general geometrical shapes, such as disks, polygons, etc. Due to its wide range of applications, there has been continuing effort to enrich our understanding of deposition processes and experimentally observed structural properties of the adsorbed phase [13–15].

The kinetics of adsorption has been mainly studied through the formulation of different models, aiming to capture the essential features of the deposition process. Random Sequential Adsorption (RSA) is the simplest model that can still provide the generic features of the adsorption phenomenon for the case of very strong interaction between particles and the substrate (for a review on RSA models see [13]). In the RSA model, adsorption process is considered as sequential addition of particles on the substrate such that at each time step only one particle is added on the substrate at a randomly selected position. During the process of addition, newly adding particles are forbidden from overlapping with the already adsorbed particles and any attempt of adsorption resulting in an overlap is rejected. The adsorbed particles are permanently fixed at their spatial positions so that they affect the geometry of all later placements. Under these conditions, the system evolves rapidly toward nonequilibrium conditions and the kinetics becomes essentially dominated by geometrical exclusion effects between particles. The most common parameter to characterize the kinetic properties of a deposition process is the coverage  $\theta(t)$ , defined as the fraction of the substrate area covered by the adsorbed particles at time  $t$ . Due to the blocking of the substrate area by the already randomly adsorbed particles, at large times the coverage  $\theta(t)$  approaches the jammed-state value  $\theta_j$ , where only gaps too small to fit new particles are left in the monolayer.

Although RSA model formulated under those conditions may accurately reproduce many experimental situations, its extension to more complex surfaces having an intrinsic structure is by no means trivial. For example, the supporting surface may be prepatterned with preferential sites for specific particle attachment, which may alter the kinetics of the process and the structure of the adsorbed layer. With the use of photolithographic techniques, high-power lasers, chemical treatments, etc., such surface modifications are routinely realized on the microscale, or even on the nanoscale [16–19].

It must be stressed that the classical RSA approach can be used for modeling the kinetics of an idealized process only, consisting in the creation of particles at a given distance from the interface with a constant rate and in a consecutive manner. For particles of a submicrometer size range, in addition to hydrodynamic and electrostatic forces, Brownian motion significantly affects their trajectories and transport to boundary surfaces. It is not possible, within the framework of the RSA model, to find a unique relationship between the kinetics of this idealized process and the kinetics of the particle adsorption process governed by various transport mechanisms. One has, therefore, to rely on approximate models being useful for specific transport mechanisms of particles [20].

There is a well-developed literature on irreversible adsorption on various types of two-dimensional (2D) patterned surfaces [21–29]. Specifically, pre-patterned substrates have been studied in a model of irreversible deposition on a random site surface (RSS), where the sites are represented by randomly distributed points [21,23]. Adamczyk et al. [24] have extended the RSS model to the situation where the size of the landing sites, in the shape of circular disks, is finite and comparable with the size of adsorbing spheres. Araújo et al. [28] and Marques et al. [29] have investigated the adsorption of disk-shaped particles on a patterned substrate consisted of equal square cells centered at the vertices of a square lattice. They studied the effect of the presence of a regular substrate pattern and particle polydispersity on the deposit morphology and density, as well as on the in-cell particle population. In addition, Araújo [30] has discussed the influence of the pattern on the adsorption kinetics. He has pointed out that time evolution towards the jammed state can be consistent with exponential or power-law behavior, depending on the geometry of the pattern.

Recently, motivated by nano-patterning, we have analyzed irreversible deposition of spherical particles of a fixed radius on nonuniform flat surfaces covered by non-overlapping rectangular cells that are *randomly* placed and fixed on the substrate surface [31]. The basic assumption of our model is that a particle can only be adsorbed if the center of its disk-shaped projection lies within one of the landing cells. We have studied structural properties of the jammed-state coverings in terms of the radial distribution function  $g(r)$  and distribution of the Delaunay ‘free’ volumes  $P(v)$ . Pore distribution  $P(v)$  has been widely used to characterize the organization of grains at the local level in disordered granular packings and to quantify the structural changes of the packing during the compaction process [32–36]. The convenient definition of a pore is based on the Delaunay triangulation. Delaunay decomposition is a natural way to subdivide a planar structure of disks into a system of minimal triangles with vertices on the centers of neighboring disks chosen in such a way that no other disks in the structure have centers within the circumcircle of each Delaunay triangle. One of the advantages of such decomposition is that it does not require the introduction of any threshold. Pore (Delaunay ‘free’ volume) is defined as a part of the Delaunay triangle not occupied by the disks [34,35]. It was shown that the porosity (pore volumes) of deposited monolayer can be controlled by the size and shape of landing cells, and by anisotropy of the cell deposition procedure [31]. Furthermore, we have shown that in the case of low densities of landing cells  $\theta_0^{(\text{cell})} \approx 0.1$  the plot of the first derivative of coverage fraction  $\theta(t)$  with respect to time  $t$  at the very late times of the deposition process is not linear on a double logarithmic scale, indicating that the approach to the jamming limit is not consistent with the power law behavior given by the time dependence:

$$\theta_j - \theta(t) \sim t^{-1/d}. \quad (1)$$

For irreversible deposition of spherically symmetric particles on continuum substrate, the above relation (1) was numerically and analytically confirmed valid by many investigators [3,37–40]. Parameter  $d$  is interpreted as substrate dimension [37] in the case of spherical particles adsorption or, more generally, as a number of degrees of freedom [41]. In addition, our results have suggested that in the case of single particle per-cell adsorption and low densities of landing cells the approach to the

jamming limit can be exponential, as in lattice RSA models [42–45]. For discrete substrates the approach of the coverage fraction  $\theta(t)$  to its jamming limit  $\theta_j$  is given by the time dependence:

$$\theta_j - \theta(t) \sim \exp(-t/\sigma), \quad (2)$$

where parameter  $\sigma$  depends on the orientational freedom of depositing objects, and on the dimensionality of the substrate [44,45].

The difference between deposition on finite-size landing cells and lattice RSA is in the particle positions, which can be uncertain within the order of the size of the cell in the former case. Very recently Privman and Yan [46] have analyzed both numerically and analytically extended model of one-dimensional deposition of segments of length  $a$ , on a lattice of spacing  $\ell$  between its sites, which instead of just being lattice points are symmetrically broadened (about the lattice points) into segments of width  $w$  in which the centers of the depositing objects can land. They reported that even an arbitrarily small imprecision in the lattice-site localization ( $w \gtrsim 0$ ) changes the convergence to jamming from fast, exponential (2), to slow, power-law (1). The present study in similar spirit investigates the rapidity of the approach to the jamming state in the case of *two-dimensional* (2D) prepatterned substrate. Unlike the models studied in our previous work [31], here we analyze deposition on the substrates patterned with a square grid of square-shaped cells onto which the particle can adhere. We consider the process of the irreversible random sequential adsorption (RSA) of fixed size disks. The present work is focused on the effect of the presence of a regular substrate pattern on the temporal evolution of the coverage fraction  $\theta(t)$ . Our aim is to quantify changes in time coverage behavior  $\theta(t)$  at densities near jamming limit  $\theta_j$ , associated with different cell size and density.

The rest of the article is organized as follows. In Section 2 we introduce the model and give some details of our simulations. We present the simulation results and discussions in Section 3. Finally, Section 4 contains some additional comments and final remarks.

## 2. Model and numerical simulation

We study irreversible monolayer deposition of identical disks onto a prepared flat nonuniform substrate, where the interparticle interaction is limited to hard-core exclusion. The substrate heterogeneities consist of non-overlapping (identical) square cells that are fixed on the substrate surface. The landing cells are arranged to form a regular pattern, i.e. squares are centered at the vertices of a square lattice and their edges are oriented parallel to the lattice principal axes. A disk is irreversibly adsorbed at random position on the substrate if it does not overlap any of previously adsorbed particles and if the center of disk lies inside one of the cells. Adsorbed disks are permanently fixed to their spatial positions.

The geometry of the pattern is controlled by the two dimensionless parameters,  $\alpha$  and  $\beta$ , measured in terms of the particle diameter  $d_0 = 2r_0$ . Parameter  $\alpha$  is the cell size, and parameter  $\beta$  is the shortest distance between the parallel sides of the nearest neighboring cells. The Monte-Carlo simulations are performed on a planar substrate with typically  $256 \times 256$  landing cells. In order to estimate coverages with higher precision, the number of cells is increased to  $1024 \times 1024$  for some landing-cell configurations (their specifications are provided later in the text). Periodic boundary conditions are used in all directions.

In numerical calculations, the time  $t$  is gradually increased by an increment  $\Delta t$ , given by  $\Delta t = \pi r_0^2/L^2$ , each time an attempt is made to deposit a disk of radius  $r_0 = d_0/2$  on a square surface (collector) of area  $L^2$ . Consequently, we define dimensionless adsorption time  $t = N_{\text{att}}\pi r_0^2/L^2$ , where  $N_{\text{att}}$  is the overall number of attempts to place disk particles. By plotting coverage  $\theta(t)$  versus the adsorption time  $t$ , defined above, one can simulate the kinetics of particle adsorption. However, in order to optimize the computing time, deposition is attempted only inside the cells. We chose a random cell and attempt to deposit a particle at random position within that cell. This optimization affects time scaling, so that the time increment can be calculated as  $\Delta t = \frac{\pi r_0^2}{L^2} \frac{(\alpha+\beta)^2}{\alpha^2}$ . In some cases, we wanted to reach very large times which required further optimizations of our calculations. When cells are small enough and can be occupied by one particle at most, we try to achieve the deposition events only at free cells. Then, the time  $t$  is increased after every deposition attempt by an increment  $\Delta t = \frac{\pi r_0^2}{N_{\text{free}}} \frac{(\alpha+\beta)^2}{\alpha^2}$ , where  $N_{\text{free}}$  is the number of free cells.

Depending on the cell size  $\alpha$ , one can place one or more disk centers inside each cell. For  $\alpha < 1/\sqrt{2} \approx 0.707$ , at most a single disk can be adsorbed at any given square cell. We denote this case as single particle per-cell adsorption (SPCA). For squares with  $\alpha \geq 1/\sqrt{2}$ , more than a single disk can be placed in the square cell, and we denote this as multiparticle per-cell adsorption (MPCA). For distances between neighboring cells  $\beta < 1$ , a disk attempting adsorption on a given cell can overlap with a previously adsorbed one belonging to a neighboring cell, resulting in a failed adsorption attempt. This excluded volume “interaction” between particles during adsorption at *different* cells affects the overall structure of the adsorbed layer and causes slower asymptotic approach of the coverage fraction  $\theta(t)$  to its jamming limit [28,31]. Such regime is denoted *interacting cell–cell adsorption* (ICCA). For  $\beta \geq 1$ , disks attempting adsorption cannot overlap other disks in neighboring cells, yielding the *noninteracting cell–cell adsorption* regime (NICCA). Deposition kinetics in the regime of NICCA is completely determined by the kinetics of adsorption of particles on finite size substrate (a single cell) with appropriate boundary conditions [28,31].

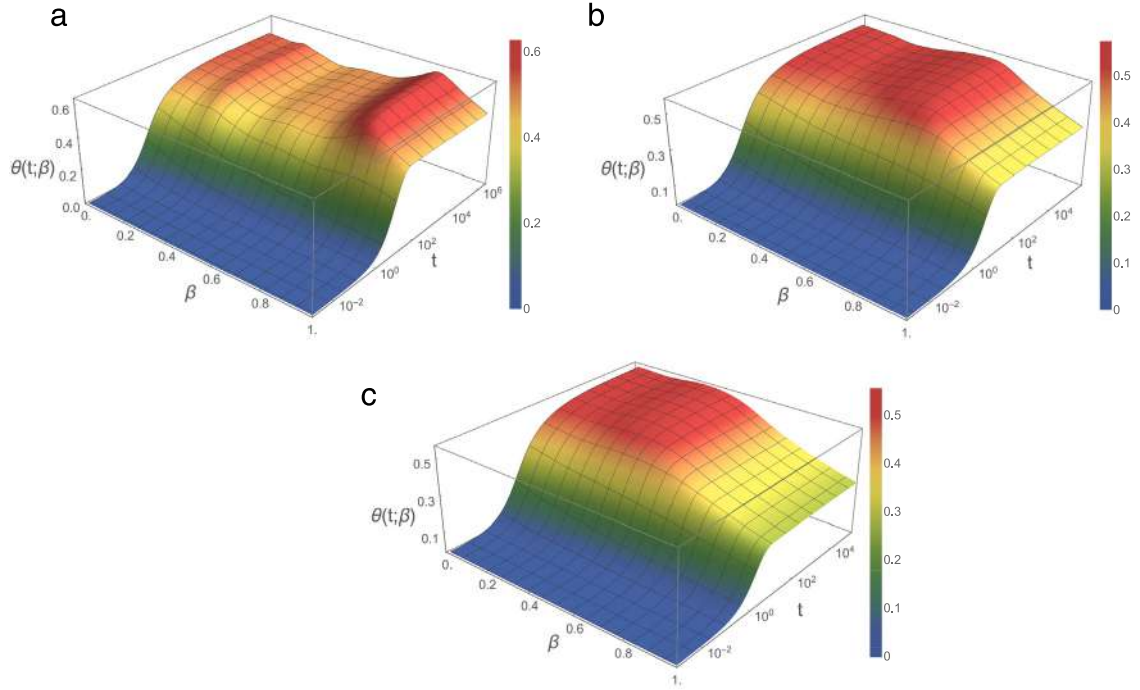


**Fig. 1.** Shown here is dependence of the time evolution of the coverage fraction  $\theta(t)$  on the gap size  $\beta$  between landing cells (in units of the disk diameter  $d_0$ ), for the three values of cell size,  $\alpha = 0.3$  (a),  $0.5$  (b), and  $0.7$  (c). For each  $\alpha$ , the gap  $\beta$  between cells is varied in the range  $[0, 1]$ , with the step of  $0.02$ .

### 3. Results and discussion

#### 3.1. Effect of varying $\beta$ on the long-time adsorption kinetics

In this work we focus on the interacting cell–cell adsorption (ICCA) regime in the case of single particle per-cell adsorption (SPCA). Kinetics of the irreversible deposition of disks is illustrated in Fig. 1(a)–(c) where the plots of time coverage behavior  $\theta(t)$  are given for the three values of cell size,  $\alpha = 0.3, 0.5$ , and  $0.7$ . Here, the plots of such time-dependence are shown for various values of the gap  $\beta$  between the cells, in the range from  $\beta = 0$  (continuous substrate and ICCA regime) to  $\beta = 1$  (upper limit of the parameter  $\beta$ , above which the NICCA occurs). These 2D plots enable us to analyze how the time evolution of the coverage  $\theta(t)$  in the case of SPCA depends on the gap size  $\beta$  between the landing cells. It can be seen that for a fixed size of landing cells  $\alpha$ , coverage  $\theta(t)$  in the early stage of the deposition process increases faster when the gaps between the cells are smaller. Indeed, at very early times of the process, when the coverage fraction  $\theta(t)$  is small, deposited objects do not “feel” the presence of the other ones, and the coverage grows rapidly in time. Then, adsorption process has overall rate proportional to the surface density of landing cells onto which the particles can adhere. Since the flux of incoming particles is fixed, the overall rate at which the coverage  $\theta(t)$  increases is progressively reduced with increasing of the gap between the landing cells.

At late enough time, when the coverage fraction is sufficiently high to make “excluded volumes” for deposited objects begin to overlap, there is a strong dependence of the adsorption rate on the parameter  $\beta$ . Reduction of the rate of adsorption events that occurs, with decreasing of the gap size  $\beta$ , corresponds to increasing of the impact the cell–cell excluded volume interaction on the late stage of the deposition process.

It is interesting to emphasize that the dependence of the jamming coverage  $\theta_j$  is a nonmonotonic function of the gap size  $\beta$  (see Fig. 1). It goes from jamming coverage for continuum  $\theta_j^{\text{cont}} = 0.5472 \pm 0.0002$  [47] ( $\beta = 0$ ), reaches some local minima ( $0 < \beta < 1$ ), and tend to a definite value which corresponds to the coverings when each cell is occupied by a single particle. Corresponding explanations of such variations of the jamming coverage  $\theta$  with parameter  $\beta$  are provided later in the text.

In order to gain a better insight into the complex kinetics of SPCA in the ICCA regime, it is useful to analyze in particular the temporal evolution of the first derivative of coverage  $\theta(t)$  with respect to time  $t$ . The time derivatives of  $\theta(t)$  are calculated numerically from the simulation data. Representative examples of double logarithmic plots of the time derivative  $d\theta/dt$  are shown in Fig. 2(a)–(c), for the three values of cell size,  $\alpha = 0.3$  (a),  $0.5$  (b),  $0.7$  (c). For each  $\alpha$ , results are presented for various values of the gap  $\beta$  between the cells in the range  $0.60 \leq \beta \leq 0.98$ . In the case of the algebraic behavior of the coverage fraction  $\theta(t)$  (see Eq. (1)), a double logarithmic plot of the first time derivative  $d\theta/dt \propto t^{-(1+d)/d}$  is a straight line. As seen

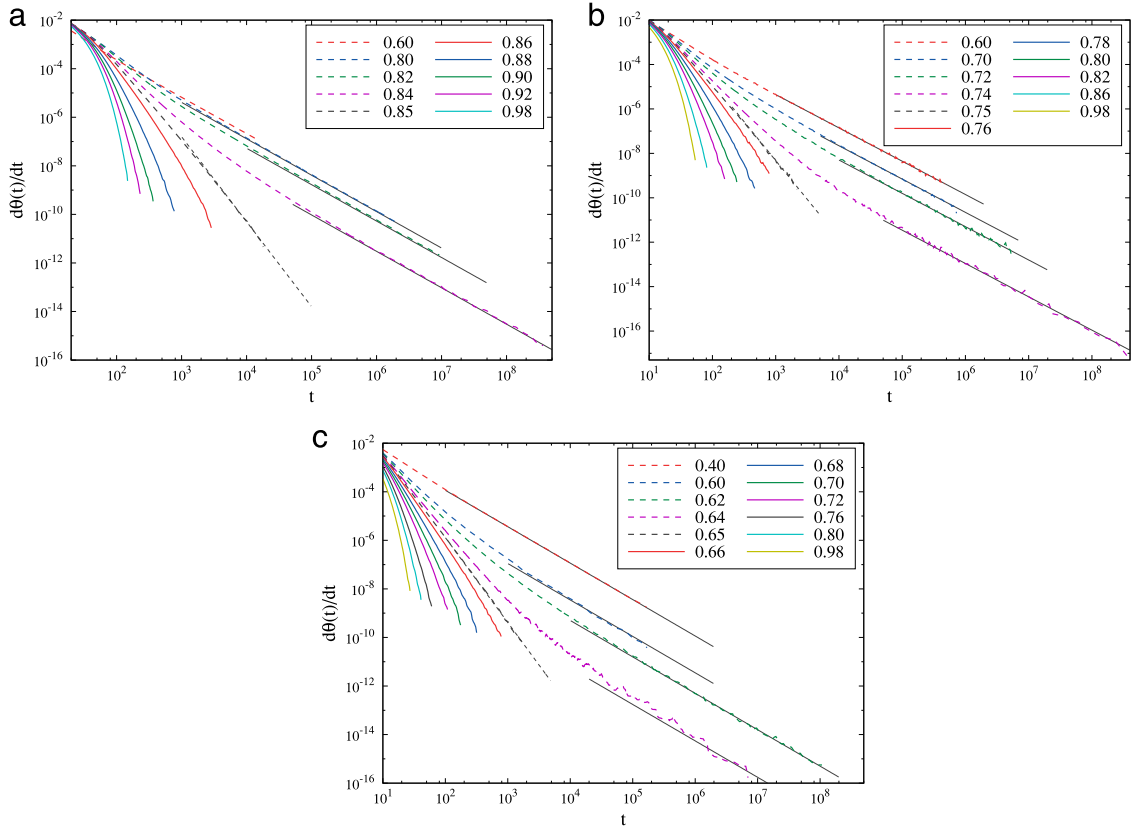


**Fig. 2.** Test for the presence of the algebraic law (1) in the approach of the coverage  $\theta(t)$  to the jamming limit  $\theta_j$  for different values of cell size,  $\alpha = 0.3$  (a), 0.5 (b), and 0.7 (c). The curves in each graph correspond to various values of the gap  $\beta$  between the cells, as indicated in the legend. Straight line sections of the curves show where the law holds. The solid straight lines have the slope  $-3/2$  and are guides for the eye. The dashed straight line has slope  $-5/2$  indicating the late time RSA behavior of the system for the critical values of the parameter  $\beta$ : (a)  $\beta_c = 0.85$ , (b) 0.75, (c) 0.65 (see Eq. (4)).

from Fig. 2, if the values of parameter  $\beta$  for cells of size  $\alpha = 0.3, 0.5, 0.7$  do not exceed, respectively,  $\approx 0.84, 0.74$  and 0.64, the late time kinetics of deposition process is similar to the one observed for disks with equal size, adsorbing on a clean substrate. Additionally, thin straight lines with the slope  $-3/2$  are shown in Fig. 2, indicating the late time RSA behavior for clean continuous substrates [3,37–40]. However, the same is not valid for large values of the parameter  $\beta$ , regardless of the cell size  $\alpha$  (obviously,  $\alpha < 1/\sqrt{2} \approx 0.707$  in the case of SPCA). As it can be seen, at the late times of the deposition process the plots of  $d\theta/dt$  vs.  $t$  are not linear on a double logarithmic scale for sufficiently large values of the gap  $\beta$ . The deviation from the power law (1) is particularly pronounced for low densities of landing cells, i.e. when  $\beta \lesssim 1$ .

Theoretical arguments supporting Feder's law (1) have been presented by Swendsen [37] and Pomeau [38]. Their analysis is based on the exclusion of the area of radius  $d_0$  around each disk of radius  $d_0/2$  for selecting the center of the newly arriving disk. After a certain time, characterizing the beginning of the asymptotic regime, the area that is available to the center of a new disk consist of small disconnected areas that can be occupied by only one additional disk. When power law (1) holds, a vanishing-small area that is available for the insertion of a new particle can be created with non-zero probability during the deposition process. Arbitrarily small areas are reached with very small probability for a uniform flux of the arriving disks that attempt deposition. In the case of ICCA-SPCA, since only one particle can fit per-cell, the existence of minimum finite area is related with particles previously adsorbed on neighboring cells. As seen from Fig. 3(a), particles adsorbed on neighboring cells can completely overlap the cell when the gap  $\beta$  and cell size  $\alpha$  satisfy the relation [30]:

$$\beta + \alpha/2 < 1. \quad (3)$$

Hence, below the critical value of the parameter  $\beta$ ,

$$\beta_c = 1 - \alpha/2, \quad (4)$$

there is no minimum *finite* area available to accommodate one particle. However, above the critical value  $\beta_c$  particles adsorbed on neighboring cells cannot prevent adsorption inside the cell. Then, there exist finite regions where the center of a disk can land without overlapping a previously adsorbed particle (see Fig. 3(b)). For the critical value of the gap  $\beta_c$  approach

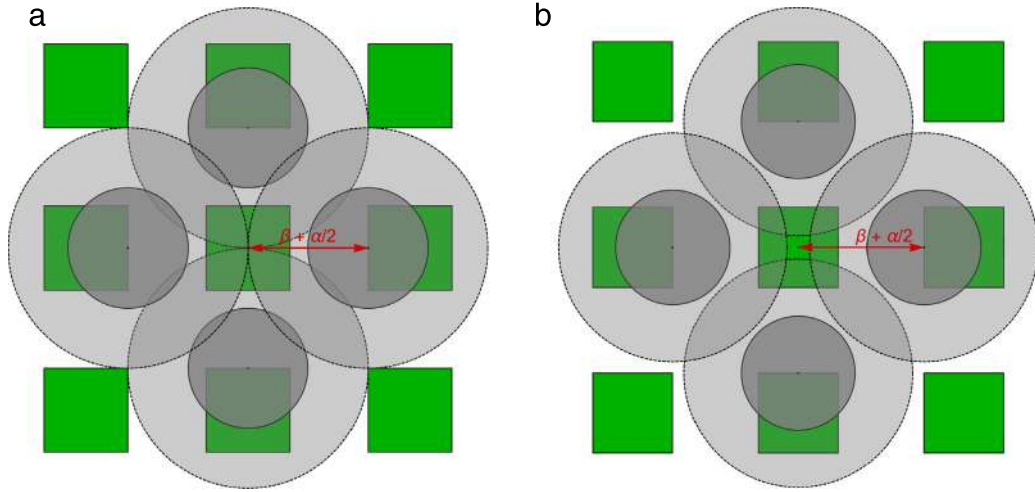


**Fig. 3.** Illustration of how a particles adsorbed in a neighboring cells can prevent adsorption on the central cell: (a) the overlap of the shadowed regions of the four neighboring particles completely overlap the central cell; (b) particles adsorbed on neighboring cells cannot prevent adsorption inside the cell.

to the jamming coverage  $\theta_j$  with time is still algebraic (1), with the exponent that approximately equals to  $-5/2$  which does not depend on the cell size  $\alpha$ .

Our numerical results suggest that for  $\beta_c < \beta < 1$ , the asymptotic approach of the coverage fraction  $\theta(t)$  to its jamming limit  $\theta_j$  is neither algebraic nor exponential. Semilogarithmic plots of the time derivative  $d\theta/dt$  are shown in Fig. 4(a)–(c), for three values of the cell size,  $\alpha = 0.3$  (a),  $0.5$  (b),  $0.7$  (c). For each  $\alpha$ , results are displayed for various values of the parameter  $\beta$  above the corresponding critical values (see Eq. (4)),  $\beta_c = 0.85$  (a),  $0.75$  (b),  $0.65$  (c). One clearly observes that for the fixed value of cell size  $\alpha$ , the time derivatives of  $\theta(t)$  decays at the very late times of the deposition process more quickly for the larger values of the gap  $\beta$  between the cells. Interestingly, in the limit of  $\beta \rightarrow 1$  approach of coverage  $\theta(t)$  to the jamming limit  $\theta_j$  is exponential of the form (2). The characteristic timescale  $\sigma$  is found to decrease with the cell size  $\alpha$  according to power-law,  $\sigma \propto \alpha^{-2.04 \pm 0.02}$ . In other words, the relaxation time  $\sigma$  in Eq. (2) is inversely proportional to the cell area. It must be stressed that the appearance of even a slight cell–cell excluded volume interaction violates the exponential asymptotic approach (2).

### 3.2. Influence of the pattern on the jamming density $\theta_j$

Let us go back to the analysis of the nonmonotonic behavior of the jamming density  $\theta_j$  as a function of the gap size  $\beta$  between the landing cells observed in Fig. 1. Dependences of the jamming coverage  $\theta_j$  on the separation distance  $\alpha + \beta$  between cell centers are presented in Fig. 5 for the three values of cell size,  $\alpha = 0.3, 0.5$  and  $0.7$ . For the case of SPCA, jamming coverage  $\theta_j$  can be exactly calculated for  $\beta$  larger than the critical value  $\beta_c$  (Eq. (4)) [28]. Indeed, since each cell at late enough time contains the center of a single deposited particle, the jamming coverage is simply

$$\theta_j^c = \frac{r_0^2 \pi}{(\alpha + \beta)^2}. \quad (5)$$

The solid black line in Fig. 5 indicates values of the jamming coverages calculated from Eq. (5). The jammed-state value  $\theta_j^{\text{cont}} = 0.5472 \pm 0.0002$  [47] of the coverage in the case of the irreversible disks deposition on continuum substrate is marked on the same figure by horizontal dashed line. When gap between the cells  $\beta$  starts to increase, cell–cell excluded volume interaction is still strong, but substrate area that is available for the insertion of a new particle is reduced, which leads to decrease of the jamming coverage below the value for continuum  $\theta_j^{\text{cont}}$ . As a gap size  $\beta$  increases further, the cell–cell excluded volume interaction weakens, but one expects a higher impact of patterning of the surface on the local particle arrangements. An increase in the pattern-induced tendency for semioordering of the coverings leads to the formation of jammed-state deposits of higher density. Then, for sufficiently large values of parameter  $\beta$ , jamming coverage exceeds the jamming limit  $\theta_j^{\text{cont}}$  for continuum substrate and continues to grow with  $\beta$ . In this case, the theoretical value of the highest possible coverage fraction is equal to  $\pi/4 \approx 0.7854$ . This value corresponds to the local configurations of quadratic symmetry when the disk centers are located at the vertices of a square with a side of  $\alpha + \beta = 1$  [48]. However, in the present model this maximum of the jamming coverage  $\theta_j$  is not reached at  $\alpha + \beta = 1$ . In Fig. 5 we observe the appearance of three pronounced maxima of  $\theta_j$  on shifted positions, approximately at  $\alpha + \beta = 1.04, 1.12$  and  $1.10$ , for  $\alpha = 0.7, 0.5$  and  $0.3$ , respectively. These maxima are not positioned at  $\alpha + \beta = 1$  due to the uncertainty in the position of the particle within the cell. Actually, for  $\beta \gtrsim 1 - \alpha$  excluded volume interaction with disks belonging to neighboring cells still substantially lowers the average number of adsorbed disks per-cell. As the parameter  $\beta > 1 - \alpha$  is increased further to the critical value

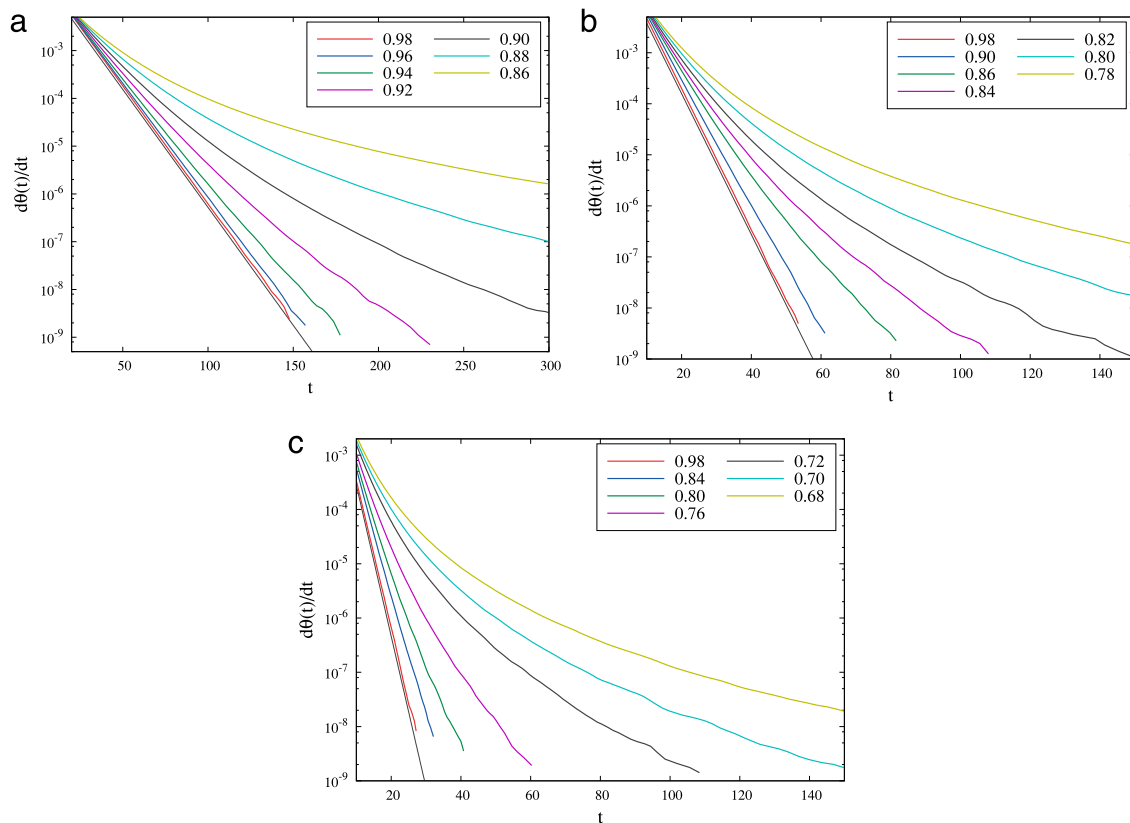


**Fig. 4.** Plots of the time derivative of coverage  $d\theta/dt$  for the three values of cell size,  $\alpha = 0.3$  (a),  $0.5$  (b),  $0.7$  (c). As indicated in the legend, the results are reported for values of the gap  $\beta$  above the corresponding critical values (Eq. (4)),  $\beta_c = 0.85$  (a),  $0.75$  (b),  $0.65$  (c). Additionally, the slanted straight line is shown, indicating the exponential approach to the jamming limit (Eq. (2)), where  $\sigma = 8.80$  (a),  $3.15$  (b), and  $1.56$  (c).

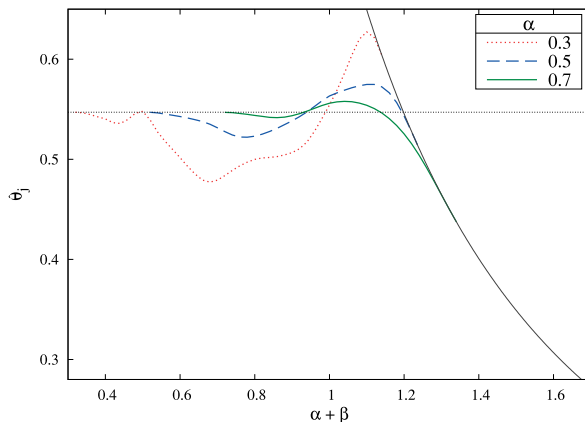


**Fig. 5.** Jamming coverage  $\theta_j$  as a function of separation distance  $\alpha + \beta$  (in units of the disk diameter  $d_0$ ) for various values of the cell size  $\alpha$ , as indicated in the legend. The solid black line indicates values of the jamming coverages  $\theta_j^c$  calculated from Eq. (5).

$\beta_c$  (Eq. (4)), the average cell population rises, and the jamming coverage  $\theta_j$  increases until the appearance of large void space between the cells, when it falls to the value given by Eq. (5).

We also study the influence of varying  $\alpha$  on the jamming coverage  $\theta_j$  and on the late time kinetics of deposition process. We carried out a series of simulations at fixed  $\alpha + \beta = 1.0, 1.1$ , and varied cell size  $\alpha$ . Numerical results regarding the jamming coverages  $\theta_j$  for various  $\alpha$  are shown in Fig. 6. For  $\alpha + \beta = 1.1$ , the criteria (3) cannot be satisfied if  $\alpha < 0.2$ . Therefore, for  $\alpha < 0.2$  each cell host exactly one particle in the jamming state so that jamming coverage has the constant value  $\theta_j = 0.6491$  given by Eq. (5). As  $\alpha > 0.2$  increases, the cell–cell exclusion leads to a further reduction of the average

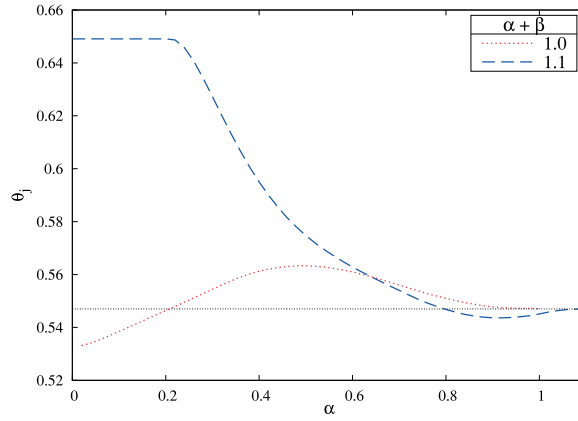


**Fig. 6.** Jamming coverage  $\theta_j$  as a function of cell size  $\alpha$  (in units of the disk diameter  $d_0$ ) for two values of separation distance  $\alpha + \beta$ , as indicated in the legend.

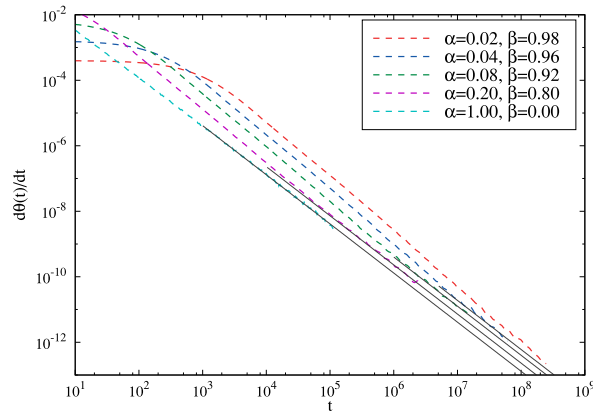


**Fig. 7.** Test for the presence of the algebraic law (1) in the approach of the coverage  $\theta(t)$  to the jamming limit  $\theta_j$  for different values of parameters  $\alpha$  and  $\beta$  that satisfy the condition  $\alpha + \beta = 1$  (see legend). Straight line sections of the curves show where the law holds. The solid straight lines have the slope  $-3/2$  and are guides for the eye.

cell population, thereby making the jamming coverage lower. However, in the case of  $\alpha + \beta = 1$  the jamming coverage  $\theta_j(\alpha)$  increases first and reaches the wide maximum at  $\alpha \approx 0.5$ , after that the curve  $\theta_j(\alpha)$  is lowered to the jamming value for continuum substrate  $\theta_j^{\text{cont}}$ . For  $\alpha < 1 - \sqrt{2}/2 \approx 0.3$ , a cell can only be blocked by disks deposited at the nearest lateral neighbor cells. In that case, for more cell–cell exclusion effects, it is needed a smaller cell size. But, when cells are larger than  $1 - \sqrt{2}/2$ , a cell can also be blocked by disks deposited at the nearest diagonal neighbor cells, which enhances the cell–cell excluded volume interaction. These two opposite effects that exist when cells increase lead to the formation of the maximum of  $\theta_j(\alpha)$  around  $\alpha \approx 0.5$ . Furthermore, when  $\alpha + \beta = 1$  there is discontinuity of the function  $\theta_j(\alpha)$  at  $\alpha = 0$ , since  $\theta_j(0) = \pi/4 \approx 0.7854$ , but  $\lim_{\alpha \rightarrow 0^+} \theta_j(\alpha) < \theta_j^{\text{cont}} \approx 0.5472$ .

### 3.3. Effects of varying $\alpha$ on the long-time adsorption kinetics

It is interesting that in the case when  $\alpha + \beta = 1$ , the approach to the jamming coverage  $\theta_j$  is always algebraic, regardless of the size  $\alpha$  of the landing cells. As can be seen from the Fig. 7, we find that for  $\alpha \geq 0.02$  the coverage  $\theta$  reaches a power-law time-behavior (1) within the length of the simulation. If a cell size  $\alpha$  decreases, the value  $\beta + \alpha/2$  increases and gets closer to unity when the condition (3) ceases to be valid. For very small cells ( $\alpha \gtrsim 0$ ), the coverage growth is slowed down by the creation of smaller fraction of the layer that is available for the insertion of a new particle. Consequently, when cell size  $\alpha$  decreases the onset of long-time power-law behavior (1) shifts to later times (Fig. 7). Generally, this effect occurs when the geometry of the pattern is close to the condition (4). In this case, it was necessary to increase the size of the substrate (typically  $1024 \times 1024$  cells) in order to gain a convincing confirmation of power-law approach of the coverage fraction  $\theta(t)$  to the jamming limit  $\theta_j$  at the very late times of the deposition process.

When  $\alpha + \beta = 1.1$ , although there is no change of jamming coverage  $\theta_j$  for  $\alpha < 0.2$  (Fig. 6), changes in the dynamics of deposition are obvious (see Fig. 8). The criteria (3) is satisfied for  $\alpha > 0.2$  and then the approach to the jamming limit is



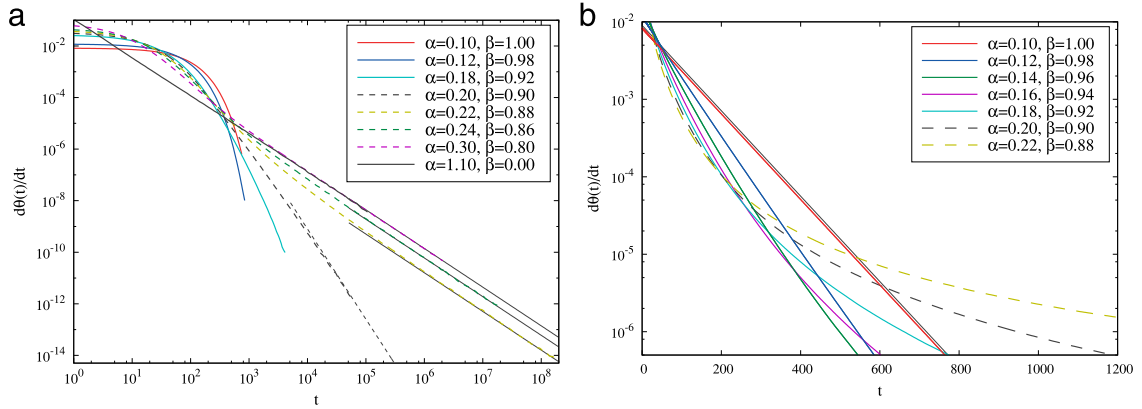


**Fig. 8.** Plots of the time derivative of coverage  $d\theta/dt$  for different values of parameters  $\alpha$  and  $\beta$  that satisfy the condition  $\alpha + \beta = 1.1$  (see legends): (a) results are shown on a double logarithmic scale. Solid straight lines have the slope  $-3/2$  and are guides for the eye. Dashed straight line has slope  $-5/2$  indicating the late time RSA behavior of the system for the critical value of parameter  $\beta$ ,  $\beta_c = 0.20$  (see Eq. (4)); (b) results for  $\alpha \leq 0.22$  are shown on a semilogarithmic scale. Slanted straight line is shown, indicating the exponential approach to the jamming limit (Eq. (2)), where  $\sigma = 78.8$ .

consistent with the power law behavior given by Eq. (1). As seen from Fig. 8(a), at the late times of the deposition process the plots of  $d\theta/dt$  vs.  $t$  are linear on a double logarithmic scale with the slope of  $-3/2$  for all  $\alpha > 0.2$ . However, the slope of  $d\theta/dt$  abruptly changes to  $\approx -5/2$  when the cell size  $\alpha$  reaches the critical value of  $\alpha = 0.2$  (see Eq. (4)). By reducing the size of cells below the critical value  $\alpha = 0.2$ , algebraic approach disappears. Under conditions when the cell size  $\alpha$  decreases towards noninteracting condition ( $\alpha \rightarrow 0.10^+$ ,  $\beta \rightarrow 1.0^-$ ), asymptotic approach of the coverage fraction  $\theta(t)$  to its jamming limit  $\theta_j$  becomes closer to the exponential law (2) (see Fig. 8(b)).

### 3.4. Spatial distribution of particles inside the cell

In order to gain additional insight into the late time kinetics of deposition process onto a nonuniform substrate it is useful to analyze in particular the spatial distribution of particles inside the cells. In Figs. 9, 10, and 11 we show the spatial distribution of particles inside the cell at the jammed state, for  $\alpha = 0.3, 0.5$  and  $0.7$ , respectively, and for the twelve different values of parameter  $\beta \in [0.02, 0.98]$ . To calculate these probability distributions, we divided cell space in mesh with  $40 \times 40$  bins and counted the number of particles falling into bins. The data are averaged over 100 independent runs for each of the investigated substrate patterns with  $256 \times 256$  landing cells. Spatial distribution of particles shown in Figs. 9–11 are accompanied by corresponding radial distribution functions  $g(r)$  (or pair-correlation functions) defined as

$$g(r) = \frac{S}{N^2} \left\langle \sum_{i=1}^N \sum_{j=1}^N \delta[\vec{r} - (\vec{r}_j - \vec{r}_i)] \right\rangle, \quad (6)$$

where  $\vec{r}$  is the position vector of a point over the adsorption plane (measured from the center of an adsorbed particle),  $\delta$  is the Dirac delta function,  $\vec{r}_i$  and  $\vec{r}_j$  are the position vectors of the particles  $i$  and  $j$ , respectively, and angle brackets mean the ensemble average. Here,  $S$  is the surface area, and  $N$  is the total number of particles adsorbed over this area. Radial distribution  $g(r)$  gives information about the long-range interparticle correlations and their organization [13,49]. This function can be interpreted as an averaged probability of finding a particle at the distance  $r$  from another particle, with the center located at  $r = 0$ . For sake of convenience, the distance  $r$  is usually normalized by using the particle radius  $d_0/2$  as a scaling variable. In the absence of external forces, when the system can be considered as isotropic, the vector  $\vec{r}$  can be replaced with the radial coordinate  $r$  and the pair correlation function may be calculated more directly by converting Eq. (6) to the form

$$g(r) = \frac{S}{N} \frac{\bar{N}_a(r)}{2\pi r \Delta r}, \quad (7)$$

where  $\bar{N}_a$  is the averaged number of particles within the annulus of the radius  $r$  and the thickness  $\Delta r$ .

To discuss the effect of the parameter  $\beta$  on the spatial distribution of particles inside the cell at the jammed state, let us first consider the fixed value  $\alpha = 0.3$ , with varying  $\beta = 0.02 - 0.98$ , as shown in Fig. 9. In the case of ICCA regime, the temporal evolution of the coverage  $\theta(t)$  towards its jamming state value  $\theta_j$  is a two-stage process. At very early times of the process, when the coverage fraction is small, the coverage grows rapidly in time. Particles adsorbed during this stage are homogeneously distributed in the cells. At late enough time, when the coverage fraction is sufficient to make the geometry of the unoccupied substrate complex, the growth of the coverage fraction  $\theta(t)$  requires the filling of holes that are large enough for the insertion of an additional particle. Consequently, the structure of the spatial distribution of particles inside the cell

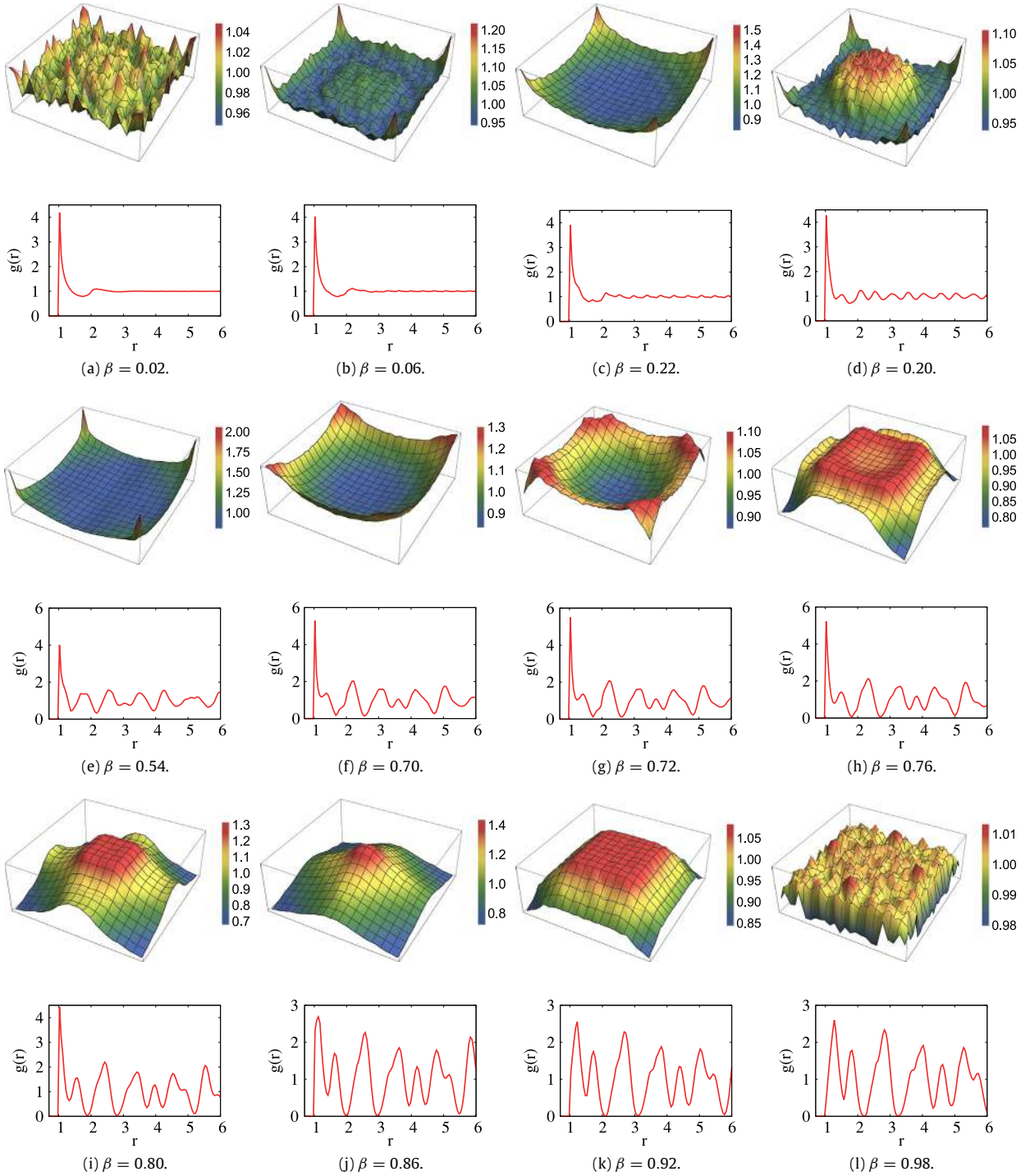


**Fig. 9.** Spatial distribution of particles inside the cell and radial distribution function  $g(r)$  at the jammed state, for the fixed value of cell size  $\alpha = 0.3$  and different values of parameter  $\beta$ .

is determined by the late stage of the deposition process. For  $\beta \leq 0.02$ , particles are distributed uniformly throughout the whole substrate and the shape of radial distribution  $g(r)$  is the same as in the case of RSA of disks on a continuous substrate. Since the cell–cell excluded volume interaction is changing with  $\beta$ , the spatial distribution of particles inside the cell reveals various preferential regions. From the probability distribution plots in Fig. 9, we can identify various regions such as corners

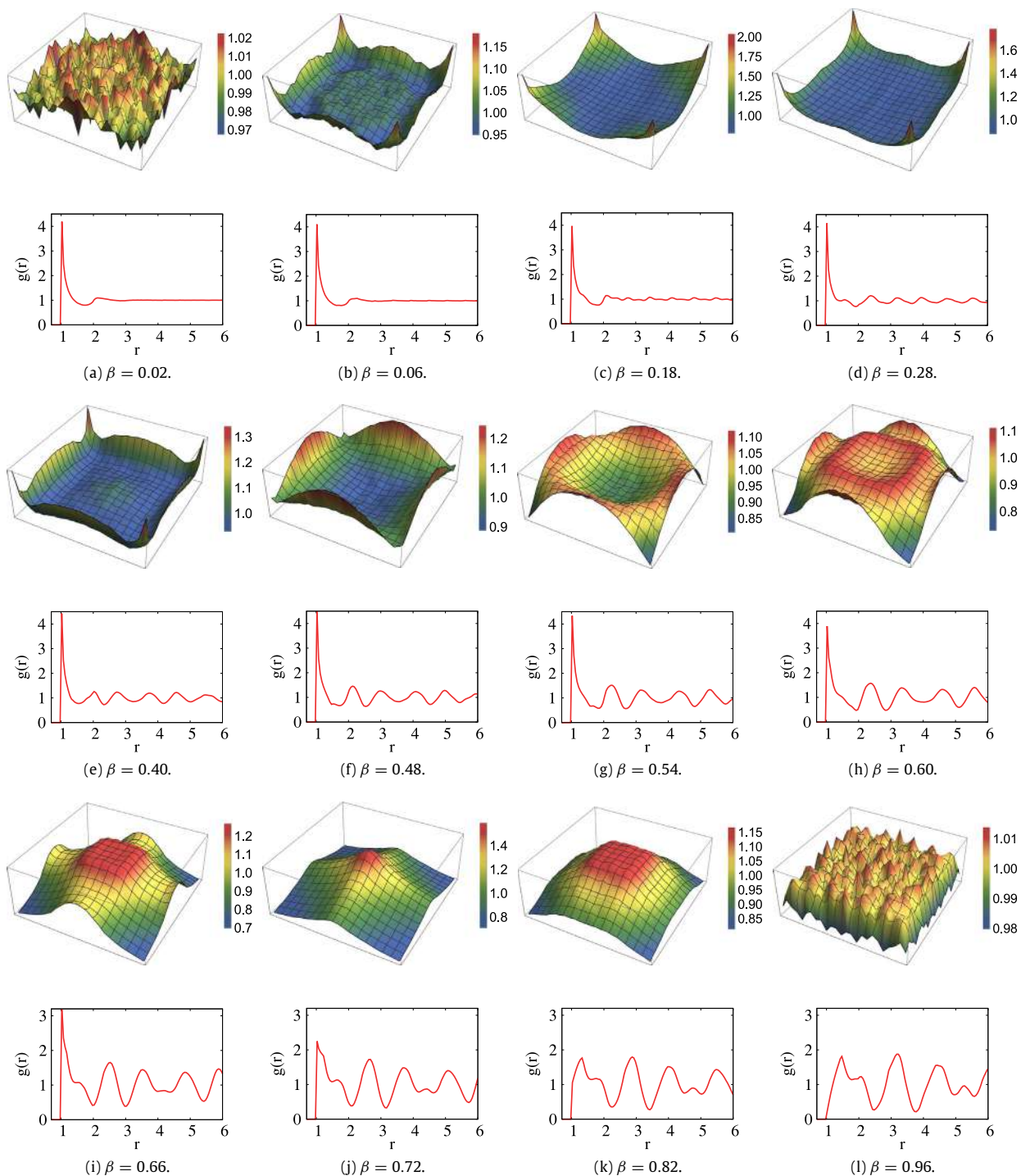


**Fig. 10.** Spatial distribution of particles inside the cell and radial distribution function  $g(r)$  at the jammed state, for the fixed value of cell size  $\alpha = 0.5$  and different values of parameter  $\beta$ .

(f), sides (g), interior ring (h), central square (i), central peak (j), etc., that are predominantly populated with particles. For  $\beta$  below the critical value  $\beta_c$  (Eq. (4)) particles adsorb preferentially at the cell edges. Approaching the critical value of  $\beta_c = 0.85$  ( $\alpha = 0.30$ ), the probability of deposition in the center of cell increases. Close to the critical value, we observe the appearance of pronounced peak of probability distribution in the center of the cell. In addition, as parameter  $\beta$  is increased,

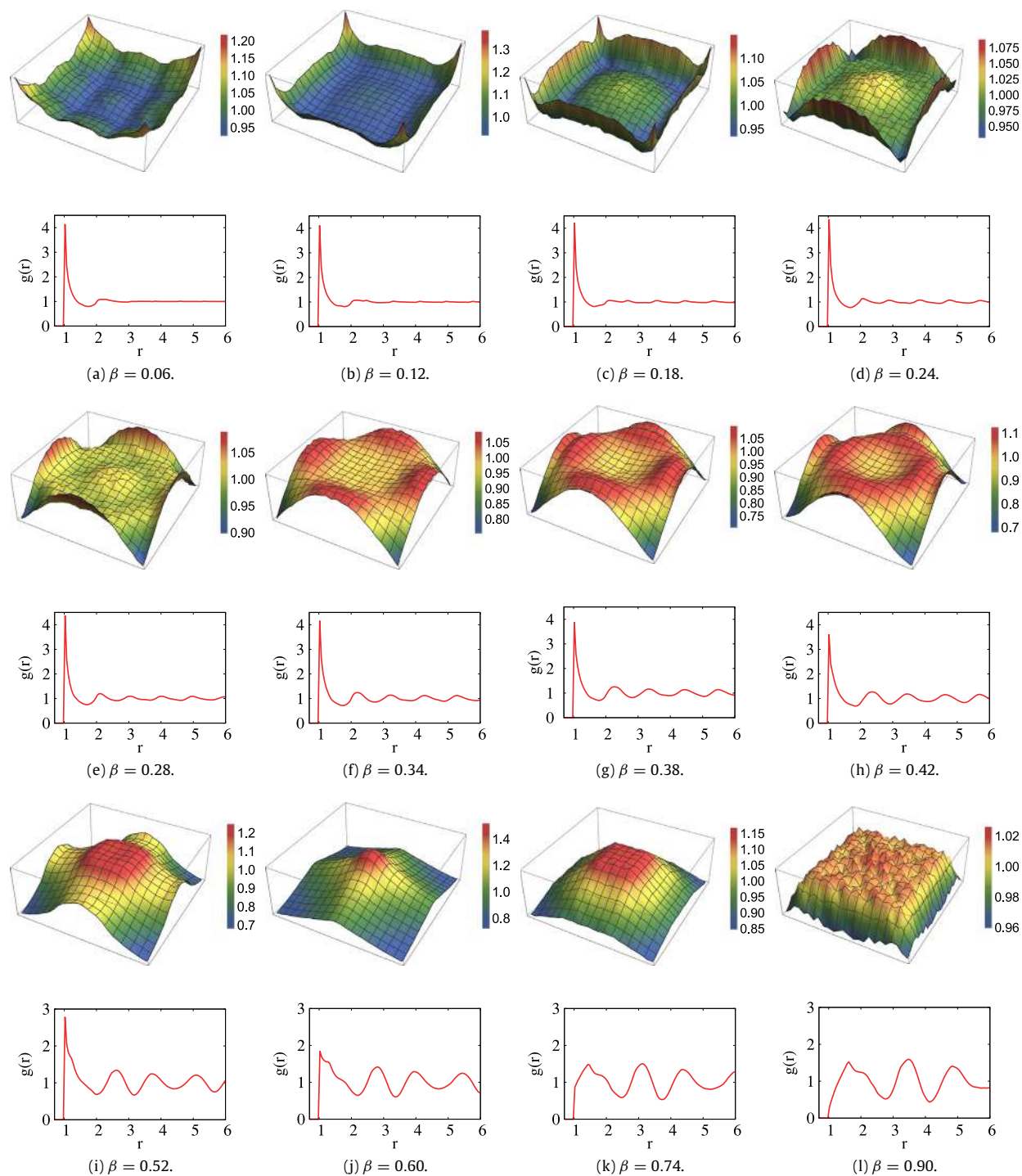


**Fig. 11.** Spatial distribution of particles inside the cell and radial distribution function  $g(r)$  at the jammed state, for the fixed value of cell size  $\alpha = 0.7$  and different values of parameter  $\beta$ .

one observes that the radial distribution functions  $g(r)$  becomes more detailed with peaks becoming sharper. There is also peak splitting, related to a weaker excluded volume interaction between particles deposited into different cells. For the large  $\beta = 0.98$ , since adsorption on an empty cell is weakly constrained by particles previously adsorbed on a neighboring one, adsorption can occur, with almost equal probability all over the cell (Fig. 9(I)). The radial distribution function now shows a

series of well developed peaks which correspond to the various cell-defined distances in the square lattice matrix. Finally, in the NICCA regime ( $\beta > 1$ ), the adsorption inside cells is entirely uniform and the shape of the radial distribution function  $g(r)$  is no longer changing (not shown here).

Numerical simulations for the other cell sizes,  $\alpha = 0.5, 0.7$ , produce qualitatively similar results for the spatial distribution of particles inside the cell leading to qualitatively same phenomenology (see Figs. 10 and 11). However, increasing the value of  $\alpha$  in the NICCA-SPCA regime increases the uncertainty in the position of the particle within the cell, i.e., it leads to peak broadening of the radial distribution function  $g(r)$ .

#### 4. Concluding remarks

We have investigated numerically RSA of disk-shaped particles on nonuniform planar substrates, with focus on the kinetics of deposition process in the interacting cell–cell adsorption (ICCA) regime. We have considered as a pattern the equal-size cells with square shape, positioned in a square-lattice matrix. An efficient numerical algorithm was implemented to simulate the disk deposition in the case of single particle per-cell adsorption (SPCA).

It was demonstrated that the two geometrical parameters, the cell size  $\alpha$  and the cell–cell separation  $\beta$ , have a striking influence on the kinetic properties of a deposition process, as well as on the in-cell particle population. By studying the temporal evolution of the first derivative of coverage  $\theta(t)$  we have found that the asymptotic approach of the coverage fraction  $\theta(t)$  to its jamming limit  $\theta_j$  is algebraic if the parameters  $\alpha$  and  $\beta$  satisfy the simple condition (3). If the relation (3) is valid, particles adsorbed on neighboring cells can block adsorption inside the central cell, so that there is no minimum finite area available for adsorption. A vanishing-small area can be created with non-zero probability and power law (1) holds in the late stage of the deposition process.

If the geometry of the pattern does not satisfy the criteria (3), the approach of the coverage fraction  $\theta(t)$  to the jamming limit is not consistent with the power law behavior. The existence of the minimum finite area where the center of a disk can land without overlapping a previously adsorbed particle is a sufficient condition for deviation from the algebraic asymptotic approach (1). When the geometry of the pattern approaches towards noninteracting condition ( $\beta \rightarrow 1.0^-$ ), the asymptotic approach of the coverage fraction  $\theta(t)$  to its jamming limit  $\theta_j$  becomes closer to the exponential law (2). It must be stressed that the appearance of even a slight cell–cell excluded volume interaction violates the exponential asymptotic approach. Consequently, changing the pattern in our numerical model allows to interpolate the deposition kinetics between the continuum limit and the lattice-like behavior.

To examine the short scale structure in the jammed-state coverings, we evaluated the spatial distribution of particles inside the cell and radial distribution function  $g(r)$ . Interesting, non-trivial spatial distributions are observed, with local order resulting not only from the constraint of the pattern, but also due to steric effects that make certain insertions of particles impossible owing to an effective high local density. Close to the critical values of parameters  $\alpha$  and  $\beta$  determined with Eq. (4), we observe the appearance of the pronounced peak of probability distribution in the center of the cell. Hence, by tuning the pattern parameters on the critical values (Eq. (4)), it is possible to obtain jammed-state covering with high ordered structure.

#### Acknowledgments

This work was supported by the Ministry of Education, Science, and Technological Development of the Republic of Serbia under projects ON171017, III43007 and OI1611005. Numerical simulations were run on the PARADOX supercomputing facility at the Scientific Computing Laboratory of the Institute of Physics Belgrade.

#### References

- [1] Irving R. Epstein, Kinetics of large-ligand binding to one-dimensional lattices: theory of irreversible binding, *Biopolymers* 18 (1979) 765–788.
- [2] Paul R. Van Tassel, Pascal Viot, Gilles Tarjus, A kinetic model of partially reversible protein adsorption, *J. Chem. Phys.* 106 (1997) 761–770.
- [3] J. Feder, Random sequential adsorption, *J. Theoret. Biol.* 87 (1980) 237.
- [4] S. Ravichandran, J. Talbot, Mobility of adsorbed proteins: a brownian dynamics study, *Biophys. J.* 78 (2000) 110–120.
- [5] Vladimir Privman, Recent theoretical results for nonequilibrium deposition of submicron particles, *J. Adhes.* 74 (2000) 421–440.
- [6] J. Alexander Liddle, Yi Cui, Paul Alivisatos, Lithographically directed self-assembly of nanostructures, *J. Vac. Sci. Technol., B: Microelectron. Nanometer Struct. Process., Meas., Phenom.* 22 (2004) 3409–3414.
- [7] Arsen V. Subashiev, Serge Luryi, Random sequential adsorption of shrinking or expanding particles, *Phys. Rev. E* 75 (2007) 011123.
- [8] Oleksandr Gromenko, Vladimir Privman, Random sequential adsorption of objects of decreasing size, *Phys. Rev. E* 79 (2009) 011104.
- [9] Ranjan D. Deshmukh, Gavin A. Buxton, Nigel Clarke, Russell J. Composto, Nanoscale block copolymer templates decorated by nanoparticle arrays, *Macromolecules* 40 (2007) 6316–6324.
- [10] J.W. Evans, D.R. Burgess, Irreversible reaction on a polymer chain with range two cooperative effects, *J. Chem. Phys.* 79 (1983) 5023–5028.
- [11] C.S. Dias, N.A.M. Araújo, A. Cadilhe, Analytical and numerical study of particles with binary adsorption, *Phys. Rev. E* 85 (2012) 041120.
- [12] Oleksandr Gromenko, Vladimir Privman, M.L. Glasser, Random sequential adsorption model of damage and crack accumulation: exact one-dimensional results, *J. Comput. Theor. Nanosci.* 5 (2008) 2119–2123.
- [13] J.W. Evans, Random and cooperative sequential adsorption, *Rev. Modern Phys.* 65 (1993) 1281–1329.
- [14] V. Privman (Ed.), *Nonequilibrium Statistical Mechanics in One Dimension*, Cambridge University Press, Cambridge, UK, 1997 (a collection of review articles).
- [15] V. Privman, *Colloids Surf. A* 165 (2000) 1 (a collection of review articles).

- [16] P. Parisse, D. Luciani, A. D'Angelo, S. Santucci, P. Zuppella, P. Tucceri, A. Reale, L. Ottaviano, Patterning at the nanoscale: atomic force microscopy and extreme ultraviolet interference lithography, *Mater. Sci. Eng. B* 165 (2009) 227–230.
- [17] T. Kraus, L. Malaquin, H. Schmid, W. Riess, N.D. Spencer, H. Wolf, Nanoparticle printing with single-particle resolution, *Nature Nanotechnol.* 2 (2007) 570–576.
- [18] R.J. Kershner, L.D. Bozano, C.M. Micheel, A.M. Hung, A.R. Fornof, J.N. Cha, C.T. Rettner, M. Bersani, J. Frommer, P.W.K. Rothmund, G.M. Wallraff, Placement and orientation of individual dna shapes on lithographically patterned surfaces, *Nature Nanotechnol.* 4 (2009) 557–561.
- [19] A. delCampo, C. Greiner, I. Álvarez, E. Arzt, Patterned surfaces with pillars with controlled 3d tip geometry mimicking bioattachment devices, *Adv. Mater.* 19 (2007) 1973–1977.
- [20] Z. Adamczyk (Ed.), *Particles At Interfaces: Interactions, Deposition, Structure*, in: *Interface Science and Technology*, vol. 9, Elsevier, 2006.
- [21] X. Jin, N.H.L. Wang, G. Tarjus, J. Talbot, Irreversible adsorption on non-uniform surfaces: the random site model, *J. Chem. Phys.* 97 (1993) 4256.
- [22] X. Jin, J. Talbot, N.H.L. Wang, Analysis of steric hindrance effects on adsorption kinetics and equilibria, *AIChE J.* 40 (1994) 1685.
- [23] C. Oleyar, J. Talbot, Reversible adsorption on random site surface, *Physica A* 376 (2007) 27–37.
- [24] Z. Adamczyk, P. Weronki, E. Musial, Irreversible adsorption of hard spheres at random site (heterogeneous) surfaces, *J. Chem. Phys.* 116 (2002) 4665.
- [25] Z. Adamczyk, B. Siwek, P. Weronki, E. Musial, Irreversible adsorption of colloid particles at heterogeneous surfaces, *Appl. Surf. Sci.* 196 (2002) 250.
- [26] Zbigniew Adamczyk, Katarzyna Jaszcz, Aneta Michna, Barbara Siwek, Lilianna Szyk-Warszyska, Maria Zembala, Irreversible adsorption of particles on heterogeneous surfaces, *Adv. Colloid Interface Sci.* 118 (2005) 25–42.
- [27] A. Cadilhe, N.A.M. Araújo, V. Privman, Random sequential adsorption: from continuum to lattice and pre-patterned substrates, *J. Phys.: Condens. Matter* 19 (2007) 065124.
- [28] N.A.M. Araújo, A. Cadilhe, Vladimir Privman, Morphology of fine-particle monolayers deposited on nanopatterned substrates, *Phys. Rev. E* 77 (2008) 031603.
- [29] J.F. Marques, A.B. Lima, N.A.M. Araújo, A. Cadilhe, Effect of particle polydispersity on the irreversible adsorption of fine particles on patterned substrates, *Phys. Rev. E* 85 (2012) 061122.
- [30] N. Araujo, *Nonequilibrium Thin-Film Growth: Kinetics of Deposition and Post Evolution Relaxation*, LAP LAMBERT Academic Publishing, 2010.
- [31] D. Stojiljković, J.R. Šćepanović, S.B. Vrhovac, N.M. Švrakić, Structural properties of particle deposits at heterogeneous surfaces, *J. Stat. Mech. Theory Exp.* 2015 (2015) P06032.
- [32] P. Philippe, D. Bideau, Numerical model for granular compaction under vertical tapping, *Phys. Rev. E* 63 (2001) 051304.
- [33] P. Richard, P. Philippe, F. Barbe, S. Bourles, X. Thibault, D. Bideau, Analysis by x-ray microtomography of a granular packing undergoing compaction, *Phys. Rev. E* 68 (2003) 020301(R).
- [34] T. Aste, Variations around disordered close packing, *J. Phys.: Condens. Matter* 17 (2005) S2361–S2390.
- [35] T. Aste, Volume fluctuations and geometrical constraints in granular packs, *Phys. Rev. Lett.* 96 (2006) 018002.
- [36] D. Arsenović, S.B. Vrhovac, Z.M. Jakšić, Lj. Budinski-Petković, A. Belić, Simulation study of granular compaction dynamics under vertical tapping, *Phys. Rev. E* 74 (2006) 061302.
- [37] R. Swendsen, Dynamics of random sequential adsorption, *Phys. Rev. A* 24 (1981) 504–508.
- [38] Y. Pomeau, Some asymptotic estimates in the random parking problem, *J. Phys. A: Math. Gen.* 13 (1980) L193.
- [39] B. Bonnier, Random sequential adsorption of binary mixtures on a line, *Phys. Rev. E* 64 (2001) 066111.
- [40] D.J. Burridge, Y. Mao, Recursive approach to random sequential adsorption, *Phys. Rev. E* 69 (2004) 037102.
- [41] Einar L. Hinrichsen, Jens Feder, Torstein Jøssang, Geometry of random sequential adsorption, *J. Stat. Phys.* 44 (1986) 793–827.
- [42] M.C. Bartelt, V. Privman, Kinetics of irreversible multilayer adsorption: one-dimensional models, *J. Chem. Phys.* 93 (1990) 6820.
- [43] S.S. Manna, N.M. Švrakić, Random sequential adsorption: line segments on the square lattice, *J. Phys. A: Math. Gen.* 24 (1991) L671–L676.
- [44] Lj. Budinski-Petković, U. Kozmidis-Luburić, Random sequential adsorption on a triangular lattice, *Phys. Rev. E* 56 (1997) 6904.
- [45] Lj. Budinski-Petković, S.B. Vrhovac, I. Lončarević, Random sequential adsorption of polydisperse mixtures on discrete substrates, *Phys. Rev. E* 78 (2008) 061603.
- [46] Vladimir Privman, Han Yan, Random sequential adsorption on imprecise lattice, *J. Chem. Phys.* 144 (2016) 244704.
- [47] Einar L. Hinrichsen, Jens Feder, Torstein Jøssang, Random packing of disks in two dimensions, *Phys. Rev. A* 41 (1990) 4199–4209.
- [48] P.G. Szabó, M.Cs. Markót, T. Csendes, E. Specht, L.G. Casado, I. García, New approaches to circle packing in a square (with program codes), in: *Optimization and Its Applications*, Vol. 6, Springer Science + Business Media, LLC, New York, USA, 2007.
- [49] Thomas M. Truskett, Salvatore Torquato, Srikanth Sastry, Pablo G. Debenedetti, Frank H. Stillinger, Structural precursor to freezing in the hard-disk and hard-sphere systems, *Phys. Rev. E* 58 (1998) 3083–3088.



# Response properties in the adsorption–desorption model on a triangular lattice



J.R. Šćepanović<sup>a</sup>, D. Stojiljković<sup>a</sup>, Z.M. Jakšić<sup>a</sup>, Lj. Budinski-Petković<sup>b</sup>,  
S.B. Vrhovac<sup>a,\*</sup>

<sup>a</sup> Scientific Computing Laboratory, Institute of Physics Belgrade, University of Belgrade, Pregrevica 118, Zemun 11080, Belgrade, Serbia

<sup>b</sup> Faculty of Engineering, University of Novi Sad, Trg D. Obradovića 6, Novi Sad 21000, Serbia

## HIGHLIGHTS

- Reversible RSA of objects of various shapes on a 2D triangular lattice is studied.
- We study the response of the model to an abrupt change in desorption probability.
- Short-time response strongly depends on the symmetry properties of the shapes.
- Density correlations decay slower for more symmetrical shapes.
- We observe the weakening of correlation features in multicomponent systems.

## ARTICLE INFO

### Article history:

Received 23 August 2015

Received in revised form 18 December 2015

Available online 2 February 2016

### Keywords:

Random sequential adsorption

Desorption

Short-term memory effects

Triangular lattice

## ABSTRACT

The out-of-equilibrium dynamical processes during the reversible random sequential adsorption (RSA) of objects of various shapes on a two-dimensional triangular lattice are studied numerically by means of Monte Carlo simulations. We focused on the influence of the order of symmetry axis of the shape on the response of the reversible RSA model to sudden perturbations of the desorption probability  $P_d$ . We provide a detailed discussion of the significance of collective events for governing the time coverage behavior of shapes with different rotational symmetries. We calculate the two-time density–density correlation function  $C(t, t_w)$  for various waiting times  $t_w$  and show that longer memory of the initial state persists for the more symmetrical shapes. Our model displays nonequilibrium dynamical effects such as aging. We find that the correlation function  $C(t, t_w)$  for all objects scales as a function of single variable  $\ln(t_w)/\ln(t)$ . We also study the short-term memory effects in two-component mixtures of extended objects and give a detailed analysis of the contribution to the densification kinetics coming from each mixture component. We observe the weakening of correlation features for the deposition processes in multicomponent systems.

© 2016 Elsevier B.V. All rights reserved.

## 1. Introduction

The understanding of random sequential adsorption (RSA) model has attracted large attention as a paradigmatic approach towards irreversibility, as well as due to the strong departure of the process from equilibrium behavior. In the RSA model [1], particles are added randomly and sequentially onto a substrate without overlapping each other. RSA model assumes that

\* Corresponding author.

E-mail address: [vrhovac@ipb.ac.rs](mailto:vrhovac@ipb.ac.rs) (S.B. Vrhovac).

URL: <http://www.ipb.ac.rs/~vrhovac/> (S.B. Vrhovac).

deposited particles can neither diffuse along, nor desorb from the surface. The kinetic properties of a deposition process are described by the time evolution of the coverage  $\theta(t)$ , which is the fraction of the substrate area covered by the adsorbed particles. Within a monolayer deposit, each adsorbed particle affects the geometry of all later placements. Due to the blocking of the substrate area, at large times the coverage approaches the jammed-state value  $\theta_j$ , where only gaps too small to fit new particles are left in the monolayer.

In pursuit of understanding the various aspects of the adsorption phenomenon large number of studies have taken place. A comprehensive survey on RSA and cooperative sequential adsorptions is given by Evans [2]. Other surveys include Privman [3–5], Cadihne et al. [4], Senger et al. [6], and Talbot et al. [7].

In many real physical situations it is necessary to consider the possibility of desorption of deposited particles [8–10]. Adsorption–desorption processes are important in the binding of ions to a Langmuir monolayer [11], and in many catalytic reactions. Binding and unbinding of kinesin motors to microtubules [12], of myosin to actin filaments, and of proteins to DNA are commonly studied biological examples. Possibility of desorption makes the process reversible and the system ultimately reaches an equilibrium state when the rate of desorption events balances the rate of adsorption events. The kinetics of the reversible RSA is governed by the ratio of adsorption to desorption rate,  $K = k_+/k_-$ . For large values of  $K$ , there is a rapid approach to density  $\theta \simeq \theta_j$ , followed by a slow relaxation to a higher steady-state value  $\theta_\infty$  [13–16].

The reversible RSA model is frequently used by many authors to reproduce qualitatively the densification kinetics and other features of weakly vibrated granular materials [9,17,10]. The phenomenon of granular compaction involves the increase of the density of a granular medium subjected to shaking or tapping [18–23]. The relaxation dynamics is extremely slow, taking many thousands of taps to approach the steady state, and it slows down for lower vibration intensities. The final steady-state density is a decreasing function of the vibration intensity [23]. Dynamics of the reversible RSA model depends on the excluded volume and geometrical frustration, just as in the case of granular compaction. This model can be regarded as a simple picture of a horizontal layer of a granular material, perpendicular to the tapping force. As a result of a tapping event, particles leave the layer at random and compaction proceeds when particles fall back into the layer under the influence of gravity. The ratio of desorption to adsorption rate  $1/K = k_-/k_+$  within the model plays a role similar to the vibration intensity  $\Gamma$  in real experiments [24] ( $\Gamma$  is defined as the ratio of the peak acceleration of the tap to the gravitational acceleration  $g$ ).

One of the striking features of granular materials are the memory effects observed by measuring the short-time response to an instantaneous change in the tapping acceleration  $\Gamma$  [25]. For a sudden decrease in  $\Gamma$  it was observed that on short-time scales the compaction rate increases, while for a sudden increase in  $\Gamma$  the system dilates for short times. This behavior is transient and after several taps there is a crossover to the “normal” behavior, with the relaxation rate becoming the same as in constant vibration intensity mode. Furthermore, Nicolas et al. [26] have also shown that periodic shear compaction exhibits a nontrivial response to a sudden change in shear amplitude. The rapid variation of volume fraction induced by the sudden change of shear angle is proportional and opposite to the angle change. The short-term memory effects observed in granular materials are reflected in the fact that the future evolution of the packing fraction  $\theta$  after time  $t_w$  depends not only on the  $\theta(t_w)$ , but also on the previous tapping history. It is important to note that the parking lot model (PLM, 1D off-lattice reversible RSA model) [24,9,27,17] is a widely used model which can reproduce qualitatively the short-term memory effects of a weakly vibrated granular material. In Ref. [10] we have presented the detailed studies of the short-term memory effects in the framework of a two-dimensional reversible RSA model on a square lattice.

An important issue in two-dimensional deposition is the influence of the shape of the adsorbed particle. It is well known that the size, aspect ratio and symmetry properties of the object have a significant role in the processes of both irreversible and reversible deposition. The numerical analyses for the irreversible deposition of various shapes and their mixtures on a triangular lattice [28,29] establish that the approach to the jamming limit follows the exponential law with the rate dependent mostly on the order of symmetry axis of the shape. In the reversible case of deposition on a triangular lattice [15,30], we have found that the coverage kinetics is severely slowed down with the increase of the order of symmetry of the shape.

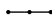


The main goal of the present study is to investigate the interplay between the response of the reversible RSA model to sudden perturbations of the desorption probability  $P_d$  and the symmetry properties of deposited shapes. Numerical simulations of adsorption–desorption processes are performed for various shapes on the triangular lattice, shown in Table 1. These shapes are made of self-avoiding walks of the same length  $\ell = 2$ , but they differ in their symmetry properties. The response in the evolution of the density  $\theta(t)$  to a change in the desorption probability  $P_d$  at a given time  $t_w$  is accompanied by transformation of the local configurations in the covering. Essentially, collective (two-particle) events are responsible for the evolution of  $\theta$  for  $\theta > \theta_j$ . Size of the objects and their symmetry properties have a significant influence on these collective events, thus affecting the kinetics of the deposition process [15,31,30]. Since we focus our interest on the influence of symmetry of the object on the response of the system to sudden perturbation of the desorption probability  $P_d$ , it is necessary to analyze the processes with the objects of the same size. In this paper we also study the response of two-component mixtures of extended objects (see, Table 1) to sudden perturbations of the desorption probability  $P_d$ . We did carry out a detailed analysis of the contribution to the densification kinetics coming from each mixture component. Finally, we study the nonequilibrium two-time density–density correlation function  $C(t, t_w)$ . We focus, in particular, on the influence of symmetry properties of the shapes on the decay of  $C(t, t_w)$  and aging effects. This work provides for the first time the link between the short-term memory effects and intrinsic properties of the shapes.

Recently, we have analyzed the growth of the coverage  $\theta(t)$  above the jamming limit to its steady-state value  $\theta_\infty$  within the framework of the adsorption–desorption model of dimers in one dimension [32]. We reported a numerical evidence



**Table 1**

Various shapes (x) of length  $\ell^{(x)} = 2$  on a triangular lattice. Here  $n_s^{(x)}$  denotes the order of the symmetry axis of the shape (x),  $s^{(x)}$  is the object size, and  $\theta_j^{(x)}$  is the jamming coverage. The numbers in parentheses are the numerical values of the standard uncertainty of  $\theta_j^{(x)}$  referred to the last digits of the quoted value.

(x)	Shape	$n_s^{(x)}$	$s^{(x)}$	$\ell^{(x)}$	$\theta_j^{(x)}$
(A)		2	2		0.8362(4)
(B)		1	1.5	2	0.8345(5)
(C)		3	1		0.7970(4)

that the time needed for a system to reach the given coverage  $\theta$  can be significantly reduced if  $P_d$  decreases both stepwise and linearly (continuously) over a certain time domain. Based on the results in the present paper, one would expect that the growth of the coverage in the case of the two-dimensional reversible RSA model can also be accelerated by decreasing the desorption rate during the deposition process. However, our results indicate that the efficiency of this process depends on the symmetry properties of the deposited objects. This must be taken into account when developing an optimal protocol which significantly hastens the process for achieving high coverage densities.

The paper is organized as follows. Section 2 describes the details of the simulations. We give the simulation results and discussions in Section 3. Finally, Section 4 contains some additional comments and final remarks.

## 2. Definition of the model and numerical simulation

The depositing shapes are modeled by directed self-avoiding walks on a triangular lattice. A self-avoiding shape of length  $\ell$  is a sequence of distinct vertices  $(\omega_0, \dots, \omega_\ell)$  such that each vertex is a nearest neighbor of its predecessor. Consequently, a walk of length  $\ell$  covers  $\ell + 1$  lattice sites. On a triangular lattice objects with a symmetry axis of first, second, third, and sixth order can be formed. Rotational symmetry of order  $n_s$ , also called  $n$ -fold rotational symmetry, with respect to a particular axis perpendicular to the triangular lattice, means that rotation by an angle of  $2\pi/n_s$  does not change the object. In Table 1 three different shapes that can be made by self-avoiding walks of length  $\ell = 2$  are shown. It should be noted that size  $s$  of an object is taken as the greatest projection of the walk that makes the object on one of the six directions. Thus the size of a dot is  $s = 0$ , the size of a one-step walk is  $s = 1$ , and for example the size of the second object (B) in Table 1 is  $s = 1.5$  in lattice spacing.

The Monte Carlo simulations are performed on a triangular lattice of size  $L^2 = 120 \times 120$ . At each Monte Carlo step adsorption is attempted with probability  $P_a$  and desorption with probability  $P_d$ . In the simulations of deposition processes with desorption, the kinetics is governed by the desorption to adsorption probability ratio  $\Gamma = P_d/P_a$  [33,34]. Since we are interested in the ratio  $\Gamma$ , in order to save computer time, it is convenient to take the adsorption probability to be  $P_a = 1$ , i.e., to try an adsorption at each Monte Carlo step.

We start with an initially empty triangular lattice. Adsorption and desorption processes perform simultaneously with corresponding probabilities. For each of these processes, a lattice site is chosen at random. In the case of adsorption, we attempt to place the object with the beginning at the selected site. If the selected site is unoccupied, one of the six possible orientations is chosen at random and deposition of the object is tried in that direction. We fix the beginning of the walk that makes the shape of length  $\ell$  at the selected site and search whether all successive  $\ell$  sites are unoccupied. If they are empty, we occupy these  $\ell + 1$  sites and place the object. If, however, any of the  $\ell$  sites are already occupied, the deposition attempt is rejected and the configuration remains unchanged. This scheme is usually called conventional or standard model of deposition. The other strategy to perform an RSA, where we check all possible directions from the selected site, is named the end-on model [28]. On the other hand, if the attempted process is desorption and if the selected site is already occupied by a previously adsorbed object, the object is removed with probability  $P_d$  from the layer.

Adsorption–desorption processes on discrete substrates display a surprisingly complex kinetics [9,35]. Here we consider the case of rapid adsorption and slow desorption ( $\Gamma = P_d/P_a \ll 1$ ). Then there exist two time scales controlling the evolution of the coverage  $\theta(t)$ . The first stage of the process is dominated by adsorption events and the kinetics displays an RSA-like behavior. With the growth of the coverage the desorption process becomes more and more important. Increasing the coverage over the jamming limit is possible only due to the collective rearrangement of the adsorbed particles in order to open a hole large enough for the adsorption of an additional particle. We are interested in the approach to the equilibrium coverage in this later, post-jamming time range.

Periodic boundary conditions are used in all directions. The time  $t$  is counted by the number of adsorption attempts and scaled by the total number of lattice sites  $L^2$ . The data are averaged over  $10^3$  independent runs for each shape and each desorption probability. The finite-size effects, which are generally weak, can be neglected for object sizes  $< L/8$  [36].

Furthermore, during the simulation of irreversible deposition we record the number of inaccessible sites in the lattice. A site is inaccessible if it is occupied or it cannot be the beginning of the shape. The jamming limit  $\theta_j$  is reached when the number of inaccessible sites is equal to the total number of lattice sites. Values of jamming coverages  $\theta_j^{(x)}$  for three objects (x)  $\in \{(A), (B), (C)\}$  of length  $\ell = 2$  are given in Table 1. Fig. 1 shows a typical snapshot configuration at coverage fraction  $\theta = 0.89$  obtained in the case of  $P_d = 0.0045$  for line-segments of length  $\ell = 2$  (object (A) from Table 1).

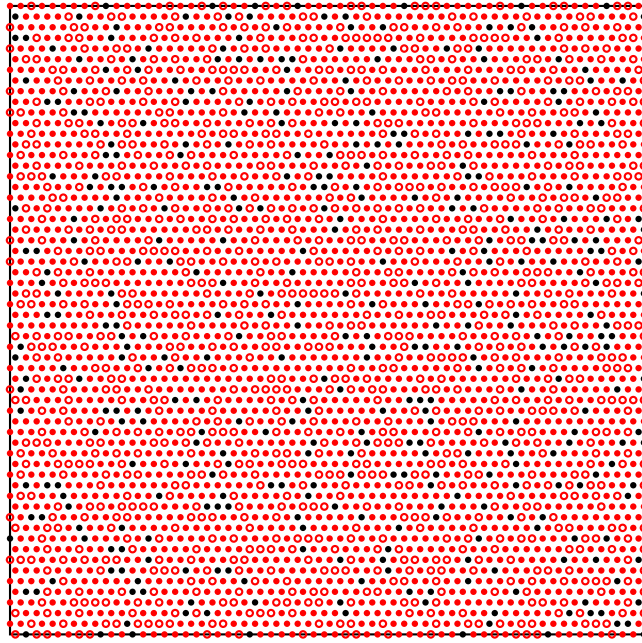


**Fig. 1.** Snapshot of pattern formed during the reversible deposition of object (A) from Table 1 correspond to coverage fraction  $\theta = 0.89$ , and  $P_d = 0.0045$ . Nodes of the grid corresponding to the beginning of the walk that makes the shape are indicated by large open points. Empty nodes are marked with black points. A lattice of size  $L^2 = 60 \times 60$  is used.

### 3. Results and discussion

In order to analyze the response of the reversible RSA model to sudden perturbations of the desorption probability  $P_d$ , we have carried out series of Monte Carlo simulations for objects (A), (B), and (C), all of them starting from an empty lattice. The system was evolved at a fixed desorption probability  $P_d^{(1)}$ . At a certain time,  $t_w$ , the value of the desorption probability  $P_d^{(1)}$  was instantaneously changed to another value  $P_d^{(2)}$ . The variations of coverage  $\theta(t)$  in the case of object (A), for three different values of  $t_w$  are reported in Fig. 2. It must be emphasized that the same kind of numerical experiments for objects (B) and (C) produce qualitatively similar results for the time evolution of the coverage  $\theta(t)$ . First, in Fig. 2 we show the response of the system to the desorption probability shift from  $P_d^{(1)} = 0.0045$  to  $P_d^{(2)} = 0.0015$  at the times  $t_w = 139, 205, 307$  needed for a system to reach the coverages  $\theta_w = 0.87, 0.88, 0.89$ , respectively, in the process of reversible RSA with  $P_d^{(1)} = 0.0045$ . As it can be seen, when  $P_d^{(1)} > P_d^{(2)}$ , the compaction rate of the perturbed system first increases on short-time scales. After a transient, compaction slows down and the rate of compaction crosses over to the one observed at constant desorption probability  $P_d^{(2)}$ .

Fig. 2 also shows typical response of the system at short times after an abrupt change of the desorption probability from  $P_d^{(1)} = 0.0015$  to  $P_d^{(2)} = 0.0045$  at the times  $t_w = 304, 441, 639$  needed for a system to reach the coverages  $\theta_w = 0.87, 0.88, 0.89$ , respectively, in the process of reversible RSA with  $P_d^{(1)} = 0.0015$ . For  $P_d^{(1)} < P_d^{(2)}$  we find a short-term response of the system opposite to the previous case. First, as the desorption probability is increased, one observes a decompaction. Later on, the larger desorption probability  $P_d^{(2)}$  begins to prevail and the compaction proceeds faster, at the normal rate for constant  $P_d^{(2)}$ . In addition, the comparison (not shown here) of the density relaxations  $\theta(t)$  at various changes in the desorption probability  $P_d$  indicates that the amplitude of the jump in the compaction rate is larger for larger jump of the desorption probability  $\Delta P_d = |P_d^{(2)} - P_d^{(1)}|$ . The probabilities of  $P_d^{(1)} = 0.0015$  and  $P_d^{(2)} = 0.0045$  are chosen to provide a wide density range  $\theta \in (0.86, 0.89)$  for all three objects where desorption probability can be abruptly changed. We have verified that usage of different, but sufficiently small, values of desorption probabilities  $P_d^{(1)}$  and  $P_d^{(2)}$  gives quantitatively similar results leading to qualitatively same phenomenology.

This shows that the system has some memory of its history at  $t_w$ . Memory effect implies that the system can be found in states, characterized by the same coverage fraction  $\theta$ , that evolve differently under further reversible deposition with the same desorption probability  $P_d$  [17]. This is illustrated in the inset of Fig. 2. The points M and N correspond to states with equal coverage fraction  $\theta_c = 0.8686$ , equal value of  $P_d = 0.0045$ , but different further evolution. Their responses to the same desorption probability  $P_d$  are different: covering M becomes looser whereas covering N pursues its compaction. In other words, the density evolution  $\theta(t)$  after the points M and N depends not only on the density  $\theta_c$ , but also on the previous tapping history. The memory of the history up to the density  $\theta_c$  is encoded in the arrangement of the objects in the covering.

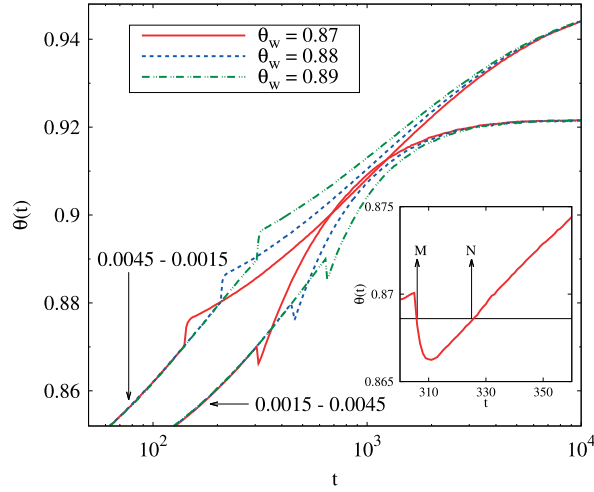


**Fig. 2.** Time evolution of the coverage  $\theta(t)$  for object (A) when the desorption probability is changed from  $P_d^{(1)} = 0.0045$  to  $P_d^{(2)} = 0.0015$  (from  $P_d^{(1)} = 0.0015$  to  $P_d^{(2)} = 0.0045$ ) at times  $t_w = 139, 205, 307$  ( $t_w = 304, 441, 639$ ) needed for the system to reach the coverages  $\theta_w = 0.87, 0.88, 0.89$ , respectively, in the process of reversible RSA with  $P_d^{(1)} = 0.0045$  ( $P_d^{(1)} = 0.0015$ ). Inset: Zoom up on the region around  $t_w = 304$  ( $\theta(t_w) = 0.87$ ) when the desorption probability switches from  $P_d^{(1)} = 0.0015$  to  $P_d^{(2)} = 0.0045$ . The points M and N correspond to states with equal density  $\theta_c = 0.8686$ , equal value of  $P_d^{(2)} = 0.0045$ , but different further evolution.

Interpretation of these results for all objects (A), (B), and (C) is quite straightforward using the results of Refs. [37,9, 34]. The compaction rate just before  $t_w$  is determined by the desorption probability  $P_d(t_w - 0)$  and by the fraction of the substrate,  $\Phi(t_w - 0)$ , that is available for the insertion of a new particle. The quantity  $\Phi(t_w - 0)$  (the insertion probability) strongly depends on the state of the system, but it is not unambiguously determined by the coverage fraction  $\theta(t_w - 0)$  at the same instant [9,10]. When  $P_d$  is abruptly lowered, the first effect is that the particles tend to decrease the fraction of the substrate that is available for deposition of new particles, and the layer becomes more compact. Therefore the rate of compaction first increases with respect to the unperturbed case. At larger times, however, the compaction is slowed down by the creation of a denser substrate and smaller fraction of the layer that is available for the insertion of a new particle.

When the desorption probability  $P_d$  is suddenly increased at  $t_w$ , the first effect is decompaction. On short-time scales, the interplay between the insertion probability and desorption probability leads to the fast density changes. During this transient stage the fraction of the substrate that is available for the insertion of a new particle is an increasing function of time. After this transient interval, the adsorption events prevail, and the compaction proceeds faster. Growing of the insertion probability,  $\Phi(t)$ , during the transient time, leads to the more efficient densification afterwards.

Here we focus our interest on the influence of the order of symmetry axis of the shape on the response of the reversible RSA model to sudden perturbation of the desorption probability  $P_d$ . Consequently, we considered series of numerical experiments where the short-term memory effects were analyzed for the three systems. In this set of experiments the objects (A), (B), and (C) were deposited to the same density  $\theta_w$  with desorption probability  $P_d^{(1)}$ . After the density  $\theta_w$  was achieved, desorption probability  $P_d$  was switched from  $P_d^{(1)}$  to  $P_d^{(2)}$  ( $P_d^{(2)} \leq P_d^{(1)}$ ). In Fig. 3 we show the time evolution of the density  $\theta(t)$  during the deposition of objects (A), (B), and (C), when the desorption probability  $P_d$  is changed from  $P_d^{(1)} = 0.0045$  to  $P_d^{(2)} = 0.0015$ . Here, the results for three different values of  $\theta_w$  are reported, namely, 0.87, 0.88, and 0.89. The time origin for each experiment has been taken at the time when the system reached the prescribed density  $\theta_w$ . In Fig. 4 the same set of numerical experiments is carried out, with the only difference that in this case the desorption probability is changed from  $P_d^{(1)} = 0.0015$  to  $P_d^{(2)} = 0.0045$ . These simulations show that the short-time response to an instantaneous change in desorption probability  $P_d$  strongly depends on the symmetry properties of the shapes. From Figs. 3 and 4, it follows that the change in the compaction rate on short-time scales is less pronounced as order of symmetry axis of the shape  $n_s$  increases.

Qualitative interpretation of these results can be attained by exploiting the mechanism of collective events for governing the late-time changes in the coverage fraction ( $\theta(t) > \theta_j$ ). In the following, we restrict ourselves to the case of weak desorption (large values of  $K = P_a/P_d$ ), when the system of adsorbed particles evolves continuously toward an equilibrium disordered state. When a value of  $\theta_j$  is reached, the rare desorption events are generally followed by immediate readsorption. The total number of particles is not changed by these *single* particle events. Essentially, collective events are responsible for the evolution of coverage fraction  $\theta$  above the jamming limit  $\theta_j$ . The rearrangement of state corresponding to  $\theta > \theta_j$ , to its steady-state value  $\theta_\infty$ , is dominated by the following *two-particle* processes:

- (a) in one process (“2 → 1”), responsible for decreasing the number of deposited objects by 1, two adjacent objects leave and a single one comes in their stead;

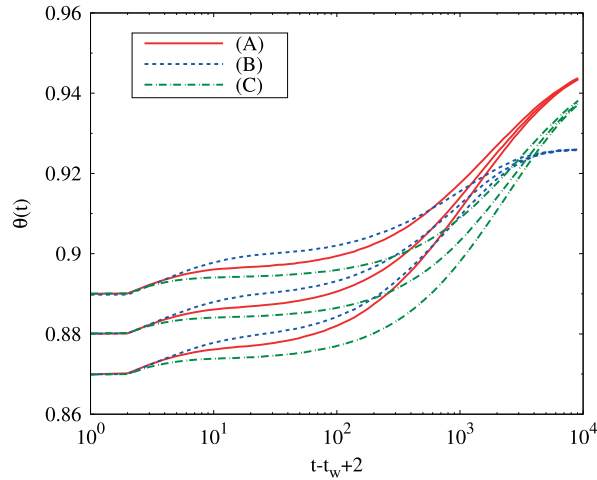


**Fig. 3.** Time evolution of the coverage  $\theta(t)$  for objects (A), (B), and (C) when the desorption probability is changed from  $P_d^{(1)} = 0.0045$  to  $P_d^{(2)} = 0.0015$  at the times  $t_w$  needed for the system to reach the coverages  $\theta_w = 0.87, 0.88, 0.89$  in the process of reversible RSA with  $P_d^{(1)} = 0.0045$ . The time origin for each experiment has been taken at the time when the system reached the prescribed density  $\theta_w$ .

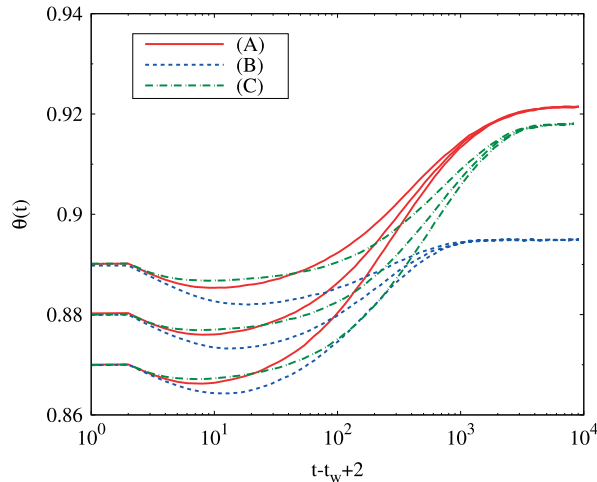


**Fig. 4.** Time evolution of the coverage  $\theta(t)$  for objects (A), (B), and (C) when the desorption probability is changed from  $P_d^{(1)} = 0.0015$  to  $P_d^{(2)} = 0.0045$  at the times  $t_w$  needed for the system to reach the coverages  $\theta_w = 0.87, 0.88, 0.89$  in the process of reversible RSA with  $P_d^{(1)} = 0.0015$ . The time origin for each experiment has been taken at the time when the system reached the prescribed density  $\theta_w$ .

(b) the opposite process (“1  $\rightarrow$  2”) results in adding an extra object to the lattice: an object exits and leaves a space big enough for two objects.

The rate of the “2  $\rightarrow$  1” process has three contributions. First, an object must leave the lattice. Then, an adjacent object must leave before the hole left by the first object fills. Finally, the big hole must be blocked by a badly sited object. In the opposite, “1  $\rightarrow$  2” process, the void left by the object must be large enough for two objects. Note that the first incoming object must park with a sufficient precision in order to leave enough space for the second object.

It is obvious that the process “1  $\rightarrow$  2” has an overall rate proportional to  $P_d$  ( $P_d < 1$ ). Since the process “2  $\rightarrow$  1” includes two consecutive desorption events, it is plausible that its overall rate is proportional to  $(P_d)^2 < P_d < 1$ . That is the main reason why, for coverages that are not close to the steady-state value, the collective event “1  $\rightarrow$  2” is more frequent than the opposite event “2  $\rightarrow$  1”. This regime persists until the coverage is very close to the equilibrium value. Since the coverage fraction  $\theta(t)$  increases and the available surface function  $\Phi$  decreases, the overall rate at which the density increases is progressively reduced. The efficiency of desorption relative to adsorption increases, and the process reaches a steady state in which the rate of the “2  $\rightarrow$  1” process is balanced by the “1  $\rightarrow$  2” process.

Note that in Ref. Kolan et al. [24], the authors calculated the transition rates for the collective processes “1  $\rightleftharpoons$  2” in the case of a 1D RSA model and found that these rates account for the additional slow time scales. Ghaskadvi and Dennin [11] directly monitored the transition rates for the two-particle processes “1  $\rightleftharpoons$  2” as part of the simulation. They have directly confirmed the importance of multiparticle transitions “1  $\rightleftharpoons$  2” for governing the late time behavior of the system.

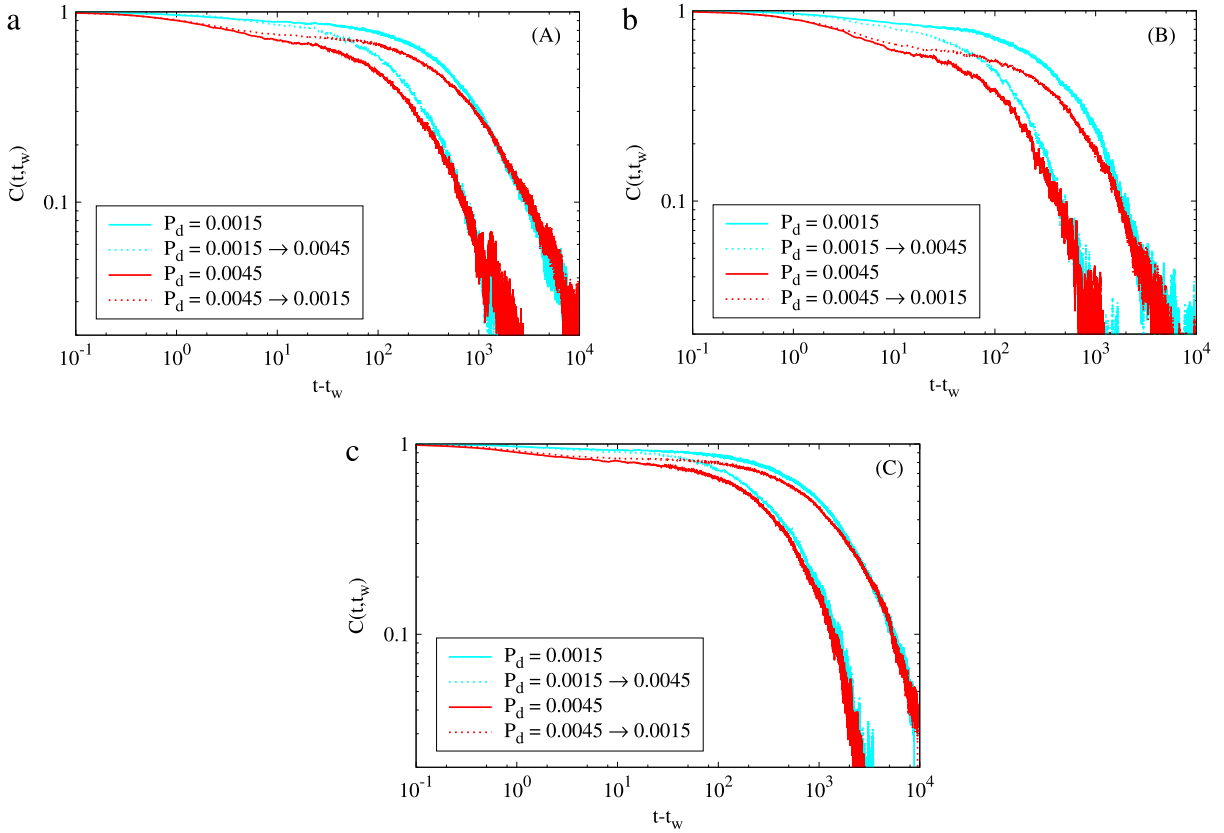


**Fig. 5.** Two-time density–density correlation function  $C(t, t_w)$  for objects (a) (A), (b) (B), and (c) (C), as a function of  $t - t_w$ . The waiting time  $t_w$  corresponds to the time needed for the system to reach the coverage  $\theta_w = 0.88$ . The solid lines represent the temporal behavior of  $C(t, t_w)$  obtained for the fixed desorption probabilities  $P_d = 0.0015, 0.0045$ , as indicated in the legend. The dashed lines represent the temporal dependence of  $C(t, t_w)$  obtained from the runs during which an abrupt change of desorption probability  $P_d^{(1)} = 0.0045 \rightarrow P_d^{(2)} = 0.0015$  ( $P_d^{(1)} = 0.0015 \rightarrow P_d^{(2)} = 0.0045$ ) occurs at instant  $t_w$ , as indicated in the legend.

Now we try to explain how the order of symmetry axis of the shape changes the dynamics of the collective processes. Symmetry properties of the shapes have a significant influence on the filling of small isolated targets on the lattice. Indeed, there is only a restricted number of possible orientations in which an object can reach a previously opened location, provided the location is small enough. A shape with a symmetry axis of higher order has a greater number of possible orientations for deposition into small isolated locations on the lattice, and therefore enhanced probability of single-particle readsorption. This extends the mean waiting time between consecutive two-particle events “1 → 2”, responsible for the density growth above  $\theta_j$ , and causes a slowing down of the density growth. On the contrary, for the asymmetrical shapes (angled objects) there is a greater probability for blocking the neighboring sites. The noticeable drop in the probability of single-particle readsorption for the asymmetrical shapes is thus a clear consequence of the enhanced frustration of the spatial adsorption. Therefore, desorption process effectively opens holes that are large enough for insertion of two or more particles. This reduces the mean waiting time between consecutive multiparticle events which leads to more rapid growth of the density. When  $P_d$  is abruptly lowered, such a different object view is the cause of the enhanced density growth in the case of asymmetrical shapes as compared to those in the case of more round (symmetric) shapes. When the desorption probability  $P_d$  is suddenly increased, decompaction rate of the perturbed system on short-time scales is larger for shapes with a symmetry axis of lower order (Fig. 4). This is a consequence of the fact that unlike for the more symmetrical objects, much less orientations are allowed for irregular and asymmetric shapes falling in the isolated selective target spaces.

Below we try to further quantitatively characterize the out-of equilibrium dynamics in our system. Specifically, we have evaluated the two-time density–density correlation function,  $C(t, t_w)$ , and qualitatively analyzed its dependence on symmetry properties of the shapes. The normalized two-time density–density correlation function is defined as follows,

$$C(t, t_w) = \frac{\langle \theta(t)\theta(t_w) \rangle - \langle \theta(t) \rangle \langle \theta(t_w) \rangle}{\langle \theta^2(t_w) \rangle - \langle \theta(t_w) \rangle^2}, \quad t \geq t_w, \quad (1)$$

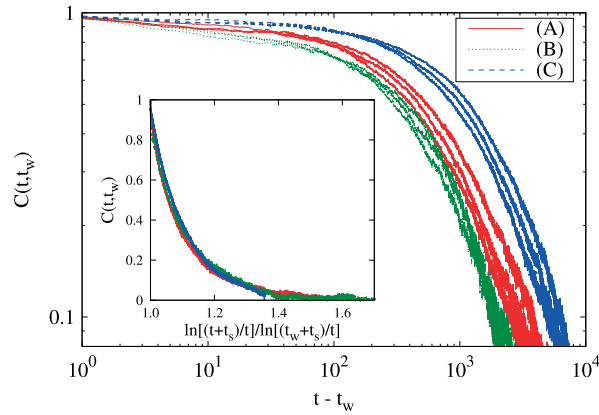


**Fig. 6.** Two-time density–density correlation function  $C(t, t_w)$  for objects (A), (B), and (C), as a function of  $t - t_w$ . The waiting times  $t_w$  for each object correspond to the time needed for the system to reach the coverages  $\theta_w = 0.87, 0.88, 0.89$  in the process of reversible RSA with  $P_d = 0.0015$ . The aging behavior is evident. Inset: The correlation  $C(t, t_w)$  as a function of the scaling variable  $\alpha = \ln[(t_0 + t_s)/\tau] / \ln[(t + t_s)/\tau]$ . Fitting parameters are  $t_s = 1760$ , and  $\tau(A) = 81, \tau(B) = 210, \tau(C) = 43$ .

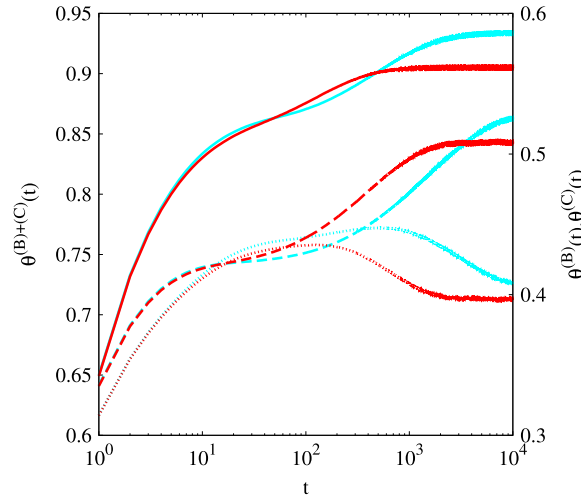


**Fig. 7.** Shown here is the time dependence of the coverage fraction  $\theta^{(B)+(C)}$  for the mixture (B) + (C) and its components for two different values of desorption probability,  $P_d = 0.0015, 0.0045$ . Black (red) and grey (light blue) lines represent the results obtained for  $P_d = 0.0045$  and  $P_d = 0.0015$ , respectively. The solid lines represent the temporal behavior of the coverage fraction  $\theta^{(B)+(C)}(t)$  (left-hand axis). The dashed and dotted lines are plotted against the right-hand axis and give the coverage fraction versus time  $t$  of the component shapes (C),  $\theta^{(C)}(t)$  (dashed), and (B),  $\theta^{(B)}(t)$  (dotted). (For interpretation of the references to color in this figure legend, the reader is referred to the web version of this article.)

where the angular brackets  $\langle \dots \rangle$  denote an average over independent runs. In order to obtain reasonable statistics, it is necessary to average over many independent runs (typically  $10^4$ ). Out of equilibrium,  $C(t, t_w)$  is a function of both times,  $t$  and  $t_w$ .

In Fig. 5 we show the behavior of the correlation function  $C(t, t_w)$  for objects (A), (B), and (C). The waiting time  $t_w$  corresponds to the time needed for a system to reach the coverage  $\theta_w = 0.88$ . Numerical simulations for other densities,  $\theta_w = 0.87, 0.89$ , produce qualitatively similar results for the time evolution of the correlation function  $C(t, t_w)$ . In each plot of Fig. 5, the temporal dependence of  $C(t, t_w)$  is displayed for the fixed desorption probabilities,  $P_d = 0.0015, 0.0045$ . For comparison, we also show the temporal dependence of  $C(t, t_w)$  calculated from  $10^4$  independent runs during which an abrupt change of desorption probability  $P_d^{(1)} = 0.0045 \rightarrow P_d^{(2)} = 0.0015$  ( $P_d^{(1)} = 0.0015 \rightarrow P_d^{(2)} = 0.0045$ ) occurs at instant  $t_w$ . Correlation function obtained from the numerical simulation in which there is an instantaneous change of desorption probability  $P_d^{(1)} \rightarrow P_d^{(2)}$ , interpolates between two correlation functions calculated for constant desorption probabilities  $P_d^{(1)}$  and  $P_d^{(2)}$ . At short times, this correlation function behaves as  $C(t, t_w)$  obtained in the case when the desorption probability has the constant value  $P_d^{(1)} = 0.0045$  ( $P_d^{(1)} = 0.0015$ ). However, its long time behavior is consistent with the decay of  $C(t, t_w)$  obtained in the case when the desorption probability has the constant value  $P_d^{(2)} = 0.0015$  ( $P_d^{(2)} = 0.0045$ ). By comparing the three panels in Fig. 5, it is obvious that global properties of the correlation function  $C(t, t_w)$  of the density fluctuations depend on the order of symmetry axis of the shape  $n_s$ : as  $n_s$  grows, the correlation decays slower. In

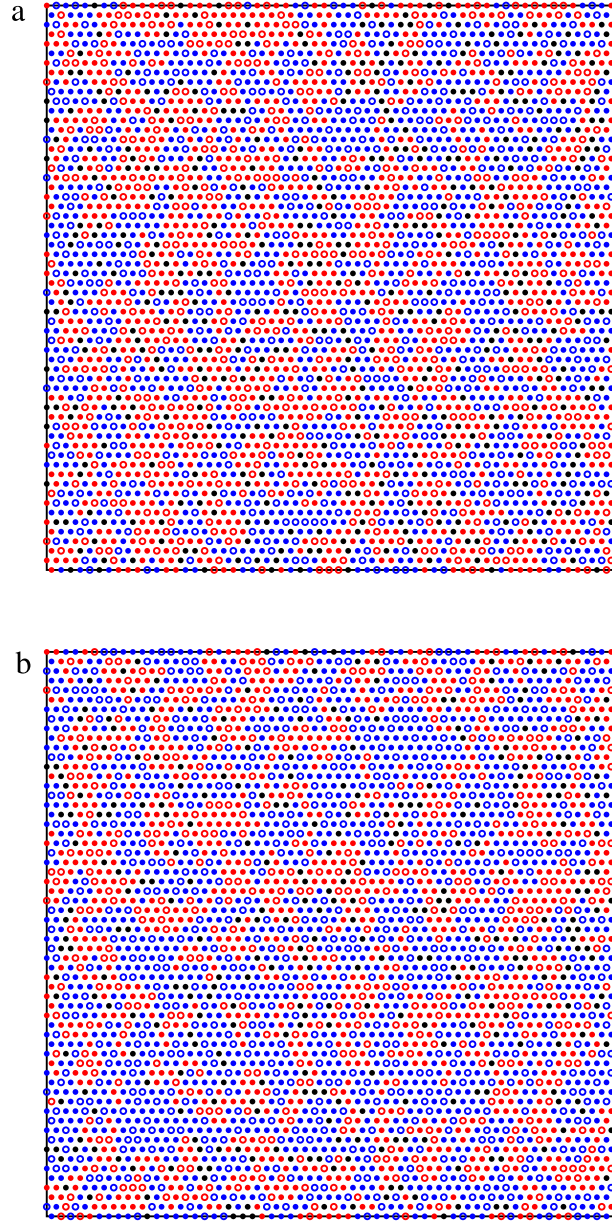


**Fig. 8.** Snapshot of pattern formed during the reversible deposition of mixture (B) + (C) ((B)-red, (C)-blue) from Table 1 correspond to (a) coverage fraction  $\theta^{(B)+(C)} = 0.88$ , and (b) steady-state coverage  $\theta_{\infty}^{(B)+(C)} = 0.9066$ . Nodes of the grid corresponding to the beginning of the walk that makes the shapes are indicated by large open points. Empty nodes are marked with black points. A lattice of size  $L^2 = 60 \times 60$  and  $P_d = 0.0045$  are used. (For interpretation of the references to color in this figure legend, the reader is referred to the web version of this article.)

other words, longer memory of the initial state persists for the more symmetrical shapes. Indeed, the increase of the order of symmetry of the shape enhances the rate of *single* particle readsorption. This extends the time needed for a system to forget the initial configuration. However, the correlation curves do not differ qualitatively and they have similar shapes for all objects.

It is well known that the aging properties of the system are characterized by specific scaling properties of  $C(t, t_w)$ . For example, in the Tetris and Ising frustrated lattice gas models, it was found that the relaxation of  $C(t, t_w)$  is given by the form [38]:

$$C(t, t_w) = (1 - c_{\infty}) \frac{\ln[(t_w + t_s)/\tau]}{\ln[(t + t_s)/\tau]} + c_{\infty}, \quad (2)$$

where  $\tau$ ,  $t_s$  and  $c_{\infty}$  are fitting parameters. The above behavior is found in our model. In Fig. 6 we show the behavior of the correlation function  $C(t, t_w)$  for objects (A), (B), and (C), when  $P_d = 0.0015$ . The waiting times  $t_w$  correspond to the

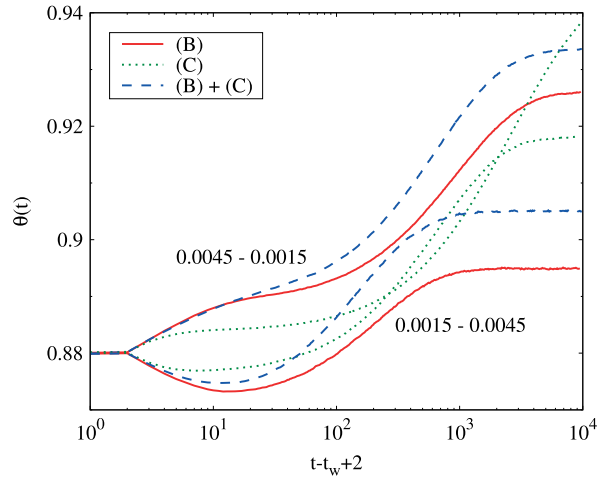


**Fig. 9.** Time evolution of coverage fraction  $\theta^{(B)+(C)}$  for the mixture (B) + (C) when the desorption probability is changed from  $P_d^{(1)} = 0.0045$  to  $P_d^{(2)} = 0.0015$  (from  $P_d^{(1)} = 0.0015$  to  $P_d^{(2)} = 0.0045$ ) at the time  $t_w = 126$  ( $t_w = 182$ ) needed for the system to reach the coverage  $\theta_w^{(B)+(C)} = 0.88$ , in the process of reversible RSA with  $P_d^{(1)} = 0.0045$  ( $P_d^{(1)} = 0.0015$ ). The time origin for each experiment has been taken at the time when the system reached the prescribed density  $\theta_w$ .

time needed for a system to reach the coverages  $\theta_w = 0.87, 0.88, 0.89$ . For all the shapes, the typical aging behavior is observed: the larger  $t_w$ , the longer memory of the initial state persists. The inset of Fig. 6 illustrates that when the two-time correlation function  $C(t, t_w)$  is plotted as a function of  $\ln[(t + t_s)/\tau]/\ln[(t_w + t_s)/\tau]$  the data for all three objects collapse onto single curve. This figure clearly demonstrates the existence of the single universal master function. It is interesting that the parameter  $t_s$  is equal for all objects,  $t_s = 1760$ . However, parameter  $\tau$  depends on the shape:  $\tau(A) = 81$ ,  $\tau(B) = 210$ ,  $\tau(C) = 43$ . The shapes of higher order of symmetry  $n_s$  have lower values of scaling parameter  $\tau$ .

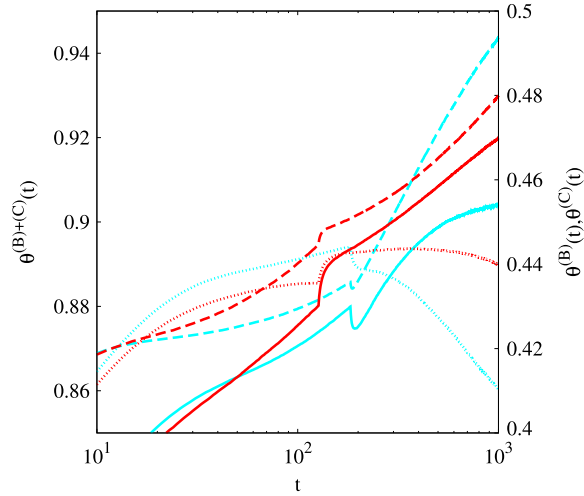
### 3.1. Memory effects in mixtures

In the following, we shall investigate the role that the mixture composition and the symmetry properties of component shapes play in the deposition process. We shall mainly concentrate on the response of the reversible RSA model to sudden perturbations of the desorption probability  $P_d$  in the case of binary mixtures, composed of the shapes of different rotational symmetries but of the same number of segments.

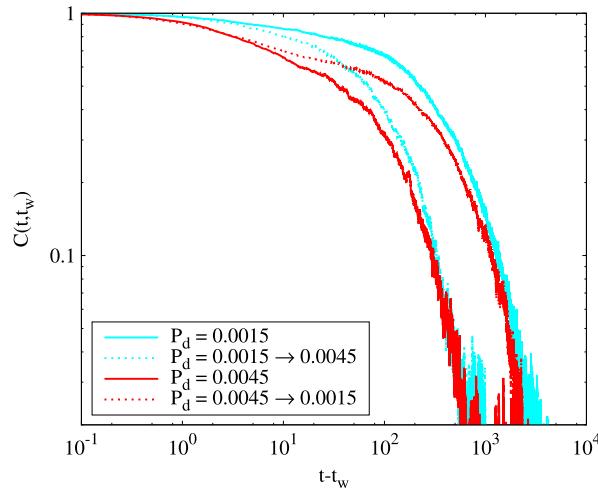
Consider the two-component mixture of objects (B) and (C) with the symmetry axis of  $n_s^{(B)} = 1$  and  $n_s^{(C)} = 3$  order, respectively. The reversible RSA process for a binary mixture is as follows. From a large reservoir of shapes, that contains the shapes (B) and (C) with equal fractional concentrations, we choose one shape at random. We randomly select a lattice site and try to deposit the chosen shape in the same manner as in the case of the reversible RSA of pure depositing objects. Each adsorption attempt is followed by a desorption one with probability  $P_d$ . The quantity of interest is the fraction of total lattice sites,  $\theta^{(B)+(C)}(t)$ , covered by the deposited objects (B) and (C) at time  $t$ .

Fig. 7 shows the time dependence of the partial coverages  $\theta^{(B)}(t)$  and  $\theta^{(C)}(t)$  resulting from the reversible RSA of the binary mixture of (B) and (C) shapes, for two values of desorption probability,  $P_d = 0.0045, 0.0015$ . For shape (C) of higher order of symmetry  $n_s^{(C)} = 3$ , the partial coverage  $\theta^{(C)}(t)$  is a monotonously increasing function of time and has the same general features as the coverage  $\theta^{(B)+(C)}(t)$  for the mixture (B) + (C). On the other hand, for shape (B) of lower order of symmetry  $n_s^{(B)} = 1$ , the partial coverage  $\theta^{(B)}(t)$  is not monotonic in time. When the coverage  $\theta^{(B)+(C)}(t)$  approaches to the coverage fraction that is equal to the jamming limit  $\theta_j^{(B)+(C)} = 0.8624$ , the partial coverage  $\theta^{(B)}(t)$  reaches a broad maximum. This is followed by a slow relaxation of  $\theta^{(B)}(t)$  to the smaller steady-state value  $\theta_\infty^{(B)}$ . At late enough time, when the coverage fraction is sufficient to make the geometry of the unoccupied sites complex, there is a strong dependence of the adsorption rate on the adsorbed shape [28,15]. Then, both rotational symmetry of the shapes and desorption events manage the single-particle readsorptions on the lattice and, eventually, allow replacements of the less symmetric particles by the more symmetric ones. This is reflected in the gradual decrease of the coverage fraction with time for the shape with the symmetry axis of lower order. Our results confirm that, for sufficiently high coverages of a mixture, the large times coverage fraction of more symmetric shapes exceeds the coverage fraction of less symmetric ones [31]. The steady-state value of the coverage fraction of the mixture components is always larger for the shapes with the symmetry axis of higher order  $n_s$  [31]. In Fig. 8 we compare the geometric status of the representative snapshots of patterns formed during the reversible deposition of mixture (B) + (C). The snapshots are taken at the times  $t_w$  needed for the system to reach (a) the coverage  $\theta^{(B)+(C)}(t_w) = 0.88$ , and (b) the steady-state coverage  $\theta_\infty^{(B)+(C)} = 0.9066$  in the process of reversible deposition with  $P_d = 0.0045$ . In Fig. 8(a) the partial coverage of triangles (C) ( $\theta^{(C)}(t_w) = 0.4375$ ) is slightly smaller than that of angled





**Fig. 10.** Shown here is the response of the mixture (B) + (C) to the desorption probability shift  $P_d^{(1)} \rightarrow P_d^{(2)}$ . Black (red) lines represent the results obtained for the abrupt change  $P_d^{(1)} = 0.0045 \rightarrow P_d^{(2)} = 0.0015$  at the time  $t_w$  needed for the system to reach the coverage  $\theta_w^{(B)+(C)} = 0.88$  in the process of reversible RSA with  $P_d^{(1)} = 0.0045$ . Grey (light blue) lines represent the results obtained for the abrupt change  $P_d^{(1)} = 0.0015 \rightarrow P_d^{(2)} = 0.0045$  at the time  $t_w$  needed for the system to reach the coverage  $\theta_w^{(B)+(C)} = 0.88$  in the process of reversible RSA with  $P_d^{(1)} = 0.0015$ . The solid lines represent the temporal behavior of the coverage fraction  $\theta^{(B)+(C)}(t)$  (left-hand axis). The dashed and dotted lines are plotted against the right-hand axis and give the coverage fraction versus time  $t$  of the component shapes (C),  $\theta^{(C)}(t)$  (dashed), and (B),  $\theta^{(B)}(t)$  (dotted). (For interpretation of the references to color in this figure legend, the reader is referred to the web version of this article.)



**Fig. 11.** Two-time density–density correlation function  $C(t, t_w)$  for the mixture (B) + (C), as a function of  $t - t_w$ . The waiting time  $t_w$  corresponds to the time needed for the system to reach the coverage  $\theta_w^{(B)+(C)} = 0.88$ . The solid lines represent the temporal behavior of  $C(t, t_w)$  obtained for the fixed desorption probabilities  $P_d = 0.0015$  and  $0.0045$ , as indicated in the legend. The dashed lines represent the temporal dependence of  $C(t, t_w)$  obtained from the runs during which an abrupt change of desorption probability  $P_d^{(1)} = 0.0045 \rightarrow P_d^{(2)} = 0.0015$  ( $P_d^{(1)} = 0.0015 \rightarrow P_d^{(2)} = 0.0045$ ) occurs at instant  $t_w$ , as indicated in the legend.

objects (B) ( $\theta^{(B)}(t_w) = 0.4433$ ). However, at the steady-state density  $\theta_\infty^{(B)+(C)} = 0.9066$  (Fig. 8(b)) the partial coverage fraction is larger for the shape with symmetry axis of higher order, i.e.  $\theta_\infty^{(C)} = 0.5266 > \theta_\infty^{(B)} = 0.3800$ .

Fig. 9 shows typical short-term memory effects after an abrupt change of the desorption probability  $P_d$  for the mixture (B) + (C) and for pure component shapes, (B) and (C). Desorption probability  $P_d$  is switched from  $P_d^{(1)} = 0.0045$  to  $P_d^{(2)} = 0.0015$  and vice-versa, at the time  $t_w$  needed for a mixture to reach the coverage  $\theta_w = 0.88$ . Again, we observe that after several adsorption/desorption events the “anomalous” response ceases and there is a crossover to the “normal” behavior, with the relaxation rate becoming the same as in the constant forcing mode. However, it is interesting to note that during this transient stage, the temporal evolution of the total coverage fraction  $\theta^{(B)+(C)}(t)$  is very similar to the one observed for the shape with the symmetry axis of lower order. Hence, the dynamics of the short-time response of the mixture (B) + (C) to sudden perturbation of the desorption probability  $P_d$  is usually determined by the shape (B) of lower order of

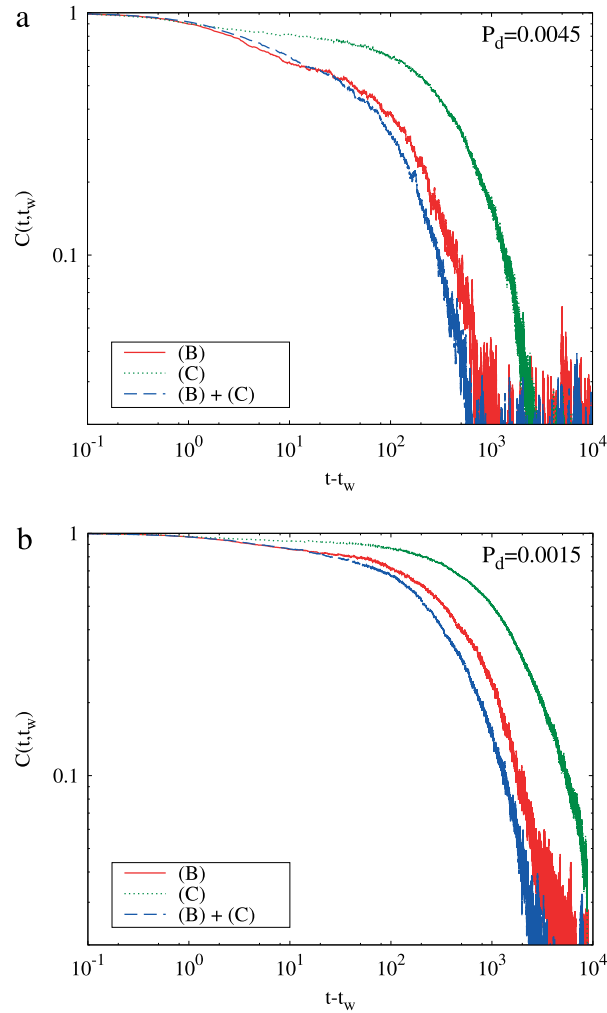


**Fig. 12.** Two-time density–density correlation function  $C(t, t_w)$  for objects (B), (C), and mixture (B) + (C), as a function of  $t - t_w$ . The waiting time  $t_w$  corresponds to the time needed for the system to reach the coverage  $\theta_w = 0.88$  when the desorption probability has the constant values (a)  $P_d^{(1)} = 0.0045$ , and (b)  $P_d^{(1)} = 0.0015$ .

symmetry,  $n_s^{(B)} = 1$ . Fig. 10 puts into evidence the temporal behavior of the partial coverage fraction for component shapes (B) and (C) during the transient time. As in the case of pure lattice shapes, we observe that the change in the compaction rate on short-time scales is less pronounced for the component shape of higher symmetry order.

In Fig. 11 we show the temporal dependence of  $C(t, t_w)$  (see, Eq. (1)) for the mixture (B) + (C), when the waiting time  $t_w$  corresponds to the time needed for a system to reach the coverage  $\theta_w^{(B)+(C)} = 0.88$ . Correlation function  $C(t, t_w)$  is displayed both for the fixed desorption probabilities,  $P_d = 0.0015, 0.0045$ , and for the cases with abrupt changes of desorption probability  $P_d^{(1)} = 0.0045 \rightarrow P_d^{(2)} = 0.0015$ , and  $P_d^{(1)} = 0.0015 \rightarrow P_d^{(2)} = 0.0045$  at instant  $t_w$ . As for the pure lattice shapes, correlation functions calculated for the mixture (B) + (C) in the case of perturbed systems ( $\Delta P_d = P_d^{(1)} - P_d^{(2)} \leq 0$ ) interpolates between the two correlation functions obtained for the systems with constant desorption probabilities  $P_d^{(1)}$ , and  $P_d^{(2)}$ .

It is instructive to compare the temporal behavior of the correlation function  $C(t, t_w)$  for the mixture with results for  $C(t, t_w)$  in the case of reversible deposition of pure component shapes. In Fig. 12 we show the time evolution of  $C(t, t_w)$  during the deposition of objects (B), (C), and the mixture (B) + (C), for the waiting time  $t_w$  needed for a system to reach the coverage  $\theta_w = 0.88$  when the desorption probability has the constant values  $P_d^{(1)} = 0.0045$  (Fig. 12(a)) and  $P_d^{(1)} = 0.0015$  (Fig. 12(b)). We can clearly see that for short times,  $C(t, t_w)$  for the mixture (B) + (C) decays in a similar way as for shape (B) with the symmetry axis of lower order,  $n_s^{(B)} = 1$ . This changes slightly at intermediate times, when the correlation function  $C(t, t_w)$  for the mixture starts to decay faster than the density correlations of component shapes. Hence, we observe the weakening of correlation features in multicomponent systems.

## 4. Conclusions

Along this paper, we have studied the nonequilibrium response of reversible RSA model to an instantaneous change in the value of desorption probability  $P_d$ . We have performed extensive simulations of reversible deposition using objects of different rotational symmetries on a triangular lattice. The shapes are made by self-avoiding lattice steps. First, it was shown that the change in the compaction rate has opposite sign than that of the modification of the desorption probability  $P_d$ , in contrast with the long-time behavior, where the relaxation is faster for larger  $P_d$ . These results are in a qualitative agreement with the observations in experiments on granular compaction [25]. Further, our numerical simulations have shown that the short-time response to an instantaneous change in the desorption probability  $P_d$  strongly depends on the symmetry properties of the shapes. We have found that the dynamical behavior is severely slowed down with the increase of the order of symmetry of the shape. When the desorption probability  $P_d$  is suddenly decreased/increased, compaction/decompaction rate of the perturbed system on short-time scales is larger for shapes with symmetry axis of lower order. We have also pointed out the importance of collective events for governing the short-time coverage behavior of shapes with different rotational symmetry.

We have also considered the nonequilibrium two-time density–density correlation function  $C(t, t_w)$ . We have observed that decay of the correlation function  $C(t, t_w)$  depends on the order of symmetry axis of the shape  $n_s$ . It was confirmed that the density correlation decays slower for more symmetrical shapes. Eq. (2) states that, for the long enough times, the correlation  $C(t, t_w)$  is a function of the ratio  $\ln(t_w)/\ln(t)$ . Such scaling behavior is in agreement with the Ising frustrated lattice gas model and the Tetris model [38], but in contrast with the parking lot model [27], for which a  $t/t_w$  behavior has been observed.

Special attention has been paid to the mixtures containing objects of various shapes, but made of the same number of segments. It was found that the dynamics of the short-time response of the mixture to sudden perturbation of the desorption probability  $P_d$  is determined by the shape of lower order of symmetry. In addition, our results confirm the weakening of correlation features for the deposition processes in multicomponent systems.

## Acknowledgments

This work was supported by the Ministry of Education, Science, and Technological Development of the Republic of Serbia under projects ON171017 and III45016. Numerical simulations were run on the PARADOX supercomputing facility at the Scientific Computing Laboratory of the Institute of Physics Belgrade.

## References

- [1] P.J. Flory, Intramolecular reaction between neighboring substituents of vinyl polymers, *J. Am. Chem. Soc.* 61 (1939) 1518.
- [2] J.W. Evans, Random and cooperative sequential adsorption, *Rev. Modern Phys.* 65 (1993) 1281–1329.
- [3] V. Privman, Dynamics of nonequilibrium deposition, *Colloids Surf. A* 165 (2000) 231–240.
- [4] A. Cadilhe, N.A.M. Araújo, V. Privman, Random sequential adsorption: from continuum to lattice and pre-patterned substrates, *J. Phys.: Condens. Matter* 19 (2007) 065124.
- [5] V. Privman (Ed.), *Nonequilibrium Statistical Mechanics in One Dimension*, Cambridge University Press, Cambridge, UK, 1997.
- [6] B. Senger, J.C. Voegel, P. Schaaf, Irreversible adsorption of colloidal particles on solid substrates, *Colloids Surf. A* 165 (2000) 255–285.
- [7] J. Talbot, G. Tarjus, P.R. Van Tassel, P. Viot, From car parking to protein adsorption: an overview of sequential adsorption processes, *Colloids Surf. A* 165 (2000) 287–324.
- [8] J.J. Ramsden, G.I. Bachmanova, A.I. Archakov, Kinetic evidence for protein clustering at a surface, *Phys. Rev. E* 50 (1994) 5072.
- [9] J. Talbot, G. Tarjus, P. Viot, Adsorption–desorption model and its application to vibrated granular materials, *Phys. Rev. E* 61 (2000) 5429–5438.
- [10] Lj. Budinski-Petković, S.B. Vrhovac, Memory effects in vibrated granular systems: Response properties in the generalized random sequential adsorption model, *Eur. Phys. J. E* 16 (2005) 89–96.
- [11] R.S. Ghaskadvi, M. Dennin, Reversible random sequential adsorption of dimers on a triangular lattice, *Phys. Rev. E* 61 (2000) 1232–1238.
- [12] E. Frey, A. Vilfan, Anomalous relaxation kinetics of biological latticeliquid binding models, *Chem. Phys.* 284 (2002) 287.
- [13] P.L. Krapivsky, E. Ben-Naim, Collective properties of adsorption–desorption processes, *J. Chem. Phys.* 100 (1994) 6778–6782.
- [14] Lj. Budinski-Petković, U. Kozmidis-Luburić, Adsorption–desorption processes of extended objects on a square lattice, *Physica A* 301 (2001) 174.
- [15] Lj. Budinski-Petković, M. Petković, Z.M. Jakšić, S.B. Vrhovac, Symmetry effects in reversible random sequential adsorption on triangular lattice, *Phys. Rev. E* 72 (2005) 046118.
- [16] I. Lončarević, Lj. Budinski-Petković, S.B. Vrhovac, A. Belić, Adsorption, desorption, and diffusion of  $k$ -mers on a one-dimensional lattice, *Phys. Rev. E* 80 (2009) 021115.
- [17] G. Tarjus, P. Viot, Statistical mechanical description of the parking–lot model for vibrated granular materials, *Phys. Rev. E* 69 (2004) 011307.
- [18] J.B. Knight, C.G. Fandrich, C.N. Lau, H.M. Jaeger, S.R. Nagel, Density relaxation in a vibrated granular material, *Phys. Rev. E* 51 (1995) 3957–3963.
- [19] F.X. Villarruel, B.E. Lauderdale, D.M. Mueth, H.M. Jaeger, Compaction of rods: Relaxation and ordering in a vibrated, anisotropic granular material, *Phys. Rev. E* 61 (2000) 6914–6921.
- [20] P. Philippe, D. Bideau, Compaction dynamics of granular medium under vertical tapping, *Europhys. Lett.* 60 (2002) 677.
- [21] P. Ribière, P. Richard, D. Bideau, R. Delannay, Experimental compaction of anisotropic granular media, *Eur. Phys. J. E* 16 (2005) 415–420.
- [22] P. Richard, M. Nicodemi, R. Delannay, P. Ribière, D. Bideau, Slow relaxation and compaction of granular systems, *Nature Mater.* 4 (2005) 121–128.
- [23] P. Ribière, P. Richard, P. Philippe, D. Bideau, R. Delannay, On the existence of stationary states during granular compaction, *Eur. Phys. J. E* 22 (2007) 249–253.
- [24] A.J. Kolan, E.R. Nowak, A.V. Tkachenko, Glassy behavior of the parking lot model, *Phys. Rev. E* 59 (1999) 3094–3099.
- [25] C. Jossierand, A. Tkachenko, D.M. Mueth, H.M. Jaeger, Memory effects in granular materials, *Phys. Rev. Lett.* 85 (2000) 3632–3635.
- [26] M. Nicolas, P. Duru, O. Poulliquen, Compaction of a granular material under cyclic shear, *Eur. Phys. J. E* 3 (2000) 309–314.
- [27] J. Talbot, G. Tarjus, P. Viot, Aging and response properties in the parking–lot model, *Eur. Phys. J. E* 5 (2001) 445–449.
- [28] Lj. Budinski-Petković, U. Kozmidis-Luburić, Random sequential adsorption on a triangular lattice, *Phys. Rev. E* 56 (1997) 6904.
- [29] Lj. Budinski-Petković, S.B. Vrhovac, I. Lončarević, Random sequential adsorption of polydisperse mixtures on discrete substrates, *Phys. Rev. E* 78 (2008) 061603.

- [30] D. Dujak, I. Lončarević, Lj. Budinski-Petković, S.B. Vrhovac, A. Karač, Adsorption–desorption processes of polydisperse mixtures on a triangular lattice, *Phys. Rev. E* 91 (2015) 032414. <http://dx.doi.org/10.1103/PhysRevE.91.032414>.
- [31] I. Lončarević, Lj. Budinski-Petković, S.B. Vrhovac, Reversible random sequential adsorption of mixtures on a triangular lattice, *Phys. Rev. E* 76 (2007) 031104.
- [32] S. Živković, Z.M. Jakšić, I. Lončarević, Lj. Budinski-Petković, S.B. Vrhovac, A. Belić, Optimization of the monolayer growth in adsorption–desorption processes, *Phys. Rev. E* 88 (2013) 052131. <http://dx.doi.org/10.1103/PhysRevE.88.052131>.
- [33] Lj. Budinski-Petković, U. Kozmidis-Luburić, A. Mihailović, Random sequential adsorption with diffusional relaxation on a square lattice, *Physica A* 293 (2001) 339.
- [34] Lj. Budinski-Petković, T. Tošić, Adsorption, desorption and diffusion of extended objects on a square lattice, *Physica A* 329 (2003) 350.
- [35] P. Ranjith, J.F. Marko, Filling of the one-dimensional lattice by  $k$ -mers proceeds via fast power-law-like kinetics, *Phys. Rev. E* 74 (2006) 041602.
- [36] S.S. Manna, N.M. Švrakić, Random sequential adsorption: line segments on the square lattice, *J. Phys. A: Math. Gen.* 24 (1991) L671–L676.
- [37] J. Talbot, G. Tarjus, P. Viot, Sluggish kinetics in the parking lot model, *J. Phys. A: Math. Gen.* 32 (1999) 2997–3003.
- [38] M. Nicodemi, A. Coniglio, Aging in out-of-equilibrium dynamics of models for granular media, *Phys. Rev. Lett.* 82 (1999) 916–919.

# Structural properties of particle deposits at heterogeneous surfaces

D Stojiljković<sup>1</sup>, J R Šćepanović<sup>1</sup>, S B Vrhovac<sup>1</sup>  
and N M Švrakić<sup>1,2</sup>

<sup>1</sup> Institute of Physics Belgrade, University of Belgrade, Pregrevica 118, Zemun 11080, Belgrade, Serbia

<sup>2</sup> Texas A&M University at Qatar, Doha, Qatar  
E-mail: [vrhovac@ipb.ac.rs](mailto:vrhovac@ipb.ac.rs)

Received 17 March 2015

Accepted for publication 23 May 2015

Published 23 June 2015



Online at [stacks.iop.org/JSTAT/2015/P06032](http://stacks.iop.org/JSTAT/2015/P06032)  
[doi:10.1088/1742-5468/2015/06/P06032](https://doi.org/10.1088/1742-5468/2015/06/P06032)

**Abstract.** The random sequential adsorption (RSA) approach is used to analyze adsorption of spherical particles of a fixed radius on nonuniform flat surfaces covered by rectangular cells. The configuration of the cells (heterogeneities) was produced by performing RSA simulations to a prescribed coverage fraction  $\theta_0^{(\text{cell})}$ . Adsorption was assumed to occur if the particle (projected) center lies within a rectangular cell area, i.e. if sphere touches the cells. The jammed-state properties of the model were studied for different values of cell size  $\alpha$  (comparable with the adsorbing particle size) and density  $\theta_0^{(\text{cell})}$ . Numerical simulations were carried out to investigate adsorption kinetics, jamming coverage, and structure of coverings. Structural properties of the jammed-state coverings were analyzed in terms of the radial distribution function  $g(r)$  and distribution of the Delaunay ‘free’ volumes  $P(v)$ . It was demonstrated that adsorption kinetics and the jamming coverage decreased significantly, at a fixed density  $\theta_0^{(\text{cell})}$ , when the cell size  $\alpha$  increased. The predictions following from our calculation suggest that the porosity (pore volumes) of deposited monolayer can be controlled by the size and shape of landing cells, and by anisotropy of the cell deposition procedure.

**Keywords:** adsorbates and surfactants (theory), stochastic processes (theory)

---

**Contents**

<b>1. Introduction</b>	<b>2</b>
<b>2. Model and numerical simulation</b>	<b>4</b>
<b>3. Results and discussion</b>	<b>5</b>
3.1. Circles on squares .....	5
3.1.1. Densification kinetics. ....	6
3.1.2. Radial distribution function. ....	12
3.1.3. Volume distribution of the pores. ....	14
3.2. Circles on rectangles .....	18
<b>4. Concluding remarks</b>	<b>20</b>
<b>Acknowledgments</b>	<b>22</b>
<b>References</b>	<b>22</b>

---

**1. Introduction**

Recent developments in new and emerging technologies have generated increased demand for nano and micro-sized particles with carefully tailored properties for use in applications such as photonics, micro-electronics, plasmonics, biosensors, bio-medical devices, etc. In many applications, such nanoparticles are often integrated onto surfaces in the form of deposits in order to achieve improved performance and/or new functionalities of the final product. Thus, in addition to specific requirements for particles of definite shape, size, internal structure, surface properties or chemical composition, it is also important to be able to manipulate collective arrangements of such particles with firm control over the morphology and structure of their surface layers. To achieve this goal, the supporting surfaces are frequently prepatterned to form the templates favoring particle attachments at specific locations [1,2], or dimples, or along specified shapes, regular or otherwise [3,4]. With the use of photolithographic techniques, high-power lasers [1], chemical treatments, etc, such surface modifications are routinely realized on the microscale, but the trend is towards the nanosize patterning [1–4].

In contrast with homogeneous surfaces, the prepatterned *heterogeneous* substrates are designed with preferential attachment sites, or regions [4]. Thus, it is of theoretical and experimental interest to understand and analyze how specific surface modifications affect the morphology of deposited layers, late-stage kinetics of attachment, etc. Our analysis, described below, focuses on structural properties of particle deposits and is applicable to the presence of *randomness* in surface patterning on the scales comparable to particle size.

Specifically, in the present work, we report a study of the irreversible deposition of spherical particles on flat nonuniform substrates covered by rectangular cells onto which the particles can adhere. The adsorption sites (landing cells) have finite size, comparable with the adsorbing particle size. We consider the process of the irreversible random sequential adsorption (RSA) of fixed size disks (projection of spherical particles). RSA is a process in which the objects of specified shape are randomly and sequentially deposited onto a substrate [5–10]. The particle-particle interaction is incorporated by rejection of deposition overlap (the hard sphere model), while the particle-substrate interaction is modeled by the irreversibility of deposition. Adsorption attempt of a particle at a randomly chosen cell is abandoned if there is an overlap with a previously adsorbed one, at the same or at a neighboring cell. Since the dominant effect in RSA is the blocking of the available surface area, after sufficiently long time a jammed state is reached when there is no more possibility for a deposition event on any landing cell. In this work we focus on the jammed-state properties.

There is a well-developed literature on irreversible adsorption on heterogeneous surfaces where particles are represented as hard spheres that bind to adsorption sites [10–15]. Our present model represents a generalized version of deposition on a random site surface (RSS), where the sites are represented by randomly distributed points [11, 13]. Adamczyk *et al* [14] has extended the RSS model to the situation where the size of the landing sites, in the shape of circular disks, is finite and comparable with the size of adsorbing spheres. The available surface function, adsorption kinetics, jamming coverage, and the structure of the particle monolayer were determined as a function of the site density and the particle/site size ratio.

The motivation of our present work comes from Margues *et al* [16] and Araújo *et al* [17], who investigated the adsorption of disk-shaped particles on a patterned substrate. The pattern consisted of equal square cells centered at the vertices of a square lattice. They studied the effect of the presence of a regular substrate pattern and particle polydispersity on the deposit morphology and density, as well as on the in-cell particle population. A specific distribution function was used to describe the degree to which the cell pattern affects the overall structure of the adsorbed layer for various values of cell size and cell-cell separation parameters. It was found that the structural organization of the deposit could be latticelike, locally homogeneous, and locally oriented.

The present work is focused on the effect of the presence of randomness in substrate pattern on the structural properties of the disordered jammed state. Our aim is to quantify structural changes of the jamming covering associated with different cell size and density. Analysis at the ‘microscopic’ scale is based on the Voronoï tessellation [18]. Voronoï tessellation divides a two-dimensional region occupied by disks into space filling, nonoverlapping convex polygons. Further, the Delaunay triangulation is used to quantify the volume distribution of pores  $P(v)$  for disk monolayers deposited on a heterogeneous substrate. This quantity has been widely used to characterize the structure of disordered granular packings and to quantify the structural changes during compaction process [19–23]. We choose as our additional tool of exploration the shape of radial correlation function  $g(r)$  [24]. This is because this function provides a simple yet powerful encoding of the distribution of interparticle gaps. We also study the effect of the presence of a regular substrate pattern on the temporal evolution of the coverage fraction  $\theta(t)$  and the pore distribution  $P(v)$ . The pattern consists of an array of cells centered on the vertices of a square lattice [16, 17].

The following section 2 describes the details of our numerical simulations. We present simulation results and discussions in section 3. Finally, section 4 contains some additional comments and concluding remarks.

## 2. Model and numerical simulation

We study irreversible monolayer deposition of identical disks (sphere projections) with hard-core exclusion on a prepared flat nonuniform substrate. The substrate heterogeneities are represented by non-overlapping rectangular cells that are randomly placed and fixed on the substrate surface. The basic assumption of our model is that a particle can only be adsorbed if it is in contact with one of the cells, i.e. if the center of its disk-shaped projection lies within one of the rectangles. The substrates can be prepared in a number of ways by arranging the rectangles to form different patterns, e.g. by placing the midpoint of rectangles at the vertices of a square or triangular lattice (regular pattern), or by performing random deposition (random pattern), the procedure adopted in our work. We consider particles of fixed radius, comparable with the typical geometrical cell length. Moreover, we assume that the size of the particles is much larger than the length scale between binding sites, so that adsorption over the length scales of cell linear dimensions can be regarded as an off-lattice process. We impose the condition that deposited particles can neither diffuse along, nor desorb from the substrate on the time scales of the dense coverage formation. These assumptions are typical of the RSA model.

The simplest RSA model is defined by the following three rules: (i) objects are placed one after another at a random position on the substrate; (ii) adsorbed objects do not overlap; and (iii) adsorbed objects are permanently fixed to their spatial positions. The kinetic properties of a deposition process are described by the time evolution of the coverage  $\theta(t)$ , which is the fraction of the substrate area covered by the adsorbed particles. Within a monolayer deposit, each adsorbed particle affects the geometry of all later placements. Due to the blocking of the substrate area by the previously adsorbed particles, at large times the coverage approaches the jammed-state value  $\theta_J$ , where only gaps too small to accommodate new particles (provided their centers fall within landing cells) are left in the monolayer.

The entire simulation procedure consisted of two main stages:

1. The simulation area was covered with identical rectangles (or squares) to a prescribed coverage fraction  $\theta_0^{(\text{cell})} < \theta_J^{(\text{cell})}$ , where  $\theta_J^{(\text{cell})}$  is the jamming coverage for landing cells. During this stage the usual RSA simulation algorithm was used. In this way we are able to prepare the randomly patterned heterogeneous substrate with a statistically reproducible density  $\theta_0^{(\text{cell})}$ .
2. Then, for each initially prepared configuration, we switch the cell deposition events off and initiate a random deposition of disks, with diameter  $d_0$ , by choosing at random their position within the simulation area. The overlapping test between disks was carried out by considering the distances between the disk centers. A disk deposition attempt fails if disk's center falls outside the deposited landing cells, or if the arriving disk overlaps at least one of previously adsorbed ones.



The Monte-Carlo simulations are performed on a planar continuous substrate of size  $L \times L = (256d_0)^2$  with periodic boundary conditions. In calculations, the time  $t$  is gradually increased by an increment  $\delta t$ , given by  $\delta t = \pi r_0^2 / L^2$ , each time an attempt is made to deposit a disk of radius  $r_0 = d_0/2$ . Consequently, we define dimensionless parameter  $t = N_{\text{att}} \pi r_0^2 / L^2$ , where  $N_{\text{att}}$  is the overall number of attempts to place disk particles. The dimensionless adsorption time  $t$  was set to zero at the beginning of the second stage. By plotting  $\theta(t)$  versus the adsorption time  $t$ , defined above, one can simulate the kinetics of particle adsorption.

For purposes of our modeling, each landing cell is a rectangle with sides  $a$  and  $b$  ( $b \leq a$ ) whose midpoint is located on a continuous substrate. The cells can take arbitrary orientations, but in some numerical simulations we have introduced anisotropy in the deposition procedure for landing cells. This simple modification introduces a preferential direction in the deposition process and, depending on the aspect ratio of deposited rectangles, imposes specific ‘patterning’ on the deposited layer. We rescale the lengths relative to the diameter of the disks  $d_0$ , and define three dimensionless parameters:

$$\alpha = \frac{a}{2r_0}, \quad \beta = \frac{b}{2r_0} \quad (1)$$

$$\gamma = \frac{\alpha}{\sqrt{\theta_0^{(\text{cell})}}} \quad (2)$$

The parameter  $\gamma$  (an average distance between cell centers) is a meaningful measure only if the landing cells are squares ( $a = b$ ).

For a fixed values of parameters  $\alpha$  and  $\beta$ , simulations were carried out for various values of  $\theta_0^{(\text{cell})}$ , ranging from 0.10 to 0.50. For each case, the simulations are carried out up to  $10^{10}$  deposition attempts, or up until  $L^2 \times 10^4$  consecutive deposition attempts are rejected. The results are obtained by averaging over 100 simulation runs.

### 3. Results and discussion

In the first part of this section simulation results are presented and discussed for random deposition of identical disks on nonuniform substrates covered by squares of arbitrary orientation. We characterize the jammed state in terms of radial distribution function of distances between the particle centers and distribution of the Delaunay ‘free’ volumes. After that, further analysis is extended to adsorption of disks on rectangular cells deposited with arbitrary or fixed orientation.

#### 3.1. Circles on squares

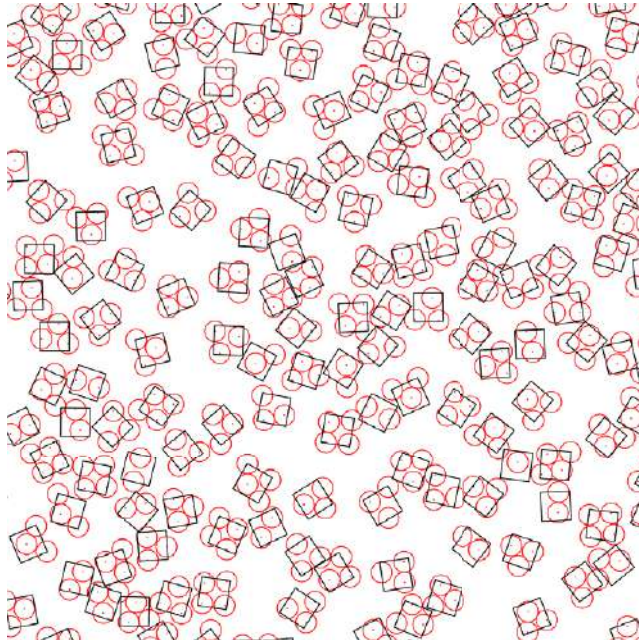
First, we consider the irreversible deposition of disks of fixed diameter  $d_0 = 1$  whose centers are inside the square cells arranged randomly at the surface. Depending on the cell size  $\alpha$ , one can place one or more disk centers inside each cell. We are interested in the range of  $\alpha$  where the number of disks adsorbed per cell is a small number (less than five). For  $\alpha < 1/\sqrt{2}$ , at most a single disk can be adsorbed at any given square cell. We denote this case as single particle per-cell adsorption (SPCA). For

squares with  $\alpha \geq 1/\sqrt{2}$ , more than a single disk can be placed in the square cell, and we denote this as multiparticle per-cell adsorption (MPCA). The cases of up-to-two, -three and -four disks per square cell are obtained, respectively, for  $\alpha$  in the ranges  $1/\sqrt{2} \leq \alpha < (1 + \sqrt{3})/(2\sqrt{2})$ ,  $(1 + \sqrt{3})/(2\sqrt{2}) \leq \alpha < 1$ , and  $1 \leq \alpha < \sqrt{2}$ . In other words, the numbers  $\{\alpha_k : k = 1, 2, 3, 4\} = \{1/\sqrt{2}, (1 + \sqrt{3})/(2\sqrt{2}), 1, \sqrt{2}\}$  determine the size of the largest cell in which at most  $k = 1, 2, 3, 4$  disks can be deposited, respectively.

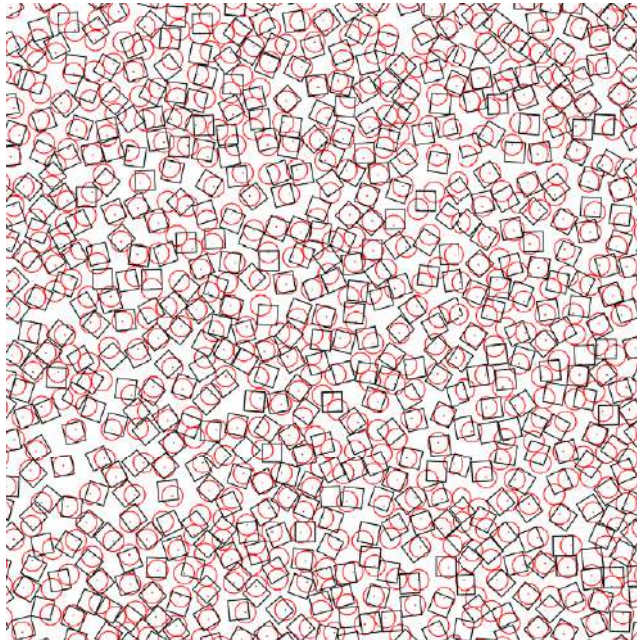
The effect of density of landing cells  $\theta_0^{(\text{cell})}$  on the adsorption process is illustrated in figure 1 by snapshots of the jammed-state coverings for (a)  $\theta_0^{(\text{cell})} = 0.3$  and (b)  $\theta_0^{(\text{cell})} = 0.5$ , for two values of the cell size  $\alpha$ , namely,  $\alpha_4 = \sqrt{2} \approx 1.41$  (figure 1(a)) and  $\alpha_2 = (1 + \sqrt{3})/(2\sqrt{2}) \approx 0.966$  (figure 1(b)). For low values of  $\theta_0^{(\text{cell})}$ , adsorption on a given cell is weakly affected by disks previously adsorbed on neighboring cells. Therefore, most of the cells shown in figure 1(a) contain at least three discs. However, in the case shown in figure 1(b) one can see a significant impact of the cell-cell excluded volume interaction on the cell population. Although each cell has enough area to accommodate up to two disks, only one disk is deposited on most of the cells.

*3.1.1. Densification kinetics.* Kinetics of the irreversible deposition of disks is illustrated in figures 2(a)–(e) where the plots of time coverage behavior  $\theta(t)$  are given for the five values of coverage fraction of landing cells,  $\theta_0^{(\text{cell})} = 0.1, 0.2, 0.3, 0.4, 0.5$ . Here the plots of such time-dependence are shown for various values of the cell size,  $\alpha_k$  ( $k = 1, 2, 3, 4$ ). It can be seen that for a fixed density of landing cells  $\theta_0^{(\text{cell})}$ , jamming coverage  $\theta_J = \lim_{t \rightarrow \infty} \theta(t)$  decreases with increasing the cell size  $\alpha_k$ . This effect is clearly visible in the case of the lowest density of the landing cells  $\theta_0^{(\text{cell})} = 0.1$  (figure 2(a)), when the average distance between the squares  $\gamma$  (equation (2)) is several times larger than the diameter of the disks. Then, the cell-cell separation is large enough so that adsorption on a given cell is negligibly affected by disks previously adsorbed on neighboring cells. Therefore, for sufficiently low densities  $\theta_0^{(\text{cell})} \lesssim 0.2$ , the global kinetics of deposition is determined by the kinetics of independent adsorption processes on finite-size substrates (landing cells) with specific boundary conditions (disks can be adsorbed on finite  $\alpha \times \alpha$  square as long as their centers are within the square). Consequently, for this range of  $\theta_0^{(\text{cell})}$  values, formula  $\theta_J = (\pi/4\alpha^2)\langle n \rangle \theta_0^{(\text{cell})}$  gives very close estimation of the jamming density  $\theta_J$ , where  $\langle n \rangle$  is the mean number of disks per cell. The dashed (black) line in figure 3 shows the simulation results for the mean number of particles per cell  $\langle n \rangle$  as a function of the cell size  $\alpha$  in the noninteracting cell-cell adsorption regime (i.e. in the case of single cell on a substrate).

Consider now the case of up-to-two disks per square cell ( $\alpha_2 = (1 + \sqrt{3})/(2\sqrt{2}) \approx 0.966$ ), when  $\langle n \rangle \lesssim 1.6$  (see, figure 3). Then, during the deposition process, disk can be adsorbed at the position inside the cell that blocks the chance for other disks to be adsorbed on the same cell at later times. Consequently, the probability of having a second adsorbed particle in any given cell is smaller than the probability of having at least one particle adsorbed on it. Similar reasoning applies as  $\alpha$  crosses  $\alpha_3, \alpha_4, \dots$ . In addition, in figure 3 we show simulation results for the probability that the configurations with only one disk, or  $n = 2, \dots, 5$  disks, occur on square cell of size  $\alpha$  in the noninteracting cell-cell adsorption regime. If  $\alpha = \alpha_1 \approx 0.707$ , each landing cell (square) can contain no more than one disk. If  $\alpha = \alpha_2 \approx 0.966$ , the number of cells with one and two disks is



(a)



(b)

**Figure 1.** Typical jammed-state configuration of a region of size  $30 \times 30$  in units of the disk diameter  $d_0$ , for (a)  $\theta_0^{(\text{cell})} = 0.3$ ,  $\alpha_4 = \sqrt{2} \approx 1.41$ , and (b)  $\theta_0^{(\text{cell})} = 0.5$ ,  $\alpha_2 = (1 + \sqrt{3})/(2\sqrt{2}) \approx 0.966$ .

approximately equal (figure 3). However, if density  $\theta_0^{(\text{cell})}$  is unchanged, then the increasing of the cell size  $\alpha_1 \rightarrow \alpha_2$  reduces the total number of landing cells on the substrate by a factor  $\approx 2$ . Reduction in number of adsorbed disks is a consequence of these two effects.

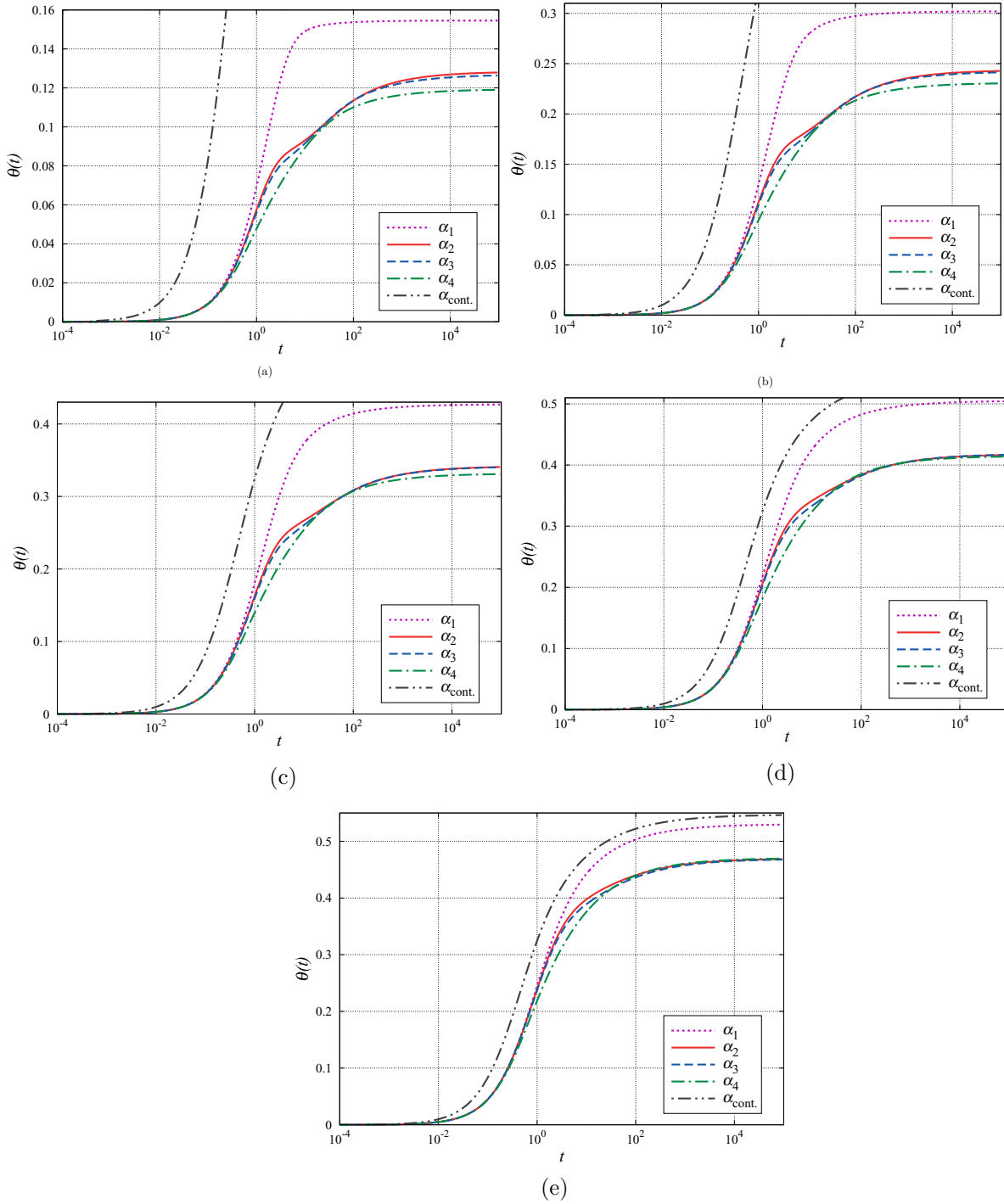


**Figure 2.** Shown here is the time evolution of the coverage fraction  $\theta(t)$  for the five values of density of landing cells,  $\theta_0^{(\text{cell})} = 0.1$  (a), 0.2 (b), 0.3 (c), 0.4 (d), 0.5 (e). The curves in each graph correspond to various values of the cell size,  $\alpha_k$  ( $k = 1, 2, 3, 4$ ), as indicated in the legend. The  $\alpha_{\text{cont}}$  line shows the time dependence of the coverage  $\theta(t)$  for RSA of disks on a continuous substrate. The entire  $\alpha_{\text{cont}}$  curve can be seen in plot (e).

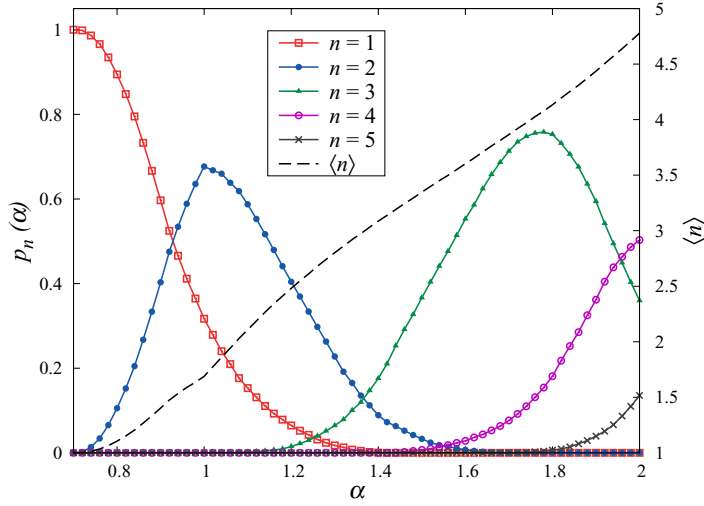


**Figure 3.** Simulation results for the probability that the configurations with  $n = 1, 2, \dots, 5$  disks occur on square cell of size  $\alpha$  in the noninteracting cell–cell adsorption regime (left-hand axis). The dashed line is plotted against the right-hand axis and gives the simulation results for the average number of particles per cell  $\langle n \rangle$  as a function of the cell size  $\alpha$  in the noninteracting cell–cell adsorption regime.

This discussion indicates that the jamming density  $\theta_J$  decreases with cell size  $\alpha$  at fixed density  $\theta_0^{(\text{cell})}$ .

As can be seen from figure 2, the time coverage behavior  $\theta(t)$  is markedly slowed down with the increase of the cell size  $\alpha$  for the fixed density of landing cells  $\theta_0^{(\text{cell})}$ . Indeed, in MPCA case the large times are needed for filling of small isolated vacant targets on landing cells, remaining in the late stages of deposition. Furthermore, in this regime, density curves  $\theta(t)$  show a noticeable slowing down of deposition process at coverages that are significantly smaller than jamming densities. Coverage growth starts to slow down at the moment when the number of adsorbed disks reaches the number of landing cells. After this initial filling of the landing cells, adsorption events take place on isolated islands of partially occupied cells. This extends the time interval between successful consecutive adsorption events and causes a slowing down of the densification.

The results for the time evolution of the coverage  $\theta(t)$  in the case of up-to-two disks per square cell ( $\alpha = \alpha_2$ ) are shown in figure 4 for various values of  $\theta_0^{(\text{cell})}$ . Qualitatively similar results are obtained with landing cells of other sizes  $\alpha$ . As expected, the jamming density  $\theta_J$  increases with higher coverage fraction of landing cells  $\theta_0^{(\text{cell})}$ . At high values of  $\theta_0^{(\text{cell})} \lesssim 0.5$  when  $\gamma \sim 1$ , a disk attempting adsorption can overlap with a previously adsorbed one belonging to a different cell, resulting in a failed adsorption attempt. This excluded volume interaction between particles during adsorption at *different* cells causes even slower asymptotic approach of the coverage fraction  $\theta(t)$  to its jamming limit. In addition, the analysis of the time evolution of the coverage  $\theta(t)$  was carried out for deposition on square cells centered at the vertices of a square lattice. Consequently, the temporal evolution of the coverage  $\theta(t)$  obtained for regular substrate pattern are included in figure 4. Here, the size  $\alpha$  and density  $\theta_0^{(\text{cell})}$  of landing cells are the same as those used in

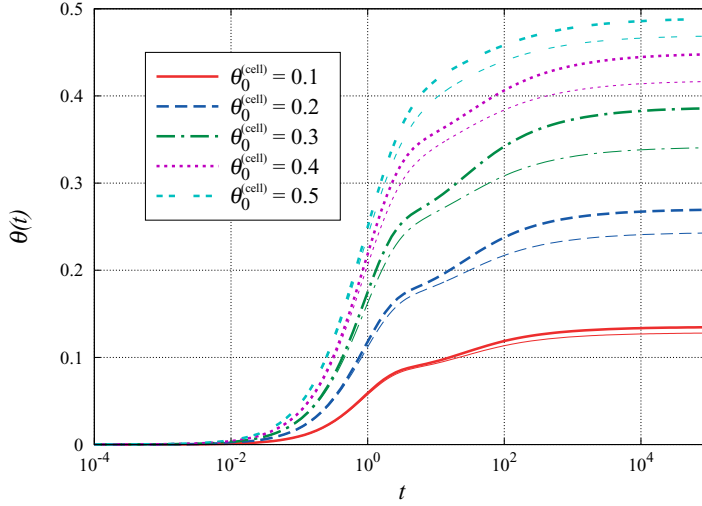


**Figure 4.** Temporal behavior of the coverage  $\theta(t)$  for various values of  $\theta_0^{(\text{cell})}$  in the case of up-to-two disks per square cell (cell size:  $\alpha_2 = (1 + \sqrt{3})/(2\sqrt{2}) \approx 0.966$ ). The curves correspond to various values of density  $\theta_0^{(\text{cell})} = 0.1-0.5$ , as indicated in the legend. Thick lines represent results obtained for regular substrate pattern while thin lines are results for random pattern case.

our previous calculations for random pattern case. It can be seen that lower values of the jamming coverage fraction are reached by the deposition process involving randomness in the pattern compared to a deposition process in the presence of a regular substrate pattern, regardless of the value of the density  $\theta_0^{(\text{cell})}$ .

Below we try to characterize quantitatively the time dependence of the approach to the jammed state at large times. Depending on the system of interest modeled by RSA, the substrate can be continuous (off lattice) or discrete. Asymptotic approach of the coverage fraction  $\theta(t)$  to its jamming limit,  $\theta_J = \theta(t \rightarrow \infty)$ , is known to be given by an algebraic time dependence for continuous substrates [25–29]:

$$\theta(t) \sim \theta_J - At^{-1/d}, \quad (3)$$

where  $A$  is a constant coefficient and  $d$  is interpreted as substrate dimension [26] in case of spherical particles adsorption or, more generally, as a number of degrees of freedom [30]. For lattice RSA models, the approach to the jamming coverage is exponential [31–36]:

$$\theta(t) \sim \theta_J - \Delta\theta \exp(-t/\sigma), \quad (4)$$

where parameters  $\theta_J$ ,  $\Delta\theta$ , and  $\sigma$  depend on the shape and orientational freedom of depositing objects [34, 36].

Representative examples of the double logarithmic plots of the first derivative of coverage  $\theta(t)$  with respect to time  $t$  are shown in Figure 5(a), for various values of the cell size,  $\alpha_k$  ( $k = 1, 2, 3, 4$ ), and for high density of landing cells,  $\theta_0^{(\text{cell})} = 0.5$ . The time derivatives of  $\theta(t)$  are calculated numerically from the simulation data. In the case of the algebraic behavior of the coverage fraction  $\theta(t)$  (equation (3)), a double logarithmic plot of the first time derivative  $\frac{d\theta}{dt} \propto t^{-\frac{1+d}{d}}$  is a straight line. One can see that curves shown in figure 5(a) are straight lines in the late stage of deposition process. However, the same is not valid for all values of densities of landing cells  $\theta_0^{(\text{cell})}$ . The double logarithmic plots

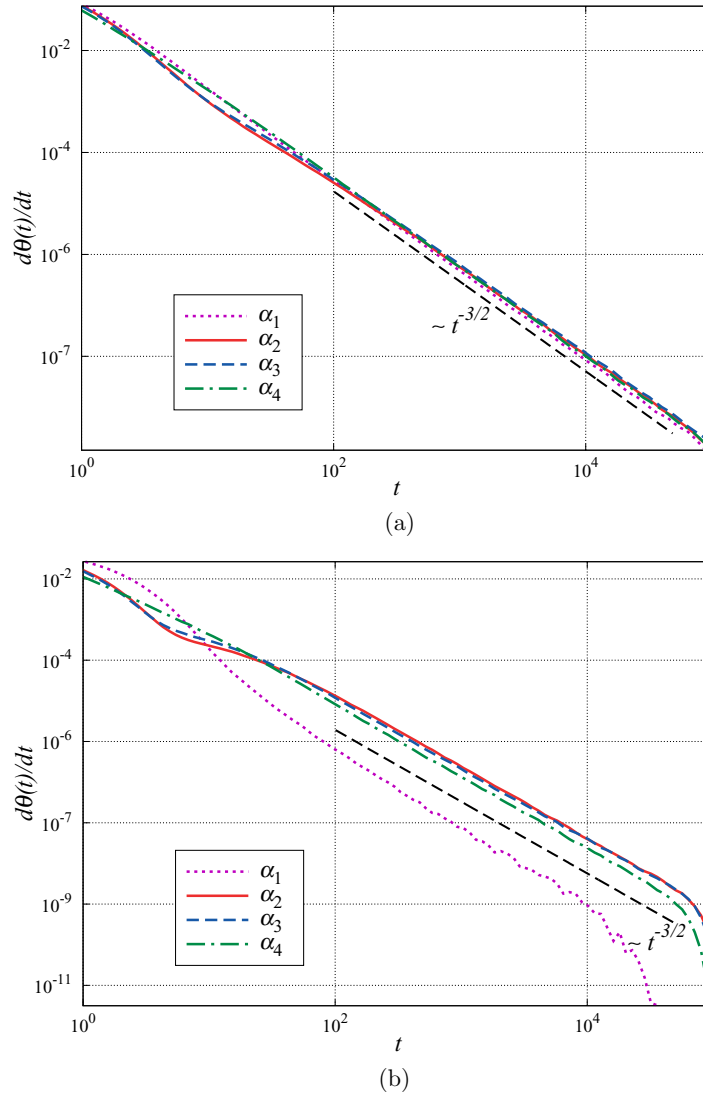


**Figure 5.** Test for the presence of the algebraic law (3) in the approach of the coverage  $\theta(t)$  to the jamming limit for different densities of landing cells: (a)  $\theta_0^{(\text{cell})} = 0.5$ , and (b)  $\theta_0^{(\text{cell})} = 0.1$ . The curves in each graph correspond to various values of the cell size,  $\alpha_k$  ( $k = 1, 2, 3, 4$ ), as indicated in the legend. Straight line sections of the curves show where the law holds. The dashed black line has slope  $-3/2$  and is a guide for the eye.

of the numerically calculated derivatives of  $\theta(t)$  for the data obtained in the case of low density of landing cell  $\theta_0^{(\text{cell})} = 0.1$  are shown in figure 5(b). As it can be seen, at the very late times of the deposition process the plot of the first derivative of coverage fraction  $\theta(t)$  with respect to time  $t$  is not linear on a double logarithmic scale, indicating that the approach to the jamming limit is not consistent with the power law behavior given by equation (3). The deviation from the power law is particularly pronounced in the case of single particle per-cell adsorption (SPCA).

Kinetics of the irreversible deposition under SPCA conditions is illustrated in figure 6 where a logarithmic plots of  $\theta_J - \theta(t)$  versus  $t$  are shown for various densities of landing

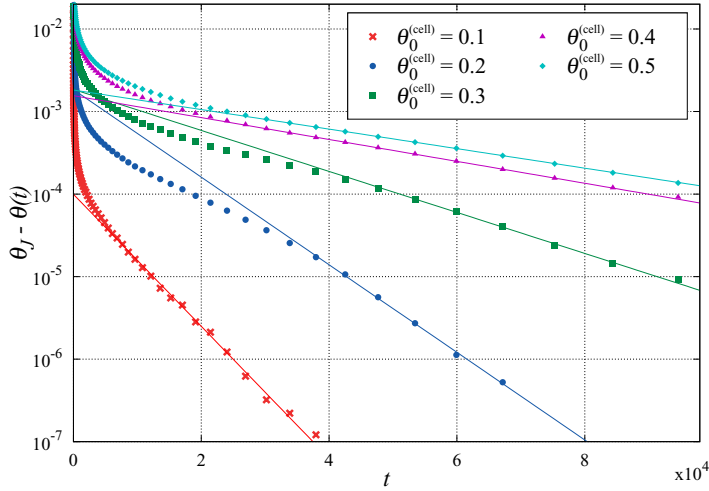


**Figure 6.** Plots of  $\theta_J - \theta(t)$  versus  $t$  in the single particle per-cell adsorption case for various densities of landing cells  $\theta_0^{(\text{cell})} = 0.1\text{--}0.5$ . The solid lines are the exponential fit of equation (4).

cells  $\theta_0^{(\text{cell})}$ . These plots are straight lines for the late times of deposition, suggesting that in the case of SPCA the approach to the jamming limit is indeed exponential, as in lattice RSA models. Indeed, the kinetics of deposition in SPCA case is determined by the kinetics of adsorption processes on finite-size landing cells. The difference relative to the lattice RSA is in the particle positions, which here are uncertain within the order of the size of the cell.

*3.1.2. Radial distribution function.* Here we compare quantitatively the structural characteristics of jamming coverings corresponding to different values of the cell size  $\alpha$  for various densities  $\theta_0^{(\text{cell})}$ . In order to gain basic insight into the ‘microstructure’ of the jammed state, we first consider the radial distribution function  $g(r)$  (or pair-correlation function) which gives information about the long-range interparticle correlations and their organization [24]. In absence of external forces, the pair correlation function can be calculated from expression

$$g(r) = \frac{S \overline{N}_a(r)}{N 2\pi r \Delta r}, \quad (5)$$

where  $r$  is the radial coordinate,  $S$  is the surface area,  $N$  is total number of particles adsorbed over this area, and  $\overline{N}_a$  is the averaged number of particles within the annulus of the radius  $r$  and the thickness  $\Delta r$ . In figure 7(a) we compare the radial distribution function  $g(r)$  at various densities  $\theta_0^{(\text{cell})} = 0.1\text{--}0.5$  in the SPCA case. As expected, the random deposition process never leads to correlation distances between the deposited particles exceeding two or three particle diameters. The position of the first peak measures typical distances between the closest disks. Decreasing the value of  $\theta_0^{(\text{cell})}$  in the SPCA case increases the uncertainty in the position of the particles which leads to peak broadening. The shape of radial distribution  $g(r)$  is more structured at higher densities, showing higher first and second peaks, because, when the system gets denser, particles will be deposited closer to one another. As can be seen from figure 7(a), the minima of  $g(r)$  curves shift to



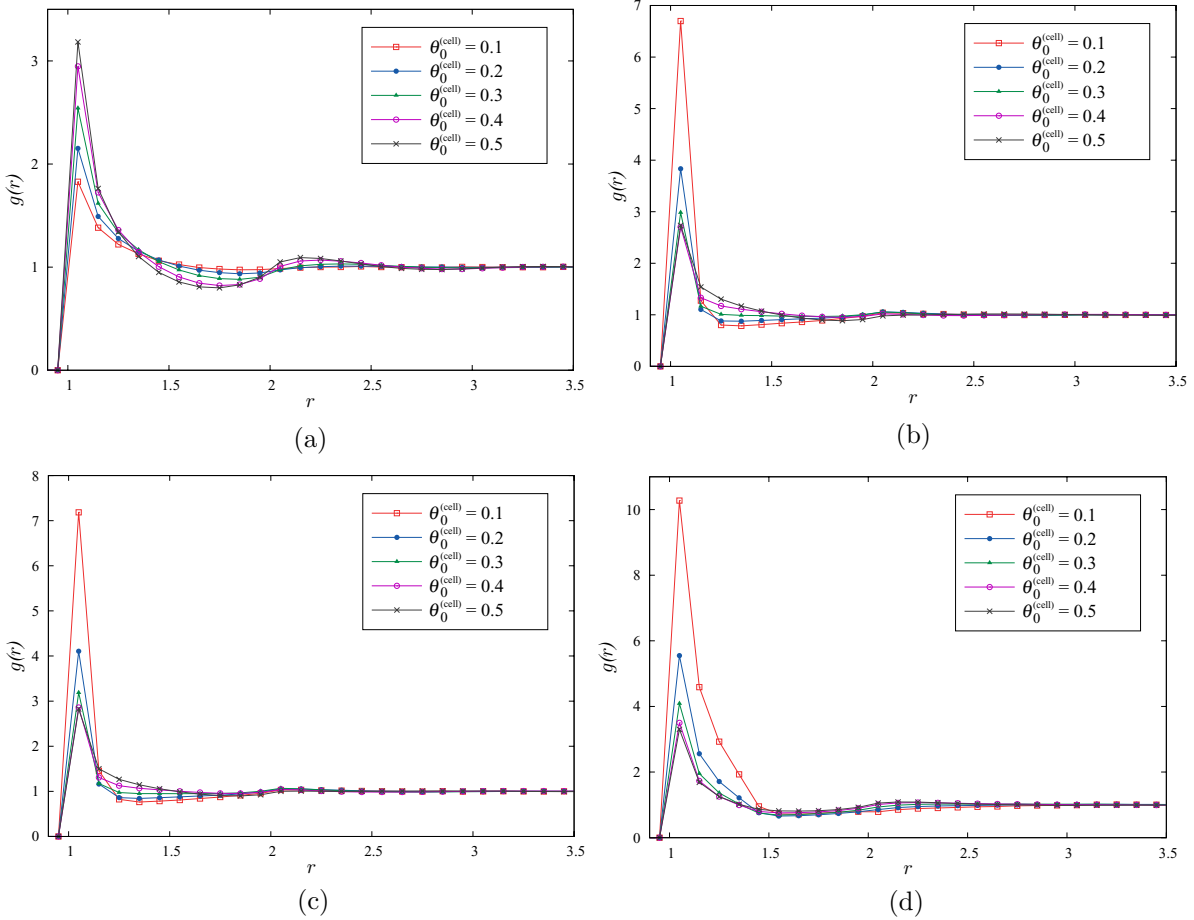


**Figure 7.** Radial distribution function  $g(r)$  for jamming coverings as a function of separation  $r$  (in units of the disk diameter  $d_0$ ) for various values of the cell size  $\alpha$ : (a)  $\alpha_1 = 1/\sqrt{2}$ , (b)  $\alpha_2 = (1 + \sqrt{3})/(2\sqrt{2})$ , (c)  $\alpha_3 = 1$ , (d)  $\alpha_4 = \sqrt{2}$ . The curves in each graph correspond to various values of density  $\theta_0^{(\text{cell})} = 0.1, 0.2, 0.3, 0.4, 0.5$ , as indicated in the legend.

shorter distances ( $\sim \sqrt{3}$ ) when the density  $\theta_0^{(\text{cell})}$  increases. At a very low densities, the broad minima are located near the distance  $\sim 2d_0$ . Indeed, since the particles are added at random, the probability that disks are connected as a three-bead chain is negligible.

The results for  $g(r)$  in the MPCA case are shown in figures 7(b)–(d). The shape of the radial distribution function  $g(r)$  is significantly affected by the values of the cell size  $\alpha$ . In the case of up-to-two disks per square cell (figure 7(b)) the peak which appears at unit distance is the most pronounced for low densities of landing cells  $\theta_0^{(\text{cell})}$ . For low values of  $\theta_0^{(\text{cell})}$ , one expects a lower impact of the cell–cell excluded volume interaction on the cell population. However, as  $\theta_0^{(\text{cell})}$  increases, the first peak of  $g(r)$  becomes broader because excluded volume interaction with disks belonging to neighboring cells reduces the average number of adsorbed disks per cell. This is opposite to what is observed under SPCA conditions (figure 7(a)), where the distance to the closest disk, on average, is determined by the distance of the nearest-neighbor landing cells.

The comparison of figures 7(b) and (c) shows that the results for  $g(r)$  in the case of up-to-two and up-to-three disks per square cell are very similar. This arises as a direct consequence of the fact that cells with sizes  $\alpha_2 \approx 0.966$  and  $\alpha_3 = 1$  have very similar population of particles (see figure 3). Figure 7(d) shows the radial distribution function  $g(r)$  of jamming coverings at several densities  $\theta_0^{(\text{cell})}$  obtained in simulations carried out with the cell size of  $\alpha_4 = \sqrt{2}$ . For this value of the parameter  $\alpha$ , each cell is of sufficient size to accommodate up to four particles. As can be seen in figures 7(b)–(d), increasing the value of parameter  $\alpha$  in the MPCA case increases the uncertainty in the position of the disk within the cell, i.e. it leads to peak broadening.

*3.1.3. Volume distribution of the pores.* Further analysis is based on the Voronoï tessellation, which allows us to unambiguously decompose any arbitrary arrangement of disks into space-filling set of cells. Given a set  $\mathcal{A}$  of discrete points in the plane  $\pi$  (centers of disks), for almost any point  $x \in \pi$  in the plane  $\pi$  there is one specific point  $a_i \in \mathcal{A}$  which is closest to  $x$ . The set of all points of the plane which are closer to a given point  $a_i \in \mathcal{A}$  than to any other point  $a_j \neq a_i$ ,  $a_j \in \mathcal{A}$ , is the interior of a convex polygon  $\mathcal{P}_i$  usually called the Voronoï cell of  $a_i$ . The set of the polygons  $\{\mathcal{P}_i\}$ , each corresponding to (and containing) one point  $a_i \in \mathcal{A}$ , is the Voronoï tessellation corresponding to  $\mathcal{A}$ , and provides a partitioning of the plane  $\pi$ . Voronoï cells are convex and their edges join at trivalent vertices, i.e. each vertex is equidistant to three neighboring disks. Two disks sharing a common cell edge are neighbors. In this work, the Quickhull algorithm [37] is used to compute the Voronoï diagrams in MATLAB<sup>®</sup> for a given set of disks on a plane.

The jammed-state coverings are analyzed in terms of volume distributions of the pores. The convenient definition of a pore is based on the Delaunay triangulation (DT), which is a natural way to subdivide a 2D structure of disks into a system of triangles with vertices at the centers of neighboring disks. Consequently, the circle circumscribing a Delaunay triangle has its center at the vertex of a Voronoï polygon. In this work we define the pore as a part of the Delaunay triangle not occupied by the disks (Delaunay ‘free’ volume) [21, 22]. The pore volume  $v$  is normalized by the ‘volume’ of the disks,  $v_0 = d_0^2\pi/4$ . In figure 8 we show Delaunay triangulation of typical jammed-state covering obtained for the same conditions as in figure 1(a) ( $\theta_0^{(\text{cell})} = 0.3$ ,  $\alpha_4 = \sqrt{2} \approx 1.41$ ). Looking at the diagram of figure 8, one can observe variations in the area of Delaunay triangles, which indicates the presence of pores of various sizes in the deposit.

Here we consider the probability distribution  $P(v)$  of the Delaunay ‘free’ volume  $v$ . The distribution function  $P(v)$  represents the probability of finding a pore with volume  $v$ . Fluctuations in the measurements of  $P(v)$  are reduced by averaging over 100 different simulations, performed under the same conditions. We compare volume distribution of the pores  $P(v)$  for jamming coverings corresponding to different values of the cell size  $\alpha$  and various densities of landing cells  $\theta_0^{(\text{cell})}$ , as illustrated in figures 9(a)–(e). Here, the pore distributions  $P(v)$  obtained for densities  $\theta_0^{(\text{cell})} = 0.1, 0.2, 0.3, 0.4, 0.5$  have been plotted. At very low value of  $\theta_0^{(\text{cell})} = 0.1$  (figure 9(a)), the curves of volume distribution  $P(v)$  are asymmetric with a quite long tail on the right-hand side, which progressively reduces while the cell size  $\alpha$  increases at the fixed density. At the same time, the distribution  $P(v)$  becomes narrower and more localized around the low values of the pore volume  $v$ .

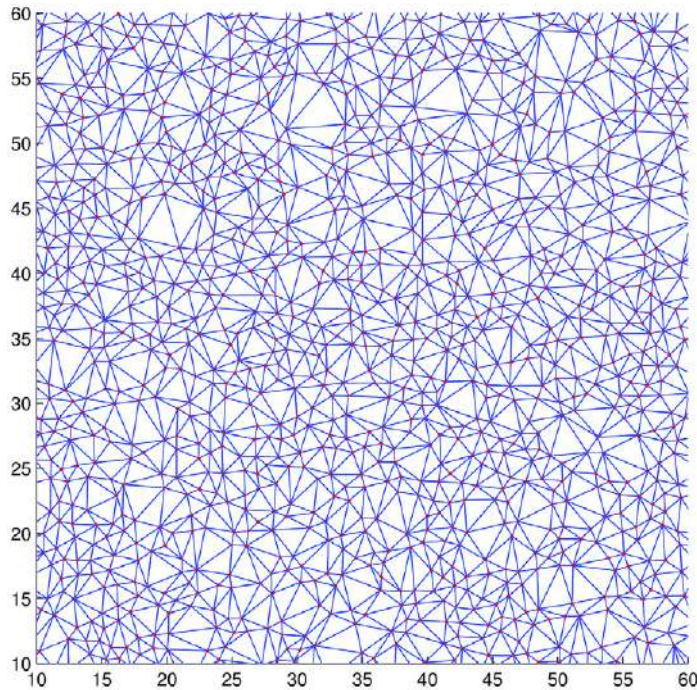


**Figure 8.** Delaunay triangulation of a set of points (centers of disks). Diagram corresponds to jammed-state covering obtained for density of landing cells  $\theta_0^{(\text{cell})} = 0.3$  and cell size  $\alpha_4 = \sqrt{2}$ ; see figure 1(a) for a typical configuration. The red dots are centers of the adsorbed disks. Length is measured in units of the disk diameter  $d_0$ .

This behavior of the distribution  $P(v)$  was not observed for all densities of landing cells  $\theta_0^{(\text{cell})} = 0.1\text{--}0.5$  (see figures 9(a)–(e)). For densities  $\theta_0^{(\text{cell})} \geq 0.2$ , the pore distributions  $P(v)$  obtained for deposition on square cells of size  $\alpha_2$  and  $\alpha_3$  are broader and shifted to higher values of volumes  $v$  compared to the pore distribution  $P(v)$  corresponding to SPCA case ( $\alpha_1$ ). Qualitative interpretation of this result is given below.

In the case of up-to-four disks per square cell ( $\alpha_4 = \sqrt{2}$ ), we observe the appearance of pronounced peak of  $P(v)$  at low values of  $v$ , approximately at  $v = 0.15\text{--}0.20$ . It is easy to understand which kind of local configuration contributes mostly to this peak of the  $P(v)$ . The Delaunay cells with free dimensionless volume  $v_{\text{hex}} = \sqrt{3}/\pi - 1/2 \approx 0.051$  correspond to the local arrangements of hexagonal symmetry, when three disks are all in touch with each other with centers on the vertices of a unilateral triangle. The cells with free volume  $v_{\text{quad}} = 2/\pi - 1/2 \approx 0.13$  correspond to the local configurations of quadratic symmetry, when centers of four touching disks are positioned on the vertices of a square. These are minimal values of pore volumes that can be formed with three and four disks deposited on a single landing cell of size  $\alpha_4 = \sqrt{2}$ . However, the probability that the previously described structures of quadratic and hexagonal symmetry arise during the process of random deposition is negligibly small. Therefore, the ‘free’ volumes formed with random deposition of disks into a single cell are larger than the minimal values  $v_{\text{hex}} \approx 0.051$  and  $v_{\text{quad}} \approx 0.13$ , so that observed peak of  $P(v)$  is around  $v \lesssim 0.20$ .

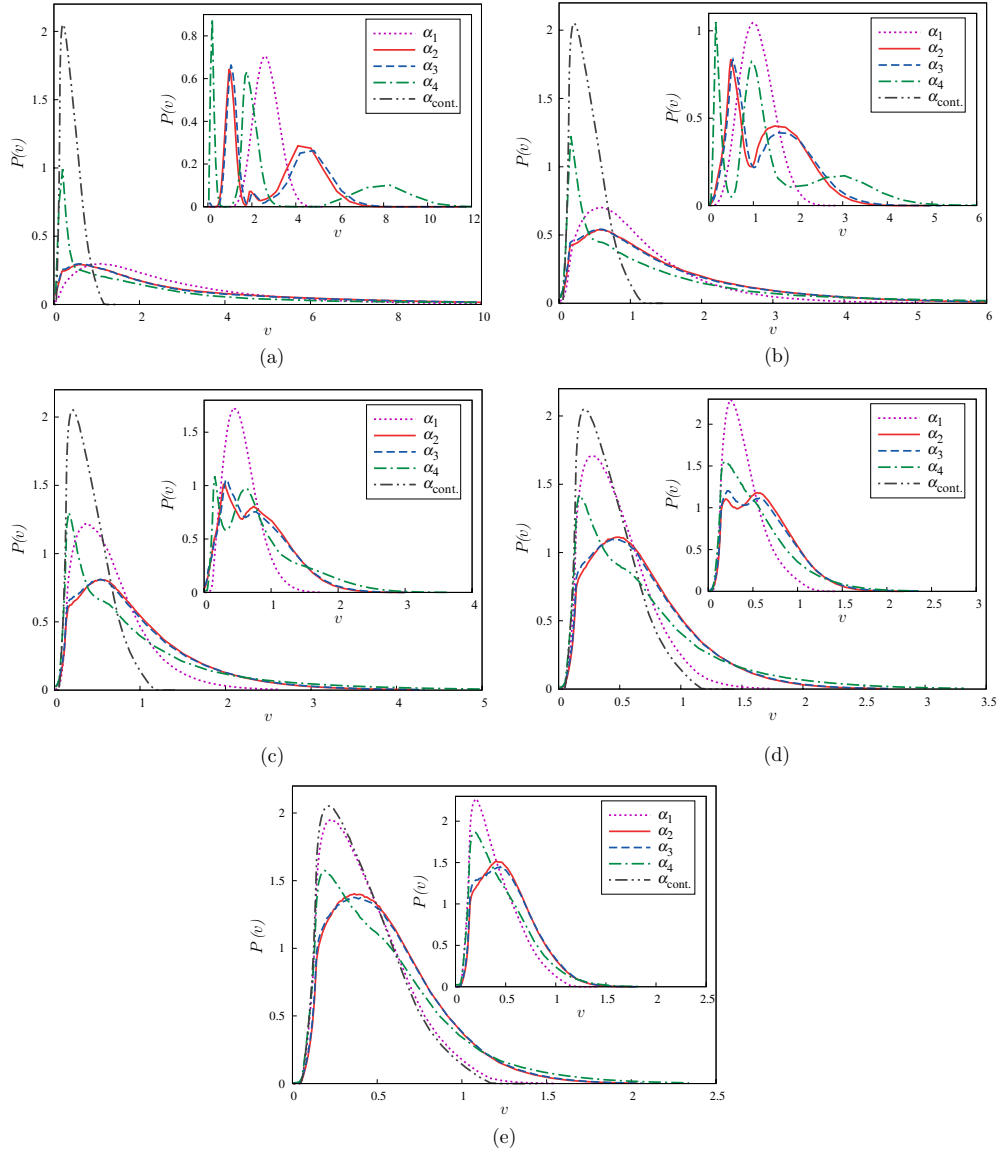


**Figure 9.** Main panel: Volume distribution of the pores  $P(v)$  for jamming coverings at different values of density of the landing cells corresponding to  $\theta_0^{(\text{cell})} = 0.1$  (a), 0.2 (b), 0.3 (c), 0.4 (d), 0.5 (e) are shown in the case of random pattern. The curves in each graph correspond to various values of the cell size,  $\alpha_k$  ( $k = 1, 2, 3, 4$ ), as indicated in the legend. The  $\alpha_{\text{cont}}$  line shows distribution  $P(v)$  for jamming covering in the case of the irreversible disks deposition on a continuous substrate. Insets: Volume distribution of the pores  $P(v)$  for jamming coverings obtained from simulations carried out using the heterogeneous surface covered by square cells centered at the vertices of a square lattice. The size  $\alpha$  and density  $\theta_0^{(\text{cell})}$  of landing cells are the same as those used in the main panel.

At high values of density of landing cells  $\theta_0^{(\text{cell})} = 0.5$  (figure 9(e)), distribution  $P(v)$  obtained under SPCA conditions becomes very similar to pore volume distribution for RSA of disks on a continuous substrate, as expected. The results for the volume distribution of the pores  $P(v)$  obtained in the cases of up-to-two and up-to-three disks

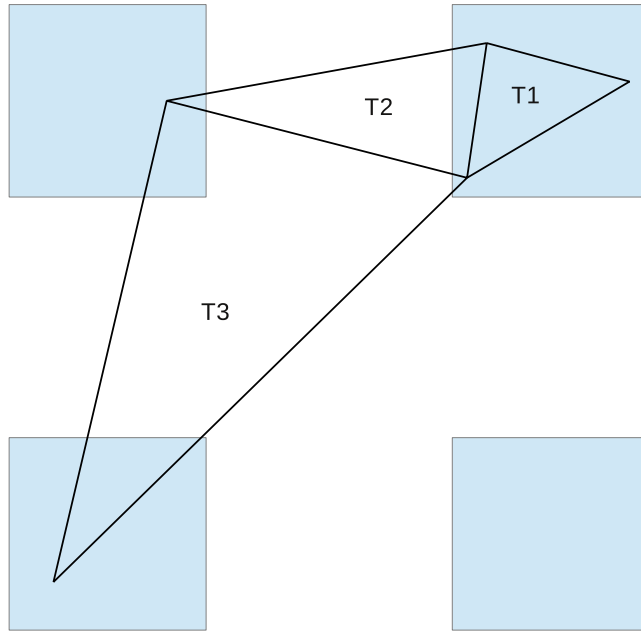


**Figure 10.** Various types of Delaunay triangles (T1–T3) depending on the position of vertices.

per square cell are almost identical at all densities  $\theta_0^{(\text{cell})}$  (see figure 9). The similarity of these distributions at small values of pore volumes can be explained by the results shown in figure 3. Small pores appear due to the presence of configurations with three or more disks on a single landing cell. But, in the case of up-to-three disks per square cell, the number of in-cell configurations with three disk is considerably smaller than the number of configurations with one or two disks. Consequently, broad maximum in  $P(v)$ , centered at  $v = 0.4\text{--}0.6$  is caused by contribution of large pores formed mostly in the space between the landing cells.

Further, we study the effect of the presence of a regular substrate pattern of squares on volume distribution of the pores  $P(v)$ . Distributions  $P(v)$  for jamming coverings corresponding to  $\theta_0^{(\text{cell})} = 0.1\text{--}0.5$  and different values of the cell size  $\alpha_k$  ( $k = 1, 2, 3, 4$ ) are shown in insets of figure 9. At low density of landing cells  $\theta_0^{(\text{cell})} = 0.1$  and for large cell size  $\alpha \geq \alpha_4 = \sqrt{2}$  (see inset of figure 9(a)) we observe the appearance of three peaks of  $P(v)$ . The first peak at  $v \approx 0.2$  is due to Delaunay triangles with their vertices inside a single landing cell (see T1 triangle in figure 10). The third peak at  $v \approx 8$  corresponds to Delaunay triangles with vertices located in different landing cells (see T3 triangle in figure 10). Central peak at  $v \approx 2$  arises due to Delaunay triangles with two vertices belonging to single cell, while the third one is located in a neighboring cell (see T2 triangle in figure 10). The first peak at very low values of pore volumes  $v$  does not appear for the smaller landing cells,  $\alpha = \alpha_1, \alpha_2, \alpha_3$ . Indeed, if  $\alpha \leq \alpha_3$ , the Delaunay triangles that lie within a single landing cell are very rare ( $\alpha = \alpha_3$ ) or they can not exist ( $\alpha \leq \alpha_2$ ). In the case of single particle per-cell adsorption ( $\alpha = \alpha_1$ ) vertices of each Delaunay triangle are located in three different cells, so that distribution  $P(v)$  has only one broad maximum. As can be seen from insets of figure 9, the difference between distribution  $P(v)$  for regular

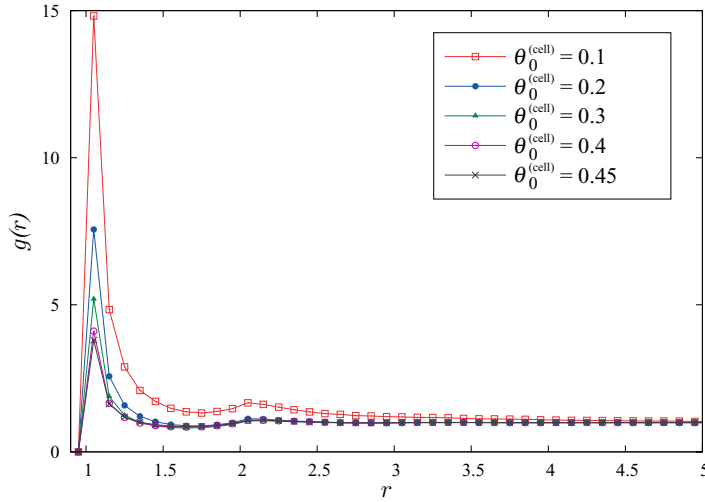


**Figure 11.** Radial distribution function  $g(r)$  for jamming coverings as a function of separation  $r$  (in units of the disk diameter  $d_0$ ) obtained from simulations carried out using the heterogeneous surface covered by rectangles of arbitrary orientation. The curves correspond to various values of density  $\theta_0^{(\text{cell})} = 0.1, 0.2, 0.3, 0.4, 0.45$ , as indicated in the legend.

substrate pattern of squares and for random pattern case decreases with the increase of the cell density  $\theta_0^{(\text{cell})}$ .

### 3.2. Circles on rectangles

We have also performed numerical simulations of random deposition of identical disks on heterogeneous surfaces covered by rectangles of arbitrary orientation. In these simulations, each landing cell is a rectangle with sides  $\alpha = 8$  and  $\beta = 1$  (in units of the disk diameter  $d_0$ ). The choice of the value of aspect ratio  $\alpha/\beta$  plays important role in our model. Increasing of the aspect ratio of the landing cells (rectangles) leads to the formation of domains of increased regularity. The chosen value of  $\alpha/\beta = 8$  is large enough to provide patterned substrate that is significantly different from the surfaces in the case with the square cells. We have verified that usage of a different, but large, values of aspect ratio  $\alpha/\beta$  gives quantitatively very similar results leading to qualitatively same phenomenology.

To characterize the jammed state we studied radial distribution function  $g(r)$  and probability distribution  $P(v)$  of pore volume  $v$  for different values of density of landing cells:  $\theta_0^{(\text{cell})} = 0.1, 0.2, 0.3, 0.4, 0.45$ . Figure 11 shows the corresponding results for radial distribution function  $g(r)$ . Comparing the results from figures 7(b)–(d) and 11, one can see that the first peak near  $r/d_0 = 1$  and local maximum at  $r/d_0 \gtrsim 2$  of  $g(r)$  are more pronounced in the case of elongated rectangular cells than in the case of multi-particle adsorption (MPCA) at squares. This emergence of a better local order is a correlation effect that develops during the deposition stage, due to the formation of arrays of disks along a single elongated rectangular cells.

Figure 12 compares volume distribution of the pores  $P(v)$  for jamming coverings corresponding to different densities  $\theta_0^{(\text{cell})}$ . Similar to the case of MPCA on square cells,

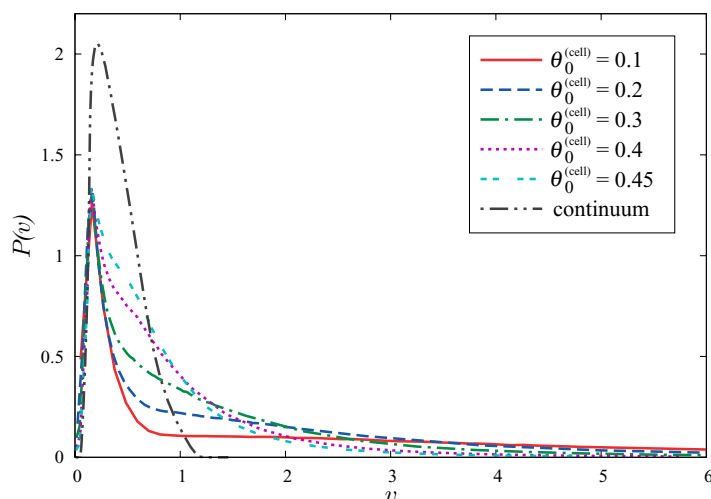


**Figure 12.** Volume distribution of the pores  $P(v)$  obtained from simulations carried out using the heterogeneous surface covered by rectangles of arbitrary orientation. The curves correspond to various values of density  $\theta_0^{(\text{cell})} = 0.1, 0.2, 0.3, 0.4, 0.45$ , as indicated in the legend. Distribution  $P(v)$  for jamming covering in the case of the irreversible disks deposition on a continuous substrate is shown for comparison.

here we observe the peak of  $P(v)$  at small values of  $v \approx 0.2$ . As previously mentioned, such small pores are feature of coverings which occurs when three or more particles can be adsorbed on a single cell. The observed peak of the distribution  $P(v)$  broadens when density  $\theta_0^{(\text{cell})}$  increases. Deposition of elongated objects at high densities is characterized with compact domains of parallel objects and large islands of unoccupied substrate area. Figure 13 shows typical snapshot of the jammed-state covering obtained for rectangular cells of arbitrary orientation and density  $\theta_0^{(\text{cell})} = 0.45$ . Relatively high local packing of nearly parallel adsorbed rectangles reduces the number of disks effectively adsorbed at a cell. This process is associated with the appearance of larger interstitial voids, which causes the peak broadening.

It is now useful to explore the interplay between the anisotropy in deposition procedure for landing cells and structural characteristics of jamming coverings. In this case the orientation of rectangular cells is fixed to the one preferential direction. The configuration formed in the long time regime is made up of a large number of domains; see figure 14 for typical configuration. As expected, any such domain contains parallel cells all close to each other. This produces better packing of landing cells and higher impact of the cell-cell excluded volume interaction on the average cell population. Hence, anisotropic deposition of landing cells lowers the average cell population, which enhances the appearance of larger pores, resulting in a peak broadening. Volume distributions of pores  $P(v)$  for jamming coverings of disks corresponding to anisotropic deposition of cells are shown in figure 15 with thick lines, while the case of arbitrarily oriented cells from figure 12 is drawn with thin lines for comparison. Figure 15 clearly shows enhanced peak broadening of  $P(v)$  in the case of anisotropic deposition of landing cells, which is consistent with previous discussion.

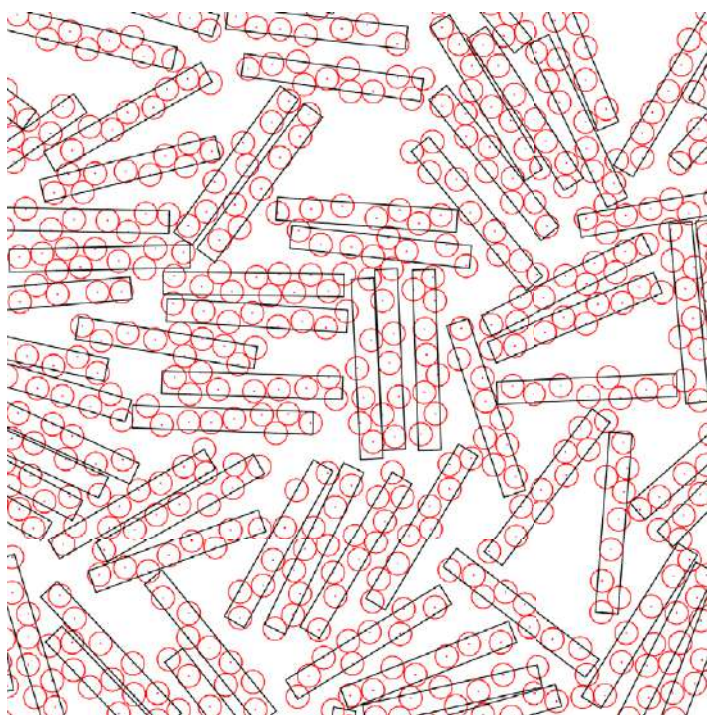


**Figure 13.** Typical jammed-state configuration of a region of size  $30 \times 30$  (in units of the disk diameter  $d_0$ ), for  $\theta_0^{(\text{cell})} = 0.45$ . Orientation of rectangular cells with sides  $\alpha = 8$  and  $\beta = 1$  is arbitrary. Deposition of elongated objects (cells) is characterized with domains of nearly parallel objects and large islands of unoccupied space.

#### 4. Concluding remarks

We investigated numerically RSA of disk-shaped particles on a nonuniform substrates, with focus on the jammed-state properties. A surface heterogeneities consisting of square cells and elongated rectangles were considered. The influence of the cell size and density of landing cells on kinetics of deposition process, and on morphological characteristics of the coverings were studied.

We found that for a given density of landing cells, the highest jamming coverage and the fastest kinetics of the deposition process can be achieved in the SPCA case. Due to the fact that the densification kinetics is dictated by geometric exclusion effects, the coverage kinetics is severely slowed down in the MPCA case.

To examine the short scale structure in the jammed-state coverings, we evaluated the radial correlation function  $g(r)$  which measures the particle density-density correlation at distance  $r$  for various shapes and sizes of the landing cells. The oscillation of  $g(r)$  quickly decays for all densities of landing cells  $\theta_0^{(\text{cell})}$ , which means that long-range order does not exist in the system. In the MPCA case, the peak of  $g(r)$  which appears at unit distance is the most pronounced for low densities of landing cells  $\theta_0^{(\text{cell})}$ . This is opposite to what is observed under SPCA conditions when the shape of radial distribution  $g(r)$  is more structured at higher densities  $\theta_0^{(\text{cell})}$ .



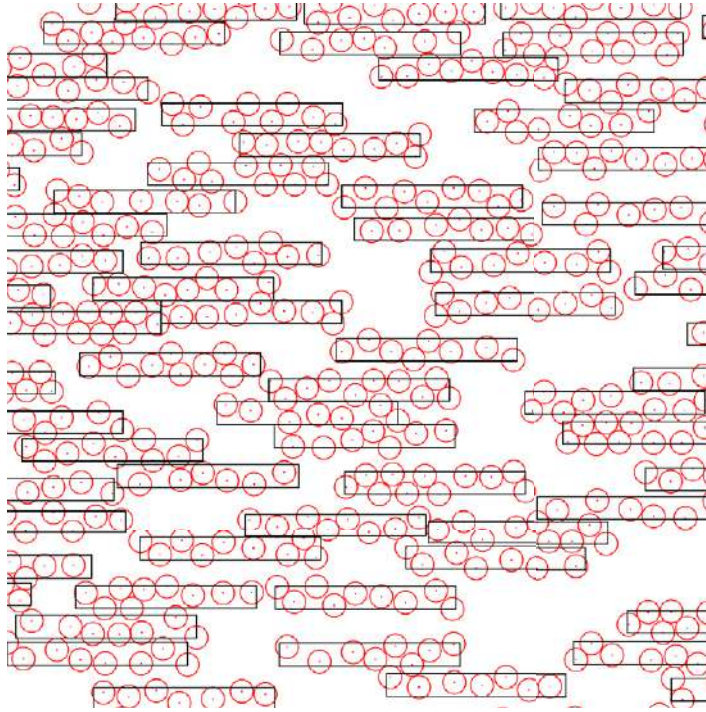


**Figure 14.** Typical jammed-state configuration of a region of size  $30 \times 30$  (in units of the disk diameter  $d_0$ ,) for  $\theta_0^{(\text{cell})} = 0.45$ . Orientation of rectangular cells with sides  $\alpha = 8$  and  $\beta = 1$  is fixed to the horizontal direction.

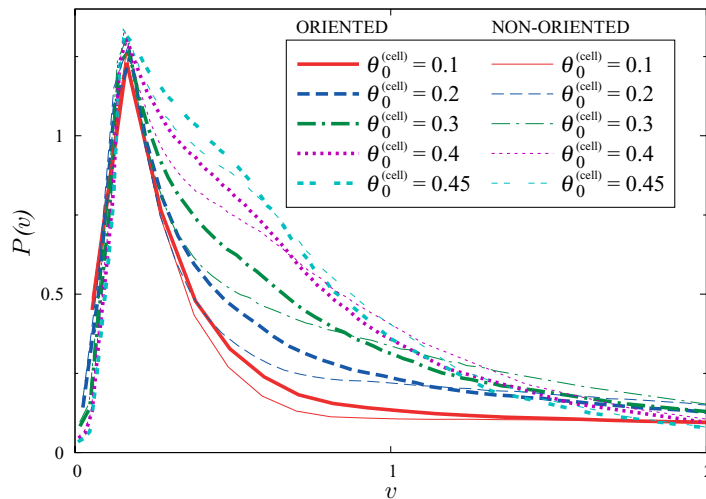


**Figure 15.** Volume distribution of the pores  $P(v)$  obtained from simulations carried out using the heterogeneous surface covered by rectangles of fixed orientation (thick lines) and arbitrary orientations (thin lines). The curves correspond to various values of density  $\theta_0^{(\text{cell})} = 0.1, 0.2, 0.3, 0.4, 0.45$ , as indicated in the legend.

Morphology of deposited disks has also been analyzed through the distribution of pore volumes. This distribution is sensitive to small structural changes of the covering and therefore describes the degree to which the cell size and cell density affects the deposit

morphology. Delaunay ‘free’ volumes have a distribution with a long tail, particularly at low densities  $\theta_0^{(\text{cell})}$ . We have found that the distribution  $P(v)$  becomes narrower and more localized around the low values of  $v$  with increasing of  $\theta_0^{(\text{cell})}$ . In the case of the largest cells ( $\alpha \geq \alpha_4 = \sqrt{2}$ ), we have observed the pronounced peak of  $P(v)$  at low values of  $v = 0.15$ – $0.20$ , which appears due to presence of configurations with three or more disks on a single landing cell. We have also studied the influence of a regular substrate pattern on volume distribution of the pores  $P(v)$ . At low densities  $\theta_0^{(\text{cell})}$ , distribution function  $P(v)$  shows a well developed peaks which correspond to the various types of Delaunay triangles, as shown in figure 10. Cell–cell excluded volume interaction increases with the cell density  $\theta_0^{(\text{cell})}$ , so that distribution  $P(v)$  for regular substrate pattern of squares becomes similar to  $P(v)$  for random pattern case at densities near jamming limit for RSA of square cells.

Numerical simulations of random deposition on heterogeneous substrates covered by elongated rectangles have shown that the shape of the pore distribution function  $P(v)$  is affected by the anisotropy in deposition procedure for landing cells. It is shown that anisotropic deposition of landing cells lowers the average cell population and reduces the number of small pores. Our results suggest that the porosity of deposit (pore volumes) can be controlled by the size and shape of landing cells, and by anisotropy of cell deposition procedure. It must be emphasized that radial correlation function  $g(r)$  for jamming coverings of disks corresponding to anisotropic deposition of rectangles is quite similar to  $g(r)$  for the case of isotropic landing-cell pattern and is not detailed here.

## Acknowledgments

This work was supported by the Ministry of Education, Science and Technological Development of the Republic of Serbia, under Grant No. ON171017. Work at TAMUQ was supported by NPRP grant #6-021-1-005 and from the Qatar National Research Fund (a member of Qatar Foundation).

## References

- [1] Parisse P, Luciani D, D’Angelo A, Santucci S, Zuppella P, Tucceri P, Reale A and Ottaviano L 2009 Patterning at the nanoscale: atomic force microscopy and extreme ultraviolet interference lithography *Mater. Sci. Eng. B* **165** 227–30
- [2] Kraus T, Malaquin L, Schmid H, Riess W, Spencer N D and Wolf H 2007 Nanoparticle printing with single-particle resolution *Nat. Nanotechnol.* **2** 570–6
- [3] Kershner R J *et al* 2009 Placement and orientation of individual dna shapes on lithographically patterned surfaces *Nat. Nanotechnol.* **4** 557–61
- [4] delCampo A, Greiner C, Àlvarez I and Arzt E 2007 Patterned surfaces with pillars with controlled 3d tip geometry mimicking bioattachment devices *Adv. Mater.* **19** 1973–7
- [5] Flory P J 1939 Intramolecular reaction between neighboring substituents of vinyl polymers *J. Am. Chem. Soc.* **61** 1518
- [6] Evans J W 1993 Random and cooperative sequential adsorption *Rev. Mod. Phys.* **65** 1281–329
- [7] Privman V 2000 Dynamics of nonequilibrium deposition *Colloids Surf. A* **165** 231–40
- [8] Talbot J, Tarjus G, Van Tassel P R and Viot P 2000 From car parking to protein adsorption: an overview of sequential adsorption processes *Colloids Surf. A* **165** 287–324

- [9] Senger B, Voegel J C and Schaaf P 2000 Irreversible adsorption of colloidal particles on solid substrates *Colloids Surf. A* **165** 255–85
- [10] Cadilhe A, Araújo N A M and Privman V 2007 Random sequential adsorption: from continuum to lattice and pre-patterned substrates *J. Phys.: Condens. Matter* **19** 065124
- [11] Jin X, Wang N H L, Tarjus G and Talbot J 1993 Irreversible adsorption on non-uniform surfaces: the random site model *J. Chem. Phys.* **97** 4256
- [12] Jin X, Talbot J and Wang N H L 1994 Analysis of steric hindrance effects on adsorption kinetics and equilibria *AIChE J.* **40** 1685
- [13] Oleyar C and Talbot J 2007 Reversible adsorption on random site surface *Physica A* **376** 27–37
- [14] Adamczyk Z, Weronki P and Musial E 2002 Irreversible adsorption of hard spheres at random site (heterogeneous) surfaces *J. Chem. Phys.* **116** 4665
- [15] Adamczyk Z, Siwek B, Weronki P and Musial E 2002 Irreversible adsorption of colloid particles at heterogeneous surfaces *Appl. Surf. Sci.* **196** 250
- [16] Marques J F, Lima A B, Araújo N A M and Cadilhe A 2012 Effect of particle polydispersity on the irreversible adsorption of fine particles on patterned substrates *Phys. Rev. E* **85** 061122
- [17] Araújo N A M, Cadilhe A and Privman V 2008 Morphology of fine-particle monolayers deposited on nanopatterned substrates *Phys. Rev. E* **77** 031603
- [18] Aurenhammer F 1991 Voronoi diagrams: a survey of a fundamental geometric data structure *ACM Comput. Surv.* **23** 345
- [19] Philippe P and Bideau D 2001 Numerical model for granular compaction under vertical tapping *Phys. Rev. E* **63** 051304
- [20] Richard P, Philippe P, Barbe F, Bourles S, Thibault X and Bideau D 2003 Analysis by x-ray microtomography of a granular packing undergoing compaction *Phys. Rev. E* **68** 020301
- [21] Aste T 2005 Variations around disordered close packing *J. Phys.: Condens. Matter* **17** S2361–90
- [22] Aste T 2006 Volume fluctuations and geometrical constraints in granular packs *Phys. Rev. Lett.* **96** 018002
- [23] Arsenović D, Vrhovac S B, Jakšić Z M, Budinski-Petković Lj and Belić A 2006 Simulation study of granular compaction dynamics under vertical tapping *Phys. Rev. E* **74** 061302
- [24] Truskett T M, Torquato S, Sastry S, Debenedetti P G and Stillinger F H 1998 Structural precursor to freezing in the hard-disk and hard-sphere systems *Phys. Rev. E* **58** 3083–8
- [25] Feder J 1980 Random sequential adsorption *J. Theor. Biol.* **87** 237
- [26] Swendsen R 1981 Dynamics of random sequential adsorption *Phys. Rev. A* **24** 504
- [27] Pomeau Y 1980 Some asymptotic estimates in the random parking problem *J. Phys. A: Math. Gen.* **13** L193
- [28] Bonnier B 2001 Random sequential adsorption of binary mixtures on a line *Phys. Rev. E* **64** 066111
- [29] Burrige D J and Mao Y 2004 Recursive approach to random sequential adsorption *Phys. Rev. E* **69** 037102
- [30] Hinrichsen E L, Feder J and Jøssang T 1986 Geometry of random sequential adsorption *J. Stat. Phys.* **44** 793–827
- [31] Bartelt M C and Privman V 1990 Kinetics of irreversible multilayer adsorption: one-dimensional models *J. Chem. Phys.* **93** 6820
- [32] Nielaba P, Privman V and Wang J S 1990 *J. Phys. A: Math. Gen.* **23** L1187
- [33] Manna S S and Švrakić N M 1991 Random sequential adsorption: line segments on the square lattice *J. Phys. A: Math. Gen.* **24** L671–6
- [34] Budinski-Petković Lj and Kozmidis-Luburić U 1997 Random sequential adsorption on a triangular lattice *Phys. Rev. E* **56** 6904
- [35] Budinski-Petković Lj and Kozmidis-Luburić U 1997 Jamming configurations for irreversible deposition on a square lattice *Physica A* **236** 211–9
- [36] Budinski-Petković Lj, Vrhovac S B and Lončarević I 2008 Random sequential adsorption of polydisperse mixtures on discrete substrates *Phys. Rev. E* **78** 061603
- [37] Barber C B, Dobkin D P and Huhdanpaa H 1996 The quickhull algorithm for convex hulls *ACM Trans. Math. Softw.* **22** 469

## SPEEDUP Code for Calculation of Transition Amplitudes via the Effective Action Approach

Antun Balaž\*, Ivana Vidanović, Danica Stojiljković,  
Dušan Vudragović, Aleksandar Belić and Aleksandar Bogojević

*Scientific Computing Laboratory, Institute of Physics Belgrade,  
University of Belgrade, Pregrevica 118, 11080 Belgrade, Serbia.*

Received 13 December 2010; Accepted 18 April 2011

Communicated by Leonardo Golubovic

Available online 28 October 2011

---

**Abstract.** We present Path Integral Monte Carlo C code for calculation of quantum mechanical transition amplitudes for 1D models. The SPEEDUP C code is based on the use of higher-order short-time effective actions and implemented to the maximal order  $p=18$  in the time of propagation (Monte Carlo time step), which substantially improves the convergence of discretized amplitudes to their exact continuum values. Symbolic derivation of higher-order effective actions is implemented in SPEEDUP Mathematica codes, using the recursive Schrödinger equation approach. In addition to the general 1D quantum theory, developed Mathematica codes are capable of calculating effective actions for specific models, for general 2D and 3D potentials, as well as for a general many-body theory in arbitrary number of spatial dimensions.

**AMS subject classifications:** 81Q05, 81Q15, 65Y04, 65B99

**Key words:** Transition amplitude, effective action, path integrals, Monte Carlo.

---

## 1 Introduction

Exact solution of a given many-body model in quantum mechanics is usually expressed in terms of eigenvalues and eigenfunction of its Hamiltonian

$$\hat{H} = \sum_{i=1}^M \frac{\hat{\mathbf{p}}_i^2}{2m_i} + \hat{V}(\hat{\mathbf{q}}_1, \dots, \hat{\mathbf{q}}_M), \quad (1.1)$$

but it can be also expressed through analytic solution for general transition amplitude  $A(\mathbf{a}, \mathbf{b}; T) = \langle \mathbf{b} | e^{-iT\hat{H}/\hbar} | \mathbf{a} \rangle$  from the initial state  $|\mathbf{a}\rangle$  to the final state  $|\mathbf{b}\rangle$  during the time of

---

\*Corresponding author. *Email addresses:* antun@ipb.ac.rs (A. Balaž), ivanavi@ipb.ac.rs (I. Vidanović), danica@ipb.ac.rs (D. Stojiljković), dusan@ipb.ac.rs (D. Vudragović), abelic@ipb.ac.rs (A. Belić), alex@ipb.ac.rs (A. Bogojević)

propagation  $T$ . Calculation of transition amplitudes is more suitable if one uses path integral formalism [1–3], but in principle, if eigenproblem of the Hamiltonian can be solved, one should be able to calculate general transition amplitudes, and vice versa. However, mathematical difficulties may prevent this, and even more importantly, exact solutions can be found only in a very limited number of cases. Therefore, use of various analytic approximation techniques or numerical treatment is necessary for detailed understanding of the behavior of almost all models of interest.

In numerical approaches it could be demanding and involved to translate numerical knowledge of transition amplitudes to (or from) eigenstates, but practically can be always achieved. It has been implemented in various setups, e.g. through extraction of the energy spectra from the partition function [2–5], and using the diagonalization of space-discretized matrix of the evolution operator, i.e. matrix of transition amplitudes [6–10]. All these applications use the imaginary-time formalism [11, 12], typical for numerical simulations of such systems.

Recently introduced effective action approach [13–17] provides an ideal framework for exact numerical calculation of quantum mechanical amplitudes. It gives systematic short-time expansion of amplitudes for a general potential, thus allowing accurate calculation of short-time properties of quantum systems directly, as has been demonstrated in [8–10]. For numerical calculations that require long times of propagation to be considered using e.g. Monte Carlo method, effective action approach provides improved discretized actions leading to the speedup in the convergence of numerically calculated discretized quantities to their exact continuum values. This has been also demonstrated in Monte Carlo calculations of energy expectation values using the improved energy estimators [5, 18].

In this paper we present SPEEDUP codes [19] which implement the effective action approach, and which were used for numerical simulations in [4, 5, 8–10, 13–17]. The paper is organized as follows. In Section 2 we briefly review the recursive approach for analytic derivation of higher-order effective actions. SPEEDUP Mathematica codes capable of symbolic derivation of effective actions for a general one- and many-body theory as well as for specific models is described in detail in Section 3, while in Section 4 we describe SPEEDUP Path Integral Monte Carlo C code, developed for numerical calculation of transition amplitudes for 1D models. Section 5 summarizes presented results and gives outlook for further development of the code.

## 2 Theoretical background

From inception of the path integral formalism, expansion of short-time amplitudes in the time of propagation was used for the definition of path integrals through the time-discretization procedure [2, 3]. This is also straightforwardly implemented in the Path Integral Monte Carlo approaches [20], where one usually relies on the naive discretization of the action. Several improved discretized actions, mainly based on the Trotter formula

and its generalizations, were developed and used in the past [21–23]. A recent analysis of this method can be found in Jang et al [24]. Several related investigations dealing with the speed of convergence have focused on improvements in short-time propagation [25, 26] or the action [27]. More recently, split-operator method has also been developed [28–32], later extended to include higher-order terms [33–36], and systematically improved using the multi-product expansion [37–39].

The effective action approach is based on the ideal discretization concept [16]. It was introduced first for single-particle 1D models [13–15] and later extended to general many-body systems in arbitrary number of spatial dimensions [5, 17]. This approach allows systematic derivation of higher-order terms to a chosen order  $p$  in the short time of propagation.

Recursive method for deriving discretized effective actions, established in [17], is based on solving the underlying Schrödinger equation for the amplitude. It has proven to be the most efficient tool for treatment of higher-order expansion. In this section we give brief overview of the recursive method, which will be implemented in Mathematica in the next section. We start with the case of single particle in 1D, used in the SPEEDUP C code. Throughout the paper we will use natural system of units, in which  $\hbar$  and all masses are set to unity.

## 2.1 One particle in one dimension

In the effective action approach, transition amplitudes are expressed in terms of the ideal discretized action  $S^*$  in the form

$$A(a, b; T) = \frac{1}{\sqrt{2\pi T}} e^{-S^*(a, b; T)}, \quad (2.1)$$

which can be also seen as a definition of the ideal action [16]. Therefore, by definition, the above expression is correct not only for short times of propagation, but for arbitrary large times  $T$ . We also introduce the ideal effective potential  $W$ ,

$$S^*(a, b; T) = T \left[ \frac{1}{2} \left( \frac{b-a}{T} \right)^2 + W \right], \quad (2.2)$$

reminiscent of the naive discretized action, with the arguments of the effective potential  $(a, b, T)$  usually written as  $W\left(\frac{a+b}{2}, \frac{b-a}{2}; T\right)$ , to emphasize that we will be using mid-point prescription.

However, ideal effective action and effective potential can be calculated analytically only for exactly solvable models, while in all other cases we have to use some approximative method. We use expansion in the time of propagation, assuming that the time  $T$  is small. If this is not the case, we can always divide the propagation into  $N$  time steps, so that  $\varepsilon = T/N$  is small. Long-time amplitude is then obtained by integrating over all short-time ones,

$$A(a, b; T) = \int dq_1 \cdots dq_{N-1} A(a, q_1; \varepsilon) A(q_1, q_2; \varepsilon) \cdots A(q_{N-1}, b; \varepsilon), \quad (2.3)$$

paving the way towards Path Integral Monte Carlo calculation, which is actually implemented in the SPEEDUP C code.

If we consider general amplitude  $A(q, q'; \varepsilon)$ , introduce the mid-point coordinate  $x = (q + q')/2$  and deviation  $\bar{x} = (q' - q)/2$ , and express  $A$  using the effective potential,

$$A(q, q'; \varepsilon) = \frac{1}{\sqrt{2\pi\varepsilon}} e^{-\frac{2}{\varepsilon}\bar{x}^2 - \varepsilon W(x, \bar{x}; \varepsilon)}, \quad (2.4)$$

the time-dependent Schrödinger equation for the amplitude leads to the following equation for  $W$

$$W + \bar{x}\bar{\partial}W + \varepsilon\partial_\varepsilon W - \frac{1}{8}\varepsilon\partial^2W - \frac{1}{8}\varepsilon\bar{\partial}^2W + \frac{1}{8}\varepsilon^2(\partial W)^2 + \frac{1}{8}\varepsilon^2(\bar{\partial}W)^2 = \frac{1}{2}(V_+ + V_-), \quad (2.5)$$

where  $V_\pm = V(x \pm \bar{x})$ , i.e.  $V_- = V(q)$ ,  $V_+ = V(q')$ . The short-time expansion assumes that we expand  $W$  to power series in  $\varepsilon$  to a given order, and calculate the appropriate coefficients using Eq. (2.5). We could further expect that this results in coefficients depending on the potential  $V(x)$  and its higher derivatives. However, this scheme is not complete, since the effective potential depends not only on the mid-point  $x$ , but also on the deviation  $\bar{x}$ , and the obtained equations for the coefficients cannot be solved in a closed form. In order to resolve this in a systematic way, we make use of the fact that, for short time of propagation, deviation  $\bar{x}$  is on the average given by the diffusion relation  $\bar{x}^2 \propto \varepsilon$ , allowing double expansion of  $W$  in the form

$$W(x, \bar{x}; \varepsilon) = \sum_{m=0}^{\infty} \sum_{k=0}^m c_{m,k}(x) \varepsilon^{m-k} \bar{x}^{2k}. \quad (2.6)$$

Restricting the above sum over  $m$  to  $p-1$  leads to level  $p$  effective potential  $W_p(x, \bar{x}; \varepsilon)$  which gives expansion of the effective action  $S_p^*$  to order  $\varepsilon^p$ , and hence the level designation  $p$  for both the effective action and the corresponding potential  $W_p$ . Thus, if the diffusion relation is applicable (which is always the case in Monte Carlo calculations), instead of the general double expansion in  $\bar{x}$  and  $\varepsilon$ , we are able to obtain simpler, systematic expansion in  $\varepsilon$  only.

As shown previously [13–15], when used in Path Integral Monte Carlo simulations for calculation of long time amplitudes according to Eq. (2.3), use of level  $p$  effective action leads to the convergence of discretized amplitudes proportional to  $\varepsilon^p$ , i.e. as  $1/N^p$ , where  $N$  is the number of time steps used in the discretization.

If we insert the above level  $p$  expansion of the effective potential to Eq. (2.5), we obtain the recursion relation derived in [17],

$$\begin{aligned} 8(m+k+1)c_{m,k} &= (2k+2)(2k+1)c_{m,k+1} + c''_{m-1,k} - \sum_{l=0}^{m-2} \sum_r c'_{l,r} c'_{m-l-2,k-r} \\ &\quad - \sum_{l=1}^{m-2} \sum_r 2r(2k-2r+2)c_{l,r} c_{m-l-1,k-r+1}, \end{aligned} \quad (2.7)$$

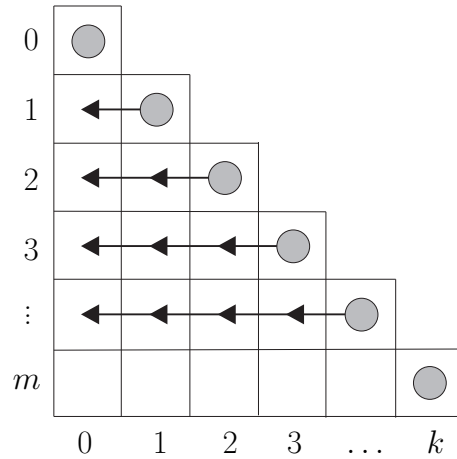


Figure 1: Order in which the coefficients  $c_{m,k}$  are calculated: diagonal ones from Eq. (2.8), off-diagonal from recursion (2.7).

where the sum over  $r$  goes from  $\max\{0, k-m+l+2\}$  to  $\min\{k, l\}$ . This recursion can be used to calculate all coefficients  $c_{m,k}$  to a given level  $p$ , starting from the known initial condition,  $c_{0,0} = V$ . The diagonal coefficients can be calculated immediately,

$$c_{m,m} = \frac{V^{(2m)}}{(2m+1)!} \tag{2.8}$$

and for a given value of  $m=0, \dots, p-1$ , the coefficients  $c_{m,k}$  follow recursively from evaluating (2.7) for  $k=m-1, \dots, 1, 0$ , as illustrated in Fig. 1.

### 2.2 Extension to many-body systems

The above outlined approach can be straightforwardly applied to many-body systems. Again the amplitude is expressed through the effective action and the corresponding effective potential, which now depends on mid-point positions and deviations of all particles. For simplicity, these vectors are usually combined into  $D \times M$  dimensional vectors  $\mathbf{x}$  and  $\bar{\mathbf{x}}$ , where  $D$  is spatial dimensionality, and  $M$  is the number of particles. In this notation,

$$A(\mathbf{q}, \mathbf{q}'; \epsilon) = \frac{1}{(2\pi\epsilon)^{DM/2}} e^{-\frac{2}{\epsilon}\bar{\mathbf{x}}^2 - \epsilon W(\mathbf{x}, \bar{\mathbf{x}}; \epsilon)}, \tag{2.9}$$

where initial and final position  $\mathbf{q} = (\mathbf{q}_1, \dots, \mathbf{q}_M)$  and  $\mathbf{q}' = (\mathbf{q}'_1, \dots, \mathbf{q}'_M)$  are analogously defined  $D \times M$  dimensional vectors. Here we will not consider quantum statistics of particles. The required symmetrization or antisymmetrization must be applied after transition amplitudes are calculated using the effective potential.

Many-body transition amplitudes satisfy  $D \times M$ -dimensional generalization of the time-dependent Schrödinger equation, which leads to the equation for the effective po-



tential similar to Eq. (2.5), with vectors replacing previously scalar quantities,

$$W + \bar{\mathbf{x}} \cdot \bar{\partial} W + \varepsilon \partial_\varepsilon W - \frac{1}{8} \varepsilon \partial^2 W - \frac{1}{8} \varepsilon \bar{\partial}^2 W + \frac{1}{8} \varepsilon^2 (\partial W)^2 + \frac{1}{8} \varepsilon^2 (\bar{\partial} W)^2 = \frac{1}{2} (V_+ + V_-). \quad (2.10)$$

The effective potential for short-time amplitudes again can be written in the form of the double expansion in  $\varepsilon$  and  $\bar{\mathbf{x}}$ . However, it turns out to be advantageous to use the expansion

$$W(\mathbf{x}, \bar{\mathbf{x}}; \varepsilon) = \sum_{m=0}^{\infty} \sum_{k=0}^m \varepsilon^{m-k} W_{m,k}(\mathbf{x}, \bar{\mathbf{x}}), \quad (2.11)$$

and work with fully contracted quantities  $W_{m,k}$

$$W_{m,k}(\mathbf{x}, \bar{\mathbf{x}}) = \bar{x}_{i_1} \bar{x}_{i_2} \cdots \bar{x}_{i_{2k}} c_{m,k}^{i_1, \dots, i_{2k}}(\mathbf{x}), \quad (2.12)$$

rather than with the respective coefficients  $c_{m,k}^{i_1, \dots, i_{2k}}$ . In this way we avoid the computationally expensive symmetrization over all indices  $i_1, \dots, i_{2k}$ . After inserting the above expansion into the equation for the effective potential, we obtain the recursion relation which represents a generalization of previously derived Eq. (2.7) for 1D case, and has the form

$$\begin{aligned} 8(m+k+1)W_{m,k} &= \partial^2 W_{m-1,k} + \bar{\partial}^2 W_{m,k+1} - \sum_{l=0}^{m-2} \sum_r (\partial W_{l,r}) \cdot (\partial W_{m-l-2,k-r}) \\ &\quad - \sum_{l=1}^{m-2} \sum_r (\bar{\partial} W_{l,r}) \cdot (\bar{\partial} W_{m-l-1,k-r+1}). \end{aligned} \quad (2.13)$$

The sum over  $r$  runs from  $\max\{0, k-m+l+2\}$  to  $\min\{k, l\}$ , while diagonal quantities  $W_{m,m}$  can be calculated directly,

$$W_{m,m} = \frac{1}{(2m+1)!} (\bar{\mathbf{x}} \cdot \partial)^{2m} V. \quad (2.14)$$

The above recursion disentangles, in complete analogy with the previously outlined case of one particle in 1D, and is solved in the order shown in Fig. 1.

### 3 SPEEDUP Mathematica codes for deriving the higher-order effective actions

The effective action approach can be used for numerically exact calculation of short-time amplitudes if the effective potential  $W_p$  can be analytically derived to sufficiently high values of  $p$  such that the associated error is smaller than the required numerical precision. The error  $\varepsilon^p$  for the effective action, obtained when level  $p$  effective potential is used, translates into  $\varepsilon^{p-DM/2}$  for a general many-body short-time amplitude. However, when amplitudes are calculated using the Path Integral Monte Carlo SPEEDUP C

code [19], which will be presented in the next section, the errors of numerically calculated amplitudes are always proportional to  $\varepsilon^p \sim 1/N^p$ , where  $N$  is number of time-steps in the discretization of the propagation time  $T$ .

Therefore, accessibility of higher-order effective actions is central to the application of this approach if it is used for direct calculation of short-time amplitudes [8–10], as well as in the case when PIMC code is used [4, 5, 18]. However, increase in the level  $p$  leads to the increase in complexity of analytic expressions for the effective potential. On one hand, this limits the maximal accessible level  $p$  by the amount of memory required for symbolic derivation of the effective potential. On the other hand, practical use of large expressions for  $W_p$  may slow down numerical calculations, and one can opt to use lower than the maximal available level  $p$  when optimizing total CPU time required for numerical simulation. The suggested approach is to study time-complexity of the algorithm in practical applications, and to choose optimal level  $p$  by minimizing the execution time required to achieve fixed numerical precision.

We have implemented efficient symbolic derivation of higher-order effective actions in Mathematica using the recursive approach. All source files described in this section are located in the `Mathematica` directory of the SPEEDUP code distribution.

### 3.1 General 1D Mathematica code

SPEEDUP code [19] for symbolic derivation of the effective potential to specified level  $p$  is implemented in Mathematica [40], and is available in the `EffectiveAction-1D.nb` notebook. It implements the algorithm depicted in Fig. 1 and calculates the coefficients  $c_{m,k}$  for  $m = 0, \dots, p-1$  and  $k = m, \dots, 0$ , starting from the initial condition  $c_{0,0} = V$ . For a given value of  $m$ , the diagonal coefficient  $c_{m,m}$  is first calculated from Eq. (2.8), and then all off-diagonal coefficients are calculated from the recursion (2.7).

In this code the potential  $V(x)$  is not specified, and the effective potential is derived for a general one-particle 1D theory. The resulting coefficients  $c_{m,k}$  and the effective potential are expressed in terms of the potential  $V$  and its higher derivatives. Level  $p$  effective potential, constructed as

$$W_p(x, \bar{x}; \varepsilon) = \sum_{m=0}^{p-1} \sum_{k=0}^m c_{m,k}(x) \varepsilon^{m-k} \bar{x}^{2k}, \quad (3.1)$$

contains derivatives of  $V$  to order  $2p-2$ .

The only input parameter of this Mathematica code is the level  $p$  to which the effective potential should be calculated. As the code runs, it prints used amount of memory (in MB) and CPU time. This information can be used to estimate the required computing resources for higher values of  $p$ . The calculated coefficients can be exported to a file, and later imported for further numerical calculations. As an illustration, the file `EffectiveAction-1D-export-p5.m` contains exported definition of all the coefficients  $c_{m,k}$  calculated at level  $p=5$ , while the notebook `EffectiveAction-1D-matching-p5.nb`

contains matching output from the interactive session used to produce the above  $p = 5$  result.

The execution of this code on a typical 2 GHz CPU for level  $p = 10$  requires 10-15 MB of RAM and several seconds of CPU time. We have successfully run this code for levels as high as  $p = 35$  [19]. SPEEDUP C code implements effective actions to the maximal level  $p = 18$ , with the size of the corresponding C function around 2 MB. If needed, higher levels  $p$  can be easily implemented in C and added to the existing SPEEDUP code.

### 3.2 General 2D and 3D Mathematica code

Although we have developed Mathematica code capable of deriving effective actions for a general many-body theory in arbitrary number of spatial dimensions, in practical applications in 2D and 3D it can be very advantageous to use simpler codes, able to produce results to higher levels  $p$  than the general code [9, 10].

This is done in files `EffectiveAction-2D.nb` and `EffectiveAction-3D.nb`, where the recursive approach is implemented directly in 2D and 3D. Execution of these codes requires more memory: for  $p = 10$  effective action one needs 60 MB in 2D case, while in 3D case the needed amount of memory increases to 860 MB. On the other hand, the execution time is several minutes for 2D code and around 30 minutes for 3D code.

The distribution of the SPEEDUP code contains exported  $p = 5$  definitions of contractions  $W_{m,k}$  for both 2D and 3D general potential, as well as matching outputs from interactive sessions used to generate these results.

### 3.3 Model-specific Mathematica codes

When general expressions for the effective actions, obtained using the above described SPEEDUP Mathematica codes, are used in numerical simulations, one has to specify the potential  $V$  and its higher derivatives to order  $2p - 2$  in order to be able to calculate transition amplitudes. Such approach is justified for systems where the complexity of higher derivatives increases. However, for systems where this is not the case, or where only a limited number of derivatives is non-trivial (e.g. polynomial interactions), it might be substantially beneficial to specify the potential at the beginning of the Mathematica code and calculate the derivatives explicitly when iterating the recursion.

Using this approach, one is able to obtain coefficients  $c_{m,k}$  and the effective potential  $W$  directly as functions of the mid-point  $x$ . This is implemented in the notebooks `EffectiveAction-1D-AHO.nb` and `EffectiveAction-2D-AHO.nb` for the case of anharmonic oscillators in 1D and 2D,

$$V_{1D-AHO}(x) = \frac{A}{2}x^2 + \frac{g}{24}x^4, \quad (3.2)$$

$$V_{2D-AHO}(x) = \frac{A}{2}(x^2 + y^2) + \frac{g}{24}(x^2 + y^2)^2. \quad (3.3)$$

These codes can be easily executed within few seconds and with the minimal amounts of memory even for  $p = 20$ . For 1D anharmonic oscillator we have successfully calculated effective actions to excessively large value  $p = 144$ , and in 2D to  $p = 67$  [19], to illustrate the advantage of this model-specific method.

Similar approach can be also used in another extreme case, when the complexity of higher derivatives of the potential  $V$  increases very fast, so that entering the corresponding expressions to the code becomes impractical. Even in this situation expressions for effective actions can be usually simplified using some appropriate model-specific ansatz. The form of such ansatz can be deduced from the form of model-specific effective potentials, and then used to simplify their derivation. Such use-case is illustrated in the SPEEDUP Mathematica code for the modified Pöschl-Teller potential,

$$V_{1D-MPT}(x) = -\frac{\lambda}{(\cosh \alpha x)^2}. \quad (3.4)$$

For this potential, the coefficients  $c_{m,k}$  of the effective potential can be expressed in the form

$$c_{m,k}(x) = \sum_{l=0}^m d_{m,k,l} \frac{(\tanh \alpha x)^{2l}}{(\cosh \alpha x)^{2m-2l+2}}, \quad (3.5)$$

and newly introduced constant coefficients  $d_{m,k,l}$  can be calculated using the model-specific recursion in `EffectiveAction-1D-MPT.nb`. The form of the ansatz (3.5) is deduced from the results of executing general 1D Mathematica code, with the model-specific potential (3.4) defined before the recursion calculation of the coefficients is performed. Using this approach, we were able to obtain maximal level  $p = 41$  effective action [19].

### 3.4 General many-body Mathematica code

SPEEDUP Mathematica code for calculation of effective action for a general many-body theory is implemented using the `MathTensor` [41] package for tensorial calculations in Mathematica. This general implementation required some new functions related to the tensor calculus to be defined in the source notebook `EffectiveAction-ManyBody.nb` provided with the SPEEDUP code.

The function `GenNewInd[n]` generates the required number  $n$  of upper and lower indices using the `MathTensor` function `UpLo`, with the assigned names `up1, lo1, ...`, as well as lists `upi` and `loi`, each containing  $n$  strings corresponding to the names of generated indices. These new indices are used in the implementation of the recursion for calculation of derivatives of  $W_{m,k}$ , contractions of the effective potential, and for this reason had to be explicitly named and properly introduced.

The expressions obtained by iterating the recursion contain large numbers of contractions, and function `NewDefUnique[contr]` replaces all contracted indices with the newly-introduced dummy ones in the contraction `contr`, so that they do not interfere with the calculation of derivatives in the recursion. This is necessary since the derivatives in recursion do not distinguish contracted indices from non-contracted ones if their names

happen to be generated by the function `GenNewInd`. Note that the expression `contr` does not have to be full contraction, i.e. function `NewDefUnique` will successfully act on tensors of any kind if they have contracted indices, while it will leave them unchanged if no contractions are present.

The function `NewDerivativeVec[contr, vec, ind]` implements calculation of the first derivative of the tensor `contr` (which may or may not contain contracted indices, but if it does, they are supposed to be uniquely defined dummy ones, which is achieved using the function `NewDefUnique`). The derivative is calculated with respect to vector `vec` with the vectorial index `ind`. The index `ind` can be either lower or upper one, and has to be generated previously by the function `GenNewInd`.

Finally, the function `NewLaplacianVec[contr, vec]` implements the Laplacian of the tensor `contr` with respect to the vector `vec`, i.e. it performs the calculation of contractions of the type

$$\frac{\partial}{\partial \text{vec}_i} \frac{\partial}{\partial \text{vec}^i} \text{contr}. \quad (3.6)$$

After all described functions are defined, the execution of the code proceeds by setting the desired level of the effective action  $p$ , generating the needed number of named indices using the function call `GenNewInd[2 p + 2]`, and then by performing the recursion according to the scheme illustrated in Fig. 1. The use of `MathTensor` function `CanAll` in the recursion ensures that the obtained expressions for  $W[m, k]$  will be simplified if possible. This is achieved in `MathTensor` by sorting and renaming all dummy indices using the same algorithm and trying to simplify the expression obtained in such way. By default, `Mathematica` will distinguish contracted indices in two expressions if they are named differently, and `MathTensor` works around it using the renaming scheme implemented in `CanAll`.

The computing resources required for the execution of the many-body SPEEDUP `Mathematica` code depend strongly on the level of the effective action. For example, for level  $p = 5$  the code can be run within few seconds with the minimal memory requirements. The notebook with the matching output of this calculation is available as `EffectiveAction-ManyBody-matching-p5.nb`, and the exported results for  $W[m, k]$  are available in `EffectiveAction-ManyBody-export-p5.m`. We were able to achieve maximal level  $p = 10$  [19], with the CPU time of around 2 days on a recent 2 GHz processor. The memory used by `Mathematica` was approximately 1.6 GB.

Note that exporting the definition of the effective potential from `Mathematica` to a file will yield lower and upper indices named `ll1`, `uu1`, etc. In order to import previous results and use them for further calculations with the provided `Mathematica` code, it is necessary to replace indices in the exported file to the proper index names used by the function `GenNewInd`. This is easily done using `find/replace` feature of any text editor. Prior to importing definition of the effective potential, it is necessary to initialize `MathTensor` and all additional functions defined in the notebook `EffectiveAction-ManyBody.nb`, and to generate the needed number of named indices using the function call `GenNewInd[2p+2]`.

## 4 SPEEDUP C codes for Monte Carlo calculation of 1D transition amplitudes

For short times of propagation, the effective actions derived using the above described Mathematica codes can be directly used. This has been extensively used in [8, 9], where SPEEDUP codes were applied for numerical studies of several lower-dimensional models and calculation of large number of energy eigenvalues and eigenfunctions. The similar approach is used in [10], where SPEEDUP code was used to study properties of fast-rotating Bose-Einstein condensates in anharmonic trapping potentials. The availability of a large number of eigenstates allowed not only precise calculation of global properties of the condensate (such as condensation temperature and ground state occupancy), but also study of density profiles and construction of time-of-flight absorption graphs, with the exact quantum treatment of all available eigenfunctions.

However, in majority of applications the time of propagation cannot be assumed to be small. The effective actions are found to have finite radius of convergence [8], and if the typical propagation times in the considered case exceed this critical value, Path Integral Monte Carlo approach must be used in order to accurately calculate the transition amplitudes and the corresponding expectation values [4, 18]. As outlined earlier, in this case the time of propagation  $T$  is divided into  $N$  time steps, such that  $\varepsilon = T/N$  is sufficiently small and that the effective action approach can be used. The discretization of the propagation time leads to the following expression for the discretized amplitude

$$A_N^{(p)}(a, b; T) = \int \frac{dq_1 \cdots dq_{N-1}}{(2\pi\varepsilon)^{N/2}} e^{-S_N^{(p)}}, \quad (4.1)$$

where  $S_N^{(p)}$  stands for the discretized level  $p$  effective action,

$$S_N^{(p)} = \sum_{k=0}^{N-1} \left[ \frac{(q_{k+1} - q_k)^2}{2\varepsilon} + \varepsilon W_p(x_k, \bar{x}_k; \varepsilon) \right], \quad (4.2)$$

and  $q_0 = a$ ,  $q_N = b$ ,  $x_k = (q_{k+1} + q_k)/2$ ,  $\bar{x}_k = (q_{k+1} - q_k)/2$ .

Level  $p$  discretized effective action is constructed from the corresponding effective potential  $W_p$ , calculated as power series expansion to order  $\varepsilon^{p-1}$ . Since it enters the action multiplied by  $\varepsilon$ , this leads to discretized actions correct to order  $\varepsilon^p$ , i.e. with the errors of the order  $\varepsilon^{p+1}$ . The long-time transition amplitude  $A_N^{(p)}(a, b; T)$  is a product of  $N$  short-time amplitudes, and its errors are expected to scale as  $N \cdot \varepsilon^{p+1} \sim 1/N^p$ , as has been shown in [5, 13–15] for transition amplitudes, and in [5, 18] for expectation values, calculated using the corresponding consistently improved estimators.

### 4.1 Algorithm and structure of the code

SPEEDUP C source is located in the src directory of the code distribution [19]. It uses the standard Path Integral Monte Carlo algorithm for calculation of transition amplitudes.

The trajectories are generated by the bisection algorithm [20], hence the number of time-steps  $N$  is always given as a power of two,  $N = 2^s$ . When the amplitude is calculated with  $2^s$  time steps, we can also easily calculate all discretized amplitudes in the hierarchy  $2^{s-1}, \dots, 2^0$  at no extra cost. This requires only minor additional CPU time and memory, since the needed trajectories are already generated as subsets of maximal trajectories with  $2^s$  time-steps.

The trajectory is constructed starting from bisection level  $n = 0$ , where we only have initial and final position of the particle. At bisection level  $n = 1$  the propagation is divided into two time-steps, and we have to generate coordinate  $q$  of the particle at the moment  $T/2$ , thus constructing the piecewise trajectory connecting points  $a$  at the time  $t = 0$ ,  $q$  at  $t = T/2$ , and  $b$  at  $t = T$ . The coordinate  $q$  is generated from the Gaussian probability density function centered at  $(a+b)/2$  and with the width  $\sigma_1 = \sqrt{T/2}$ . The procedure continues iteratively, and each time a set of points is added to the piecewise trajectory. At each bisection level  $n$  the coordinates are generated from the Gaussian centered at midpoint of coordinates generated at level  $n - 1$ , with the width  $\sigma_n = \sqrt{T/2^n}$ . To generate numbers  $\eta$  from the Gaussian centered at zero we use Box-Müller method,

$$\eta = \sqrt{-2\sigma_n^2 \ln \zeta_1} \cos 2\pi \zeta_2, \quad (4.3)$$

where numbers  $\zeta_1$  and  $\zeta_2$  are generated from the uniform distribution on the interval  $[0,1]$ , using the SPRNG library [42]. If the target bisection level is  $s$ , then at bisection level  $n \leq s$  we generate  $2^{n-1}$  numbers using the above formula, and construct the new trajectory by adding to already existing points the new ones, according to

$$q[(1+2i) \cdot 2^{s-n}] = \eta_i + \frac{q[i \cdot 2^{s-n+1}] + q[(i+1) \cdot 2^{s-n+1}]}{2}, \quad (4.4)$$

where  $i$  runs from 0 to  $2^{n-1} - 1$ . This ensures that at bisection level  $s$  we get trajectory with  $N = 2^s$  time-steps, consisting of  $N + 1$  points, with boundary conditions  $q[0] = a$  and  $q[N] = b$ . At each lower bisection level  $n$ , the trajectory consists of  $2^n + 1$  points obtained from the maximal one (level  $s$  trajectory) as a subset of points  $q[i \cdot 2^{s-n}]$  for  $i = 0, 1, \dots, 2^n$ .

The use of trajectories generated by the bisection algorithm requires normalization factors from all Gaussian probability density functions with different widths to be taken into account. This normalization is different for each bisection level, but can be calculated easily during the initialization phase.

The basic C code is organized in three source files, `main.c`, `p.c` and `potential.c`, with the accompanying header files. The file `potential.c` (its name can be changed, and specified at compile time) must contain a user-supplied function `V0()`, defining the potential  $V$ . For a given input value of the coordinate, `V0()` should initialize appropriate variables to the value of the potential  $V$  and its higher derivatives to the required order  $2p - 2$ . When this file is prepared, SPEEDUP code can be compiled and used. The distributed source contains definition of 1D-AHO potential in the file `potential.c`, the same as in the file `1D-AHO.c`.

The execution of the SPEEDUP code starts with the initialization and allocation of memory in the `main()` function, and then the array of amplitudes and associated MC error estimates for each bisection level  $n = 0, \dots, s$  is calculated by calling the function `mc()`. After printing the output, `main()` deallocates used memory and exits. Function `mc()` which implements the described MC algorithm is also located in the file `main.c`, as well as the function `distr()`, which generates maximal (level  $s$ ) trajectories.

The function `mc()` contains main MC sampling loop. In each step new level  $s$  trajectory is generated by calling the function `distr()`. Afterwards, for each bisection level  $n$ , function `func()` is invoked. This function is located in the file `p.c`, and returns the value of the function  $e^{-S}$ , properly normalized, as described earlier. This value (and its square) is accumulated in the MC loop for each bisection level  $n$  and later averaged to obtain the estimate of the corresponding discretized amplitude and the associated MC error.

The function `func()` makes use of C implementation of earlier derived effective actions for a general 1D potential. For a given trajectory at the bisection level  $n$ , `func()` will first initialize appropriate variables with the values of the potential and its higher derivatives (to the required level  $2p-2$ ) by calling the user-supplied function `V0()`, located in the file `potential.c`. Afterwards the effective action is calculated according to Eq. (4.2), where the effective potential is calculated by the function `Wp()`, located in the file `p.c`. The desired level  $p$  of the effective action is selected by defining the appropriate pre-processor variable when the code is compiled.

In addition to this basic mode, when SPEEDUP code uses general expression for level  $p$  effective action, we have also implemented model-specific mode, described earlier. If effective actions are derived for a specific model, then user can specify an alternative `p.c` file to be used within the directory `src/models/<model>`, where `<model>` corresponds to the name of the model. If this mode is selected at compile time, the compiler will ignore `p.c` from the top `src` directory, and use the model-specific one, defined by the user. The distributed source contains model definitions for 1D-AHO and 1D-MPT potentials in directories `src/models/1D-AHO` and `src/models/1D-MPT`. Note that in this mode the potential is specified directly in the definition of the effective potential, and therefore the function `V0()` is not used (nor the `potential.c` file).

## 4.2 Compiling and using SPEEDUP C code

SPEEDUP C source can be easily compiled using the `Makefile` provided in the top directory of the distribution. The compilation has been thoroughly tested with GNU, Intel and IBM XLC compilers. In order to compile the code one has to specify the compiler which will be used in the `Makefile` by setting appropriately the variable `COMPILER`, and then to proceed with the standard command of the type `make <target>`, where `<target>` could be one of `all`, `speedup`, `sprng`, `clean-all`, `clean-speedup`, `clean-sprng`.

The SPRNG library [42] is an external dependency, and for this reason it is located in the directory `src/deps/sprng4.0`. In principle, it has to be compiled only once, after the compiler has been set. This is achieved by executing the command `make sprng`. After-



wards the SPEEDUP code can be compiled and easily linked with the already compiled SPRNG library. Note that if the compiler is changed, SPRNG library has to be recompiled with the same compiler in order to be successfully linked with the SPEEDUP code.

To compile the code with level  $p=10$  effective action and user-supplied function  $V0()$  located in the file `src/1D-AH0.c`, the following command can be used:

```
make speedup P=10 POTENTIAL=1D-AH0.c
```

If not specified, `POTENTIAL=potential.c` is used, while the default level of the effective action is  $P=1$ . To compile the code using a model-specific definition of the effective potential, instead of the `POTENTIAL` variable, we have to appropriately set the `MODEL` variable on the command line. For example, to compile the supplied `p.c` file for 1D-MPT model located in the directory `src/models/1D-MPT` using the level  $p=5$  effective action, the following command can be used:

```
make speedup P=5 MODEL=1D-MPT
```

All binaries compiled using the `POTENTIAL` mode are stored in the `bin` directory, while the binaries for the `MODEL` mode are stored in the appropriate `bin/models/<model>` directory. This information is provided by the `make` command after each successful compilation is done.

The compilation is documented in more details in the supplied `README.txt` files. The distribution of the SPEEDUP code also contains examples of compilation with the GNU, Intel and IBM XLC compilers, as well as matching outputs and results of the execution for each tested compiler, each model, and for a range of levels of the effective action  $p$ .

Once compiled, the SPEEDUP code can be used to calculate long-time amplitudes of a system in the specified potential  $V$ . If executed without any command-line arguments, the binary will print help message, with details of the usage. The obligatory arguments are time of propagation  $T$ , initial and final position  $a$  and  $b$ , maximal bisection level  $s$ , number of MC samples  $N_{mc}$  and `seed` for initialization of the SPRNG random number generator. All further arguments are converted to numbers of the `double` type and made available in the array `par` to the function  $V0()$ , or to the model-specific functions in the file `src/models/<model>/p.c`. The output of the execution contains calculated value of the amplitude for each bisection level  $n=0, \dots, s$  and the corresponding MC estimate of its error (standard deviation). At bisection level  $n=0$ , where no integrals are actually calculated and the discretized  $N=1$  amplitude is simply given by an analytic expression, zero is printed as the error estimate.

Fig. 2 illustrates the typical results obtained from the SPEEDUP code on the example of 1D-MPT theory. In this figure we can see the convergence of numerically calculated amplitudes with the number of time-steps  $N$  to the exact continuum value, obtained in the limit  $N \rightarrow \infty$ . Such convergence is obtained for each level  $p$  of the effective action used. However, the convergence is much faster when higher-order effective action is used. Note that all results corresponding to the one value of level  $p$  on the graph are obtained from a single run of the SPEEDUP code with the maximal bisection level  $s=10$ . The simplest way to estimate the continuum value of the amplitude is to fit numerical

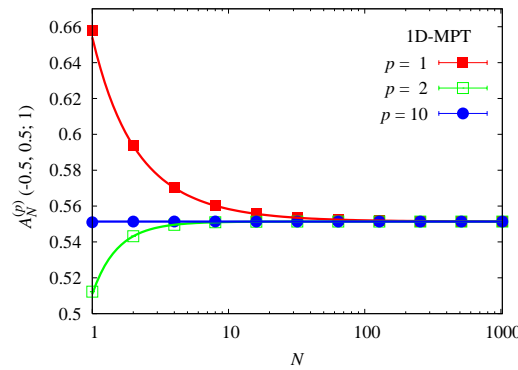


Figure 2: Convergence of SPEEDUP Monte-Carlo results for the transition amplitude  $A_N^{(p)}(-0.5, 0.5; 1)$  of 1D-MPT potential as a function of the number of time steps  $N$ , calculated with level  $p=1, 2, 10$  effective actions, with the parameters of the potential  $\lambda=\alpha=1$ . The full lines give the fitted functions (4.5), where the constant term  $A_p$  corresponds to the continuum-theory amplitude  $A(-0.5, 0.5; 1)$ . The number of Monte-Carlo samples was  $N_{MC}=10^6$ .

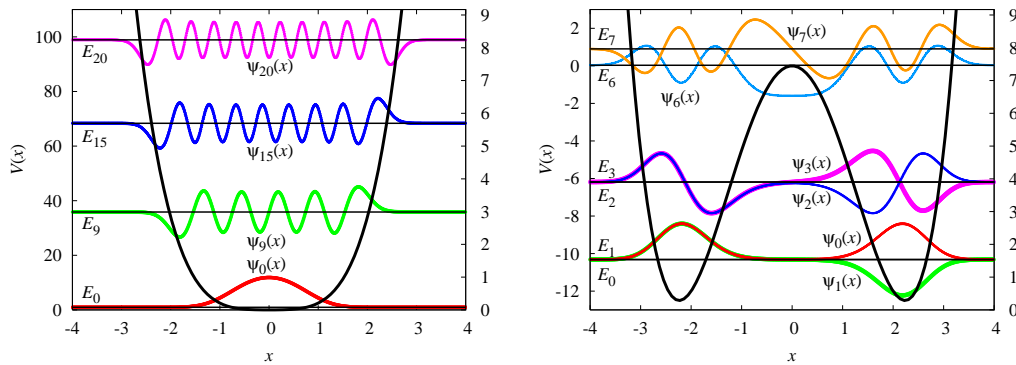


Figure 3: (left) The anharmonic potential 1D-AHO, its energy eigenvalues (horizontal lines) and eigenfunctions, obtained by direct diagonalization of the space-discretized matrix of the evolution operator with level  $p=21$  effective action and parameters  $A=1, g=48$ . The discretization cutoff was  $L=8$ , spacing  $\Delta=9.76 \cdot 10^{-4}$ , and time of propagation  $t=0.02$ . (right) Results for the double-well potential,  $A=-10, g=12, L=10, \Delta=1.22 \cdot 10^{-3}$ ,  $t=0.1$ . On both graphs, left  $y$ -axis corresponds to  $V(x)$  and energy eigenvalues, while scale on the right  $y$ -axis corresponds to values of eigenfunctions, each vertically shifted to level with the appropriate eigenvalue.

results from single run of the code to the appropriate level  $p$  fitting function [13–15],

$$A_N^{(p)} = A^{(p)} + \frac{B^{(p)}}{N^p} + \frac{C^{(p+1)}}{N^{p+1}} + \dots \quad (4.5)$$

The constant term obtained by fitting corresponds to the best estimate of the exact amplitude which can be found from the available numerical results.

As mentioned earlier, the effective action approach can be used for accurate calculation of a large number of energy eigenstates and eigenvalues by diagonalization of the space-discretized matrix of transition amplitudes [6–10]. Fig. 3 illustrates this for the case

of an anharmonic and double-well potential. The graph on the left gives several eigenvalues and eigenstates for 1D-AHO potential with  $A = 1$  and quartic anharmonicity  $g = 48$ , while the graph on the right gives low-lying spectrum and eigenfunctions of the double-well potential, obtained for  $A = -10$ , with the moderate anharmonicity  $g = 12$ . More details on this approach, including study of all errors associated with the discretization process, can be found in [8,9].

## 5 Conclusions

In this paper we have presented SPEEDUP Mathematica and C codes, which implement the effective action approach for calculation of quantum mechanical transition amplitudes. The developed Mathematica codes provide an efficient tool for symbolic derivation of effective actions to high orders for specific models, for a general 1D, 2D and 3D single-particle theory, as well as for a general many-body systems in arbitrary number of spatial dimensions. The recursive implementation of the code allows symbolic calculation of extremely high levels of effective actions, required for high-precision calculation of transition amplitudes.

For calculation of long-time amplitudes we have developed SPEEDUP C Path Integral Monte Carlo code. The C implementation of a general 1D effective action to maximal level  $p = 18$  and model-specific effective actions provide fast  $1/N^p$  convergence to the exact continuum amplitudes.

Further development of the SPEEDUP C codes will include parallelization using MPI, OPENMP and hybrid programming model, C implementation of the effective potential to higher levels  $p$ , as well as providing model-specific effective actions for relevant potentials, including many-body systems.

## Acknowledgments

The authors gratefully acknowledge useful discussions with Axel Pelster and Vladimir Slavnić. This work was supported in part by the Ministry of Education and Science of the Republic of Serbia, under project No. ON171017, and bilateral project NAD-BEC funded jointly with the German Academic Exchange Service (DAAD), and by the European Commission under EU FP7 projects PRACE-1IP, HP-SEE and EGI-InSPIRE.

## References

- [1] R. P. Feynman, Rev. Mod. Phys. 20, 367 (1948).
- [2] R. P. Feynman and A. R. Hibbs, Quantum Mechanics and Path Integrals (McGraw-Hill, New York, 1965).
- [3] H. Kleinert, Path Integrals in Quantum Mechanics, Statistics, Polymer Physics, and Financial Markets, 5th ed. (World Scientific, Singapore, 2009).

- [4] D. Stojiljković, A. Bogojević, and A. Balaž, *Phys. Lett. A* 360, 205 (2006).
- [5] A. Bogojević, I. Vidanović, A. Balaž, and A. Belić, *Phys. Lett. A* 372, 3341 (2008).
- [6] A. Sethia, S. Sanyal, and Y. Singh, *J. Chem. Phys.* 93, 7268 (1990).
- [7] A. Sethia, S. Sanyal, and F. Hirata, *Chem. Phys. Lett.* 315, 299 (1999).
- [8] I. Vidanović, A. Bogojević, and A. Belić, *Phys. Rev. E* 80, 066705 (2009).
- [9] I. Vidanović, A. Bogojević, A. Balaž, and A. Belić, *Phys. Rev. E* 80, 066706 (2009).
- [10] A. Balaž, I. Vidanović, A. Bogojević, and A. Pelster, *Phys. Lett. A* 374, 1539 (2010).
- [11] R. P. Feynman, *Statistical Mechanics* (W. A. Benjamin, New York, 1972).
- [12] G. Parisi, *Statistical Field Theory* (Addison Wesley, New York, 1988).
- [13] A. Bogojević, A. Balaž, and A. Belić, *Phys. Rev. Lett.* 94, 180403 (2005).
- [14] A. Bogojević, A. Balaž, and A. Belić, *Phys. Rev. B* 72, 064302 (2005).
- [15] A. Bogojević, A. Balaž, and A. Belić, *Phys. Lett. A* 344, 84 (2005).
- [16] A. Bogojević, A. Balaž, and A. Belić, *Phys. Rev. E* 72, 036128 (2005).
- [17] A. Balaž, A. Bogojević, I. Vidanović, and A. Pelster, *Phys. Rev. E* 79, 036701 (2009).
- [18] J. Grujić, A. Bogojević, and A. Balaž, *Phys. Lett. A* 360, 217 (2006).
- [19] SPEEDUP code distribution, <http://www.scl.rs/speedup/>
- [20] D. M. Ceperley, *Rev. Mod. Phys.* 67, 279 (1995).
- [21] M. Takahashi and M. Imada, *J. Phys. Soc. Jpn.* 53, 3765 (1984).
- [22] X. P. Li and J. Q. Broughton, *J. Chem. Phys.* 86, 5094 (1987).
- [23] H. De Raedt and B. De Raedt, *Phys. Rev. A* 28, 3575 (1983).
- [24] S. Jang, S. Jang, and G. Voth, *J. Chem. Phys.* 115, 7832 (2001).
- [25] N. Makri and W. H. Miller, *Chem. Phys. Lett.* 151, 1 (1988); N. Makri and W. H. Miller, *J. Chem. Phys.* 90, 904 (1989).
- [26] N. Makri, *Chem. Phys. Lett.* 193, 435 (1992).
- [27] M. Alford, T. R. Klassen, and G. P. Lepage, *Phys. Rev. D* 58, 034503 (1998).
- [28] S. A. Chin and E. Krotscheck, *Phys. Rev. E* 72, 036705 (2005).
- [29] E. R. Hernández, S. Janecek, M. Kaczmarek, E. Krotscheck, *Phys. Rev. B* 75, 075108 (2007).
- [30] O. Ciftja and S. A. Chin, *Phys. Rev. B* 68, 134510 (2003).
- [31] K. Sakkos, J. Casulleras, and J. Boronat, *J. Chem. Phys.* 130, 204109 (2009).
- [32] S. Janecek and E. Krotscheck, *Comput. Phys. Comm.* 178, 835 (2008).
- [33] A. D. Bandrauk and H. Shen, *J. Chem. Phys.* 99, 1185 (1993).
- [34] S. A. Chin and C. R. Chen, *J. Chem. Phys.* 117, 1409 (2002).
- [35] I. P. Omelyan, I. M. Mryglod, and R. Folk, *Comput. Phys. Commun.* 151, 272 (2003).
- [36] G. Goldstein and D. Baye, *Phys. Rev. E* 70, 056703 (2004).
- [37] S. A. Chin, arXiv:0809.0914.
- [38] S. A. Chin, S. Janecek, and E. Krotscheck, *Comput. Phys. Comm.* 180, 1700 (2009).
- [39] S. A. Chin, S. Janecek, and E. Krotscheck, *Chem. Phys. Lett.* 470, 342 (2009).
- [40] Mathematica software package, <http://www.wolfram.com/mathematica/>
- [41] MathTensor package, <http://smc.vnet.net/mathtensor.html>
- [42] Scalable Parallel Random Number Generator library, <http://sprng.fsu.edu/>

# Efficient calculation of energy spectra using path integrals<sup>☆</sup>

D. Stojiljković\*, A. Bogojević, A. Balaž

*Scientific Computing Laboratory, Institute of Physics, P.O. Box 57, 11001 Belgrade, Serbia*

Received 26 July 2006; accepted 4 August 2006

Available online 22 August 2006

Communicated by V.M. Agranovich

## Abstract

A newly developed method for systematically improving the convergence of path integrals for transition amplitudes [A. Bogojević, A. Balaž, A. Belić, Phys. Rev. Lett. 94 (2005) 180403, A. Bogojević, A. Balaž, A. Belić, Phys. Rev. B 72 (2005) 064302, A. Bogojević, A. Balaž, A. Belić, Phys. Lett. A 344 (2005) 84] and expectation values [J. Grujić, A. Bogojević, A. Balaž, Phys. Lett. A 360 (2006) 217] is here applied to the efficient calculation of energy spectra. We show how the derived hierarchies of effective actions lead to substantial speedup of the standard path integral Monte Carlo evaluation of energy levels. The general results and the ensuing increase in efficiency of several orders of magnitude are shown using explicit Monte Carlo simulations of several distinct models.

© 2006 Elsevier B.V. All rights reserved.

PACS: 05.30.-d; 05.10.Ln; 03.65.Db

Keywords: Path integral; Quantum theory; Effective action; Energy spectra

## 1. Introduction

Feynman's path integrals [5,6] provide the general mathematical framework for dealing with quantum and statistical systems. The formalism has been successfully applied in generalizing the quantization procedure from the archetypical quantum mechanical problem of the dynamics of a single particle moving in one dimension, to more particles, more dimensions, as well as to more complicated objects such as fields, strings [7], etc. Symmetries of physical systems can be more easily treated and applied in this formalism, since it gives a simple and natural setup for their use [8]. Various approximation techniques are more easily derived within the framework of this formalism, and it has been successfully used for deriving non-perturbative results. The parallel application of this formalism in both high energy and condensed matter physics makes it an important

general tool [9,10]. The analytical and numerical approaches to path integrals have by now become central to the development of many other areas of physics, chemistry and materials science, as well as to the mathematics and finance [11–14]. In particular, general numerical approaches such as the path integral Monte Carlo method have made possible the treatment of a wealth of non-trivial and previously inaccessible models.

The key impediment to the development of the path integral formalism is a lack of complete understanding of the general mathematical properties of these objects. In numerical approaches limited analytical input generally translates into lower efficiency of employed algorithms. The best path generating algorithms, for example, are efficient precisely because they have built into them the kinematic consequences of the stochastic self-similarity of paths [15]. A recent series of papers [1–3] has for this reason focused on the dynamical implications of stochastic self-similarity by studying the relation between path integral discretizations of different coarseness. This has resulted in a systematic analytical construction of a hierarchy of  $N$ -fold discretized effective actions  $S_N^{(p)}$  labeled by a whole number  $p$  and built up from the naively discretized action in the mid-point ordering prescription (corresponding to  $p = 1$ ).

<sup>☆</sup> Supported by the Ministry of Science and Environmental Protection of the Republic of Serbia through project No. 141035.

\* Corresponding author.

E-mail addresses: [danica@phy.bg.ac.yu](mailto:danica@phy.bg.ac.yu) (D. Stojiljković),  
[alex@phy.bg.ac.yu](mailto:alex@phy.bg.ac.yu) (A. Bogojević), [antun@phy.bg.ac.yu](mailto:antun@phy.bg.ac.yu) (A. Balaž).

The level  $p$  effective actions lead to discretized transition amplitudes and expectation values differing from the continuum limit by a term of order  $1/N^p$ .

In this Letter we extend the applicability of the above method for improving the efficiency of path integral calculations to the evaluation of energy spectra. We show how the increased convergence of path integrals translates into the speedup in the numerical calculation of energy levels. Throughout the Letter we present and comment on the Monte Carlo simulations conducted using the hierarchy of effective actions for the case of several different models including anharmonic oscillator, Pöschl–Teller potential, and Morse potential. All the numerical simulations presented were done using Grid-adapted Monte Carlo code and were run on EGEE-II and SEE-GRID-2 infrastructure [16,17]. The effective actions and the codes used can be found on our web site [18].

## 2. Partition function and energy spectra

The partition function is the central object in statistical mechanics. The path integral formalism gives us an elegant framework for calculating partition functions which can be used either for deriving analytical approximation techniques or for carrying out numerical evaluation. The starting point is the expression for the partition function in the coordinate basis,

$$Z(\beta) = \int_{-\infty}^{\infty} da A(a, a; \beta), \quad (1)$$

where  $A(a, b; \beta) = \langle b | e^{-\beta \hat{H}} | a \rangle$  is the quantum mechanical transition amplitude for going from  $a$  to  $b$  in (Euclidean) time  $\beta$ . In the path integral formalism transition amplitudes are given as the  $N \rightarrow \infty$  limit of the  $(N - 1)$ -fold integral expression

$$A_N(a, b; \beta) = \left( \frac{1}{2\pi\epsilon_N} \right)^{N/2} \int dq_1 \cdots dq_{N-1} e^{-S_N}. \quad (2)$$

$S_N$  is the naively discretized action of the theory,  $\epsilon_N = \beta/N$  the discrete time step. For the physical models that we consider the action is of the form

$$S = \int_0^\beta dt \left( \frac{1}{2} \dot{q}^2 + V(q) \right), \quad (3)$$

and its naive discretization equals

$$S_N = \sum_{n=0}^{N-1} \left( \frac{\delta_n^2}{2\epsilon_N} + \epsilon_N V(\bar{q}_n) \right), \quad (4)$$

where  $\delta_n = q_{n+1} - q_n$ , and  $\bar{q}_n = \frac{1}{2}(q_{n+1} + q_n)$ . Note that we are using units in which the particle mass and  $\hbar$  have been set to unity and that we are evaluating path integrals in the so-called mid-point ordering prescription.

From the above we have obtained a path integral representation for the partition function that is directly amenable to numerical evaluation. On the other hand, by evaluating the trace

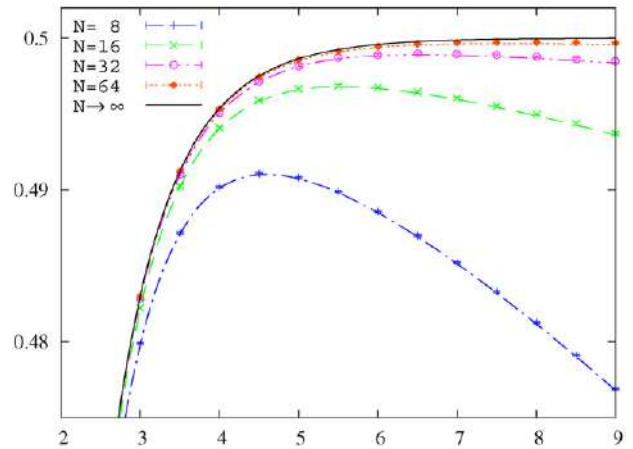


Fig. 1. The curves depict the exact solution of the discretized free energies  $F_N(\beta)$  for the harmonic oscillator in the left ordering prescription given in Eq. (7) for various values of  $N$ . The data points give the results and error bars of the corresponding numerical calculations, used to verify the code. Parameters are  $\omega = 1$  and  $N_{MC} = 10^7$ .

in Eq. (1) in the energy basis we find

$$Z(\beta) \equiv e^{-\beta F(\beta)} = \sum_{n=0}^{\infty} e^{-\beta E_n}. \quad (5)$$

As we can see, the partition function, or equivalently the free energy  $F(\beta)$ , completely determines the energy spectrum and vice-versa. For example, if we define a series of auxiliary functions as

$$F_n(\beta) = -\frac{1}{\beta} \ln \left( e^{-\beta F} - \sum_{i=0}^{n-1} e^{-\beta E_i} \right), \quad (6)$$

then it immediately follows that  $F_n(\beta) \rightarrow E_n$  for large  $\beta$ . It would be ideal, therefore, if we could calculate the free energy (and the other auxiliary functions) for arbitrarily large values of  $\beta$ . This is not possible in numerical calculations. First of all the calculations become much more demanding with growth of “time of propagation”  $\beta$  (just as the physics becomes more interesting). More importantly, when doing numerical calculations we evaluate discretized quantities such as  $F_N$ , and the  $N \rightarrow \infty$  and  $\beta \rightarrow \infty$  limits that one would need to perform do not commute. The best way to see this is to look at the free energy of an exactly solvable model—the harmonic oscillator. In this case the  $N$ -fold discretized free energy (in the left ordering prescription) equals [14]

$$F_N(\beta) = \frac{1}{\beta} \ln(2 \sinh(\tilde{\omega}\beta)), \quad (7)$$

where  $\tilde{\omega} = (2/\epsilon_N) \operatorname{arcsinh}(\omega\epsilon_N/2)$ . This solution is illustrated in Fig. 1. It follows that, unlike its continuum limit  $F(\beta)$ , the discretized free energy  $F_N(\beta)$  does not tend to a constant value for large  $\beta$ . Said another way, the discretized energy levels themselves depend on  $\epsilon_N$  and thus on  $\beta$ . For example, for the harmonic oscillator we have  $E_{N,n}(\epsilon_N) = \tilde{\omega}(n + 1/2)$ .

In the case of a general theory the free energy is related to its discretized value as  $F(\beta) - F_N(\beta) = \mathcal{O}(\epsilon_N)$ . We see that  $F_N(\beta)$  slowly converges to its continuum limit, i.e. that we

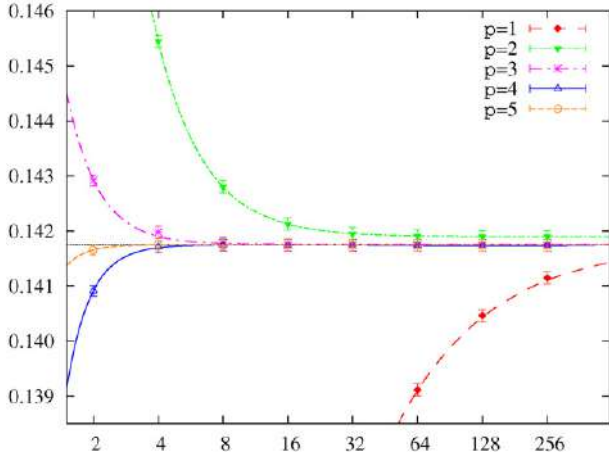


Fig. 2. The dependance of  $F_N^{(p)}(\beta)$  on  $N$  for different levels  $p$ . The plot is for the anharmonic oscillator with quartic coupling  $g = 1$ , inverse temperature  $\beta = 1$  and  $N_{MC} = 10^7$  Monte Carlo samples. The same kind of behavior is seen for other parameters as well as for other potentials.

need a large number of discretization points  $N$  to approach that value. In addition, the larger the value of  $\beta$  we want, the larger  $N$  must be in order to achieve a given accuracy. The price we pay is in the computer time which grows linearly with  $N$ .

A recent series of papers [1–3] analytically studied the relation between path integral discretizations of different coarseness for the case of a general theory. This work resulted in a systematic construction of a hierarchy of  $N$ -fold discretized effective actions  $S_N^{(p)}$  labeled by a whole number  $p$  and built up from the naively discretized action in the mid-point prescription (corresponding to  $p = 1$ ). The level  $p$  effective action leads to discretized transition amplitudes and expectation values differing from the continuum limit by a term of order  $1/N^p$ . Thus, moving up the hierarchy we are guaranteed to get expressions which converge ever faster to the continuum limit. The direct application of these results to the free energy gives

$$F(\beta) - F_N^{(p)}(\beta) = O(\epsilon_N^p). \quad (8)$$

For a given inverse temperature  $\beta$ , and for  $\epsilon_N \lesssim 1$  the discretized free energy  $F_N^{(p)}(\beta)$  converges faster to the continuum as we increase the hierarchy level  $p$ . This is illustrated in Fig. 2.

When using the path integral Monte Carlo method to calculate the free energy  $F(\beta)$  there are two sources of errors. The first comes from the limited number of Monte Carlo samples  $N_{MC}$  and is proportional to  $N_{MC}^{-1/2}$ . The second type of error comes from discretization—in our case from approximating the free energy with  $F_N^{(p)}(\beta)$  for some  $N$  and  $p$ . As we have seen, for a given  $\beta$  this discretization error is proportional to  $N^{-p}$ . These two types of errors should optimally be of the same order, e.g. there is no point in decreasing the discretization error below the Monte Carlo error as this would not decrease the overall error. In practice we fix the precision we want by choosing the number of Monte Carlo samples and then decrease the discretization error to match this either by increasing  $N$  or the hierarch level  $p$ . The second choice is far better; however, since computation times grow linearly with  $N$ , but are almost independent of  $p$  (at least for  $p \leq 9$ , the hierarchy levels studied

in [1,2]). As a consequence of this, the speedup coming from using higher values of  $p$  at fixed precision  $\delta$  is proportional to  $\delta^{-1+1/p}$ . Therefore, by using  $p = 9$  we are in fact quite near to the point of optimal benefit for which the speedup of the new method is inversely proportional to the precision. As an illustration, for two decimal precision the new method gives a hundred fold speedup over the defining algorithm, for four decimal precision the speedup is ten thousand fold, etc. It is important to note that the greatest utility of the new evaluation scheme is, therefore, when calculating quantities with high precision. We stress that all of this holds for  $\epsilon_N \lesssim 1$ , i.e. as long as  $N \gtrsim \beta$  is satisfied.

### 3. Numerical results

As we have seen in the previous section,  $F(\beta)$  can be evaluated with arbitrary precision on any interval of inverse temperatures  $[0, \beta_{max}]$  for any given potential by appropriately increasing and adjusting  $N$ ,  $p$ , and  $N_{MC}$ . Let us now numerically compare the quality of different discretizations of the free energy  $F_N^{(p)}$  with  $F^*$ , the most accurate one that may be calculated on a given set  $\{\beta_i\}$ . To do this we use the standard  $\chi^2$  function,

$$\chi^2(N, p) = \frac{1}{M} \sum_{\{\beta_i\}} \frac{(F_N^{(p)}(\beta_i) - F^*(\beta_i))^2}{(\Delta F_N^{(p)}(\beta_i))^2 + (\Delta F^*(\beta_i))^2}, \quad (9)$$

where  $M$  is the number of points in the set  $\{\beta_i\}$ , and  $\Delta F$  is the Monte Carlo error. By including the Monte Carlo error of  $F^*$  into the  $\chi^2$  weights we took into account the fact that it is also calculated numerically.  $\chi^2$  should be around one for well optimized  $N$  and  $p$ . Note that  $\chi^2 \gg 1$  if the exact value of  $F^*$  is not within the error bars of  $F_N^{(p)}$ , while  $\chi^2 \ll 1$  if the Monte Carlo error is too large.

We conducted this test on the anharmonic oscillator with quartic coupling  $V(q) = \frac{1}{2}q^2 + \frac{g}{4}q^4$ . The discretized free energies were calculated for  $\beta \in [0.5, 8]$  with step 0.5,  $N \leq 1024$  and  $p = 1, 2, \dots, 9$ . The number of Monte Carlo samples used was  $10^6$ . The comparisons were done for a range of coupling constants  $g \in \{0, 0.1, 1, 10, 100, 1000\}$ . Taking  $F_{1024}^{(9)}$  as the exact result, we calculated  $\chi^2$  for each pair of parameters  $(N, p)$  and coupling  $g$ , and looked for  $(N, p)$  pairs with approximately the same values of  $\chi^2$ . These pairs are given in Fig. 3. As we can see, the relation  $1/\log_2 N \propto p$  that is implicit in Eq. (8) actually holds, i.e. the error indeed scales as  $N^{-p}$ .

We now turn to calculating the energy spectrum using the outlined efficient procedure for evaluating the free energy of a general theory. For the range of inverse temperatures  $\beta$  that will be used for numerical calculations of the energies we choose  $\beta_{max}$  so that  $F_N(\beta) = F(\beta)$  within the error bars on the whole  $[0, \beta_{max}]$  interval. We also need to ensure that all the assumptions mentioned above hold ( $\epsilon_N \lesssim 1$ ,  $\beta_{max}$  fixed). The free energy  $F(\beta)$  and all its auxiliary functions can be written as

$$F_n(\beta) = E_n - \frac{1}{\beta} \ln \left( 1 + \sum_{i=n+1}^{\infty} e^{-\beta(E_i - E_n)} \right). \quad (10)$$

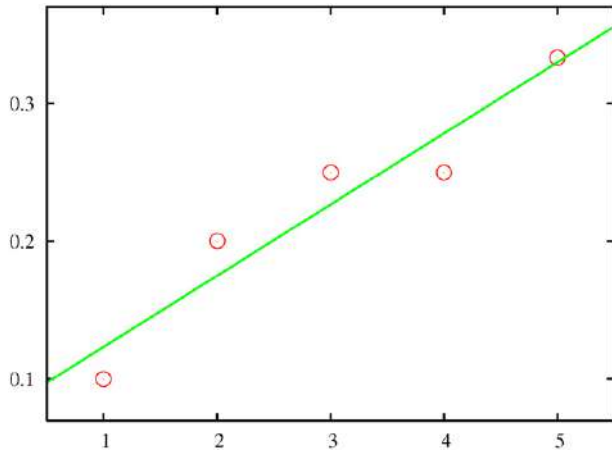


Fig. 3. Pairs of  $N$  and  $p$  which give similar values of  $\chi^2$ . The plot gives  $1/\log_2 N$  on y axis as a function of  $p$ . The general behavior is illustrated on the case of the anharmonic oscillator with quartic coupling  $g = 1$ ,  $\beta_{\max} = 8$ ,  $N_{\text{MC}} = 10^6$ ,  $\chi^2 \approx 2-4$ .

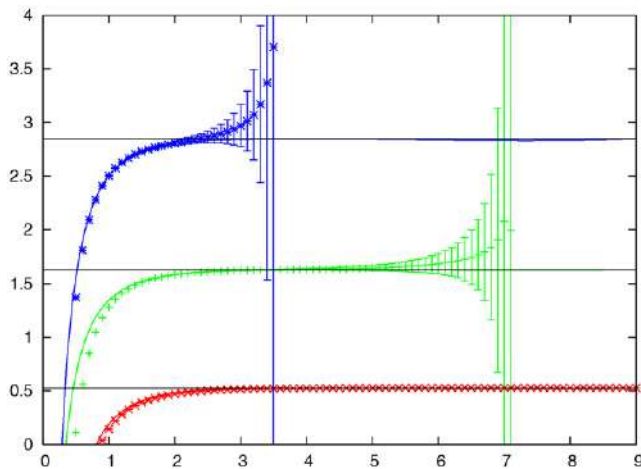


Fig. 4. Dependence of the free energy  $F$  and the associated auxiliary functions  $F_1$  and  $F_2$  on  $\beta$  for the anharmonic oscillator with quartic coupling  $g = 1$ . The solid lines are the fits to curves of the form given in Eq. (11). The horizontal lines in black correspond to the energy levels  $E_n$  determined from these fits (see Table 1). Numerical simulations were performed with  $p = 9$  level improved actions,  $N = 256$ , and  $N_{\text{MC}} = 10^7$ .

As a result, we have fit the numerical data to functions of the form

$$F_n(\beta) = E_n - \frac{1}{\beta} \ln(1 + A e^{-B\beta}), \quad (11)$$

where  $E_n$ ,  $A$  and  $B$  are the parameters of the fit. Fig. 4 shows the free energy  $F(\beta)$  (approximated by its discretization for  $N = 256$  and  $p = 9$ ) along with the associated auxiliary functions  $F_1(\beta)$ , and  $F_2(\beta)$  for the anharmonic oscillator with quartic coupling  $g = 1$ . Note that the class of functions given in Eq. (11) gives a better fit for larger values of  $\beta$ . This can indeed be explicitly seen from Fig. 4. The data points for the free energy  $F(\beta)$  were obtained directly from our Monte Carlo simulations and were used to determine the ground state energy  $E_0$ . The auxiliary functions  $F_n(\beta)$  were obtained recursively using Eq. (6) and the already determined energy levels. The error bars presented in the figure also follow directly from Eq. (6) and are

Table 1

Low lying energy levels of the anharmonic oscillator with quartic coupling  $g$ , calculated using  $N = 256$ ,  $p = 9$ , and  $N_{\text{MC}} = 10^7$

$g$	$E_0$	$E_1$	$E_2$	$E_3$
0	0.49993(2)	1.502(2)	2.48(6)	3.6(5)
0.1	0.50301(2)	1.516(1)	2.54(5)	3.5(2)
1	0.52765(2)	1.6295(8)	2.85(2)	3.98(7)
10	0.67335(2)	2.230(1)	4.12(2)	
100	1.16247(4)	4.058(6)		
1000	2.3578(2)			

given by

$$\Delta F_n = \frac{\Delta F e^{-\beta F} + \sum_{i=0}^{n-1} \Delta E_i e^{-\beta E_i}}{e^{-\beta F} - \sum_{i=0}^{n-1} e^{-\beta E_i}}. \quad (12)$$

For large inverse temperatures  $\beta$  the above denominator becomes exponentially small, and so the error bars become very large. Such points soon cease to give relevant contributions to the calculations of the corresponding energy level owing to the fact that we use a weighted fit. Note that, in fact, the lack of exponential growth of error bars with  $\beta$  is an indication of bad data points!

This effect of growing error bars becomes more pronounced for higher energy levels. In addition, from Eq. (12) we see that there is an accumulation of errors associated with all the lower energy levels. Both of these effects taken together give practical limits to the number of energy levels we can calculate. The precise depth to which we can probe the energy spectrum depends on the number of Monte Carlo samples used as well as the number of points  $\beta_i$  selected within the range of inverse temperatures available to us. As an illustration, Table 1 gives the low lying energy levels of the anharmonic oscillator for several values of coupling  $g$ . For all of these calculations we use the same range of  $\beta$ . The ground state energy level was calculated to five significant digits for all values of  $g$ . As we have already noted the errors increase as we go to higher energy levels. In fact, this increase is faster for larger couplings since then the energies themselves become higher and so the  $e^{-\beta E_n}$  terms become much smaller.

We have conducted explicit Monte Carlo calculations of the spectra of the Pöschl–Teller and Morse potentials and have obtained the same qualitative behavior. In particular, we have explicitly determined that the expected speedup in convergence, coming from using the  $p$ -level hierarchy of effective actions, holds for all of these potentials.

Obtained low lying energy levels for several values of the parameters of the modified Pöschl–Teller potential,

$$V(q) = -\frac{\alpha^2 \lambda(\lambda-1)}{2 \cosh^2 \alpha x}, \quad (13)$$

are given in Table 2. We considered this exactly solvable potential since it allows comparison of numerically calculated energy levels and the exact ones, given by

$$E_n^{\text{exact}} = -\frac{\alpha^2}{2} (\lambda - 1 - n)^2, \quad 0 \leq n \leq \lambda - 1, \quad n \in \mathbb{N}.$$



Table 2

Low lying energy levels of the modified Pöschl–Teller potential, calculated using  $N = 256$ ,  $p = 9$ , and  $N_{MC} = 10^7$

$\alpha$	$\lambda$	$E_0$	$E_0^{\text{exact}}$	$E_1$	$E_1^{\text{exact}}$
0.25	5.5	-0.6329(2)	-0.63281	-0.3819(7)	-0.38281
0.25	15.5	-6.5704(6)	-6.57031	-5.694(9)	-5.69531
0.5	5.5	-2.5313(3)	-2.53125	-1.530(3)	-1.53125
0.5	15.5	-26.281(1)	-26.2813	-22.80(3)	-22.7813
$\alpha$	$\lambda$	$E_2$	$E_2^{\text{exact}}$	$E_3$	$E_3^{\text{exact}}$
0.25	5.5	-0.18(2)	-0.19531	-0.09(3)	-0.07031
0.25	15.5	-4.92(2)	-4.88281	-3.8(4)	-4.13281
0.5	5.5	-0.80(2)	-0.78125	-0.31(6)	-0.28125
0.5	15.5	-19.6(5)	-19.5313	-16.9(9)	-16.5313

As can be seen from Table 2, numerical results are in excellent agreement with the exact energy levels even for a small value of discretization coarseness  $N$ .

As a conclusion, we have investigated a newly developed method for increasing the convergence of path integrals to the continuum limit. The method has previously been shown to lead to a many order of magnitude speedup in the numerical evaluation of path integrals for transition amplitudes [1–3] and expectation values [4]. In this Letter we have applied that method to the evaluation of energy spectra. We have shown that the above stated increase in convergence leads to a significant increase of the efficiency of path integral Monte Carlo calculations of low

lying energy levels of a generic theory. The analytical results were checked explicitly in a series of Monte Carlo simulations of several distinct models over a wide range of parameters.

## References

- [1] A. Bogojević, A. Balaž, A. Belić, Phys. Rev. Lett. 94 (2005) 180403.
- [2] A. Bogojević, A. Balaž, A. Belić, Phys. Rev. B 72 (2005) 064302.
- [3] A. Bogojević, A. Balaž, A. Belić, Phys. Lett. A 344 (2005) 84.
- [4] J. Grujić, A. Bogojević, A. Balaž, Phys. Lett. A 360 (2006) 217.
- [5] R.P. Feynman, A.R. Hibbs, Quantum Mechanics and Path Integrals, McGraw–Hill, New York, 1965.
- [6] R.P. Feynman, Statistical Mechanics, Benjamin, New York, 1972.
- [7] C. Itzykson, J.-B. Zuber, Quantum Field Theory, McGraw–Hill, New York, 1980.
- [8] S. Coleman, Aspects of Symmetry, Cambridge Univ. Press, Cambridge, 1985.
- [9] C. Itzykson, J.-M. Drouffe, Statistical Field Theory, Cambridge Univ. Press, Cambridge, 1991.
- [10] G. Parisi, Statistical Field Theory, Addison–Wesley, New York, 1988.
- [11] J.A. Barker, D. Henderson, Rev. Mod. Phys. 48 (1976) 587.
- [12] E.L. Pollock, D.M. Ceperley, Phys. Rev. B 30 (1984) 2555.
- [13] D.M. Ceperley, Rev. Mod. Phys. 67 (1995) 279.
- [14] H. Kleinert, Path Integrals in Quantum Mechanics, Statistics, Polymer Physics, and Financial Markets, World Scientific, Singapore, 2004.
- [15] A. Bogojević, A. Balaž, A. Belić, Phys. Lett. A 345 (2005) 258.
- [16] <http://www.eu-egee.org/>.
- [17] <http://www.see-grid.eu/>.
- [18] <http://scl.phy.bg.ac.yu/speedup/>.

# Optimization and Porting of the Path Integral Monte Carlo SPEEDUP Code to New Computing Architectures

V. Slavnić, A. Balaž, D. Stojiljković, A. Belić, A. Bogojević

Scientific Computing Laboratory  
Institute of Physics Belgrade  
Pregrevica 118, 11080 Belgrade, Serbia  
<http://www.scl.rs/>

**Abstract**— Many complex quantum physical systems can be most effectively described by the path integral formalism. The SPEEDUP code implements recently introduced analytical approach that systematically improves convergence of numerically calculated transition amplitudes of a generic quantum non-relativistic theory that leads to significant speedup of Path Integral Monte Carlo algorithms. In this paper we report on the optimization, porting and testing of the SPEEDUP code, done on several new computing architectures: IBM POWER6, PowerXCell and the latest Intel CPUs. We give overview of optimization techniques used and present results on the use of advanced features of new CPU types, which can be efficiently applied for the optimization of the SPEEDUP code.

**Keywords**- Monte Carlo; SCL; SPEEDUP; Path Integral; Optimization; Porting;

## I. INTRODUCTION

Path integral Monte Carlo code SPEEDUP [1] is used for various calculations, mainly for studies of Quantum Mechanical systems and investigation of global and local properties of Bose-Einstein condensates. Porting of this code to new computing architectures will enable its use on a broader set of clusters and supercomputer facilities. The purpose of the code optimization is to fully utilize available computing resources, eliminating bottlenecks that may be located in different parts of the code, depending on the details of hardware implementation and architecture of the CPU. In some situations even compiling, linking or choosing more appropriate (optimized) libraries can lead to significant reduction in program execution times. However, the optimization must be performed carefully and the new code has to be verified after each change by comparison of its numerical results with the correct reference values.

In addition to obtaining highly optimized code, the above procedure can be also used to benchmark different hardware platforms and to compare their performance on a specific application/code. Such application-specific benchmarking, based on the assessment of hardware performance for the chosen set of applications, can be also used for the proper planning of hardware upgrades of computing centers supporting several user communities.

## II. SPEEDUP CODE

Functional formalism in quantum theories naturally introduces Monte Carlo simulations as a method of choice for numerical studies of relevant physical systems. The discretization of the phase space (necessary in any numerical calculation) is already built in to the functional formalism through the definition of continuous (path) integrals, and can be directly translated into the Monte Carlo algorithm. A detailed study of the relationship between discretization of different coarseness in the case of a general quantum theory leads to substantial increase in convergence of path integral to its continuum limit [2-4]. This study resulted in an analytic procedure for deriving a hierarchy of effective actions up to an arbitrary level  $p$ . We will illustrate the use of higher-level effective actions for calculation of the transition amplitude  $A$  for a quantum system that evolves from the initial state  $i$  to the final state  $f$  in time  $T$ . In the path integral formalism, this amplitude is given as  $N \rightarrow \infty$  limit of the  $(N-1)$ -fold integral expression:

$$A_N(i; f; T) = \left( \frac{1}{2\pi\epsilon_N} \right)^{N/2} \int dq_1 \cdots dq_{N-1} e^{-S_N}$$

where  $S_N$  is the discretized action of the theory and  $\epsilon_N = T/N$  is the discrete time step. Using naively discretized action, the transition amplitude would converge to its continuum limit as slow as  $1/N$ . Numerical simulations based on the use of effective action of the level  $p$  have much faster convergence, approaching the continuous limit as  $1/N^p$ . The effective discretized actions up to level  $p=18$  are implemented in the Path Integral Monte Carlo SPEEDUP code [1] in C programming language. It is used for efficient calculation of transition amplitudes, partition functions, expectation values, as well as low lying energy spectra.

The algorithm of a serial SPEEDUP code can be divided to the following steps:

1. Initialize variables; allocate memory; set input parameters of the model, number of time and MC steps, and random number generator (RNG) seed.

2. Main Monte Carlo loop, which accumulates contributions of sampled trajectories to intermediate variables; each loop step consists of the following steps:
  - a. Generate trajectory using the bisection method [5]. The number of time steps is  $N=2^s$ , where  $s$  is the discretization level (input parameter).
  - b. Calculate effective action for a generated trajectory and each sub-trajectory with smaller discretization level ( $s-1, \dots, 1$ ).
  - c. Accumulate variables used to calculate observables and their error estimates at each discretization level.
3. Calculate observables and associated errors by averaging variables accumulated in the previous step at each discretization level.
4. Print the results, deallocate memory and exit the program.

Parallelization of the above Monte Carlo algorithm is very simple, since each loop step 2 is independent. Therefore, the total number of Monte Carlo steps can be easily and evenly divided to a desired number of CPU threads or parallel processes (in MPI or in other available parallelization environment).

The SPEEDUP code generates large numbers of random trajectories and relies on the MC theory to achieve no correlations between the generated trajectories. This necessitates high-quality RNG, able to produce large numbers of uncorrelated random numbers from the uniform probability density distribution, in a form suitable for parallel simulation. For the SPEEDUP code we have used SPRNG - Scalable Parallel Random Number Generator [6], which is verified to satisfy all of the above criteria. SPRNG can generate large numbers of separate uncorrelated streams of random numbers, making it ideal for parallel applications.

### III. TESTED HARDWARE ARCHITECTURES

The hardware platform used for the testing reported in this paper was IBM BladeCenter with 3 kinds of servers within the H-type chassis commonly used in high performance computing and a separate 1U server based on latest Intel Nehalem Xeon processors:

- HX21XM blade Server based on Intel Xeon technology. It features two Intel Xeon E5405 processors that run on 2.0 GHz with front side bus of 1333MHz and level two cache (L2) of 12MB with support for Intel SSE2, SSE3, SSE4.1 extensions. Along with standard GCC (GNU Compiler Collection) compiler (gcc version 4.1.2), Intel C++ Compiler Professional Edition 11.1 by Intel Corporation (ICC) [7] that includes advanced optimization, multithreading, and processor support, as well as automatic processor dispatch, vectorization, and loop unrolling was used for testing in this paper.

- The BladeCenter JS22 server is a single-wide, 4-core, 2-socket with two cores per socket, 4.0 GHz POWER6 [8] SCM processors. Each processor includes 64 KB I-cache and 32 KB D-cache L1 cache per core with 4 MB L2 cache per core. Processors in this blade server are based on POWER RISC instruction set architecture (ISA) with Altivec, a single-instruction, multiple-data (SIMD) extensions. IBM provides XL C/C++ compiler solution (XLC) [9] that offers automated SIMD capabilities for application code that can be quite help for programmers. Beside GCC compiler IBM XLC/C++ is used for benchmark purposes in this paper.

- The IBM BladeCenter QS22 is based on 2 multi-core IBM PowerXCell 8i processors, based on Cell Broadband Engine Architecture (Cell/B.E.) [10]. The Cell Broadband Engine is a single-chip multiprocessor with 1+8 processors, specialized into two types:
  1. The PowerPC Processor Element (PPE) is a general-purpose, dual-threaded, 64-bit RISC processor fully compliant with the 64-bit PowerPC Architecture, with the Vector/SIMD Multimedia Extension operating at 3.2 GHz. It is intended primarily for control processing, running operating systems, managing system resources, and managing SPE threads.
  2. The SPE (Synergetic Processing Element) is core optimized for running compute-intensive applications. SPEs are single-instruction, multiple-data (SIMD) processor elements that are meant to be used for data-rich operations allocated to them by the PPE. Each SPE contains a RISC core, 256 KB software-controlled locale storage (LS) for instructions and data, and a 128-bit, 128-entry unified register file. The SPEs provide a deterministic operating environment. An SPE accesses both main memory and the local storage of other SPE's exclusively with DMA commands. They do not have caches, so cache misses are not a factor in their performance and programmer should to avoid branch intensive code.

Such a heterogeneous multi-core architecture of the Cell CPU requires that a developer adopts several new programming paradigms in order to fully utilize the full potential of Cell B/E processor. In addition to the GNU tools (including C and C++ compilers) which are provided with the Software Developer's Kit for Multicore Acceleration [11], one can also use IBM XL C/C++ Compiler [9] for Multicore Acceleration, specialized for Cell Broadband Engine solution.

- Intel Server System SR1625UR based on latest Intel Xeon processors with Nehalem micro-architecture. Two quad-core Xeon X5570 processors are present within the system. These CPUs run on 2.93GHz with triple channel DDR3 memory subsystem with support of latest SSE4.2 extensions. They are equipped with 256 Kb of Mid-Level cache per core and 8MB of cache shared between cores (L3). With this micro-architecture Intel reintroduced its Hyper-Threading technology that supposed to enhance parallelization of computational tasks. Beside GCC, Intel ICC compiler, as for the other Intel system, was used for obtaining results of testing described in this paper.

## IV. RESULTS

Here we describe the performed optimization and the obtained benchmarking results. In all benchmarks in this paper we have executed the code with  $N_{mc}=5120000$  MC samples for the quantum-mechanical amplitude of the quartic anharmonic oscillator with the boundary conditions  $q(t=0)=0$ ,  $q(t=T=1)=1$ , with zero anharmonicity and with level  $p=9$  effective action. We always used the same seed for SPRNG generator so that the results can be easily compared. Section A gives results for a serial SPEEDUP code on each platform with different compilers. These results are later used as a reference in benchmarking and in verification of the optimized code. Section B gives results for SPEEDUP MPI code tested on Intel platform, while Section C presents the threaded SPEEDUP code and results obtained with Intel and POWER architectures. In Section D we give results for the Cell SPEEDUP code, and in Section E we compare all results.

## A. Serial SPEEDUP code

For Intel Xeon 5405 Blade server we compiled the serial code with GCC C compiler using optimization flag `-O1`, which turns to give the best performance. Along with GCC, we also used ICC compiler with optimization flag `-fast`, equivalent to the combination `-O3 -xHOST -ipo -no-prec-div -static`.

Intel Nehalem platform shows best results with GCC flags `-O1 -funroll-loops` (loop unrolling), and with the `-fast` flag for Intel's ICC.

On POWER6 and Cell Blades the code was compiled with both GCC and IBM XLC compiler. On Cell Blade we used the flags `-O1 -funroll-loops` with GCC, and with XLC flags `-O5 -qaltivec -qenablevmx`. Appropriate versions of GCC and XLC binaries were used (ppu-gcc and ppxlcl). On POWER6 Blade -q64 -O5 -qaltivec -qenablevmx flags were used with XLC and `-O3 -funroll-loops` with GCC. Results for the serial program benchmarking are presented in Table 1.

Platform/Compiler	GCC	ICC	XLC
Intel Xeon 5405	(6280±20) s	(1600±20) s	-
Intel Nehalem	(3520±10) s	(920±10) s	-
POWER6	(8980±10) s	-	(1830±10) s
Cell	(25350±50) s	-	(12550±50) s

Table 1: Average times of execution of a serial SPEEDUP code on all tested platforms with different compilers. The flags used are given in the text.

Table 1 demonstrates the significant increase in the speed of the execution of the code when platform-specific compiler is used. New Nehalem platform in conjunction with ICC compiler gives the best performance compared to all other platforms. On the other hand, it is clear that Cell version, running only on the PPE is no match for other two platforms. Real utilization of the Cell platform can be achieved only when additional available SPEs are used.

## B. MPI SPEEDUP code

On the Intel Blade Xeon 5405 and Intel Nehalem platform, we tested the performance of the SPEEDUP code with MPI implementation, compiled by the ICC compiler with `-fast` flag. Also we tested the behavior of Nehalem CPUs with Hyper-Threading feature enabled and disabled. The results are shown in Figure 1.

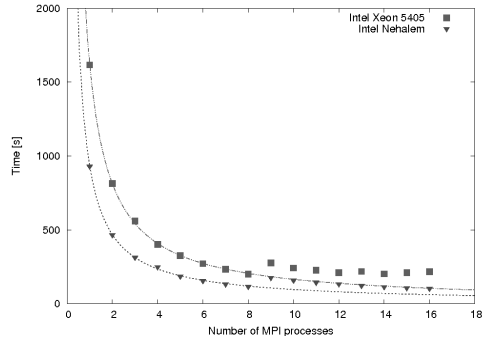


Figure 1: Average times of execution of the MPI SPEEDUP code on Intel Xeon 5405 and Intel Nehalem platforms compiled with ICC (`-fast` flag). The curves give fits to the expected dependence  $A + B / (\text{Number of MPI processes})$ .

As we can see, the MPI version of the code shows excellent scalability with the number of MPI processes. When the number of MPI processes exceeds the number of physical cores in the system (eight), the operating system is trying to distribute the load among already fully loaded cores, which creates additional overhead. This is less pronounced at the Nehalem platform, with the Hyper-Threading enabled. In that case, as shown in Figure 2, slightly better results are achieved when the numbers of MPI instances exceeds the number of physical cores. Below this threshold the results are identical.

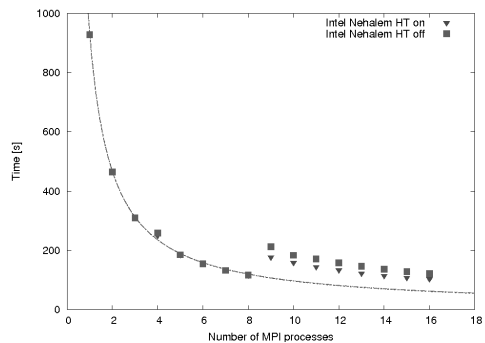


Figure 2: Average times of execution of the MPI SPEEDUP code on Intel Nehalem platform compiled with ICC (`fast` flag) with Hyper-Threading technology enabled (HT on) and disabled (HT off).

MPI implementation gives minimal execution time of around 100s for Nehalem platform and around 200s for Intel Xeon 5405.

### C. Modified SPEEDUP code

To fully optimize the parallel SPEEDUP code, instead of using MPI API, we implemented its threaded version using the POSIX threads (pthreads). Each thread calculates  $Nmc/Nth$  of Monte Carlo samples, where  $Nth$  represents the number of initiated threads. Also, some minor additional modifications of the code were performed, focusing on specific improvements for  $p=9$  effective action. The Intel version of the code was compiled with ICC, while the POWER version was compiled with XLC. The obtained numerical results are summarized in Figure 3.

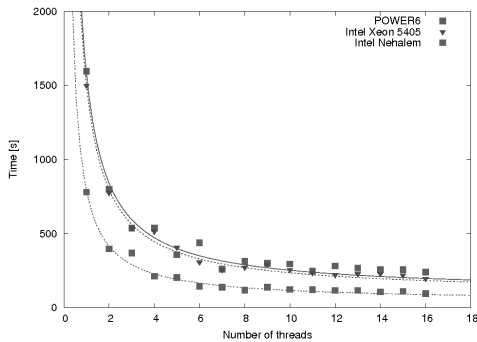


Figure 3: Average times of execution of the threaded SPEEDUP code on Intel and POWER6 platforms.

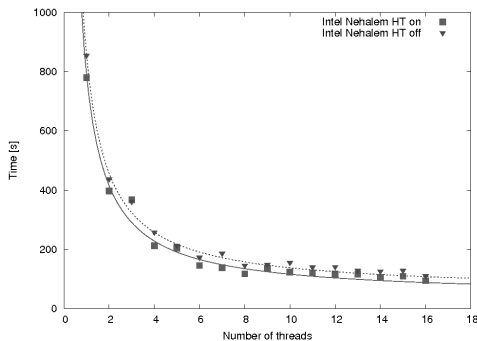


Figure 4: Average times of execution of the threaded SPEEDUP code on Intel Nehalem platform with Hyper-Threading enabled (HT on) and disabled (HT off).

With the threaded code we obtained non-negligible increase in the speed of the code compared to previous

implementations. Again, Intel Nehalem with the ICC compiler was much faster than all other platforms. If we compare the increase in the speed gained by implementing the threaded code, the POWER6 platform shows a 12% performance gain (threaded vs. the serial code), while we get around 6% gain for Intel platforms (threaded vs. MPI code).

The minimal execution time with the threaded code was 190s on Intel Xeon 5405 Blade, 95s on Intel Nehalem and 235s on the POWER Blade. Again, we can see a small impact on the execution speed when Hyper-Threading technology is enabled on the Intel Nehalem CPUs (Figure 4.).

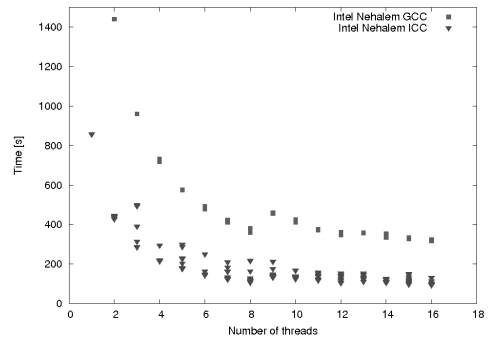


Figure 5: Times of execution of the threaded SPEEDUP code on Intel Nehalem platform with ICC and GCC compiler.

We have also observed an interesting behavior on Intel platforms, which is presented in Figure 5. Although the threaded code gives better performance when compiled with ICC compared to the code compiled with GCC, the times of execution of the ICC-compiled code for the same parameters and the same number of threads differ significantly for several consecutive runs. Such relatively large scattering of execution times around the average might be accredited to the low-level hardware implementation details of Intel CPUs, as well as to the aggressive optimization techniques used by the `-fast` flag. On the other hand, the execution of the same code compiled with GCC did not exhibit such behavior. This might point to the load-balancing issues when aggressive optimization is used with ICC, while GCC is not able to achieve such level of optimization and thus is not affected. The similar behavior was also observed on Intel Xeon 5405 platform.

### D. Cell SPEEDUP code

The heterogeneity of the Cell architecture required the slight rearrangement of the SPEEDUP code. We used MPI version of the code as a basis, and modified it so as to separate serial sections to be executed on the PPE from the parallel sections that can be executed on as many SPEs as available in the system. Our main implementation idea was to create a number of pthreads on the PPE that will pass control and start

execution of the code on the dedicated SPE for each pthread. Each SPE performs  $Nmc/Number\_of\_SPEs$  Monte Carlo steps, running the same code, only with different parameters passed by the PPE. After all SPEs finish their work, the final processing of gathered data is done on the PPE.

The main problem in a proper porting of the SPEEDUP code to the Cell architecture was missing Cell SPRNG library code that can be compiled and executed on each SPU. For this reason, we have compiled SPRNG for the PPE and performed all random number generation operations only on PPEs. This was done in parallel through several pthreads, distributed between both PPE processors of a QS22 Blade. Each pthread was associated with one of SPEs and synchronized with it using the mailbox technique. It is one of the simplest hardware based ways of communication within Cell CPU. The PPE mailbox checking is implemented through the interrupt, without active waiting (such as polling through the loop). Access to the main memory by all SPEs is realized through the Direct Memory Access (DMA) transfers. We have one initial transfer where control data from the PPE are received, one final transfer where computation results are sent back to the main memory and intermediate transfers of generated random numbers for each MC step. The XLC-compiled code was superior in the performance compared to the GCC-compiled code. The results for the XLC-compiled code are shown in Figure 6.

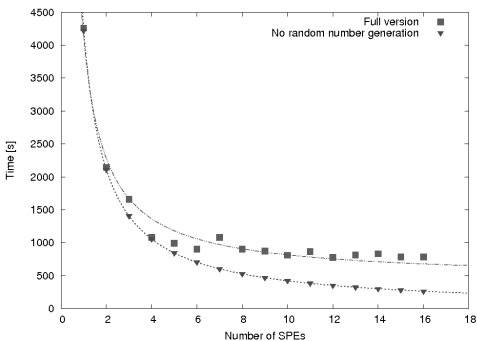


Figure 6: Average times of execution of the Cell SPEEDUP code. For comparison, we also give execution times for the code without generation of random numbers.

As we can see, the fact that only PPEs are used for generation of random trajectories leads to a saturation of the performance when we increase the number of used SPEs to around 4. After that, PPEs are not able to generate random numbers sufficiently enough, and further increase in the number of SPEs used does not lead to any improvement in the performance. In the ideal case, if PPEs would be able to produce enough random trajectories for all SPEs, the simulation execution time would be around 260s, as can be seen in Figure 6 for the code without random number generation. We also tested the code with the communication part disabled (no DMA memory transfers). From Table 2 we see that the communication does not have significant impact on the execution time and does not represent a bottleneck. To

confirm this, we tested also the code that only generates random trajectories on PPEs, and observed the saturation in its performance at about 770s for the given number of Monte Carlo samples  $Nmc$ . This clearly corresponds to the minimal execution time for the full version of the Cell code in Figure 6.

Number of SPEs	No random trajectories generation	No communication
1	(4220±5) s	(4200±5) s
2	(2110±5) s	(2100±5) s
4	(1055±5) s	(1050±5) s
8	(530±5) s	(525±5) s
16	(265±5) s	(260±5) s

Table 2: Average times of execution of the Cell SPEEDUP code without random trajectories generation and without PPE-SPE communication.

Therefore, as we can see, the missing implementation of the SPRNG library was a limiting factor in fully utilizing the capabilities of all SPEs of the Cell Blade. However, this problem would not be even seen in the case when individual MC steps take more time to finish their calculation, since then PPEs would be able to generate random trajectories at a sufficient rate. Such situation can be easily achieved e.g. if one uses higher effective action level  $p$  code [1-4]. We have demonstrated similar situation in Figure 7, where we have used unoptimized Cell SPEEDUP code, and where we observe perfect scaling of the code with the number of SPEs. Disabling the optimization leads to a much slower execution of the code, and each MC step takes much more time to be completed, thus giving enough time to PPEs to generate needed random trajectories according to the bisection algorithm. This also demonstrates the fact that specific details of the optimal porting of an application to the Cell architecture can significantly depend on the execution run-time parameters. Such situation is not frequently encountered on other computing platforms, and is here due to the current limitations of the Cell SPUs, as well as limitations in their communication model.

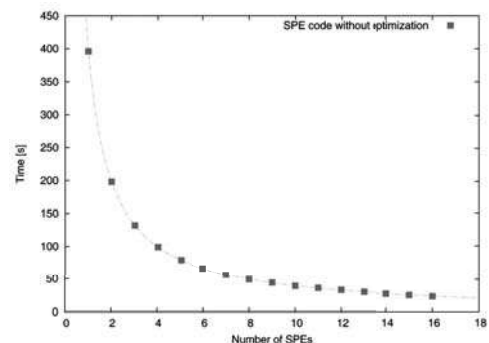


Figure 7: Average times of execution of the Cell SPEEDUP code compiled without optimization. The number of Monte Carlo steps is decreased to  $Nmc=5120$ , since the code without optimization is executed much slower.

### E. Comparison of hardware performance results

The overview of the obtained performance results for all tested hardware platforms is presented in Table 3. For Intel and POWER6 platform we give the results for the fully optimized threaded SPEEDUP code. For the Cell platform we give the minimal obtained execution time, as well as the execution time obtained with random trajectories generation disabled, which corresponds to the full utilization of all SPEs.

Intel Xeon 5405	Intel Nehalem	POWER6	Cell	Cell ideal
190s	95s	235s	770s	260s

Table 3: Minimal average execution time for each tested platform for the fully optimized SPEEDUP code. For each platform we have selected the optimal implementation.

The difference in performance of two tested Intel platforms can be partially explained by the higher clock frequency of 2.93 GHz for the Nehalem CPU, compared to only 2.0GHz frequency for the Intel Xeon 5405. However, even if we rescale the performances of both platforms to the same frequency, we still see a 30% better performance of the Nehalem platform. Such significantly better performance is due to the improved architecture of the newer CPU.

## V. CONCLUSIONS

We have ported and optimized Path Integral Monte Carlo SPEEDUP code to four different computing architectures (Intel Xeon 5405, Intel Nehalem X5570, IBM POWER6 and Cell) and used the obtained code for benchmarking of these hardware platforms. For Intel and POWER6 platforms full optimization was obtained with the straightforward threaded version of the code, while the Cell platform required more complex changes of the code (implementation of separate PPE and SPE sections of the code). For benchmarking purposes we have also used different available compilers for each of architectures, and our results clearly show that platform-specific compilers always give much better performance.

The SPEEDUP code was most easily optimized on the both Intel platforms, especially on Intel Nehalem where it achieves superior performance compared to all other hardware platforms. Contrary to our expectations based on previous experiences with the Hyper-Threading technology, it did not improve the performance of the code significantly.

The Cell platform is demonstrated to be able to achieve respectable level of performance in the case when individual MC steps take more time to complete. In the current implementation, due to the missing Cell SPRNG library, SPEEDUP code can fully utilize all Cell SPEs only for higher effective action levels  $p$ . However, the tested Cell CPU is no match for POWER6 or latest Intel CPUs. The Nehalem

platform also significantly outperforms POWER6 CPU, despite its much higher frequency of 4.0 GHz.

The plans for further development and testing include porting of SPRNG library to SPEs and implementation of platform-specific instructions (vectorization) for each tested platform.

### ACKNOWLEDGMENTS

This work was supported in part by the Serbian Ministry of Science, under project No. OI141035, and the European Commission under EU Centre of Excellence grant CX-CMCS. Numerical simulations were run on the AEGIS e-Infrastructure, supported in part by FP7 projects EGEE-III and SEE-GRID-SCI. The authors also acknowledge support by IBM Serbia and Intel Corporation (UK) Ltd.

### REFERENCES

- [1] SPEEDUP, <https://viewvc.scl.rs/viewvc/speedup/>
- [2] A. Bogojevic, A. Balaz, A. Belic, Phys. Rev. Lett. **94** (2005) 180403
- [3] A. Bogojevic, I. Vidanovic, A. Balaz and A. Belic, Phys. Lett. A **372** (2008) 3341-3349
- [4] A. Balaz, A. Bogojevic, I. Vidanovic and A. Pelster, Phys. Rev. E **79** (2009) 036701
- [5] D. M. Ceperley, Rev. Mod. Phys. **67** (1995) 279
- [6] <http://sprng.cs.fsu.edu/>
- [7] ICC, <http://software.intel.com/en-us/intel-compilers/>
- [8] POWER, <http://www-03.ibm.com/technology/power/>
- [9] POWER, <http://www-03.ibm.com/technology/power/>
- [10] Cell B/E, <http://www-03.ibm.com/technology/cell/>
- [11] IBM SDK for Multicore Acceleration, <http://www.ibm.com/developerworks/power/cell/>

# SPEEDUP - optimization and porting of path integral MC Code to new computing architectures

V. Slavnić, A. Balaž, D. Stojiljković, A. Belić, A. Bogojević  
*Scientific Computing Laboratory, Institute of Physics Belgrade, Serbia*

Path integral formalism presents the concise and flexible formulation of quantum theories at different levels, providing also simple description of many other complex physical systems. Recently introduced analytical approach that systematically improves convergence of numerically calculated path integrals of a generic theory leads to a significant speedup of Path Integral Monte Carlo algorithms. This is implemented in the SPEEDUP code. Here we report on optimization, porting and testing of the SPEEDUP code on new computing architectures: latest Intel, and IBM POWER6 and PowerXCell CPUs. We find that the code can be highly optimized and take substantial advantage of the features of new CPU types.

## 1. Introduction

Path integral Monte Carlo code SPEEDUP [1] is used for various calculations mainly for studies of Quantum Mechanical systems and investigation of global and local properties of Bose-Einstein condensates. Porting of this code to new computing architectures will enable its use on a broader set of clusters and supercomputer facilities. The purpose of the code optimization is to fully utilize available computing resources, eliminating bottlenecks that may be located in different parts of the code, depending on the details of hardware implementation and architecture of the CPU. In some situations even compiling, linking or choosing more appropriate (optimized) libraries can lead to significant reduction in program execution times. However, the optimization must be performed carefully and the new code has to be verified after each change by comparison of its numerical results with the correct reference values.

In addition to obtaining highly optimized code, the above procedure can be also used to benchmark different hardware platforms and to compare their performance on a specific application/code. Such application-specific benchmarking, based on the assessment of hardware performance for the chosen set of applications, can be also used for the proper planning of hardware upgrades of computing centers supporting several user communities.

## 2. SPEEDUP code

Functional formalism in quantum theories naturally introduces Monte Carlo simulations as a method of choice for numerical studies of relevant physical systems. The discretization of the phase space (necessary in any numerical calculation) is already built in to the functional formalism through the definition of continuous (path) integrals, and can be directly translated into the Monte Carlo algorithm. A detail study of the relationship between discretization of different coarseness in the case of a general quantum theory leads to substantial increase in convergence of path integral to its continuum limit [2-4]. This study resulted in an analytic procedure for deriving a hierarchy of effective actions up to an arbitrary level  $p$ . We will illustrate the use of higher-level effective actions for calculation of the transition amplitude  $A$  for a quantum system that evolves from the initial state  $i$  to the final state  $f$  in time  $T$ . In the path integral formalism, this amplitude is given as  $N \rightarrow \infty$  limit of the  $(N-1)$ -fold integral expression:

$$A_N(i, f; T) = \left( \frac{1}{2\pi\epsilon_N} \right)^{N/2} \int dq_1 \cdots dq_{N-1} e^{-S_N},$$

where  $S_N$  is the discretized action of the theory and  $\epsilon_N = T/N$  is the discrete time step. Using naively discretized action, the transition amplitude would converge to its continuum limit as



slow as  $1/N$ . Numerical simulations based on the use of effective action of the level  $p$  have much faster convergence, approaching the continuous limit as  $1/N^p$ . The effective discretized actions up to level  $p=18$  are implemented in the Path Integral Monte Carlo SPEEDUP code [1] in C programming language. It is used for efficient calculation of transition amplitudes, partition functions, expectation values, as well as low lying energy spectra.

The algorithm of a serial SPEEDUP code can be divided to the following steps:

1. Initialize variables; allocate memory; set input parameters of the model, number of time and MC steps, and random number generator (RNG) seed.
2. Main Monte Carlo loop, which accumulates contributions of sampled trajectories to intermediate variables; each loop step consists of the following steps:
  - a. Generate trajectory using bisection method [5]. The number of time steps is  $N=2^s$ , where  $s$  is the discretization level (input parameter),
  - b. Calculate effective action for a generated trajectory and each sub-trajectory with smaller discretization level ( $s-1, \dots, 1$ ),
  - c. Accumulate variables used to calculate observables and their error estimates at each discretization level,
3. Calculate observables and associated errors by averaging variables accumulated in the previous step at each discretization level,
4. Print the results, deallocate memory and exit the program.

Parallelization of the above Monte Carlo algorithm is very simple, since each loop step 2 is independent. Therefore, the total number of Monte Carlo steps can be easily and evenly divided to a desired number of CPU threads or parallel processes (in MPI or in other available parallelization environment).

The SPEEDUP code generates large numbers of random trajectories and relies on the MC theory to achieve no correlations between the generated trajectories. This necessitates high-quality RNG, able to produce large numbers of uncorrelated random numbers from the uniform probability density distribution, in a form suitable for parallel simulation. For the SPEEDUP code we have used SPRNG - Scalable Parallel Random Number Generator [6], which is verified to satisfy all of the above criteria. SPRNG can generate large numbers of separate uncorrelated streams of random numbers, making it ideal for parallel applications.

### 3. Tested hardware architectures

The hardware platform used for the testing reported in this paper was IBM BladeCenter with 3 kinds of servers within the H-type chassis commonly used in high performance computing:

- HX21XM blade Server based on Intel Xeon technology. It features two Intel Xeon 5405 processors that run on 2.0 GHz with front side bus of 1333MHZ and level two cache (L2) of 12MB with support for Intel SSE2, SSE3, SSE4.1 extensions. Along with standard GCC (GNU Compiler Collection) compiler (gcc version 4.1.2), Intel C++ Compiler Professional Edition 11.1 by Intel Corporation (ICC) [7] that includes advanced optimization, multithreading, and processor support, as well as automatic processor dispatch, vectorization, and loop unrolling was used for testing in this paper.
- The BladeCenter JS22 server is a single-wide, 4-core, 2-socket with two cores per socket, 4.0 GHz POWER6 [8] SCM processors. Each processor includes 64 KB I-cache and 32 KB D-cache L1 cache per core with 4 MB L2 cache per core. Processors in this blade server are based on POWER RISC instruction set architecture (ISA) with AltiVec, a single-instruction, multiple-data (SIMD) extensions. IBM provides XL C/C++ compiler solution (XLC) [9] that offers automated SIMD capabilities for application code that can

be quite help for programmers. Beside GCC compiler IBM XLC/C++ is used for benchmark purposes in this paper.

- The IBM BladeCenter QS22 is based on 2 multi-core IBM PowerXCell 8i processors, based on Cell Broadband Engine Architecture (Cell/B.E.) [10]. The Cell Broadband Engine is a single-chip multiprocessor with nine processors specialized into two types:
  1. The PowerPC Processor Element (PPE) is a general-purpose, dual-threaded, 64-bit RISC processor fully compliant with the 64-bit PowerPC Architecture, with the Vector/SIMD Multimedia Extension operating at 3.2 GHz. It is intended primarily for control processing, running operating systems, managing system resources, and managing SPE threads.
  2. The SPE (Synergetic Processing Element) is core optimized for running compute-intensive applications. SPEs are single-instruction, multiple-data (SIMD) processor elements that are meant to be used for data-rich operations allocated to them by the PPE. Each SPE contains a RISC core, 256 KB software-controlled locale storage (LS) for instructions and data, and a 128-bit, 128-entry unified register file. The SPEs provide a deterministic operating environment. An SPE accesses both main memory and the local storage of other SPE's exclusively with DMA commands. They do not have caches, so cache misses are not a factor in their performance and programmer should to avoid branch intensive code.

The Cell Broadband Engine has one PPE and eight SPEs.

Such a heterogeneous multi-core architecture of the Cell CPU requires that a developer adopts several new programming paradigms in order to fully utilize the full potential of Cell B/E processor. In addition to the GNU tools (including C and C++ compilers) which are provided with the Software Developer's Kit for Multicore Acceleration [11], one can also use IBM XL C/C++ Compiler [9] for Multicore Acceleration, specialized for Cell Broadband Engine solution.

## 4. Results

Here we describe the performed optimization and the obtained benchmarking results. In all benchmarks in this paper we have executed the code with  $N_{mc}=5120000$  MC samples for the quantum-mechanical amplitude of the quartic anharmonic oscillator with the boundary conditions  $q(t=0)=0$ ,  $q(t=T)=1$ , with zero anharmonicity and with level  $p=9$  effective action. We always used the same seed for SPRNG generator so that the results can be easily compared. Section 4.1 gives results for a serial SPEEDUP code on each platform with different compilers. These results are later used as a reference in benchmarking and in verification of the optimized code. Section 4.2 gives results for SPEEDUP MPI code tested on Intel platform and Section 4.3 presents the threaded SPEEDUP code and results obtained with Intel and POWER architectures. In Section 4.4 we give results for the Cell SPEEDUP code, and in Section 4.5 we compare all obtained results.

### 4.1. Serial SPEEDUP code

For Intel Blade server we compiled the serial code with GCC C compiler using optimization flags *O1* and *funroll-loops* which give the best performance (better than the *O3* flag, with or without loop unrolling). Along with GCC, we also used ICC compiler with maximal optimization flag *O2*.

On POWER6 and Cell Blades the code was compiled with both GCC and IBM XLC compilers. On Cell Blade we used the flags *O3*, *funroll-loops*, *mabi=altivec*, and *maltivec*

with GCC, and *O5*, *qaltivec* and *qenablevmx* with XLC. Appropriate versions of GCC and XLC binaries were used (ppu-gcc and ppxlcl). On POWER6 Blade the *O5* flag was used with XLC and *O3* and *funroll-loops* with GCC. Results for serial program testing are presented in Table 1.

Table 1. Average time of execution of a serial SPEEDUP code on all tested platforms with different compilers

Compiler Platform	GCC	ICC	XLC
Intel	(13760±50) s	(10160±30) s	-
POWER6	(17000±10) s	-	(1900±10) s
Cell	(49410±50) s	-	(14020±20) s

Table 1 demonstrates the significant increase in the speed of the code when platform-specific compiler is used. We also see that in this specific case the POWER6 platform in combination with the XLC compiler shows order of magnitude improvement in the speed compared to the Intel platform. On the other hand, it is clear that Cell version, running only on the PPE is no match for other two platforms. Real utilization of the Cell platform can be achieved only when SPEs are used.

#### 4.2. MPI SPEEDUP code

On the Intel Blade multicore, we tested the performance of the SPEEDUP code with MPI implementation, compiled with GCC and ICC compilers. The results are shown in Fig. 1.

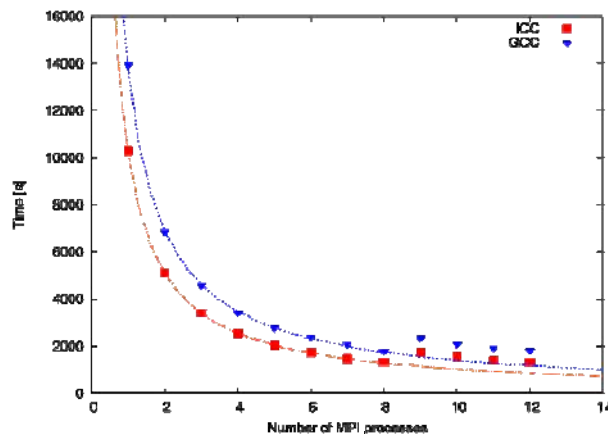


Fig. 1. Average times of execution of the MPI SPEEDUP code on Intel platform compiled with ICC (*O2* flag) and GCC (*O1* and *funroll-loops*). The curves give fits to the expected dependence  $A + B / (\text{Number of MPI processes})$ .

As we can see, the MPI version of the code shows excellent scalability with the number of MPI processes. When the number of MPI processes exceeds the number of physical cores in the system, the operating system is trying to distribute the load among

already fully loaded cores, which creates additional overhead. This implementation gives minimal execution time of 1320s.

### 4.3. Modified SPEEDUP code

To fully optimize the parallel SPEEDUP code, instead of using MPI API we implemented its threaded version using POSIX threads (pthreads). Each thread calculates  $N_{mc}/N_{th}$  of Monte Carlo samples where  $N_{th}$  is the number of threads. Also, some minor additional modifications of the code were performed, focusing on specific improvements for  $p=9$  effective action. The Intel version was compiled with ICC, while the POWER version was compiled with XLC. The obtained numerical results are shown in Fig. 2.

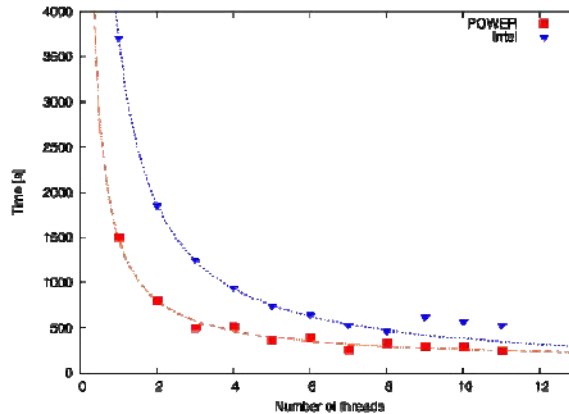


Fig. 2. Average times of execution of the threaded SPEEDUP code on Intel and POWER platforms

With the threaded code we obtained a significant increase in the speed of the code, even without implementing specific vector instructions (AltiVec on POWER6 or SSE on Intel). Again, POWER6 Blade in conjunction with XLC compiler was faster than Intel Blade. However, the relative increase in the speed of threaded code was larger on the Intel platform. The minimal execution time was 460s on Intel and 250s on POWER Blade. This gives relative increase in the speed of the code of 2.8 (threaded vs. MPI) for Intel and 1.3 (one thread vs. serial) for POWER6 platform.

We also note an interesting scaling issue on POWER6 system. While the threaded code scales perfectly on Intel Blade, POWER6 Blade shows strange behavior for even number of threads, where execution times are slightly higher than expected. When the code is compiled with GCC, the same behavior is observed for odd number of threads. Such throttling may be related to low-level hardware details that are not properly implemented in different compilers.

### 4.4. Cell SPEEDUP code

The heterogeneity of the Cell architecture required the slight rearrangement of the SPEEDUP code. We used MPI version of the code as a basis, and modified it so as to separate parts that are executed on the PPE and parts that are executed in parallel on SPEs. Our implementation was to create a number of pthreads on the PPE that will pass control and start execution of the code on the dedicated SPE for each pthread. Each SPE performs  $N_{mc}/Number\_of\_SPEs$  MC steps, running the same code, only with different parameters passed by the PPE. After all SPEs finish their work, the final processing of gathered data is done on the PPE.

The main problem in a proper porting of the SPEEDUP code to the Cell architecture was missing Cell SPRNG code that can be compiled for the SPU. For this reason, we have compiled SPRNG for the PPE and performed all RNG operations only on the PPEs. This was done in parallel through several pthreads, distributed between both PPU processors of a QS22 Blade. Each pthread is associated with one of SPEs and synchronizes with it using mailbox technique, one of the simplest, hardware based, ways of communication within Cell CPU. The PPE mailbox checking is implemented through the interrupt, without active waiting (such as polling through the loop). Access to the main memory by all SPEs is realized through the Direct Memory Access (DMA) transfers. We have one initial transfer where control data from the PPE are received, one final transfer where computation results are sent back to the main memory and intermediate transfers of generated random numbers for each MC step. The XLC-compiled code was superior in the performance compared to the GCC-compiled code. The results for the XLC-compiled code are shown in Fig. 3.

As we can see, the fact that only PPEs are used for generation of random trajectories leads to a saturation of the performance when we increase the number of used SPEs to around 4. In the ideal case, when PPEs would be able to produce enough random trajectories for all SPEs, the simulation execution time would be around 250s, as can be seen in Fig. 3 for the code without random number generation). We also tested the code with the communication part disabled (no DMA memory transfers). From Table 2 we see that the communication does not have significant impact on the execution time and does not represent a bottleneck. To confirm this, we tested also the code that only generates random trajectories on PPEs, and observed the saturation in its performance at about 750s for the given  $Nmc$  number. This clearly corresponds to the minimal execution time for the full version of the Cell code in Fig. 3.

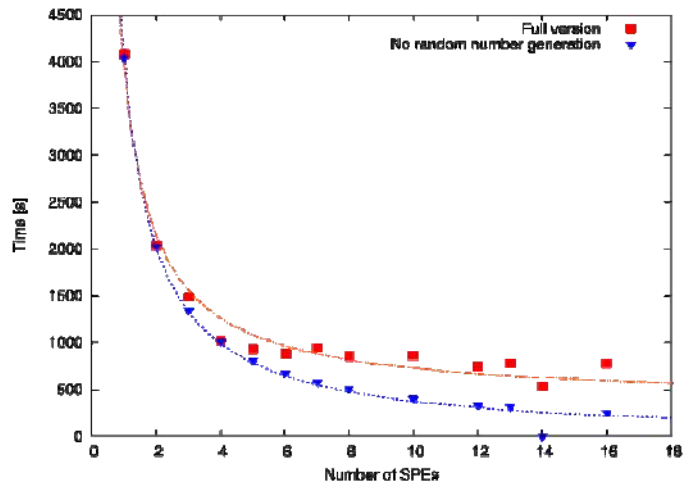


Fig. 3. Average times of execution of the Cell SPEEDUP code (full version) and for the code without generation of random numbers

Table 2. Average times of execution of the Cell SPEEDUP code without random trajectories generation and without PPE-SPE communication

Number of SPEs	No random trajectories generation	No communication
1	(4040±5) s	(4020±5) s
2	(2020±5) s	(2010±5) s
4	(1010±5) s	(1000±5) s
6	(675±5) s	(670±5) s
8	(505±5) s	(500±5) s
10	(405±5) s	(400±5) s
16	(255±5) s	(250±5) s

Therefore, as we can see, the missing implementation of the SPRNG library was limiting factor in fully utilizing the capabilities of all SPEs of the Cell Blade. This would not be the case if individual MC step calculation would require more time to complete, since then PPEs would be able to generate random trajectories at a sufficient rate. Such situation can be easily achieved e.g. if one uses higher effective action level  $p$  code. We have demonstrated similar situation in Fig. 4, where we have used unoptimized Cell SPEEDUP code, and where we observe perfect scaling of the code with the number of SPEs. Note that we used only 5120 MC samples for these tests since the code is now executed much slower.

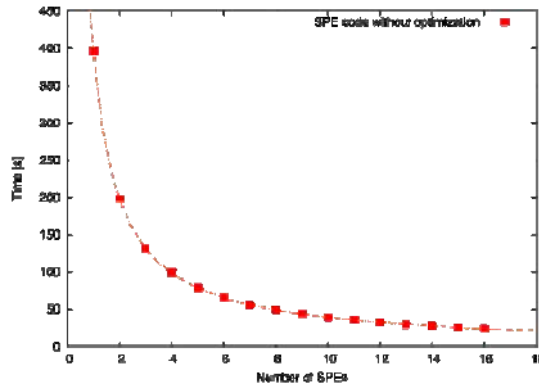


Fig. 4. Average times of execution of the Cell SPEEDUP code compiled without optimization

#### 4.5. Comparison of hardware performance results

The overview of the obtained performance results for all tested hardware platforms is presented in Table 3. For Intel and POWER6 platform we give the results for the fully optimized threaded SPEEDUP code. For the Cell platform we give the minimal obtained execution time, as well as the execution time obtained with random trajectories generation disabled, which corresponds to the full utilization of all SPEs.

Table 3. Minimal average execution time per Blade of the fully optimized SPEEDUP code for each tested platform

Intel	POWER6	Cell	Cell Ideal
460s	250s	750s	250s

## 5. Conclusion

We have ported and optimized Path Integral Monte Carlo SPEEDUP code to three different computing architectures (Intel, POWER6 and Cell) and used the obtained code for benchmarking of these hardware platforms. For Intel and POWER6 platforms full optimization was obtained with the straightforward threaded version of the code, while the Cell platform required more complex changes of the code (implementation of separate PPE and SPE parts of the code). For benchmarking purposes we have also used different available compilers for each of architectures, and our results clearly show that platform-specific compilers always give much better performance.

The SPEEDUP code was most easily optimized on the POWER6 platform, where it also achieves superior performance (per Blade server) compared to all other hardware platforms. The Cell platform is demonstrated to be able to achieve the same level of performance in the case when individual MC steps take more time to complete. In the current implementation, due to the missing Cell SPRNG library, SPEEDUP code can fully utilize all Cell SPEs only for higher effective action levels  $p$ . The Intel platform shows also very good performance and excellent scalability, without any glitches for certain (odd or even) number of cores, observed on other platforms.

The plans for further development and testing include porting of SPRNG library to SPEs and implementation of platform-specific instructions (vectorization) for each tested platform.

## Acknowledgements

This work was supported in part by the Serbian Ministry of Science, under project No. OI141035, and the European Commission under EU Centre of Excellence grant CX-CMCS. Numerical simulations were run on the AEGIS e-Infrastructure, supported in part by FP7 projects EGEE-III and SEE-GRID-SCI. The authors also acknowledge support by IBM Serbia.

## References

- [1] SPEEDUP, <https://viewvc.scl.rs/viewvc/speedup/>
- [2] A. Bogojevic, A. Balaz, A. Belic, Phys. Rev. Lett. 94 (2005) 180403.
- [3] A. Bogojevic, I. Vidanovic, A. Balaz and A. Belic, Phys. Lett. A 372 (2008) 3341-3349.
- [4] A. Balaz, A. Bogojevic, I. Vidanovic and A. Pelster, Phys. Rev. E 79 (2009) 036701.
- [5] D. M. Ceperley, Rev. Mod. Phys. 67 (1995) 279.
- [6] <http://sprng.cs.fsu.edu/>
- [7] ICC, <http://software.intel.com/en-us/intel-compilers/>
- [8] POWER, <http://www-03.ibm.com/technology/power/>
- [9] XLC, <http://www-01.ibm.com/software/awdtools/xlcpp/>
- [10] Cell B/E, <http://www-03.ibm.com/technology/cell/>
- [11] IBM SDK for Multicore Acceleration, <http://www.ibm.com/developerworks/power/cell/>

# Energy levels and expectation values via accelerated path integral Monte Carlo

D Stojiljković, A Bogojević and A Balaz̃

Scientific Computing Laboratory, Institute of Physics, Belgrade, Serbia

E-mail: danica@phy.bg.ac.yu

**Abstract.** A recently developed method systematically improved the convergence of generic path integrals for transition amplitudes, partition functions, expectation values and energy spectra. This was achieved by analytically constructing a hierarchy of discretized effective actions indexed by a level number  $p$  and converging to the continuum limit as  $1/N^p$ . Here we apply the above general method to numerical calculations using Metropolis Monte Carlo simulations of energy expectation values and energy spectra. We analyze and compare the ensuing increase in efficiency of several orders of magnitude.

*Keywords:* Path integral, Effective action, Monte Carlo

## 1. Introduction

In the middle of the last century Feynman introduced an alternate approach to quantum mechanics known as the path integral formalism [1, 2, 3]. This approach provided us with a new intuitive picture for understanding quantum mechanics, it enabled us to make connections and analogies between different areas of physics, and it also provided a new mathematical framework for calculating properties of physical systems. In particular, the formalism made it easy to generalize quantum theories from one particle to many particles and finally to fields in a relatively straightforward way. Unfortunately, the new formalism did not increase the number of analytically solvable systems [4, 5]. The fact that it enabled us to treat models that were previously inaccessible is due to its formulation in terms of discretized quantities, making it directly amenable to numerical treatment.

In numerical simulations, our poor understanding of the inherent mathematical structure of path integrals translates into the slow convergence of the sought-after physical quantities. Substantial increase in efficiency of numerical algorithms for calculating path integrals, can, therefore, come only through the input of new analytical information about path integrals into the calculation schemes. A recent series of papers [6, 7, 8] has investigated the relationship between discretizations of different coarseness in the case of a general quantum theory. The new found analytical results were then used to construct a more efficient Path Integral Monte Carlo (PIMC) SPEEDUP code [9] which increased convergence of generic path integrals from  $1/N$  to  $1/N^p$ . For computational reasons, the level  $p$  is currently limited to  $p = 13$ , however, there are no fundamental barriers to going to even higher levels. This substantial increase in efficiency results in speedup of path integral calculations and has been applied to calculations of



amplitudes, partition functions, expectation values, as well as low lying energy spectra [10, 11]. Direct numerical calculations of a variety of different models have confirmed the analytically derived results.

All of the key properties of path integrals can be seen already on the example of one particle systems in one dimension. For this reason the current paper limits itself to systems of this kind. Let us note however that the generalization to more complex systems has also been investigated and confirms that the previously derived increase in efficiency holds for general many particle systems as well [12].

PIMC algorithms can be made more efficient either by getting better convergence to the continuum limit through the use of above mentioned hierarchy of discretized effective actions, or through better generation of relevant trajectories in the MC method. So far all the numerical verifications of improved  $1/N^p$  convergence have been implemented using a PIMC code in which paths were generated through a Levy construction. In this paper we numerically investigate the derived speedup using Metropolis [13, 14, 15] method for generating relevant paths. In general the Metropolis technique is optimally suited for calculating expectation values. We have numerically verified the  $1/N^p$  convergence, showing explicitly coexistence of improvements obtained through the use of effective actions and the Metropolis path generation method.

## 2. Path integrals

As previously stated, we focus on the motion of one particle in one dimension. The central object is the (Euclidean) amplitude for the quantum system to go from initial position  $a$  to final position  $b$  in imaginary time  $T$ . Feynman gave us three basic rules for calculating this transition amplitude:

- (i) the contribution of each path is determined by the action functional  $S[q]$ , and is proportional to  $e^{-S[q]}$ ,
- (ii) one needs to take into account the contributions of all paths consistent with the boundary conditions,
- (iii) contributions of different paths add up linearly, and the ensuing sum is called the path integral.

For a majority of physically interesting cases the action is of the form

$$S = \int_0^T dt \left( \frac{1}{2} \dot{q}^2 + V(q) \right). \quad (1)$$

Note that for simplicity we are working in units where  $\hbar$  and particle mass have been set to unity. The only problem in the outlined procedure is the enumeration of all possible paths. This is done by discretizing the time of propagation  $T$  into  $N$  equal time steps  $\varepsilon = T/N$ . The contribution of each piecewise linear trajectory is then determined by a discretized action of the form

$$S_N = \sum_{n=0}^{N-1} \varepsilon \left( \frac{(q_{n+1} - q_n)^2}{\varepsilon^2} + V(\bar{q}_n) \right), \quad (2)$$

where the potential is evaluated at  $\bar{q}_n = (q_n + q_{n+1})/2$ , corresponding to the mid-point or Weyl ordering prescription of the usual operator formalism. The final transition amplitude is given  $A(a, b; T)$  is given as  $N \rightarrow \infty$  limit of the discretized amplitude  $A_N(a, b; T)$

$$A(a, b; T) = (2\pi\varepsilon)^{-N/2} \int dq_1 \cdots dq_{N-1} e^{-S_N[q]}, \quad (3)$$

where  $q_n$  are the positions at discrete times  $n\varepsilon$ ,  $q_0 = a$ ,  $q_N = b$ , and  $(2\pi\varepsilon)^{-N/2}$  is the appropriate normalization factor.

The above discretized expression represents an  $N - 1$ -fold integral and is directly amenable to numerical treatment. In general, for large  $N$ , such expressions are nest handled using Monte Carlo techniques [13, 14, 15]. Before we proceed with this, however, let us note that the transition from continuum to discrete theory is far from unique. Said another way, there exists an infinity of discretized actions that, in the continuum limit, give the same transition amplitude. The naively discretized action given in equation (2) is just the simplest representative. While the choice of different discretized actions does not affect the final continuum amplitude, it may substantially affect the speed of convergence to that continuum limit. The naive action typically leads to  $1/N$  convergence. In a previous series of papers [6, 7, 8] we have constructed an explicit procedure for determining a hierarchy of equivalent discretized actions  $S^{(p)}$  which lead to improved convergence of generic amplitudes as  $1/N^p$ . Explicit expression for elements of the hierarchy has so far been obtained for  $p \leq 13$  and are available on our web site [9]. There are no practical impediments to going to higher values of  $p$ , the problem of determining the appropriate effective actions just gets algebraically more complex and requires the use of some package for symbolic calculus (e.g. MATHEMATICA).

Most often, however, one is interested in calculating not amplitudes but partition functions. The relation between the two is made apparent in the coordinate basis. As a result, the partition function can directly be written as a path integral. It is now an  $N \rightarrow \infty$  limit of discretized partition function

$$Z_N(T) = \int dq_0 A_N(q_0, q_0; T). \quad (4)$$

Note therefore that  $Z(T)$  is given as a limit of an  $N$ -fold integral over periodic piecewise linear trajectories. The partition function contains all thee information about the statistical properties of the system. In particular, we can use it to determine thermodynamic potentials, such as the free energy  $F = -\frac{1}{T} \ln Z$ . The free energy is also the ideal starting point for evaluating the energy spectrum of a given theory. From evaluating the partition function in the energy eigenbasis it follows that, in the large  $T$  limit, the free energy tends to the ground state energy  $E_0$ . Similarly, one can introduce auxiliary functions  $F^{(n)}$

$$F^{(n)} = -\frac{1}{T} \ln \left( Z - \sum_{i=0}^{n-1} d_i e^{-TE_i} \right). \quad (5)$$

Note that  $F^{(n)}$  tends to  $E_n$  in the large  $T$  limit. In this way, it is possible to use the free energy and the above auxiliary functions to numerically evaluate the low lying energy levels. The fact that  $F^{(n)}$  depends on all the lower energy levels and degeneracies results in an accumulation of numerical error as one looks at higher and higher energy levels. This is illustrated in figure 1 on the case of a particle moving in the quartic potential  $V(q) = q^2/2 + gq^4/24$ .

In addition to amplitudes and partition functions, path integrals are also used to evaluate expectation values of physical variables. The thermal expectation values of an observable  $\mathcal{O}$  is given by

$$\langle \mathcal{O} \rangle = \text{Tr} \left( e^{-T\hat{H}} \hat{\mathcal{O}} \right) / \text{Tr} e^{-T\hat{H}}. \quad (6)$$

This can be directly written in the form of path integrals as the  $N \rightarrow \infty$  limit of the discretized expectation values

$$\langle \mathcal{O} \rangle_N = (2\pi\epsilon Z_N(T))^{-N/2} \int dq_0 dq_1 \dots dq_{N-1} \mathcal{O}_N e^{-S_N[q]}. \quad (7)$$

In the above expression  $\mathcal{O}_N$  stands for the discretized estimator of the corresponding physical variable. One needs to be careful in how one chooses estimators. They are not just simple discretizations of the continuum expressions. In addition, the estimator must be consistently

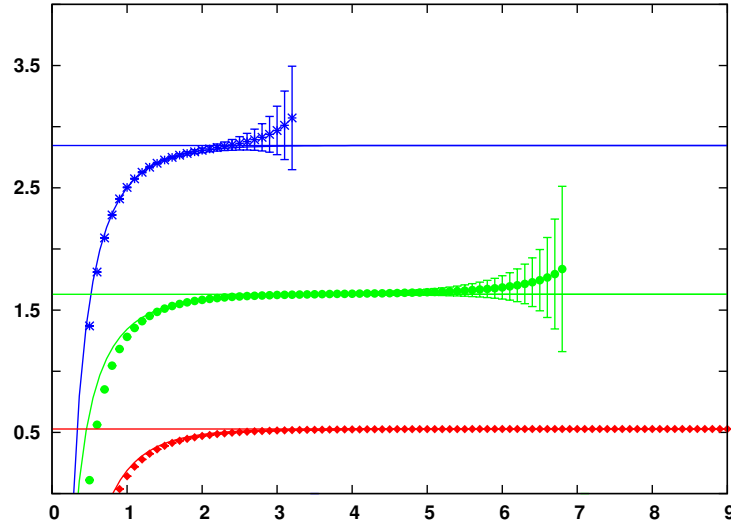


**Figure 1.** Metropolis implementation of PIMC algorithm for the calculation of low lying energy levels of a quartic potential. The plot shows the dependence of the free energy and the auxiliary function  $F^{(1)}$  and  $F^{(2)}$  as functions of  $T$ . The asymptotes are the corresponding energy levels  $E_0$ ,  $E_1$  and  $E_2$ . The parameters of the theory are  $g = 1$ ,  $N_{MC} = 10^7$ ,  $N = 256$ . The simulations were performed with  $p = 9$  level improved effective actions.

paired with the discretized effective action used in order for expectation values to profit from the same increase in convergence as transition amplitudes. As a particular example, let us look at energy estimators. The continuum expression  $\mathcal{E} = \dot{q}^2/2 + V(q)$  would naively be discretized as  $\mathcal{E}_N = (q_{n+1} - q_n)^2/2\varepsilon^2 + V(\bar{q}_n)$  for any  $n$ . An alternate, more symmetrical estimator would be  $\mathcal{E}_N = N^{-1} \sum [(q_{n+1} - q_n)^2/2\varepsilon^2 + V(\bar{q}_n)]$ , where we have made use of the fact that the energy is a conserved quantity. Both of these estimators lead to problems in the continuum limit and give divergent results. This is easily understood if we recall that for short times of propagation each theory is well approximated by a free particle (random walker), satisfying the diffusion relation  $\langle (q_{n+1} - q_n)^2 \rangle \sim \varepsilon$ . As a result, the above naive estimators have a dominant term diverging as  $1/\varepsilon$ . The source of the problem is in the  $T$ -dependence of the normalization of the above expectation value. A better way to derive the energy estimator is to use the relation

$$\langle \mathcal{E} \rangle = -\frac{\partial}{\partial T} \ln Z(T). \quad (8)$$

If we define the discretized energy expectation value to satisfy the same kind of relation with the discretized partition function, it follows that the consistent energy estimator is given by

$$\mathcal{E}_N = \frac{N}{2T} - \frac{1}{N} \sum_{n=0}^{N-1} \frac{(q_{n+1} - q_n)^2}{2\varepsilon^2} + \frac{1}{N} \sum_{n=0}^{N-1} V(\bar{q}_n). \quad (9)$$

The first two terms in the above estimator (9) both diverge in the continuum limit. However, taken together divergences cancel out and one obtains a finite result. Irrespective of this, the above (so called kinetic) estimator does not represent a good choice, as it contains within it the difference of two large numbers, making its standard deviation divergent and such numerical calculations nontractable. The standard way around this problem is to use the virial theorem

$$\left\langle \frac{\hat{p}^2}{2} \right\rangle = \left\langle \frac{1}{2} \hat{x} V'(\hat{x}) \right\rangle. \quad (10)$$

Using it we obtain what is called the virial energy estimator [16]

$$\mathcal{E}_N^{vir} = \frac{1}{2N} \sum_{n=0}^{N-1} \bar{q}_n V'(\bar{q}_n) + \frac{1}{N} \sum_{n=0}^{N-1} V(\bar{q}_n). \quad (11)$$

Each term of this estimator is well behaved and has finite continuum limit and finite standard deviation. It is important to note that the final form of the energy estimator used follows directly from the form of the discretized action. As a result, by changing the discretized action to  $S_N^{(p)}$  we immediately obtain the appropriate  $p$ -level generalization of the energy estimator. These generalized estimators have been derived and studied in [11], where it was shown that they have the correct improved  $1/N^p$  convergence.

### 3. Metropolis implementation

PIMC algorithms can be made more efficient either by getting better convergence to the continuum limit through the use of above mentioned hierarchy of discretized effective actions, or through better generation of relevant trajectories in the MC method. So far all the numerical verifications of improved  $1/N^p$  convergence have been implemented using a PIMC code in which paths were generated through a Levy construction. The Levy construction [15] samples paths with  $2^s$  time steps through a recursive halving, starting with some boundary conditions (representing the trajectory with  $2^0$  time steps). In the first step we generate one new node at the moment  $T/2$  and get a new trajectory, with  $2^1$  time steps. The procedure is then repeated recursively for each segment of the trajectory. The new nodes are generated using the free particle approximation: if the coordinates of the boundaries of the segment are  $R_1$  and  $R_2$ , and if the current time step is  $\varepsilon$ , the new node is selected from a Gaussian distribution centered at  $(R_1 + R_2)/2$  and with the standard deviation  $\sigma^2 = \varepsilon/2$ . This method, although powerful and simple, can sometimes require very long runs in order to give results with the desired precision. The generated paths are sampled using a free particle approximation, and for models with strong interactions this way of sampling is far from optimal.

In this section we investigate the analytically derived speedup of path integral calculations within the framework of a PIMC code based on the Metropolis algorithm [13, 14, 15], a path generating technique optimally suited for calculating expectation values. Metropolis rejection algorithm is a special type of Markov process, enabling sampling of arbitrary probability distributions. The desired probability distribution  $\pi(q)$  is obtained asymptotically, using a series of transformations (Metropolis moves) of the state of the system. The transformations are characterized by a transition matrix  $T(q \rightarrow q')$ , and the trial configuration  $q'$  is accepted according to the following probability

$$A(q \rightarrow q') = \min \left\{ 1, \frac{T(q' \rightarrow q)\pi(q')}{T(q \rightarrow q')\pi(q)} \right\}. \quad (12)$$

Metropolis moves in PIMC implementations are usually chosen to represent random local displacements (of given size) of individual nodes. The trajectories generated by the Metropolis technique are not independent, and we can have large correlations between consecutive paths. The correlations, however, depend on the physical quantity which is being calculated. The measure of such correlations is described through the correlation coefficient

$$c_k = \frac{\langle (O_0 - \langle O \rangle)(O_k - \langle O \rangle) \rangle}{\langle (O_0 - \langle O \rangle)^2 \rangle}, \quad (13)$$

where  $O_k$  is the expectation values of the physical quantity calculated using each  $k$ -th configuration. The correlation length is defined as a minimal value of  $k$  for which the correlation

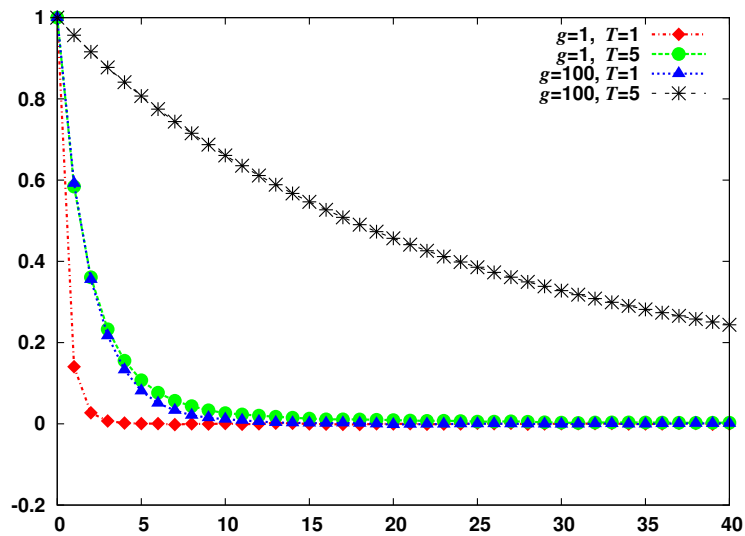


**Figure 2.** Correlation coefficient as a function of the correlation length  $k$  for the Metropolis implementation of the quartic anharmonic oscillator with  $g = 100$ ,  $T = 5$ ,  $N_{MC} = 10^6$ ,  $N = 1024$ . The simulations were performed with  $p = 9$  level improved effective actions.

coefficient  $c_k$  is sufficiently small (typically  $c_k < 0.1$ ). Figure 2 illustrates the usual behavior of correlation coefficients for an anharmonic oscillator with quartic coupling.

The described method for correlation reduction is sufficiently good for accurate estimation of expectation values of physical quantities [14]. However, the estimates of MC errors of numerical results (standard deviations) can still be affected by the remaining correlations. This is caused by the deviation of the distribution of MC samples from the Gaussian: the numerically obtained

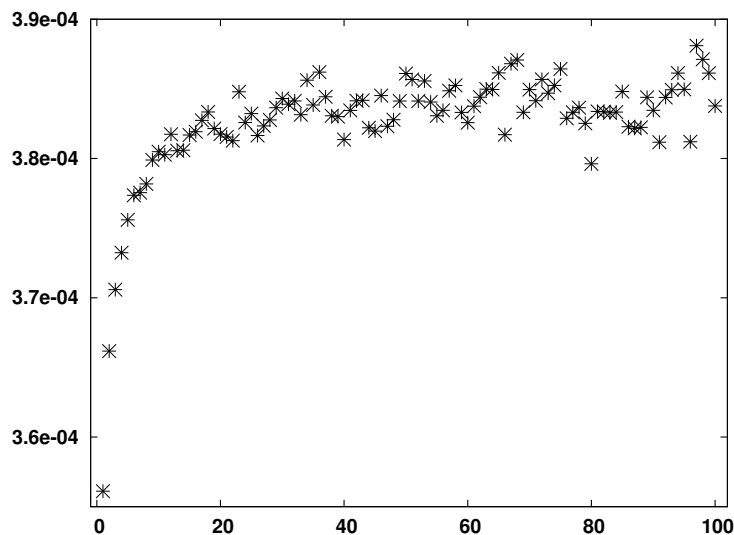


**Figure 3.** Standard deviation for Metropolis algorithm as a function of block size for a quartic anharmonic oscillator with  $g = 1$ ,  $T = 5$ ,  $N_{MC} = 10^6$ ,  $N = 1024$ . The simulations were performed with  $p = 5$  level improved effective actions.

distribution can be skewed, or have non-zero kurtosis, or both. This is dealt with by dividing the generated set of MC samples into blocks of a chosen size, and then by using just the averages over blocks as a new MC sample. By increasing the block size so that the skew and kurtosis of the obtained new distribution can be neglected, we may correctly estimate the value of MC errors. Note that this procedure does not affect the estimate for the expectation value. Figure 3 gives the dependence of the estimated standard deviation on the block size for a Metropolis implementation of a PIMC calculation of the energy expectation value for a quartic anharmonic oscillator. From this figure we see that by using small enough block sizes the MC error can be substantially underestimated.

In usual implementation of the Metropolis algorithm, the probability distribution that is to be sampled is given by the exponential of the naively discretized action

$$\pi_N[q(t)] \sim e^{-S_N[q(t)]}. \quad (14)$$

In our implementation, the naively discretized action is replaced by one of the improved effective actions in the hierarchy  $S_N^{(p)}$ , trial paths were sampled using Levy construction, and acceptance of new trajectories was done according to the Metropolis rule (12). Figure 4 illustrates the typical behavior that one uncovers. As expected, the implementation of the Metropolis algorithm does not interfere with the increased convergence obtained through the use of higher level effective actions. Indeed, by using  $p$  level effective actions we again find that the numerical results of a new PIMC code display improved convergence of the form  $1/N^p$ . In fact, far from interfering negatively, the use of higher level effective actions brings about an improved efficiency of the Metropolis algorithm per se through the generation of more relevant trajectories. This is seen through the reduction of the variance of numerical results. A more detailed investigations of this would be reported elsewhere. In particular, there we will focus on effective actions with  $p \geq 10$  and take into consideration the effects of the increased algebraic complexity of these expressions on the computation time. For levels  $p \leq 10$  numerical investigations have shown that this accumulated complexity does not have significant effects on the computation time.

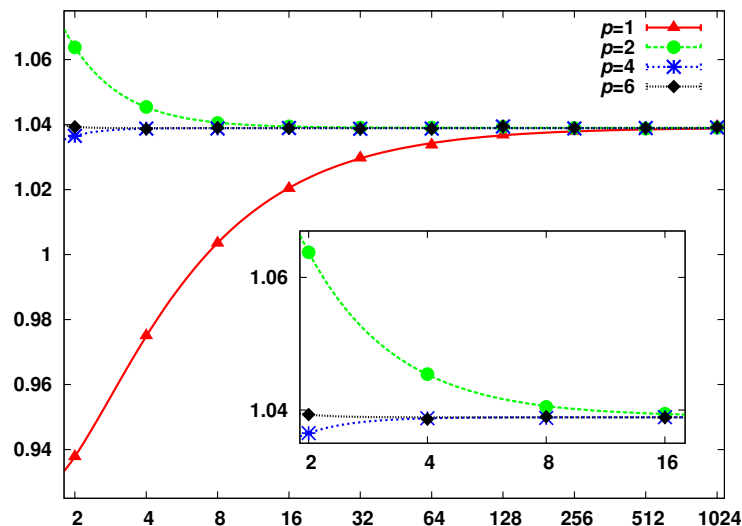


**Figure 4.** Metropolis implementation of the energy expectation value as a function of the discretization coarseness  $N$  for the quartic anharmonic oscillator with  $g = 1$ ,  $T = 1$ ,  $N_{MC} = 10^7$ . The simulations were performed with level  $p = 1, 2, 3, 4$  improved effective actions.

#### 4. Conclusions

We have given a brief overview of the current state of the research effort behind the construction of more efficient PIMC algorithms leading to improved convergence of path integral calculations. In particular, we have outlined how the developed hierarchy of effective actions may be used to calculate transition amplitudes, partition functions and energy spectra. Particular emphasis was given to the calculation of expectation values. We outlined a scheme for the derivation of estimators consistent with the hierarchy of effective actions, i.e. leading to the same increase in convergence. The second part of the paper centers around a new PIMC code encompassing the effective actions and derived estimators, implemented using the Metropolis algorithm. The new PIMC code displays the same  $1/N^p$  increase in convergence. Moreover, the use of higher level effective actions brings about an improved efficiency of the Metropolis algorithm through the generation of more relevant trajectories. In the future work we will focus on the detailed investigation of the increase in efficiency of the Metropolis algorithm brought about by the use of higher level effective actions.

#### Acknowledgments

This work was supported in part by the Ministry of Science of the Republic of Serbia, under project No. OI141035. D. S. also acknowledges support from EU Centre of Excellence grant CX-CMCS. The presented numerical results were obtained on the AEGIS e-Infrastructure whose operation is supported in part by FP6 projects EGEE-II and SEE-GRID-2.

#### References

- [1] Feynman R P 1948 *Rev. Mod. Phys.* **20** 367
- [2] Feynman R P and Hibbs A R 1965 *Quantum Mechanics and Path Integrals* (New York: McGraw-Hill)
- [3] Feynman R P 1972 *Statistical Mechanics* (New York: W. A. Benjamin)
- [4] Steiner F and Grosche C 1997 *A Table of Feynman Path Integrals* (New York: Springer)
- [5] Kleinert H 2004 *Path Integrals in Quantum Mechanics, Statistics, Polymer Physics, and Financial Markets* 3rd edition (Singapore: World Scientific)
- [6] Bogojević A, Balaž A and Belić A 2005 *Phys. Rev. Lett.* **94** 180403
- [7] Bogojević A, Balaž A and Belić A 2005 *Phys. Rev. B* **72** 064302
- [8] Bogojević A, Balaž A and Belić A 2005 *Phys. Lett. A* **344** 84
- [9] <http://scl.phy.bg.ac.yu/speedup/>
- [10] Stojiljković D, Bogojević A and Balaž A 2006 *Phys. Lett A* **360** 217
- [11] Grujić J, Bogojević A and Balaž A 2006 *Phys. Lett A* **360** 205
- [12] Balaž A, Vidanović I and Bogojević A 2007 Accelerated path integral calculations for many-body systems *QTS-5 Conference* (Valladolid, Spain), to appear in *J. Phys. A*
- [13] Metropolis N, Rosenbluth A W, Rosenbluth M N, Teller A H and Teller E 1953 *J. Chem. Phys.* **21** 1087
- [14] Kalos M H and Whitlock P A 1986 *Monte Carlo Methods* (New York: John Wiley and Sons)
- [15] Ceperley D M 1995 *Rev. Mod. Phys.* **67** 279
- [16] Janke W and Sauer T 1997 *J. Chem. Phys.* **107** 5821

## GRID APPROACH TO PATH INTEGRAL MONTE CARLO CALCULATIONS

Danica Stojiljković, Antun Balaž, Aleksandar Bogojević, Aleksandar Belić  
*Scientific Computing Laboratory, Institute of Physics, Belgrade, Serbia*

**Abstract** – Approach taken for the gridification of the developed Monte Carlo code for calculation of path integrals is described. Brief introduction to path integrals and Grids is given, and details on the implementation of SPEEDUP in the Grid environment are described. The numerical results obtained by the gridified version of the application are shortly presented, demonstrating its usefulness in the research in physics and related areas.

## 1. INTRODUCTION TO PATH INTEGRALS

Feynman functional formalism is known to be the most concise and flexible formulation of quantum theories [1, 2]. It enabled us to easily extend quantization procedure to more complicated systems, from multidimensional many particle systems, to theory of fields, strings, etc. Many different areas of physics, such as high-energy physics, condensed matter, statistical and quantum physics, but also chemistry, material science, mathematics and even modern finance are treated in the same manner, using the same mathematical tool. This initiated an exchange of key ideas between diverse research areas. Its general mathematical framework gives simple and natural setup for using and applying symmetries, deriving various approximation techniques and non-perturbative results and making connections between different theories.

Although the number of exactly solvable models was not enlarged by the introduction of functional formalism, the analytical and numerical approaches to path integrals gave us possibility to treat large number of systems that were not previously accessible. Path integral is the main mathematical object in the functional formalism and it represents an infinite limit of multiple integrals. Most often use of approach for calculation of path integrals is Monte Carlo (MC) method [3], which is defined in quite general terms as any algorithm that uses random numbers for solving numerical problems. Advance gained by using MC simulations for calculating multiple integrals is that the standard deviation of results vanishes as  $1/\sqrt{N_{MC}}$  regardless on integral dimensionality.

$N_{MC}$  here represents the number of Monte Carlo samples and it is clear that by increasing this number we can improve the precision of the results as desired.

As we already said, path integral is defined as an  $N \rightarrow \infty$  limit of an  $N$ -fold integral. Since we can numerically calculate only finite number of integrals, here in contrast to calculating ordinary  $N$ -fold integrals an additional source of error is present. Naive  $N$ -discretized value of the path integral differs from its continuum limit by a term of the order  $1/N$ . A recent series of papers [4, 5, 6, and 7] has focused on the dynamical implications of stochastic self-similarity by studying the relation between path integral discretizations of different coarseness. This has resulted in a systematic analytical construction of a hierarchy of  $N$ -fold discretized effective actions  $S_N^{(p)}$  labeled by an integer number  $p$  and built up from the naively discretized action in the mid-point

ordering prescription (corresponding to  $p=1$ ). The level  $p$  effective actions lead to discretized transition amplitudes expressed through path integrals and expectation values differing from the continuum limit by a term of the order  $1/N^p$ . The MC code implementing this approach can be found at [8].

## 2. INTRODUCTION TO GRIDS

The above described effective action approach confirms to the common experience that any analytical knowledge of the considered system can be translated into vast speedups in the convergence of numerical approaches used to tackle those complex systems. However, path integrals require substantial computing resources, even in such dramatically improved algorithms. In MC approach this means that we still need to use large numbers of MC samples  $N_{MC}$ . This is usually not possible on a single parallel cluster in one research institute, or is very inefficient to wait until enough resources are available in ones home institute. Therefore, the use of computing resources distributed across different institutions collaborating on joint RRD projects is the most efficient way of obtaining considerable computing resources on demand. In fact, this way each institution involved can obtain when needed computing resources much greater than it possesses, while other institutions can use its resources when idle. Resource sharing can be organized on reciprocity principle, on a commercial basis, or on some other suitable arrangement.

While the Internet provides a framework service for sharing the information, a framework for sharing available computing and data resources is known as Grid. It consists of a number of clusters that provides computing power and storage resources, and that are connected and enabled to interoperate through a series of Grid services. Here we will shortly describe Grid established by the EGEE-II [9] and SEE-GRID-2 [10] projects, as well as by the AEGIS (Academic and Educational Grid Initiative of Serbia [11]). The services and resources offered to interested users represent an ideal framework in which MC simulations can be executed, taking advantage of any idle resources for improving statistics of path integral calculations. Basic Grid operations offered to a user are job submission management, file transfer, database access, database management and monitoring and indexing system information. To allow these operations, core services Grid-nodes collect information published by the local information systems on each cluster. Grid user does not need to know where his/her job is executed, or where the data is stored. The user does not need to be familiar with the architecture and organization of Grid services. He or she just needs to log on to a node with installed user interface (UI) software, describe job requirements in a simple file and accompany it with necessary programs and input files, and submit it. Later, the user can monitor the job and retrieve output files when the



job is done. When job is submitted, unique job ID is generated which must be saved by the user in order to retrieve output or monitor job status at any time. Grid services allow UI to find available clusters that fulfill job requirements specified by user, and distribute it to one of those clusters. They monitor status of a job, and collect output files after the job is done, so the user could retrieve it later. If large amounts of data are used or produced by a program, data can be placed on a storage element. That way we can avoid unnecessary transfers of data and reduce possibility of problems that can occur due to "overloaded" network connections of Grid nodes.

In order to ensure secure operations on the Grid, it was necessary to introduce authentication and authorization mechanisms. Authentication of users and services is done through digital certificates based on Public Key Infrastructure (PKI). The certificates are issued through a network and national and regional certification authorities. The authorization for the use of resources and other operations is done through Virtual Organizations (VO). One needs to become a member of some VO which represents group of people working together on the same activity/project. One can be a member of more than one VO. What can one do on a Grid is determined by his/her VO privileges meaning that one can access just the resources on clusters supporting his/her VO, and with the fair-share of those resources specified by the local policies. Here the user does not need to adjust his/her behavior according to those policies, but rather the policies will be automatically implemented and imposed by Grid services.

At the time of submission of a job and during its execution, one needs to have valid credentials, *mini-certificate* (proxy) which has no password, propagates through Grid and has a significantly limited life time, specified at creation time. If job is not finished by the proxy expiration time, it would be aborted, unless the proxy is renewed. This should be kept in mind when running long jobs.

### 3. GRID APPROACH TO MC SIMULATIONS

Running one or small number of long running jobs on Grid would not be its optimal use. There is a large number of processors available and if we want to get our results faster it is necessary to divide all computational tasks to a large number of shorter programs which can be executed at the same time. This can always be done for MC simulations, but for some types of problems it may not be possible. There are three ways in which we can perform this division of tasks: parallelization, gridification, or combination of both.

Parallel program on a usual PC-cluster consists of cooperative processes, each with its own memory, which can exchange data. Communication and distribution of tasks to different processors is implemented in a program code by using libraries of functions and macros provided by implementation of e.g. Message Passing Interface (MPI). Parallelization of MC simulations is trivial. Each node is processing same number of MC samples independently, and after processing is done master node collects the raw data, performs final calculations and saves the results in a file. For running parallel program on Grid site it must have support for MPI, which is not standard configuration..

Gridification of program assumes separation of calculation tasks into a number of shorter independent programs. In MC simulations this division is performed naturally. Instead of processing, for example,  $10^9$  samples on a single node, task can be divided to 1000 nodes, each processing just  $10^6$  samples. Each process is saving raw data and when all data is collected, final processing can be done via script or some other results processing program. This is usually performed on desktop computer or user interface. This approach is based on independence of individual programs. If there is a malfunction on one node, we loose only a small amount of data, while in parallel approach this leads to breaking of the whole program and loss of all data. In addition, we can submit as many jobs as needed for statistics requested, thus replacing failed jobs with the new ones seamlessly. Separate programs can run on several sites, at different times, which enables us to divide the task into thousands of smaller programs, while parallel approach demands that all the nodes are available on one site at the same time.

Before submitting a job to the Grid it must be specified in a file written in the Job Description Language (JDL file). This file contains specifications on the type of job, executable file and its arguments, location of input files required by the job (input sandbox), names of output files that user wants to retrieve (output sandbox), many optional requirements for site properties like number of working nodes, MPI support, physical closeness to some Storage Element, specific site name, maximal allowed expected site response time for this job, etc. Executable file can be a compiled program or a script that contains sequence of commands that needs to be executed on a worker node (WN). That way code can be compiled on the worker node itself, at the execution time user can manipulate data directly from WN, pack or unpack files, transfer files from and to storage elements and execute any command according to his/her VO privileges.

There are few different middleware systems for managing jobs on grid such as gLite, LCG, Globus, UNICORE, etc. The Grids established by AEGIS, EGEE-II and SEE-GRID-2 are based on LCG [12] and gLite [13], but concept on the user side is basically the same. User submits job from command line of user interface and gets unique job ID. Sandbox and JDL files are sent to a series of Grid services which then search for available resources that meet job requirements. The job is then being dispatched to one of those sites and scheduled in the local site's queue. After job is done, files defined to be in the output sandbox are sent back to grid services (the actual component used is the Workload Management, WMS) which are waiting for the user to retrieve the output. This is also done from the command line of the user interface. User can also monitor status of submitted job at any time after submission.

For submission, monitoring and retrieving the output of large number of MC simulations for calculation of path integrals, we developed a number of scripts. Scripts for job submission use the concept of a template JDL file (TJDL) for creating a large number of JDL files which differs only in few program arguments. Jobs are then being submitted one by one, and all job IDs are stored in a file. Scripts for monitoring of job statuses and retrieving data or canceling the jobs are using this file. The scripts can be downloaded from [8].

This concept can also be used for other applications, and scripts need to be adapted for their use for particular problems. Submission of hundreds of jobs can take several hours if they are submitted one by one. New component of grid services - WMProxy in gLite - is developed recently to handle a large number of job submissions efficiently. New type of job - parametric job - is introduced. It represents a set of very similar jobs, differing only in the values of parameters, defined by some of JDL attributes. With this type of jobs, user just needs to send one JDL file with the parameter changing range specified. This new type of job then creates final JDL files and submits them to Grid on behalf of the user. Another advantage offered is that jobs can share input sandboxes, so when many single jobs are using the same input files, those can be transferred only once from UI. Disadvantage of this type of job is that, for now, there is only one parameter that can be changed.

#### 4. PRELIMINARY RESULTS AND PERFORMANCE

We are using path integrals for the calculation of quantum mechanics probability amplitudes. Here we will present some numerical results obtained using the gridified version of the SPEEDUP code [8], using the scripts described in the previous section. The evolution of a physical system during the time  $T$  can be expressed as a path integral of the quantity  $e^{-S}$ , where  $S$  is the action of the system. The integration is made over all possible trajectories of the system (thus making the infinite number of ordinary integrals necessary), and the action reduces to the energy of the system in the Euclidean time approach.

Definition of path integrals makes it necessary to make transition from continuum to the discretized theory. Time of the evolution is divided in  $N$  equal time steps, and instead of using continuum value of the action  $S$  for each trajectory, we are using its discretized value  $S_N$ . Actions  $S_N$  are not uniquely defined, and the value of the discretized path integral can approach continuum limit in different ways. Although the continuum limit of different discretizations will remain the same, the convergence properties can differ.

We recently developed a series of effective actions  $S_N^{(p)}$  that speeds up the convergence [4, 5]. They have been applied here for calculation of quantum mechanics transition amplitudes, energy levels [6] and expectation values [7], and statistical partition functions. It is analytically shown in those papers that transition amplitudes approach their continuum values as  $1/N^p$ . Expressions for  $S_N^{(p)}$  are derived for  $p$  up to 10, but the developed procedure enables us to find these actions for arbitrary value of  $p$ . This allows us to use smaller values of  $N$  for evaluation of path integrals and we gain speedup of several orders of magnitude. But there is a price to be paid. Numerical complexities of expressions for effective actions have exponential growth with  $p$ , and implementation of this analytical speedup will increase the required computational time. This growth is shown in Figure 1 for  $p$  up to 9. We can see that for  $p=9$  the simulation is about 10 times slower, which in fact is small price to pay for gain in precision of nine orders of magnitude.

In statistical mechanics path integrals can be applied for calculating values of partition function and thermal free energy. MC simulations for calculations of the free energy numerically confirmed that the use of effective actions leads to the same speed up in convergence [6]. This is illustrated in

Figure 2 where dependence of discretized free energy values (calculated using the corresponding discretized effective actions) on the number of discretization points  $N$  is shown for levels  $p$  from 1 to 5. We see that for  $p=5$  discretized values differ from their continuum limit by a term which is smaller than the stochastic error introduced by MC method. In order to further gain something from the speedup offered by higher  $p$  levels we need to reduce stochastic error by increasing number of MC samples. This is why we need to use distributed computing resources that allow large statistics to be obtained in a short time periods.

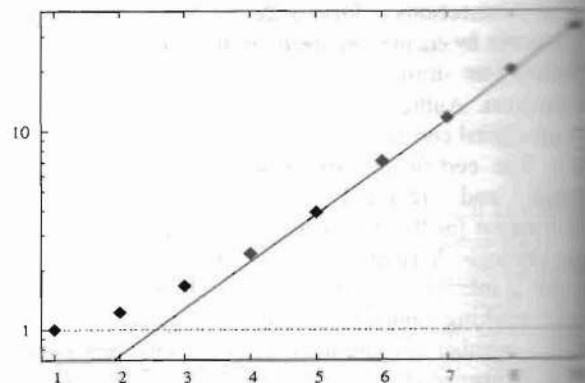


Fig. 1: Relative increase in computation time that comes about from the increased complexity of expression for higher  $p$  levels effective action

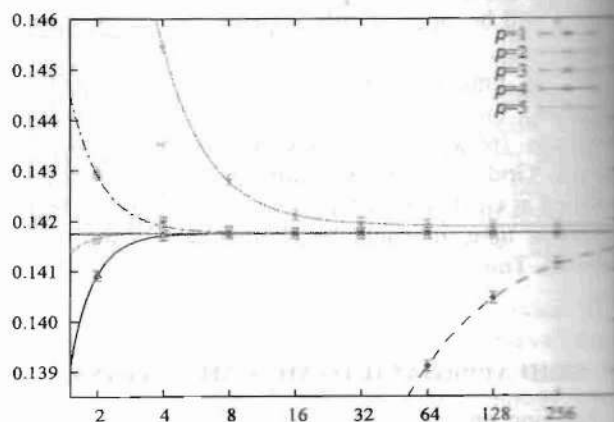


Fig. 2: The dependence of free energy  $F_N^{(p)}$  on  $N$  for different levels of  $p$ . The plot is for the anharmonic oscillator with quartic coupling  $g=1$ , inverse temperature  $\beta=1$  and  $N_{MC}=10^7$  MC samples. The same kind of behavior is seen for other parameters, as well as for other potentials.

Free energy of the physical system can be expressed in terms of its energy levels

$$e^{-\beta F(N)} = \sum_{n=0}^{\infty} e^{-\beta E_n}, \quad (1)$$

where  $\beta$  is inverse temperature. As we can see, the free energy is completely determined by system's energy spectrum and vice-versa. By calculating free energy on a set of temperatures, it is possible to extract several lowest energy levels. Calculations are conducted for several different models. In case of models that are exactly solvable, our results agree with exact values, but our approach provides means for calculation of spectra for models that can not be solved analytically, and are not in the perturbative regime.

i.e. which can not be treated by the usual methods. As an illustration we give energy levels of anharmonic oscillator with the potential of the form:

$$V(q) = \frac{1}{2}q^2 + \frac{g}{4!}q^4 \quad (2)$$

Several values of coupling constant  $g$  are considered, and results are given in Table 1. Note that the case  $g=0$  is exactly solvable, while  $g=1000$  lies deep in non-perturbative domain.

Table 1: Low lying energy levels of the anharmonic oscillator with quartic coupling  $g$ , calculated using  $N=256$ ,  $p=9$ , and  $N_{MC}=10^7$

$g$	$E_0$	$E_1$	$E_2$	$E_3$
0	0.49993(2)	1.502(2)	2.48(6)	3.6(5)
0.1	0.50301(2)	1.516(1)	2.54(5)	3.5(2)
1	0.52765(2)	1.6295(8)	2.85(2)	3.98(7)
10	0.67335(2)	2.230(1)	4.12(2)	
100	1.16247(4)	4.058(6)		
1000	2.3578(2)			

## 5. CONCLUSIONS

We presented the Grid approach that can be applied for large scale computations if some generic Monte Carlo simulations are used. On the important SPEEDUP application we demonstrated how an MC application can be gridified and efficiently deployed in production Grid environments, such as e-Infrastructure offered by the EGEE-II of SEE-GRID-2 projects, or the national AEGIS infrastructure. The usefulness of this approach is demonstrated through solving numerically complex problem of energy spectra calculation of different quantum mechanical systems.

## 6. ACKNOWLEDGMENTS

This work was supported in part by the Ministry of Science and Environmental Protection of the Republic of Serbia under project no. OI141035. D. Stojiljković has received support under EC FP6 project CX-CMCS (INCO-026343). The presented numerical results were obtained on the AEGIS GRID e-infrastructure whose operation is supported in part by EC FP6 projects EEEG-II (INFSO-RI-031688) and SEE-GRID-2 (INFSO-RI-031775).

## 7. REFERENCES

- [1] R.P. Feynman and A.R. Hibbs, Quantum mechanics and Path Integrals, New York: McGraw-Hill, 1972.
- [2] R. P. Feynman, Statistical Mechanics, New York: Benjamin, 1972
- [3] M. H. Kalos and P. A. Whitlock, Monte Carlo Methods, vol. 1: Basics, New York: John Wiley and Sons, 1986
- [4] A. Bogojević, A. Balaž and A. Belić, Phys. Rev. Lett. 94 (2005) 180403
- [5] A. Bogojević, A. Balaž and A. Belić, Phys. Rev. B 72 (2005) 064302
- [6] D. Stojiljković, A. Bogojević, A. Balaž, Efficient Calculation of Energy Spectra Using Path Integrals, Phys. Lett. A (2006), In press, doi:10.1016/j.physleta.2006.08.035
- [7] J. Grujić, A. Bogojević, A. Balaž, Energy Estimators and Calculation of Energy Expectation Values in the Path Integral Formalism, Phys. Lett. A (2006), In press, doi:10.1016/j.physleta.2006.08.044
- [8] <http://scl.phy.bg.ac.yu/speedup>
- [9] <http://www.eu-egee.org>
- [10] <http://www.see-grid.eu>
- [11] <http://aegis.phy.bg.ac.yu>
- [12] <http://lcg.web.cern.ch/LCG>
- [13] <http://glite.web.cern.ch>

**Садржај** – Описан је приступ гридификацији развијеног Монте Карло алгоритма за рачунање функционалних интеграла. Дат је кратак увод у функционалне интеграле и основни концепт Грид-а, и описани су детаљи имплементације "SPEEDUP" апликације у Грид окружење. Представљени су нумерички резултати добијени помоћу гридификоване верзије апликације који илуструју њихову корисност за истраживања у физици и сродним областима.

## ГРИД ПРИСТУП МОНТЕ КАРЛО РАЧУНАЊУ ФУНКЦИОНАЛНИХ ИНТЕГРАЛА

Даница Стојиљковић, Антун Балаж,  
Александар Богојевић, Александар Белић

UNIVERSITY OF BELGRADE  
FACULTY OF PHYSICS

Danica Stojiljković

**KINETICS AND MORPHOLOGY OF PARTICLE  
DEPOSITION AT HETEROGENEOUS SURFACES**

Doctoral Dissertation

Belgrade, 2022

УНИВЕРЗИТЕТ У БЕОГРАДУ  
ФИЗИЧКИ ФАКУЛТЕТ

Даница Стојиљковић

**КИНЕТИКА И МОРФОЛОГИЈА ДЕПОЗИЦИЈЕ  
ЧЕСТИЦА НА ХЕТЕРОГЕНИМ ПОВРШИНАМА**

докторска дисертација

Београд, 2022. година

---

# Thesis Defense Committee

Thesis advisor:

**Dr. Slobodan Vrhovac**  
Research Professor  
Institute of Physics Belgrade  
University of Belgrade

Committee member:

**Dr. Julija Šćepanović**  
Assistant Research Professor  
Institute of Physics Belgrade  
University of Belgrade

Committee member:

**Prof. Dr. Sunčica Elezović-Hadžić**  
Professor  
Faculty of Physics  
University of Belgrade

Committee member:

**Prof. Dr. Đorđe Spasojević**  
Professor  
Faculty of Physics  
University of Belgrade



---

# Acknowledgements

This thesis was completed under the mentorship of Dr. Slobodan Vrhovac, Research Professor, at the Laboratory for Statistical Physics of Complex Systems, National Center of Excellence for the Study of Complex Systems, at the Institute of Physics Belgrade, University of Belgrade. The presented research was supported by the Ministry of Education, Science, and Technological Development of the Republic of Serbia under projects ON171017 and III43007.

First, I would like to thank Dr. Slobodan Vrhovac for allowing me to be a part of his team and for guiding me through the complexity of seemingly simple models. I am grateful for the shown trust, generous help, and tremendous patience and understanding. I am thankful to our associates, Dr. Nenad Švrakić for introducing us to the subject and for fruitful discussions, and to Dr. Julija Šćepanović for many constructive conversations and immense support.

I wish to express my eternal gratitude to Dr. Antun Balaž for his continuous support over the years, for being available even when he's busy, for his professional and personal guidance, and for pushing me to do better, work harder and be wiser. He is the most remarkable boss, colleague, and friend, who has introduced me to the world of theoretical physics and (numerical) research.

Many thanks to Dr. Aleksandar Bogojević and Dr. Aleksandar Belić for accepting me to be a member of the first generation of the SCL family, giving me the chance to work at CERN, the most exciting place in the world for any physicist, and for broadening my professional interests beyond the frame of science. Many thanks to all of my colleagues at IPB, former and current, especially to numerous office-mates, for creating an enjoyable working atmosphere and for interesting everyday chats on a wide range of subjects, from daily weather to the meaning of it all.

And finally, and most importantly, my most sincere gratefulness goes out to my family for all of their love and support. To my mother who always encouraged me to be persistent and to fulfil my potential. To my father who taught me how to always look on the bright side and enjoy small moments. To my brother for never-ending discussions on every subject one could think of. To my husband for standing by my side. To my two lovely sons, who motivated me to re-learn how to play and investigate. And to many others...





---

# Abstract

Monolayer and multilayer thin film formation on solid or liquid surfaces is a growing multidisciplinary area of research of great interest for new and emerging technologies in photonics, microelectronics, nanotechnology, plasmonics, biosensors, bio-medical devices, etc. Adsorption and deposition (irreversible adsorption) of colloids, proteins, and other bio-materials on solid/liquid interfaces are of large significance for many practical and natural processes such as filtration, paper-making, chromatography, separation of proteins, viruses, bacteria, pathological cells, immunological assays, thrombosis, biofouling, biomineralization, etc. Controlled adsorption of colloid particles on sites of nanometric scale can also be exploited for direct visualization of surface features.

The Random Sequential Adsorption (RSA) model is one of the basic models used to describe the irreversible formation of monolayer deposits of microscopic and mesoscopic particles. Inter-particle interactions are approximated classically with the hard-core exclusion model, which means that overlaps between the particles are not allowed. Particles can only adsorb if they are in direct contact with the substrate. This feature ensures a monolayer deposition. Irreversible adsorption means that the adsorbed particle stays permanently fixed to the substrate and diffusion or desorption processes are not allowed. Previously adsorbed particles block a certain area of the substrate for new adsorptions and consequently, the system becomes jammed. Heterogeneities of a substrate impose further limitations on the positions of adsorbed particles. Our aim is to quantify structural changes in the jammed state that are introduced by different patterns of substrate heterogeneities. We use the RSA approach to analyze the deposition of identical spherical particles of a fixed radius on non-uniform flat surfaces covered by rectangular cells. Two different types of patterns are of interest: randomly positioned cells and square lattice centred cells.

In the first part of the dissertation, the configuration of the cells (heterogeneities) was produced by performing RSA simulations to a prescribed coverage fraction  $\theta_0^{(\text{cell})}$ . Adsorption was assumed to occur if the particle (projected) centre lies within a rectangular cell area, i.e., if the sphere touches one of the cells. The jammed-state properties of the model were studied for different values of the cell size  $\alpha$  (comparable with the adsorbing particle size) and density  $\theta_0^{(\text{cell})}$ . Numerical simulations were carried out to investigate adsorption kinetics, jamming coverage, and structure of coverings. Structural properties of the jammed-state coverings were analyzed in terms of the radial distribution function  $g(r)$  and distribution of the Delaunay ‘free’ volumes  $P(v)$ . It was demonstrated that adsorption kinetics and the jamming coverage decreased significantly, at a fixed density  $\theta_0^{(\text{cell})}$ , when the cell size  $\alpha$  increased. The predictions following our calculation suggest that the porosity (pore volumes) of the deposited monolayer can be controlled by the size and shape of landing cells, and by the anisotropy of the cell deposition procedure.

---

The second direction of research in this thesis analyses the adsorption of spherical particles of a fixed diameter on nonuniform surfaces covered by square cells arranged in a square lattice pattern. To characterize such a pattern two dimensionless parameters are used: the cell size  $\alpha$  and the cell-cell separation  $\beta$ , measured in terms of the particle diameter  $d_0$ . We focus on the kinetics of the deposition process in the case when no more than a single disk can be placed onto any square cell ( $\alpha < 1/\sqrt{2} \approx 0.707$ ). We find that the asymptotic approach of the coverage fraction  $\theta(t)$  to the jamming limit  $\theta_J$  is algebraic if the parameters  $\alpha$  and  $\beta$  satisfy the simple condition,  $\beta + \alpha/2 < 1$ . If this condition is not satisfied, the late time kinetics of the deposition process is not consistent with the power-law behaviour. However, if the geometry of the pattern approaches “noninteracting conditions” ( $\beta > 1$ ), when adsorption on each cell can be decoupled, the approach of the coverage fraction  $\theta(t)$  to  $\theta_J$  becomes closer to the exponential law. Consequently, changing the pattern parameters in the present model allows for interpolating the deposition kinetics between the continuum limit and the lattice-like behaviour. Structural properties of the jammed-state coverings are studied in terms of the radial distribution function  $g(r)$  and the spatial distribution of particles inside the cell. Various, non-trivial spatial distributions are observed depending on the geometry parameters of the pattern.

**Keywords:** random sequential adsorption, heterogeneous substrate, pair correlation function, Delaunay ‘free’ volumes

**Research field:** Physics

**Research subfield:** Statistical physics

**UDC number:** 539.233, 536.12

---

# Сажетак

Формирање једнослојних и вишеслојних танких филмова на чврстим и течним површинама је растућа мултидисциплинарна област истраживања од великог интереса у фотоници, микроелектроници, нанотехнологијама, плазмоници, за биосензоре, биомедицинске уређаје, итд. Адсорпција и депозиција (иреверзибилна адсорпција) колоида, протеина и других биоматеријала на чврстим/течним површинама су од велике важности за многе практичне и природне процесе као што су филтрација, производња папира, хроматографија, сепарација протеина, вируса, бактерија и патолошких ћелија, имунолошки тестови, тромбоза, биоминерализација, итд. Контролисана адсорпција колоидних честица на структурама на нанометарској скали се такође могу искористити за директну визуализацију структурних карактеристика.

Модел случајне секвенцијалне адсорпције (RSA модел) је један од основних модела за описивање формирања једнослојних депозита мезоскопских честица. Међучестична интеракција је апроксимирана класичним моделом крутих тела, што значи да је забрањено међусобно преклапање честица. Честице се могу адсорбовати једино ако су у директном контакту са супстратом. Ова особина доводи до формирања једнослојних депозита. Појам иреверзибилна адсорпција поразумева да су адсорбоване честице трајно причвршћене за подлогу, а процеси дифузије или десорпције су забрањени. Претходно адсорбоване честице блокирају одређени део подлоге за адсорпцију нових честица што доводи до загушења система. Нехомогеност супстрата намеће додатна ограничења на позиције адсорбованих честица. Наш циљ је да квантификујемо структурне промене загушеног стања настале услед различитих хетерогених образаца на адсорбујућој подлози. Користимо RSA приступ за анализу депозиције идентичних сферних честица на нехомогене равне површине покривене правоугаоним ћелијама. Од интереса су два различита типа распореда: случајно распоређене ћелије и ћелије распоређене у чворовима квадратне решетке.

У првом делу истраживања у оквиру ове тезе, конфигурација ћелија се формира помоћу RSA симулације док се не постигне жељена покривеност супстрата  $\theta_0^{(\text{cell})}$ . До адсорпције долази ако (пројектовани) центар честице лежи унутар правоугаоне ћелије, тј. ако сферна честица додирује неку од ћелија. Особине загушеног стања су изучаване за различите вредности величине ћелија  $\alpha$  (упоредивих са величином честице) и различите густине ћелија  $\theta_0^{(\text{cell})}$ . Извршене су нумеричке симулације како би истражили кинетику адсорпције, покривеност у загушењу и структуру депозита. Структурне особине загушеног стања анализирани су помоћу парне корелационе функције  $g(r)$  и дистрибуције Делонејевих слободних површина. Резултати наших симулација сугеришу да се контрола порозности једнослојног депозита може постићи подешавањем величине, облика и оријентације прихватних ћелија.

---

Други правац истраживања у тези је анализа адсорпције сферних честица фиксног пречника на хетерогеним површинама прекривеним квадратним ћелијама распоређеним у чворове квадратне решетке. За карактеризацију овог шаблона користимо два бездимензиона параметра: величину квадратне ћелије  $\alpha$  и размак између две суседне ћелије  $\beta$ . За јединицу мере користимо пречник адсорбујућих ћелија  $d_0$ . У фокусу истраживања је кинетика процеса депозиције у случају када било која прихватна ћелија може да адсорбује највише једну честицу ( $\alpha < \sqrt{2}/2$ ). Покривеност  $\theta(t)$  асимптотски тежи граничној вредности  $\theta_J$  по алгебарском закону ако параметри  $\alpha$  и  $\beta$  задовољавају услов  $\beta + \alpha/2 < 1$ . Ако овај услов није испуњен, кинетика касне фазе процеса депозиције није конзистента са степеном законитошћу. Ипак, како се геометрија подлоге приближава неинтерагујућем режиму ( $\beta > 1$ ), асимптотски прилаз покривености се приближава експоненцијалној законности. Сходно томе, промена параметара патерна субстрата у овом моделу омогућује интерполацију између два гранична случаја адсорпције на континууму и на квадратној решетки. За изучавање структурних особина загушеног стања користимо парну корелациону функцију  $g(r)$  и просторну дистрибуцију честица унутар ћелија. Примећене су разноврсне нетривијалне просторне дистрибуције у зависности од геометрије патерна подлоге.

**Кључне речи:** случајна секвенцијална адсорпција, хетерогени супстрати, парна корелациона функција, Делонејеве слободне површине

**Научна област:** Физика

**Ужа научна област:** Статистичка физика

**УДК број:** 539.233, 536.12

---

# Contents

<b>Acknowledgements</b>	<b>iii</b>
<b>Abstract</b>	<b>v</b>
<b>Contents</b>	<b>ix</b>
<b>List of figures</b>	<b>xi</b>
<b>1 Introduction</b>	<b>1</b>
<b>2 Monolayer growth kinetics and structure</b>	<b>7</b>
2.1 Adsorption kinetics, jamming coverage and asymptotic behaviour . . . . .	7
2.2 Radial distribution function (pair correlation function) . . . . .	10
2.3 Pore distribution . . . . .	12
<b>3 Random Sequential Adsorption model</b>	<b>15</b>
3.1 RSA on a discrete substrate . . . . .	15
3.2 RSA on a continuous substrate . . . . .	16
3.3 RSA on a patterned substrate . . . . .	17
3.4 RSA on a patterned straight line . . . . .	19
<b>4 Numerical simulation</b>	<b>23</b>
4.1 Monte Carlo method . . . . .	23
4.2 Simulation of Random Sequential Adsorption on patterned substrates . . . . .	24
4.2.1 Preparation of randomly patterned substrate . . . . .	25
4.2.2 Preparation of regularly patterned substrate . . . . .	26
4.2.3 Particle deposition . . . . .	26
4.3 Time scaling and optimizations . . . . .	27
<b>5 Randomly patterned substrates</b>	<b>29</b>

---

5.1	Square cells . . . . .	29
5.1.1	Adsorption on low cell density substrate . . . . .	30
5.1.2	Densification kinetics . . . . .	32
5.1.3	Asymptotic behaviour . . . . .	34
5.1.4	Radial distribution function . . . . .	36
5.1.5	Volume distribution of pores . . . . .	38
5.1.6	Impact of pattern regularity . . . . .	41
5.2	Rectangular cells . . . . .	43
5.2.1	Radial distribution function . . . . .	43
5.2.2	Volume distribution of pores . . . . .	44
5.2.3	Impact of pattern anisotropy . . . . .	45
<b>6</b>	<b>Adsorption on imprecise lattice</b>	<b>47</b>
6.1	Kinetics . . . . .	48
6.1.1	Effect of varying $\beta$ on the long-time adsorption kinetics . . . . .	48
6.2	Asymptotic behaviour . . . . .	49
6.3	Jamming coverage . . . . .	52
6.3.1	Influence of the pattern on the jamming density $\theta_j$ . . . . .	52
6.3.2	Effects of varying $\alpha$ on the long-time adsorption kinetics . . . . .	55
6.4	Structural properties of the jammed state . . . . .	56
<b>7</b>	<b>Conclusions</b>	<b>61</b>
<b>A</b>	<b>Dense packing of equal disks in a square</b>	<b>65</b>
	<b>References</b>	<b>69</b>
	<b>Biography of the author</b>	<b>75</b>

---

# List of figures

1.1	Dimer filling on 1D and 2D square lattice . . . . .	2
1.2	RSA of rods on a line and aligned squares on a plane . . . . .	2
1.3	Typical RSA jammed state on a continuous and pre-patterned surface . . . . .	4
2.1	RSA of disks on a continuous substrate and corresponding excluding areas . . . . .	8
2.2	Temporal evolution of coverage and corresponding adsorption rate . . . . .	9
2.3	Illustration of radial distribution function . . . . .	10
2.4	The pair correlation function for two-dimensional RSA and equilibrium of hard-spheres	11
2.5	Two definitions of inter-particle pores . . . . .	13
2.6	Delaunay triangulation . . . . .	14
2.7	Relation between Delaunay triangulation and Voronoi tessellation . . . . .	14
3.1	A schematic representation of particle adsorption over heterogeneous surfaces bearing disk-shaped and spherically shaped adsorption sites . . . . .	18
3.2	Square cells centred at square lattice nodes . . . . .	19
3.3	Phase diagram in $(\alpha, \beta)$ space . . . . .	19
3.4	Random sequential adsorption of segments on imprecise lattice [1, 2]. . . . .	20
3.5	Different regions of convergence to jamming as described in the text [2]. . . . .	20
3.6	Illustration of equivalency of two models: (I) deposition of segments on localized adsorbing sites and (II) deposition of particles on extended lattice sites. On the left is a case of $r < l$ and on the right a case of $l < r < 2l$ . . . . .	22
5.1	Typical jammed-state configurations on randomly patterned substrate . . . . .	30



---

5.2	Particle population within a single cell in non-interacting regime . . . . .	31
5.3	RSA jamming density (solid line) vs. maximal packing density in the non-interacting mode . . . . .	32
5.4	Time evolution of the coverage for RSA of disks on randomly positioned square cells	33
5.5	Time evolution of the coverage for RSA of disks on randomly vs. regularly distributed square cells . . . . .	34
5.6	Test for the presence of the algebraic law for RSA of disks on randomly distributed square cells . . . . .	35
5.7	Test for the presence of the exponential law for RSA of disks on randomly distributed square cells . . . . .	36
5.8	Radial distribution function $g(r)$ for jamming coverings for RSA of disks on randomly distributed square cells . . . . .	37
5.9	Delaunay triangulation of a set of disk centres for a jammed-state of RSA deposit on randomly distributed square cells . . . . .	39
5.10	Volume distribution of the pores $P(v)$ in the case of jamming covering on a random pattern . . . . .	40
5.11	Various types of Delaunay triangles (T1, T2, T3) depending on the position of vertices.	41
5.12	Volume distribution of the pores $P(v)$ for a jammed-state of RSA deposit on regularly distributed square cells . . . . .	42
5.13	Radial distribution function for a jammed-state of RSA deposit on randomly distributed non-oriented rectangular cells . . . . .	43
5.14	Volume distribution of the pores $P(v)$ for a jammed-state of RSA deposit on randomly distributed non-oriented rectangular cells . . . . .	44
5.15	Typical jammed-state configuration for RSA of disks on non-oriented and oriented elongated rectangular cells . . . . .	45
5.16	Volume distribution of the pores in case of rectangular cells: fixed vs. arbitrary orientation . . . . .	46
6.1	Time evolution of the coverage for RSA of disks on imprecise square lattice . . . . .	48
6.2	Test for the presence of the algebraic approach for RSA of disks on imprecise square lattice . . . . .	50
6.3	Illustration of how particles adsorbed in neighbouring cells can prevent adsorption on the central cell . . . . .	51

---

---

6.4	Time evolution of adsorption rate for RSA of disks on imprecise square lattice . . . . .	52
6.5	Jamming coverage as a function of the imprecise lattice constant . . . . .	53
6.6	Jamming coverage as function of cell size and unchanged pattern lattice constant . . . . .	54
6.7	Test for the presence of the algebraic approach for RSA of disks on imprecise square lattice with unitary lattice constant . . . . .	55
6.8	Adsorption rate for RSA of disks on imprecise square lattice for lattice constant 10% larger than the particle diameter . . . . .	56
6.9	Spatial distribution of particles inside the cell and radial distribution function for the cell size $\alpha = 0.3$ . . . . .	58
6.10	Spatial distribution of particles inside the cell and radial distribution function for the cell size $\alpha = 0.5$ . . . . .	59
6.11	Spatial distribution of particles inside the cell and radial distribution function for the cell size $\alpha = 0.7$ . . . . .	60
A.1	Dense packing of $n = 2$ disks in a square . . . . .	65
A.2	Dense packing of $n = 3$ disks in a square . . . . .	66
A.3	Dense packing of $n = 4$ disks in a square . . . . .	66
A.4	Dense packing of $n = 5$ disks in a square . . . . .	66
A.5	Dense packing of $n = 6$ disks in a square . . . . .	67
A.6	Dense packing of $n = 7$ disks in a square . . . . .	67
A.7	Dense packing of $n = 8$ disks in a square . . . . .	67
A.8	Dense packing of $n = 9$ disks in a square . . . . .	68
A.9	Dense packing of $n = 10$ disks in a square . . . . .	68



---

# Chapter 1

## Introduction

Adsorption is a general term for the processes responsible for the formation of deposits (a.k.a adsorbates). It represents the adhesion of foreign particles to the solid or liquid surfaces commonly termed as adsorbants or substrates. It is a common phenomenon that has great scientific and industrial importance as it has been linked to a wide range of applications in biology [3–6], nanotechnology [7, 8], device physics [9–11], physical chemistry [12, 13], and materials science [14]. Depending on the application in question, the depositing objects could be colloidal particles, polymer chains, globular proteins, nanotubes, DNA segments, or general geometrical shapes, such as disks, polygons, etc. Due to its wide range of applications, there has been a continuous effort to enrich our understanding of deposition processes and experimentally observed structural properties of the adsorbed phase [7, 15, 16].

One of the basic models for studying a thin film formation is known as Random Sequential Adsorption (RSA). It models the process of adsorption of objects in a sequential manner (one by one). The new object is randomly positioned on the substrate, and adsorption is successful if it doesn't overlap any of the previously adsorbed objects. If overlap occurs, the object is rejected and a new adsorption attempt is made. All accepted objects stay permanently fixed on the substrate, thus forming a monolayer deposit. They block certain areas of the substrate for the adsorption of new objects. The blocked area of the substrate expands as the number of adsorbed objects grows, and the adsorption rate slows down. A finite substrate eventually reaches a jammed state where the complete substrate is blocked for the adsorption of new objects. When a substrate is infinitely large, the jammed state is reached in the limit as time goes to infinity.

This is the most general description of the RSA process. The two general terms, 'substrate' and 'object', represent suitable entities in any adsorption process we aim to describe. We can choose whether the substrate is discrete, continuous, pre-patterned, regular, lattice-based, 1D, 2D, 3D, or (in theory) anything we can think of. In practice, our model will seek to describe a physical system within a wide range of applications in biology, nanotechnology, device physics, physical chemistry, and materials science. Most systems of interest would have flat 2D substrates, but other shapes such as spheres, cylinders and rings can also be of interest. The term 'object' can stand for line segments, circles, squares, ellipses, polygons, or any other shape representing real objects such as colloidal particles, polymer chains, globular proteins, nanotubes, DNA segments, etc. New and emerging technologies enable us to precisely tailor the shape and size of the deposition objects on micro and

even nanoscale. All this makes RSA the tool for various interdisciplinary studies.

A desorption is a process in which adsorbed particles detach from a surface. It competes with the adsorption and slows down or even prevents a deposit growth. Other processes that play their roles in kinetics and dynamics of adsorbate formation are diffusion, surface relaxation, hopping of particles, inter-particle interactions, etc. In this work, we will focus on processes in which the time needed to reach the jammed state is much smaller than the relaxation time. Relaxation processes can be neglected and we can assume that after each particle is adsorbed, it stays rigidly and irreversibly fixed to the substrate.

New technologies enable the production of particles with precise shapes on micro and even nanoscale, and the effects of particle properties on deposits and the adsorption process have been thoroughly investigated. Besides adsorbate particles, it is evident that adsorbant surface structure is just as important. Many surfaces of adsorbants are inherently heterogeneous, or they can be modified by the use of coupling agents bound to interfaces, e.g., polyelectrolytes, ligands, surfactants, polyvalent ions, or chemical coupling agents. In each stated case, adsorption occurs at heterogeneous surfaces bearing isolated adsorption sites. This enables us to create deposits with precisely tailored properties, such as coverage and morphology. A deeper theoretical understanding of these systems enhances the effectiveness of the process, rather than using the trial-error method.

We are interested in the kinetics of an adsorption process, as well as in the adsorbate structure in terms of coverage evolution, maximum (jamming) coverage, density/pair correlation function, porosity, etc. Due to the problem complexity, very few simple models can be solved analytically and those are mostly models of one-dimensional substrate. Pioneer work in this field was done by Paul Flory who studied the attachment of pendant groups in a polymer chain [17]. This problem translates to the adsorption of dimers on a one-dimensional regular lattice (see figure 1.1(a)). Flory found that if unreacted groups of a polymer chain randomly pair with its unreacted neighbour, 13.53% of them are prevented from reacting due to isolation between reacted pairs. In terms of the adsorption of dimers on and infinite 1D lattice, the exact jamming coverage is  $1 - 1/e^2 \approx 0.8647$ . In 1958, a Hungarian mathematician Alfred Rényi solved the following problem: given a street of given length and cars

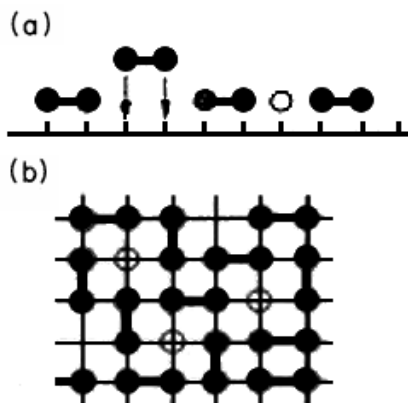


Figure 1.1: (a) Dimer filling on a 1D lattice; (b) Dimer filling on a square lattice. Isolated empty sites, which can never fill, are shown as “o” [15].

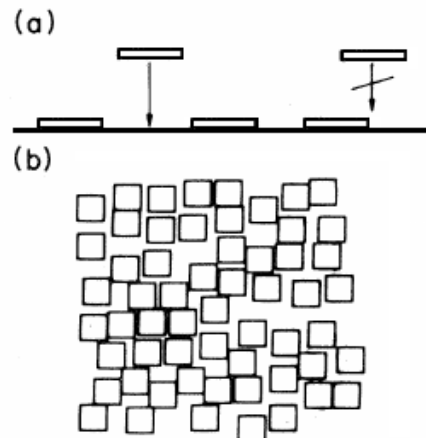


Figure 1.2: (a) Continuum “car parking” of unit length intervals on the line; (b) jammed state for RSA of aligned squares in the plane [15].

of constant length that park on a random free position on the street, what is the density of cars when there are no more free positions [18]? This translates to the adsorption of line segments of fixed length onto a one-dimensional continuous substrate (figure 1.2(a)). An exact jamming density on an infinite parking line is known as the Rényi's parking constant ( $\approx 0.7475979203$ ).

Typical configurations of hard sphere deposits created in an RSA process radically differ from configurations of a gas in thermodynamic equilibrium, as shown by Widom [19]. The RSA process favors configurations in which pairs of spheres are distant. Radial distribution function of deposit configurations created in an RSA process that is stopped when the deposit coverage reaches a predetermined value  $\theta$  below the jamming coverage  $\theta_J$ , differs from the one of the equilibrium hard-sphere gas of the same density  $\theta$ . Also, the system in equilibrium may be in a state with density  $\theta$  that is higher than jamming density  $\theta_J$ , which an RSA system can never surpass. Widom [19] also showed that if we want to use RSA to approximate equilibrium systems, this will only be correct up to the second and third virial coefficients, or cluster integrals, but incorrect fourth and higher-order ones.

Many variants of RSA systems have been studied in order to investigate the influence of shape, size, orientation and dispersion of adsorbing particles, finite-size effects, defects and impurities of a substrate [20–40]. Main focus of these studies was on systems with homogeneous substrates, but in many adsorption processes the substrate is manifestly heterogeneous. Motivated by affinity chromatography, in which solute particles bind only to ligands that are immobilized on the substrate surface, Jin et al. [41] investigated the so-called random-site surface model (RSS). They considered cases of randomly distributed ligands that are much smaller than solute particles and can be modeled as points. They found an exact mapping between the kinetics of this process and of the adsorption on a smooth continuous surface. The mapping is given by relation  $\tau = \alpha(1 - e^{-t/\alpha})$ , where  $t$  and  $\tau$  are measuring the elapsed time in RSS and continuous surface RSA, respectively, and  $\alpha$  is a dimensionless parameter related to the site density.

Based on a substrate type, research studies of RSA processes could be roughly divided into two groups: adsorption on a continuum substrate and adsorption on discrete sites, usually lattices. The crossover between two substrate types is usually treated in a way that the continuous substrate is considered as the limit case of a lattice substrate where distances between neighbouring sites are infinitely small. Another line of research tackles this crossover differently: particles can be adsorbed only within non-overlapping finite-size areas or objects, called cells, that are distributed over a flat substrate and form a desired pattern. This model can also be interpreted as adsorption on a discrete set of point-like adsorption sites that allow for error in particle positioning of the order of the size of the cell, thus treating adsorbing sites as cells of finite size.

The first generalization of the RSA model where lattice sites were treated as objects of finite size was the adsorption of dimers to equidistant adsorbing segments on a line, analyzed analytically and numerically by Bonnier et al. [42]. In the same fashion, Adamczyk et al. [43, 44] generalized the Random Site Surface model and considered surface heterogeneities as finite-size hard disks (or spheres) of fixed radius, positioned randomly in the preceding RSA process. The RSS model can also be generalized by using randomly placed adsorption cells of different shapes. A research direction exploited in this dissertation uses adsorbing cells shaped as squares or rectangles of different elongation.

Araújo et al. [45] and Marques et al. [13] numerically investigated the adsorption of disk-shaped particles on a two-dimensional pre-patterned substrate that consists of equal square cells centered at

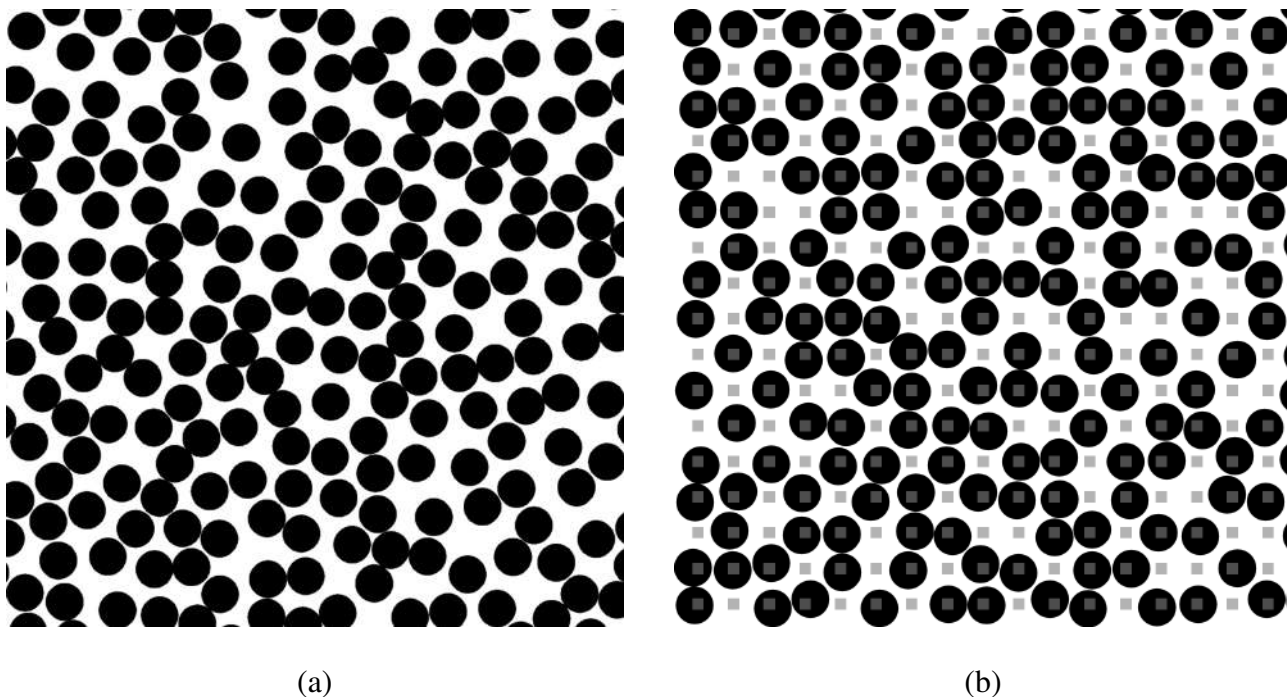


Figure 1.3: Typical configuration of jammed state yielded with random sequential adsorption (RSA) of disks on a flat continuous surface (a) and on a regular pre-patterned surface (b).

the vertices of a square lattice (Fig. 1.3(b)). They studied effects of a regular substrate pattern and particle polydispersity on the deposit density morphology, as well as on the in-cell particle population. They focused on the morphology of the final state. In this dissertation we analyze the kinetics of this model and investigate features of the deposition structure in more depth.

Privman and Yan [1] and Verma and Privman [2] analyzed the extended model of deposition of segments of length  $a$  in one-dimension, on a lattice of spacing  $l$  between its sites. Unlike sites of the precise lattice that have no size, sites of imprecise lattice are symmetrically broadened into segments of width  $w$  in which the centers of the depositing objects can land. They reported that even an arbitrarily small imprecision in the lattice-site localization ( $w \gtrsim 0$ ) changes the convergence to jamming from fast, exponential, to slow, power-law. Our study in a similar spirit investigates the rapidity of the approach to the jamming state in the case of a two-dimensional (2D) pre-patterned substrate, elucidating the crossover between discrete and continuous substrate in a different light.

## **This dissertation**

This thesis is organized as follows. In chapter 2, following this introduction, we overview the properties of the system necessary to analyze and understand the growth of a monolayer deposit and its structure. A historical overview of related research of the Random Sequential Adsorption model on various substrate types is given in chapter 3. Chapter 4 gives the details of the numerical simulation that we have developed and used to obtain the results presented in this thesis. The classical RSA model was modified to take into account the substrate inhomogeneities and adsorption was assumed to occur only if the (projected) particle center lies within a rectangular cell area, i.e., if a sphere touches one of the cells. In chapter 5, we investigated the RSA of spherical particles on a randomly patterned substrate, in which the configuration of the cells was produced by performing RSA simulations to a prescribed coverage fraction. Chapter 6 analyses the adsorption of spherical particles on surfaces covered by square cells arranged in a square lattice pattern. In the final chapter 7 we summarize the presented work and give some concluding remarks.





---

## Chapter 2

# Monolayer growth kinetics and structure

In this chapter, we describe the parameters and distributions used for the monolayer deposit characterization. The kinetic properties of a deposition process are described by the temporal evolution of the substrate coverage  $\theta(t)$ . To gain basic insight into the “microstructure” of the jammed state, we use the radial correlation function and size distribution of pores (patches of unoccupied spaces between particles).

### 2.1 Adsorption kinetics, jamming coverage and asymptotic behaviour

The most common parameter used to characterize the kinetic properties of a deposition process is coverage  $\theta(t)$ , defined as a fraction of the substrate area covered by adsorbed particles at moment  $t$ . It is calculated by dividing the size of the occupied substrate space by the total size of the substrate. In the case of adsorption of mono-dispersed particles, the coverage at a time  $t$  is calculated with the formula

$$\theta(t) = N_p(t) \frac{S_p}{S_s}, \quad (2.1)$$

where  $N_p(t)$  is the number of adsorbed particles at a time  $t$ ,  $S_p$  is the size of the substrate that a single particle occupies and  $S_s$  is the total size of the substrate. In the case of adsorption on a lattice substrate,  $S_p$  is the number of the lattice nodes that are occupied by adsorbed particles and  $S_s$  is the total number of nodes in the substrate sample. In the case of a one-dimensional continuous substrate, size refers to a length, while in the two-dimensional case it is a surface area. In experiments, the most relevant case is the adsorption of three-dimensional particles on two-dimensional surfaces, in which case the particle size  $S_p$  is calculated as the area of a particle projection onto the substrate. For example, adsorption of  $N_p$  non-overlapping identical spherical particles of radius  $r_0$  to a square flat surface with a side of length  $L$  will give the coverage as

$$\theta(t) = N_p(t) \frac{r_0^2 \pi}{L^2}. \quad (2.2)$$

The adsorption rate  $u \equiv d\theta(t)/dt$  is proportional to the number of particles striking the unit surface area per second (flux  $j$ ) and to the so-called sticking coefficient  $S(\theta)$ , which is the probability that an impinging particle actually sticks to the substrate:  $u = jS(\theta)$ . The sticking coefficient is equal to the fraction of the substrate surface that is available for new adsorptions  $B(\theta)$ , known as the available space function or the blocking function, multiplied by the probability  $P$  that a particle sticks to the substrate on contact:  $S(\theta) = PB(\theta)$ . RSA model assumes that adsorption is inevitable whenever a particle strikes the substrate at a location that satisfies the non-overlapping condition. In other words, the interaction energy between the substrate area and a particle is infinite at contact and equals zero otherwise and the probability  $P$  equals 1. Hence, the sticking coefficient equals the available space function  $S(\theta) = B(\theta)$ .

In the RSA model, the flux of the impinging particles  $j$  is considered to be uniform and at a constant rate. Time scaling  $t^* = jt$  enables us to take the flux to be unitary and yield the adsorption rate as

$$u(t^*) = \frac{d\theta(t^*)}{dt^*} = B(\theta(t^*)). \quad (2.3)$$

in the further text, for the sake of simplicity and without loss of generality, we will only use the scaled time and omit the asterisk in the scaled time symbol.

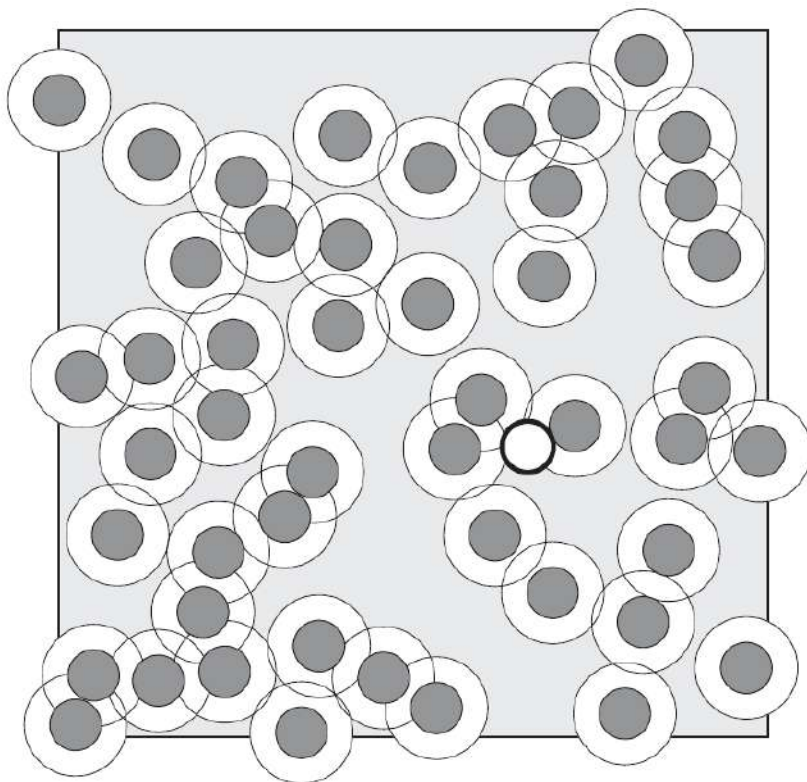


Figure 2.1: A typical configuration of particles adsorbed at an interface (dark disks); the white annuli show the exclusion areas, whereas the shadowed zones represent the areas (targets) available for the centre of the wandering particle depicted by the white disk. Figure from Adamczyk [46].

The typical RSA configuration of spherical (disk-like) particles adsorbed on a flat surface is illustrated in figure 2.1 [46]. Dark disks represent particle projections, while white annuli around them compose the space blocked for the centres of new particles. Gray surface is the “free” space available for the adsorption of new particle centres and its area represents the available space function. We get coverage versus time dependencies as shown in figure 2.2(a) by calculating the available space function and solving the equation 2.3. The available space function can be exactly calculated only in a few simple one-dimensional cases and we rely on numerical Monte Carlo simulations for its estimate. The sum of coverage  $\theta$  and available space function  $B(\theta)$  is less than 1 due to unfilled space around particles that are blocked for centres of new particles (white annuli in figure 2.1). These annuli overlap each other making the exact calculation of its area practically impossible.

Some features of the temporal evolution of the coverage are common for all RSA systems. At the start of the process, the entire surface of the substrate is available for adsorption of particles and all adsorption attempts are successful. Each adsorbed particle blocks the surrounding area for the adsorption of new particle centres and affects the geometry of all later placements. This is why  $\theta(t)$  grows linearly at the start and slows down due to the interaction with previously adsorbed particles (the non-overlapping condition). Due to the blocking of the substrate area by already adsorbed particles, the available space function decreases as more particles are being adsorbed and coverage growth gets slower and slower.

At large times the coverage  $\theta(t)$  asymptotically approaches the jammed-state value  $\theta_j$  where only gaps too small to fit new particles are left in the monolayer. In the analysis of the asymptotic approach to jamming, a plot of  $\theta_j - \theta(t)$  on a logarithmic scale strongly depends on the precise calculation of  $\theta_j$ . Instead, we will examine the adsorption rate  $u(t)$ , i.e. the coverage growth of adsorbed particles per unit time and surface area. It is yielded by the differentiation of coverage  $\theta(t)$  and the adsorption rate equals zero in the jammed state by definition ( $u(t \rightarrow \infty) = 0$ ). A typical shape of the adsorption rate is shown in figure 2.2(b).

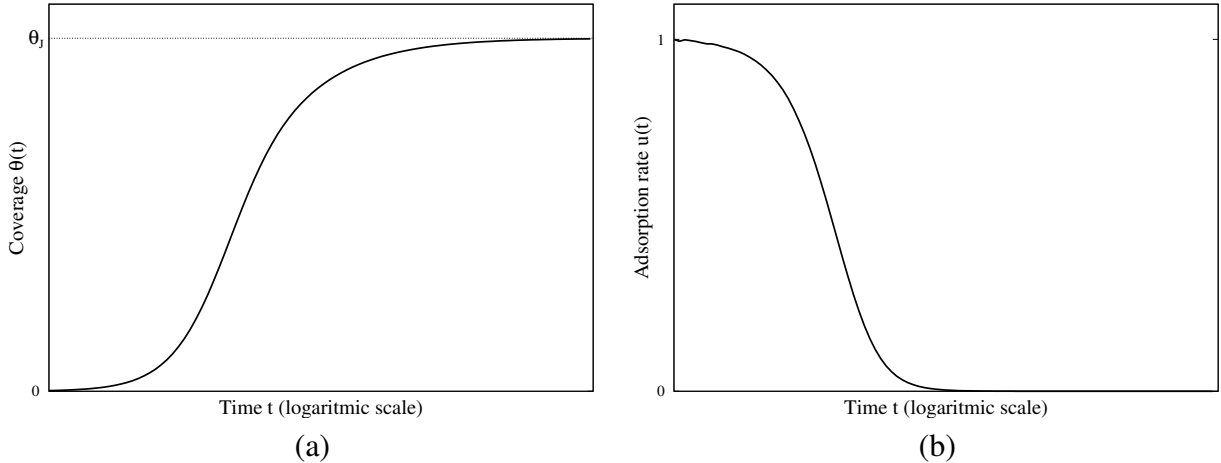


Figure 2.2: (a) Qualitative dependence of coverage  $\theta$  on time and (b) corresponding dependence of the adsorption rate  $u$  on time ( $t$ ).

## 2.2 Radial distribution function (pair correlation function)

Radial distribution function  $g(r)$ , also known as the pair-correlation function, provides a simple yet powerful encoding of the distribution of inter-particle gaps. It gives information about the long-range inter-particle correlations and their organization [47]. It is central in experimental applications of geometrical concepts to physical systems since it defines the scattering function measured in light, X-ray, and neutron diffraction experiments [48].

By definition, the pair correlation function measures the probability that a particle centre is found at a distance  $r$  from the referent particle, relative to the one of an ideal gas. In two-dimensional systems, it can be calculated from the expression

$$g(r) = \frac{S_s \Delta \bar{N}_a(r)}{N_p 2\pi r \Delta r}, \quad (2.4)$$

where  $r$  is the radial coordinate,  $S_s$  is total surface area,  $N_p$  is total number of particles adsorbed over the surface, and  $\Delta \bar{N}_a(r)$  is the average number of particles within the annulus of radius  $r$  and thickness  $\Delta r$  whose centre coincide with a particle centre (see figure 2.3). If  $N_a(r; r^*)$  is the number of particles whose centre lies inside of a circle of radius  $r$  centred at a position  $r^*$ , then averaging this value over all circles whose centres coincide with particle centres will give us  $\bar{N}_a(r)$ . For a set of  $N_p$  particles

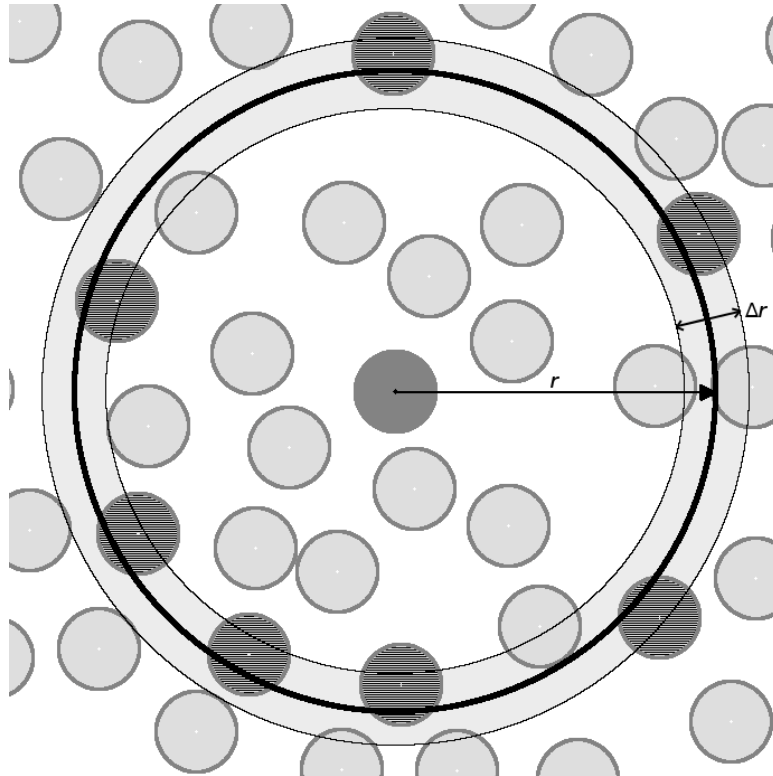


Figure 2.3: Radial distribution function: average density of particles at distance  $r$  from the centre of a reference particle.

positioned at  $r_1, r_2, \dots, r_{N_p}$  this is written as

$$\bar{N}_a(r) = \frac{1}{N_p} \sum_{j=1}^{N_p} N_a(r; r_j) = \frac{1}{N_p} \sum_j \sum_{i \neq j} \eta(r - |r_j - r_i|), \quad (2.5)$$

where  $\eta(x)$  is the Heaviside step function. From equation (2.5), we obtain

$$\Delta \bar{N}_a(r) = \frac{1}{N_p} \sum_j \sum_{i \neq j} [\eta(r + \frac{\Delta r}{2} - |r_j - r_i|) - \eta(r - \frac{\Delta r}{2} - |r_j - r_i|)], \quad (2.6)$$

which then gives

$$g(r) = \frac{S_s}{2\pi r \Delta r N_p^2} \sum_j \sum_{i \neq j} [\eta(r + \frac{\Delta r}{2} - |r_j - r_i|) - \eta(r - \frac{\Delta r}{2} - |r_j - r_i|)]. \quad (2.7)$$

Equation (2.7) is used in practice for calculating the pair correlation function of systems generated in Monte Carlo simulations. For each generated system, we find distances between particles in all pairs, bin them into a histogram, and normalize the histogram according to equation (2.7). The histogram is then further averaged over all generated systems.

Special caution should be taken in calculations of a finite system when the reference particle is closer to the edge of a surface and parts of the circle of radius  $r$  around it fall outside of the surface. Contributions of such points to the histogram should be appropriately corrected and this can be done in

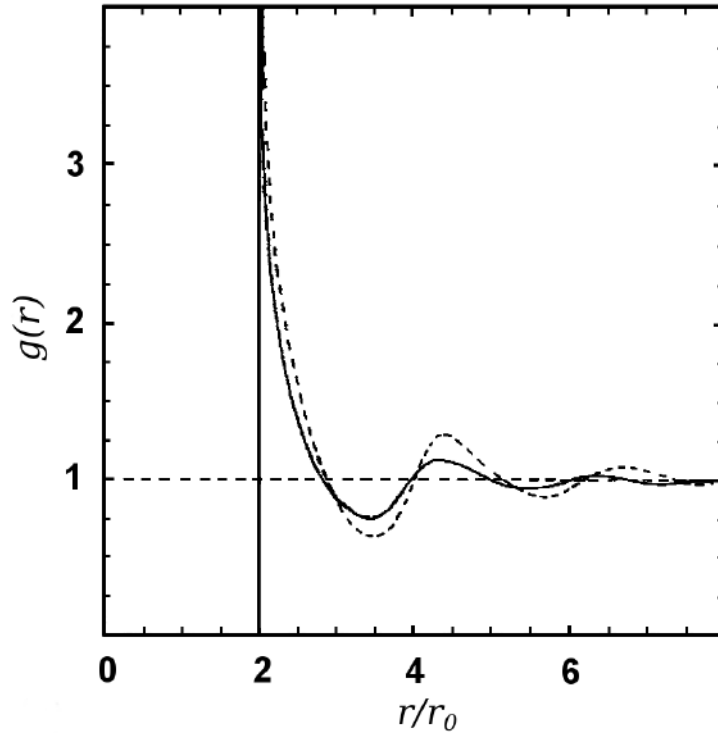


Figure 2.4: The pair correlation function for monolayers of density  $\theta = 0.547$ : the continuous line shows the smoothed numerical results for random monolayer and the dashed line shows the theoretical results for a 2D hard-sphere equilibrium. Figure from Adamczyk [46].

one of three ways: (i) completely disregarding those particles; (ii) calculating the part of the circle that falls into the surface, and replacing  $2\pi r\Delta r$  with the surface of the truncated annulus; and (iii) using periodic boundary conditions to extend the surface area and fill in the missing part of the annulus. The latter can only be done if the periodic boundary condition has been used throughout the entire simulation and it applies to the generated configurations of a system.

In the case of a system of identical hard spheres, two particles can not be at a distance smaller than  $2r_0$ , hence  $g(r < 2r_0) = 0$ . Since there can not be correlation between two infinitely separated particles,  $g(r)$  approaches 1 for  $r \rightarrow \infty$ . As an illustration, figure 2.4 shows the pair correlation function calculated for the RSA of identical disks on a flat continuous substrate derived from numerical simulations and theoretical results for the models of hard spheres in equilibrium [46]. Both systems are at the same density equal to the jamming coverage of the RSA system. For  $r/r_0 > 5$ , radial distribution function is strongly damped so that the RSA configuration looks uncorrelated (i.e.,  $g(r) = 1$ ), and it has a logarithmic divergence at contact  $r = 2r_0$  [5, 48–50].

## 2.3 Pore distribution

Gap size distribution is widely used to characterize the structure of a straight line covered with rods [19, 51–54]. A pore is analogous to a gap in a two-dimensional system and systems of higher dimensions. Defining a pore is a challenging task in a more-than-one dimensional system where inter-particle space is connected. The Delaunay triangulation is commonly used as a geometrical tool to break apart an inter-particle space into separate pores. The size distribution of pores  $P(v)$  is commonly used to characterize the structure of disordered granular packings and to quantify the structural changes during the compaction process [55–59].

Triangulation is a technique for creating a mesh of contiguous, non-overlapping triangles whose vertices belong to and exhaust a given set of points  $\mathbf{P}$ . By definition, a triangulation of a finite set of points on a plane  $\mathbf{P} \subset \mathbf{R}^2$  is called a Delaunay triangulation if the circumcircle of every triangle is empty, that is, there are no points from  $\mathbf{P}$  in its interior. A prominent characteristic of a Delaunay triangulation is that it maximizes the minimal angle of all possible triangulations, with a unique property of local equiangularity. It is also helpful in defining the nearest neighbours as two vertices of the same Delaunay triangle. An extensive review and comparison of 9 different Delaunay triangulation algorithms are given by Su and Scot Drysdale [60]. In this thesis, we used the Quickhull algorithm [61] in MATLAB<sup>®</sup> programming language to compute the Delaunay triangulation for a given set of disk centres on a plane.

By definition, the circumcircle of a Delaunay triangle is empty, i.e. it doesn't contain other points from the set. Let's view this in the context of a flat monolayer deposit of hard disks with a fixed radius  $r_0$ . The disk centres are the base set of points for a Delaunay triangulation. We single out any of the triangles and denote the radius of its circumcircle as  $R$ . Three particles of diameter  $r_0$  lie centred on the triangle vertices, and an imaginary disk with radius  $R - r_0$ , concentric with the triangle circumcircle, touches all three particles (red disk in figure 2.5). These inscribed disks are the definition of inter-particle pores.

The maximum diameter of a circular pore is less than  $r_0$  when a monolayer deposit adsorbed on

a continuous surface is in a jammed state. Otherwise, an additional particle could be adsorbed in the pore larger than  $r_0$  which is contrary to the jammed state definition. This is not true if the substrate is patterned: even if there is enough space between adsorbed particles to fit a new particle, the second condition requires that the centre of the particle must fall within the predefined cells. This allows for bigger pores in the jammed state. On the other hand, a smart design of substrate pattern can impose a certain ordering of deposit that can lead to a denser packing of particles than the one in the case of a non-patterned substrate.

The above definition of pores has a few shortcomings. In the first place, circular pores can overlap each other. This problem can be solved by carefully excluding the smallest among overlapping pores, which is not a straightforward task in the case of overlaps of multiple pores. Another flaw of this definition is that a set of circular pores does not fill up the whole volume of the inter-particle space. To avoid these two problems, we use another definition of a pore as the part of a Delaunay triangle that is not covered by disk particles (illustrated by the striped area in figure 2.5). The advantage of these pores over the circular pores is that the former ones completely cover the inter-particle space without overlapping each other. On the other hand, a pore volume doesn't indicate if the pore is big enough to fit an additional particle and can not be used to check if the jammed state condition is satisfied even in the case of a continuous substrate.

Another analysis at the *microscopic* scale is based on the Voronoi tessellation [63]. It unambiguously decomposes any arbitrary region occupied by disks into space-filling, non-overlapping convex polygons. Formally, for any set of points  $\mathbf{P}$  in a two-dimensional space, a polygonal shape surrounds each point  $p$  from the set  $\mathbf{P}$  such that any point in the polygon is closer to  $p$  than to any other point

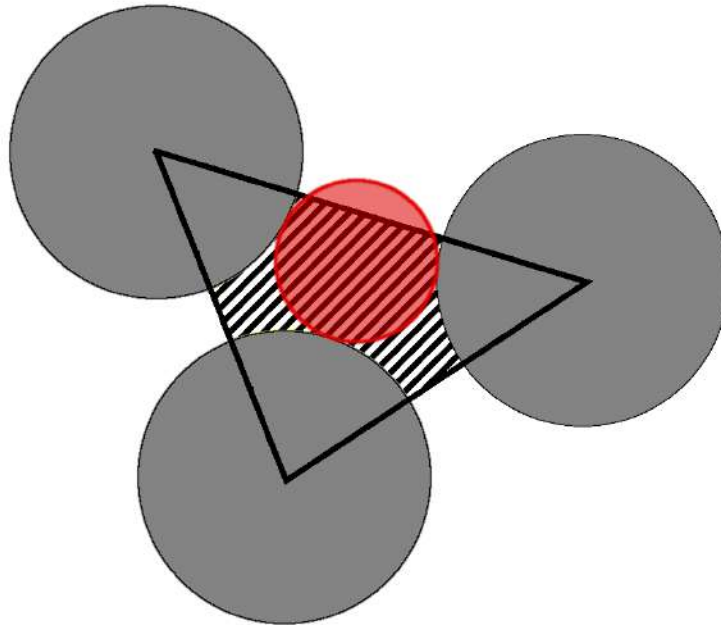


Figure 2.5: Inter-particle pore defined as (i) largest disk that is touching all three particles centred at the vertices of a Delaunay triangle (red disk); (ii) empty part of a Delaunay triangle (striped area).



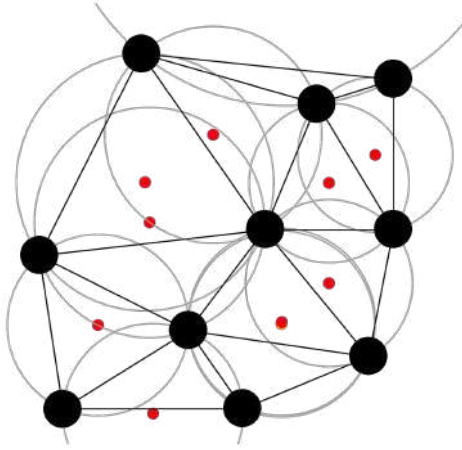


Figure 2.6: Delaunay triangulation of a set of points (black dots) with empty circumcircles and their centres marked with red dots. Figure copied from [62].

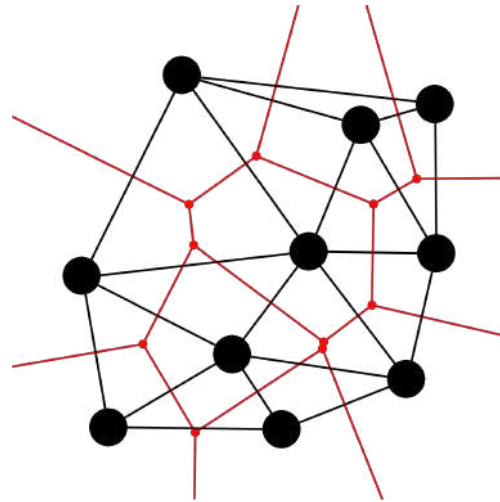


Figure 2.7: Relation between Delaunay triangulation (black lines) and Voronoi tessellation (red lines). Centres of empty circumcircles coincide with vertices of Voronoi polygons. Figure copied from [62].

from the set  $\mathbf{P}$ . These polygons are known as Voronoi cells. They are convex and their edges join at trivalent vertices. Each vertex is equidistant to three neighbouring disks. Voronoi tessellation is dual to Delaunay triangulation: vertices of Voronoi polygons are centres of Delaunay empty circumcentres and edges of Voronoi polygons bisect the edges of Delaunay triangles. Two points are considered to be nearest neighbours if associated Voronoi cells are contiguous, which is equivalent to the definition of nearest neighbours given earlier in this section.

Figure 2.6 shows an example of a Delaunay triangulation for a set of 10 points, along with all empty circumcircles and their centres marked with red dots. Figure 2.7 shows a Voronoi diagram for the same set of points alongside the Delaunay triangulation. Each object (denoted by a black circle) is located in a separate polygon. Figure 2.7 also illustrates close relation between the Delaunay triangulation and Voronoi tessellation: centres of empty circumcircles coincide with the vertices of Voronoi polygons and each side of a polygon bisects one of the triangle sides.

---

## Chapter 3

# Random Sequential Adsorption model

The kinetics of an adsorption process has been mainly studied through the formulation of different models, aiming to capture the essential features of the process. Random Sequential Adsorption (RSA) is a simple model that can provide the generic features of the adsorption phenomenon in the case of a very strong interaction between particles and substrate. The adsorption process is treated as the sequential addition of particles on the substrate such that at each time step only one particle is added to the substrate at a randomly selected position. During the process of addition, newly added particles are forbidden from overlapping with the already adsorbed particles, and any attempt of adsorption that results in overlap is rejected. The adsorbed particles are permanently fixed at their spatial positions so that they affect the geometry of all later placements. Under these conditions, the system evolves rapidly toward non-equilibrium conditions, and the kinetics becomes essentially dominated by geometrical exclusion effects between particles. Evans [15] gives a thorough historical review of RSA models and their applications.

It must be stressed that the classical RSA approach can be used for modelling the kinetics of an idealized process only, consisting of the creation of particles at a given distance from the interface with a constant rate and in a consecutive manner. For particles of a sub-micrometre size range, in addition to hydrodynamic and electrostatic forces, Brownian motion significantly affects their trajectories and transport to boundary surfaces. It is not possible, within the framework of the RSA model, to find a unique relationship between the kinetics of this idealized process and the kinetics of the particle adsorption process governed by various transport mechanisms. One has, therefore, to rely on approximate models being useful for specific transport mechanisms of particles [46].

### 3.1 RSA on a discrete substrate

A discrete substrate represents a set of isolated adsorbing sites, restricting binding positions of particles only to those sites. A basic example of the RSA on a discrete substrate is the adsorption of monomers on a lattice when one particle binds to a single site without blocking any other sites. Eventually, all sites will be occupied, regardless of the dimensionality and lattice configuration, making the jamming density equal to 1. With the assumption that the particle flux is unitary, from

$d\theta(t)/dt = 1 - \theta(t)$  it is easy to calculate the time evolution of the coverage and yield that

$$\theta(t) = 1 - e^{-t}. \quad (3.1)$$

The adsorption of dimers on a lattice turns out to be a non-trivial case. A dimer is adsorbed at a random position and occupies two neighbouring sites. Two adjacent dimers can have a single isolated site between them that can never be occupied. Consequently, the jamming coverage is smaller than 1. Jamming coverage of a one-dimensional case was first calculated by Flory [17]. He studied the condensation of pairs of consecutive substituents X of a polymer composed of  $-\text{CH}_2-\text{CHX}-$ , and found that fraction of unreacted groups equals  $e^{-2}$  and the jamming coverage equals  $1 - e^{-2} \approx 0.8647$ . The asymptotic approach to jamming limit retains the exponential form in the case of the infinitely long lattice.

Adsorption of dimers on a 2D square lattice was the subject of several studies [64–66]. Although it can't be solved analytically, numerous approximations and numerical calculations showed that  $\theta_J = 0.9068$  [65]. Vette et al. [66] studied dimers filling on triangular, square and hexagonal lattices. Further studies of adsorption of k-mers on 2D lattices concluded that in lattice RSA models [27, 67–69], the approach of the coverage fraction  $\theta(t)$  to its jamming limit  $\theta_J$  is given by the time dependence:

$$\theta_J - \theta(t) \sim \exp(-t/\sigma), \quad (3.2)$$

where parameter  $\sigma$  depends on the orientational freedom of depositing objects, and on the dimensionality of the substrate [68, 69].

## 3.2 RSA on a continuous substrate

When the adsorbing particles, such as proteins or colloids, are much larger than the structural details of the substrate surface, the surface can be considered continuous on a mesoscopic scale and the adsorption of particles is an off-lattice process. The one-dimensional case of the RSA of equal rods on a continuous line is known as Renyi's car parking problem after the Hungarian mathematician. He was the first to propose and solve this model [18]. The calculated jamming coverage ( $\theta_J = 0.7476\dots$ ) is significantly lower than the close packing coverage which equals 1. Late time approach to the jamming limit displays power-law behavior  $\theta_J - \theta(t) \sim t^{-1}$ . The pair correlation function at long distances behaves super-exponentially, unlike equilibrium systems with characteristic exponential decay [70].

Feder [5] calculated the jamming coverage of disks on a flat plane to be approximately equal to 0.547. He used numerical simulations to show that the asymptotic approach of coverage to its jamming limit obeys the power-law  $t^{-p}$  with exponent  $p \approx -1/2$ . Pomeau [50] proposed that the exponent  $p$  equals  $1/D$  where  $D$  is the dimensionality of a system. Swendsen [49] pointed to a geometrical argument which predicts that a late-stage asymptotic approach of coverage for spheroids obeys the power-law

$$\theta_J - \theta(t) \sim t^{-1/D}, \quad (3.3)$$

where  $D$  is the dimensionality of the system. For aligned squares, the power-law relation is modified by a logarithmic factor. The same arguments were used to show that the pair correlation function in the jammed state diverges logarithmically at contact.

Relation 3.3 was numerically and analytically confirmed by many investigators [5, 36, 49, 50, 71]. Swendsen's arguments initially appeared to be valid for any particle shape, but soon it was proven by numerical calculations that even though the power-law is universal for various shapes (spherocylinders, ellipses, rectangles, and needles) and elongations, the value of the exponent varies depending not only on the dimensionality but on the number of degrees of freedom [20–22, 25, 26, 29, 48]. Viot et al. [29] showed that two critical regimes exist in the late stage of the process in the limit of very small elongations of various objects. In the first regime, the asymptotic approach obeys Feder's law,  $t^{-1/2}$ , and it is directly followed by a regime in which  $t^{-1/3}$  law is obeyed. They found that the time when the crossover occurs is directly linked to the parameter that measures the anisotropy of adsorbing particles.

### 3.3 RSA on a patterned substrate

Although the basic RSA model may accurately reproduce many experimental situations, its extension to more complex surfaces having an intrinsic structure is by no means trivial. For example, the supporting surface may be pre-patterned with preferential sites for specific particle attachments, which alters the kinetics of the process and the structure of the adsorbed layer. With the use of photolithographic techniques, high-power lasers, chemical treatments, etc., such surface modifications are routinely realized on the micro-scale, or even on the nano-scale [72–75].

There is well-developed literature on irreversible adsorption of various types of two-dimensional (2D) patterned surfaces [13, 41, 43, 45, 76–80]. Historically, Jin et al. [41] were the first to study pre-patterned substrates in a model of irreversible deposition on a random site surface (RSS) where the sites are represented by randomly distributed points. Their work was motivated by affinity chromatography in which ligands are fixed on the adsorbent surface and the desired solute (or a class of solutes) can attach only to those ligands. They found a remarkable, yet simple mapping between elapsed time of the adsorption on a continuous surface  $\tau$  and on a random site surface  $t$ , given through relation

$$\tau = \alpha(1 - e^{-t/\alpha}), \quad (3.4)$$

where  $\alpha$  is an average number of adsorbing sites per surface unit. This mapping is valid in any dimension, but it is applicable only if adsorbing sites are randomly distributed.

The random-site model is only suitable if the size of ligands is much smaller than the size of adsorbing particles. The finite size of ligands will result in arrangements that are not strictly random, and the mapping given by the equation (3.4) is inapplicable. Adamczyk *et al.* [43, 44] have extended the RSS model to the situation where the size of the landing sites is finite and comparable with the size of adsorbing spheres. They explored two cases of the ligand shape: circular disks and spherically shaped sites (see figure 3.1). They concluded that in the case of circular disks, Jin's mapping holds if the disk radius is at least ten times smaller than the particle radius, but when its radius exceeds 20% of the particle radius, the behaviour radically differs from the RSS model. Their results prove that the spherically shaped sites are much more effective in binding particles than the disk-shaped sites.

Araújo et al. [45] have investigated the adsorption of disk-shaped particles on a patterned substrate that consists of equal square cells centred at the vertices of a square lattice. They investigated the

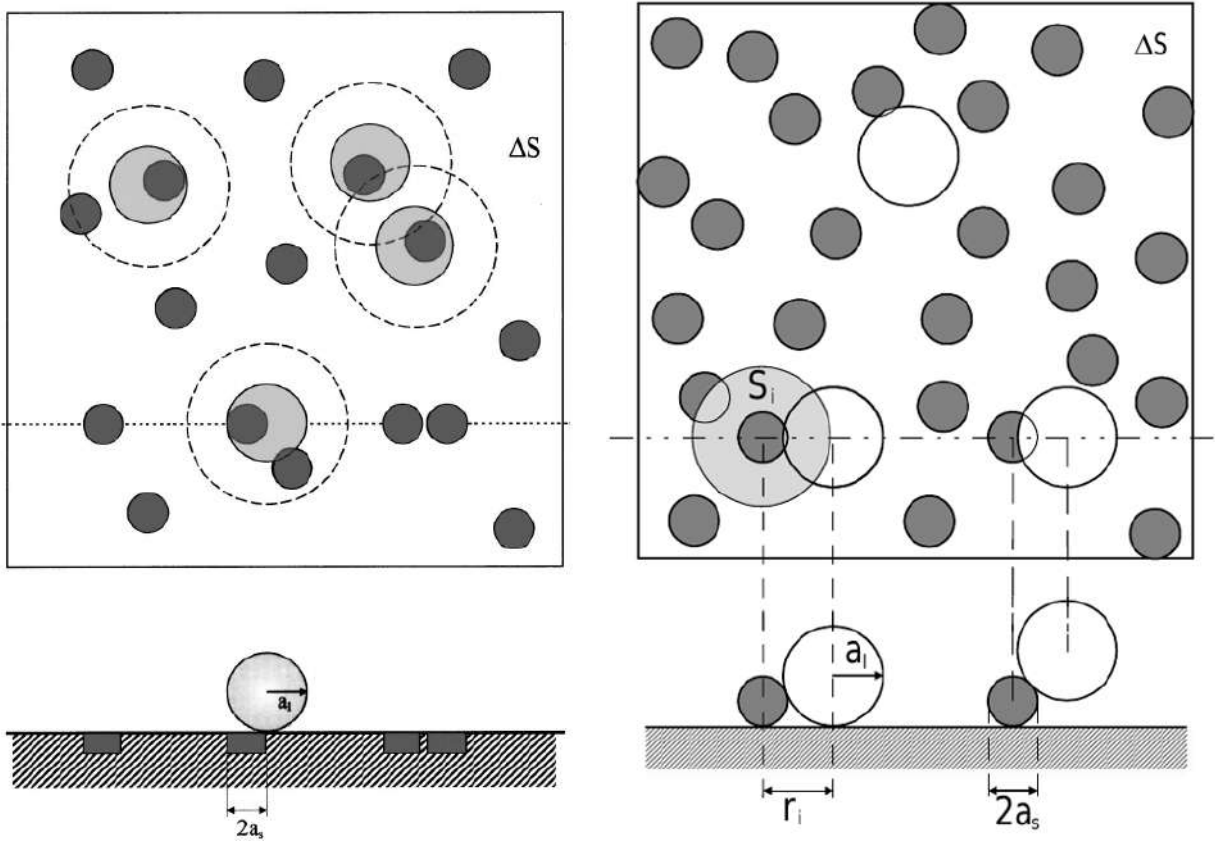


Figure 3.1: A schematic representation of particle adsorption over heterogeneous surfaces bearing disk-shaped (left) and spherically shaped (right) adsorption sites [43, 44]

phase space of parameters  $\alpha$  and  $\beta$  which stand for the size of the square cell side and the cell-cell separation, respectively, measured in units of adsorbing particle diameter (see figure 3.2). Based on the size of the square cell  $\alpha$ , one can discriminate between a *single-particle per cell* (SPPC) and a *multiple particles per cell* (MPPC) regime. SPPC regime is in force for  $\alpha < \sqrt{2}/2$  when at most single particle can be adsorbed on any cell. Another division is based on the measure of the cell-cell separation  $\beta$ . If  $\beta$  is greater than 1, the blocked area of a particle attached to a cell can't reach any other cells and this mode is named *non-interacting cell-cell adsorption*. The *interacting cell-cell adsorption* regime requires that  $\beta$  is less than 1. The phase diagram is illustrated in figure 3.3. The main focus of the work of Araújo et al. [45] was on the morphology of the jammed state. The ordering effect of the substrate competes with the randomness in particle positions and excluded volumes, yielding a variety of deposit morphologies: lattice-like, locally homogeneous or locally ordered.

In addition, Araújo [81] has discussed the influence of the pattern on the adsorption kinetics. He has pointed out that time evolution towards the jammed state can be consistent with exponential or power-law behaviour, depending on the geometry of the pattern. Marques et al. [13] studied the effect of the presence of a regular substrate pattern and particle polydispersity on the deposit morphology and density, as well as on the in-cell particle population.

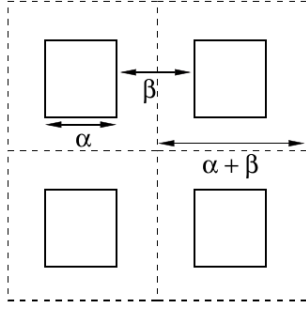


Figure 3.2: Landing sites are squares of size  $\alpha r_0$ , with centres positioned at square lattice with lattice constant  $(\alpha + \beta)r_0$  [45].

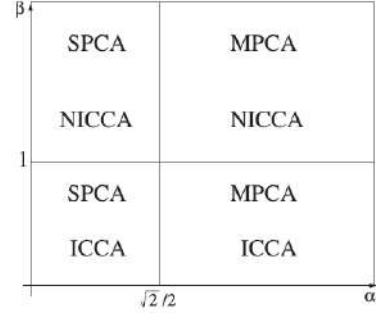


Figure 3.3: Phase diagram in  $(\alpha, \beta)$  space, separating interacting from non-interacting cell-cell adsorption, and single particle per cell from multiple particle per cell mode [45].

### 3.4 RSA on a patterned straight line

Understanding the kinetics of a model of RSA on a patterned substrate relies heavily on numerical simulations. However, analytical tools can be used to study cases of one-dimensional substrates. In [1] and [2] authors studied the adsorption on an imprecise lattice and identified regions of different types of convergence to jamming that form a repeating pattern in the phase space of model parameters. Bonnier et al. [42] studied the adsorption of dimers on a dashed line, a model that is equivalent to a special case of the adsorption on an imprecise lattice, studied in [2]. Both papers report that there are four types of an asymptotic approach to the jamming limit: continuous-like algebraic, anomalous algebraic, lattice-like exponential and modified exponential. In this subsection, we outline their main arguments and results.

The late-stage asymptotic behaviour of the RSA on a continuous surface is explained using the assumption that there exists a moment  $t_a$  after which predominant adsorptions of new particles happen at holes small enough to fit only one particle [49, 50]. The presence of larger holes is negligible and the probability that a new hole is created after the moment  $t_a$  equals zero. The probability  $n(h; t > t_a)$  that a small hole gets filled is proportional to its size  $a \sim h^d$ , where  $h$  is the characteristic linear dimension of a hole and  $d$  is the system dimensionality. Therefore, the hole size distribution declines exponentially with time:

$$n(h; t > t_a) = n(h; t_a) e^{-Rh^d t}. \quad (3.5)$$

Difference between the jamming coverage and the coverage at any instant  $t$  after the moment  $t_a$  is given by:

$$\begin{aligned} \Delta\theta(t) &= \theta_J - \theta(t) = A \int_0^{h_{\max}} n(h; t) dh \\ &= A \int_0^{h_{\max}} n(h; t_a) e^{-Rh^d t} dh, \end{aligned} \quad (3.6)$$

where  $A$  is the area of a single particle projection onto the substrate.

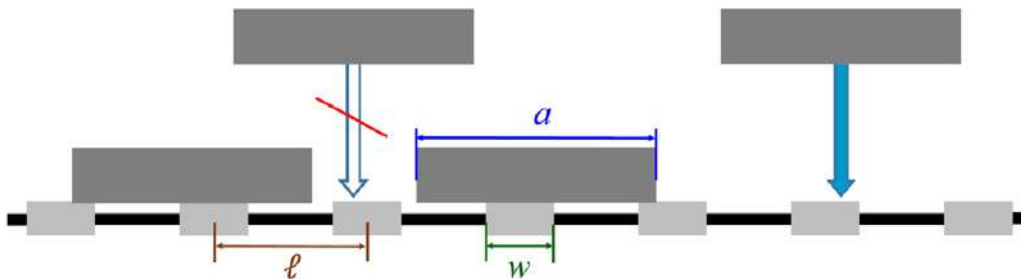


Figure 3.4: Random sequential adsorption of segments on imprecise lattice [1, 2].

The form of the hole size distribution in the small hole limit at moment  $t_a$  is crucial for determining the type of asymptotic approach. Pomeau [50] and Swendsen [49] assumed that  $n(h \rightarrow 0, t_a)$  is finite and that it can be approximated by a constant in the range of interest  $h \in [0, h_{max}]$ . As a result of this assumption, the asymptotic approach to the jamming coverage is algebraic  $\Delta\theta(t) \sim t^{-1/d}$  for spheroid particles in  $d$ -dimensional space and it has the form of  $\Delta\theta(t) \sim t^{-1}(\ln t)^{d-1}$  for aligned hyper-cubes [49]. Other forms of hole size distribution  $n(h \rightarrow 0, t_a)$  appear in models of RSA on patterned substrates, leading to different asymptotic approaches [2]. This includes cases where it is impossible to have holes smaller than a threshold  $h_{min}$ , i.e.  $n(h < h_{min}, t_a) \equiv 0$ . Accordingly, the small hole size distribution of interest is in the limit of  $h$  slightly larger than the threshold  $h_{min}$ , i.e.  $n(h \rightarrow h_{min}^+, t_a)$ .

Privman and Yan [1] and Verma and Privman [2] numerically explored the model of adsorption on a one-dimensional imprecise lattice. Particles of size  $a$  can attach to the substrate if their centres fall on a lattice site that is symmetrically broadened around the lattice site position without overlapping previously adsorbed particles (see figure 3.4). The size of a broadened site is  $w$ , while the lattice constant is  $l$ . The authors identified regions of different convergence types in the phase space of scaled parameters of the model,  $(w/l, a/l)$ , based on the numerical analysis of the hole size distribution in a late stage of the process. Rectangular blocks of phase space that lie between  $w/l \in [0, 1]$  and  $a/l \in (k-1, k]$ , where  $k = 1, 2, 3, \dots$ , are identical in terms of the late-stage asymptotic behavior. A representative block of the phase diagram for  $k = 2$  is presented in figure 3.5. The authors identified the following regions with different forms of small hole size distribution, yielding different types of convergence to jamming:

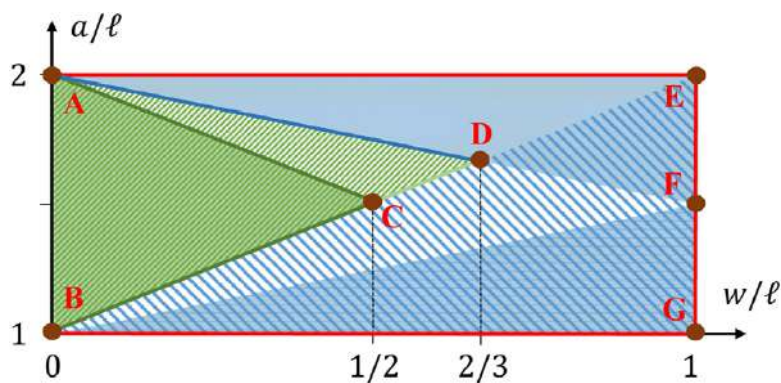


Figure 3.5: Different regions of convergence to jamming as described in the text [2].

- (i) Triangle **ABC**, including edges, excluding point **B**: exponential convergence, exact ( $k$ )-mer on a lattice adsorption dynamics  
 $n(h, t_a) \sim \delta(h - w) \Rightarrow \Delta\theta(t) \sim e^{-Rt}$
- (ii) Pentagon **ADBGE**, excluding edges: algebraic convergence  
 $n(h \rightarrow 0, t_a) \sim \text{const.} \Rightarrow \Delta\theta(t) \sim 1/t$
- (iii) Lines **[AE]**, **[EG]** and **[GB]**: exact car parking solution  
 $n(h \rightarrow 0, t_a) \sim \text{const.} \Rightarrow \Delta\theta(t) \sim 1/t$
- (iv) Triangle **ACD**, including edge **(CD)** and excluding edges **[AC]** and **[AD]**: modified exponential convergence  
 $n(h \rightarrow h_{min}^+, t_a) \sim \text{const.}$  and  $n(h < h_{min}, t_a) = 0 \Rightarrow \Delta\theta(t) \sim e^{-\Phi h_{min} t} / t$
- (v) Line **(AD)**: anomalous algebraic convergence  
 $n(h \rightarrow 0, t_a) \sim h \Rightarrow \Delta\theta(t) \sim 1/t^2$

Bonnier et al. [42] studied the following model: point-like adsorbing sites lie on a straight line at a distance  $l$  apart from each other and rods of length  $r$  are sequentially adsorbed at a random position on a line if they cover exactly one adsorbing site without overlapping any of the previously adsorbed rods. They pointed out that this model is equivalent to the RSA of dimers of length  $d + r$  on extended adsorption sites of size  $l$ , with distance  $d$  between every two adjacent sites. Adsorption occurs if both ends of a dimer fall on two adjacent sites without overlapping each other. Depending on the ratio  $r/l$ , asymptotic approach to the jamming coverage is similar to the normal continuous case ( $\Delta\theta(t) = A/t$ ) if  $r/l \in (2/3, 3/2)$ , to the monomer adsorption on a lattice if  $r/l \in (0, 1/2]$  or to the dimer adsorption on a lattice if  $r/l \in [3/2, 2)$  ( $\Delta\theta(t) = \exp(-\sigma t)$ ). In addition to the two usual late-stage approaches to jamming (algebraic and exponential), authors identified and termed asymptotic behaviour for  $r/l \in (1/2, 2/3)$  as non-trivial lattice dynamics given by

$$\Delta\theta(t) = \exp(-\sigma t) / t^2. \quad (3.7)$$

and for  $r/l = 2/3$  they found anomalous continuous dynamics:

$$\Delta\theta(t) = A/t^2. \quad (3.8)$$

We recognized that Bonnier's model is equivalent to a special case of the RSA on an imprecise lattice, the model studied in [1, 2]. In the first model, a line segment of length  $r$  sticks to the surface if it falls over exactly one localized site. In the second model, a line segment of length  $a$  will stick to an empty surface if its centre projection falls within an extended site of width  $w$ . To find the mapping of parameters between the two models let's look at the possible positions of the segment centre relative to the corresponding adsorbing site (for illustration see figure 3.6). We distinguish between two different cases:

- $r < l$ : when segment size  $r$  is smaller than the distance between two adjacent sites  $l$ , its centre can be as far as  $r/2$  to the left or right from the adsorbing site. This means that the extended site width is  $w = r$ ;





Figure 3.6: Illustration of equivalency of two models: (I) deposition of segments on localized adsorbing sites and (II) deposition of particles on extended lattice sites. On the left is a case of  $r < l$  and on the right a case of  $l < r < 2l$ .

- $l < r < 2l$ : when segment size  $r$  is larger than the distance between two adjacent sites  $l$ , its centre can be as far as  $l - r/2$  to the left or right from the adsorbing site due to the limitation that it can cover only one site. This means that the extended site width is  $w = 2l - r$ .

Non-overlapping conditions in two models are mutually consistent only if the length of the segment in the first model is equal to the length of the segment in the second model, i.e.  $r = a$ . Therefore, the first part of the phase space that Bonnier studied, having  $0 < r < l$ , corresponds exactly to a line  $a = w$  in the first quadrant of Verma's phase diagram (matching the line **B-C-D-E** in figure 3.5). The second part, where  $l < r < 2l$ , corresponds exactly to the line  $a = 2l - w$  in the second quadrant (line **G-C-A**).

There is a discrepancy between the results of the two studies [2] and [42] regarding the convergence to the jamming in the range of  $r \in (1/2, 2/3)$  which corresponds to a copy of the line **(CD)** in the first quadrant of the phase diagram (figure 3.5). Analytical study presented in [42] claims that asymptotic approach in this region has the form  $\Delta\theta(t) = \exp(-\sigma t)/t^2$ . Numerical analysis in [2] suggests the form  $\Delta\theta(t) = \exp(-\sigma t)/t$ . The authors presented only results for the second quadrant, but they claim that the results they obtained for the first quadrant are qualitatively the same. The quadratic correction to the exponential approach that Bonnier et al. [42] predict would result from a small hole size distribution that linearly vanishes at a non-zero threshold  $h_{min}$ . This type of distribution was not found by Verma and Privman [2]. The conclusions regarding the convergence to jamming in other segments are in complete agreement, with emphasis on point **D** ( $w = r = 2l/3$ ) where the anomalous algebraic approach is found:  $\Delta\theta(t) \sim 1/t^2$ . We will come back to this in section 6.2 where we find similar anomalous convergence for RSA on a two-dimensional imprecise lattice.

---

# Chapter 4

## Numerical simulation

Manipulation of the substrate pattern can yield monolayer deposits with desired properties. Our goal is to investigate the influence of substrate inhomogeneities on the coverage growth rate and the geometry of the final (jammed) state. In two-dimensional systems, it is possible to make some conjectures and reasonable ad hoc arguments to predict asymptotic behaviours, but for most practical purposes we turn to numerical simulations that are based on the Monte Carlo method. We developed a small C++ library to create and position landing cells and particles of various shapes and sizes and investigate relations between them. Using this library we easily created applications that simulated the process of random sequential adsorption of particles on a flat 2D pre-patterned substrate.

### 4.1 Monte Carlo method

The Monte Carlo method relies on random numbers, probability theory and statistics to estimate the probability of possible outcomes of an uncertain event. It is heavily exploited for numerical calculations of analytically unsolvable problems or problems with a large number of degrees of freedom in physics, mathematics, economy, finance, engineering, etc. It is used to estimate the solution of problems that are deterministic, as well as for predicting the outcomes of problems with inherently uncertain input variables. We used the Monte Carlo method in our simulation and estimated values of interest by averaging over a large number of generated RSA configurations.

Randomness is essential in our analysis, not just because we use the Monte Carlo method: the R in the RSA abbreviation stands for the word *random*. Adsorption of every particle is attempted at a randomly chosen position. This is why it was very important to use a good random number generator, capable of providing a large number of long, reproducible, unique, and independent streams of random numbers. It is time-consuming and expensive to obtain true random numbers in large quantities and numerical simulations often rely on a pseudo-random number generator. Our choice was the SPRNG library, available for FORTRAN and C/C++ programming languages. It provides high-quality pseudo-random numbers in a computationally inexpensive and scalable manner, reproducible streams of parallel pseudo-random numbers, independent of the number of processors used in the computation and of the loading produced by sharing of the parallel computer and allows for the cre-

ation of unique pseudo-random number streams on a parallel machine with minimal inter-processor communication [82]. Out of 6 available SPRNG generators, we opted for Combined Multiple Recursive Generator (CMRG) because of the good speed/quality ratio in regard to our use case. The period of this generator is around  $2^{219}$ . The number of distinct streams available is over  $10^8$ . It ensures that for a given fixed seed, each one of  $N$  total streams is independent of and uncorrelated to any other stream. To clarify, by stream we mean a unique sequence of random numbers generated by a given generator. We used the SPRNG library, version 4.4, in all of our simulations.

## 4.2 Simulation of Random Sequential Adsorption on patterned substrates

We study irreversible monolayer deposition of identical spherical particles with hard-core exclusion on a prepared flat nonuniform substrate. The substrate heterogeneities are represented by identical non-overlapping rectangular cells that are fixed on the substrate surface. The basic assumption of our model is that a particle can only be adsorbed if it is in contact with one of the cells, i.e. if the centre of its disk-shaped projection lies within one of the rectangles. The substrate can be prepared in many ways by arranging the rectangles to form different patterns. In this thesis, we are particularly interested in two types of patterns: (i) Random pattern, formed by RSA deposition of square or rectangular cells, arbitrary oriented or aligned, and (ii) square lattice pattern, formed by square cells with midpoints at the vertices of a square lattice and with sides parallel to the lattice main axes. The non-overlapping condition for cells is in force in both cases. Consequently, in the case of a square lattice pattern, the distance between cell centres (lattice constant) must be greater than the cell sides.

In our study, the radius of depositing particles is fixed and comparable with the typical geometrical cell length. Moreover, we assume that the size of the particles is much larger than the length scale between binding sites so that adsorption over the length scale of cell linear dimensions can be regarded as an off-lattice process.

Our model forbids the deposited particles to diffuse along or desorb from the substrate on the time scale of the dense coverage formation. This means that adsorbed particles are permanently fixed to their spatial positions. The deposit growth rate depends on a flux of incoming particles, and for all of our purposes, we considered that this flux is uniform and at a constant rate. To reduce the effects of a finite substrate, we use periodic boundary conditions in both directions. These assumptions are typical of the RSA model.

The entire simulation procedure consists of three main stages:

1. Initialization:

Simulation parameters are set in accordance with provided input arguments.

2. Substrate preparation:

Identical rectangle cells are positioned over the simulation area to form a selected type of pattern, with respect to the input parameters. Upon completion of this phase, the substrate is completely prepared and stays unchanged through the rest of the simulation.

### 3. Deposit formation:

An attempt of single-particle deposition is repeated in a loop. The deposition attempt starts by generating a random position of a test particle within the simulation area. Next, we check if the disk's centre falls outside of all landing cells and if it overlaps any of the previously adsorbed disks. The disk deposition attempt fails if any of these two checks are true. If the deposition attempt is successful, the particle becomes a permanent part of the deposit at its fixed position.

Simulation input parameters are following: particle radius  $r_0 = d_0/2$ , cell sides  $\alpha$  and  $\kappa\alpha$ , cell coverage  $\theta_0^{(cell)}$  (for random pattern) or lattice constant  $\gamma = \alpha + \beta$  (for regular substrate), substrate size  $L$ , maximum number of adsorption attempts  $N_{max}$ , maximum number of failed adsorption attempts  $N_{idle}$ , and random number generator initialization parameters (seed, stream ordinal number and total number of streams). Simulation outputs the particle position and the ordinal number of deposition attempts for every successful adsorption. The ordinal number is converted to time as explained later in section 4.3.

Formations of random and regular patterns in the simulation are governed by different rules and sets of parameters, and both of them are individually described in the sections that follow. While for a random pattern we have to prepare substrate differently for every run, a regular pattern is always the same for the same parameters.

## 4.2.1 Preparation of randomly patterned substrate

At the start, the simulation substrate surface is an empty flat square area of size  $L \times L$ . We used  $L = 256d_0$ , as this value gave us sufficient precision in the available amount of computer time. Substrate preparation starts by performing the basic RSA algorithm with rectangular cells: a cell is randomly positioned at the substrate, and it is permanently attached to the surface if it doesn't overlap any of the previously adsorbed cells. If an overlap occurs, the adsorption of the cell is rejected. New adsorption attempts are repeated in the same way, up to the point when we reach the desired coverage fraction. This coverage must be smaller than the jamming coverage for landing cells ( $\theta_0^{(cell)} \leq \theta_j^{(cell)}$ ). In this way, we can prepare randomly patterned heterogeneous substrate with a statistically reproducible density  $\theta_0^{(cell)}$ .

In the random pattern model, each landing cell is a rectangle with sides  $a$  and  $\kappa a$  ( $\kappa \leq 1$ ) whose midpoint is located on a continuous substrate. The cells can take arbitrary orientations, but in some numerical simulations, we introduced alignment in the deposition procedure for landing cells. This simple modification introduces a preferential direction in the deposition process and, depending on the aspect ratio of deposited rectangles, imposes specific "patterning" on the deposited layer. We re-scale the lengths relative to the diameter of the disks  $d_0$ , and define three dimensionless parameters:

$$\alpha = \frac{a}{2r_0}, \quad \lambda = \frac{a}{\kappa a} \quad (4.1)$$

$$\gamma = \frac{\alpha}{\sqrt{\theta_0^{(cell)}}} \quad (4.2)$$

The parameter  $\gamma$  (an average distance between cell centres) is a meaningful measure only if the landing cells are squares ( $\lambda = 1$ ).

For a few fixed pairs of values of parameters  $\alpha$  and  $\lambda$ , simulations were carried out for various values of  $\theta_0^{(\text{cell})}$ , ranging from 0.10 to 0.50. For each case, the simulations are carried out up to  $10^{10}$  deposition attempts, or up until  $L^2 \times 10^4$  consecutive deposition attempts are rejected. The results are obtained by averaging over 100 simulation runs.

## 4.2.2 Preparation of regularly patterned substrate

We investigated a regular pattern that consists of square cells whose midpoints are positioned in the nodes of a regular square lattice. Cell sides are parallel to the main axes of the lattice. The geometry of the regular pattern is controlled by the two dimensionless parameters,  $\alpha$  and  $\beta$ , measured in terms of the particle diameter  $d_0 = 2r_0$ . Parameter  $\alpha$  is the cell side size, and parameter  $\beta$  is the shortest distance between the parallel sides of the nearest neighbouring cells. The distance between neighbouring cell midpoints is  $\gamma = \alpha + \beta$ . We considered only configurations in which cells do not overlap each other ( $\beta > 0$ ). The case of  $\beta = 0$  is equivalent to a homogeneous substrate for all values of  $\alpha$ . Cases where cells can accommodate one particle at most ( $\alpha < \sqrt{2}/2$ ) and cell-cell separation is larger than the particle diameter ( $\beta > 1$ ) are equivalent to the lattice site adsorption in regard to kinetics.

One or more disks can attach to each cell depending on the cell size  $\alpha$ . For  $\alpha < 1/\sqrt{2} \approx 0.707$ , at most a single disk can be adsorbed at any given square cell. We denote this case as single-particle per-cell adsorption (SPCA). For squares with  $\alpha \geq 1/\sqrt{2}$ , more than a single disk can be placed in the square cell, and we denote this as multi-particle per-cell adsorption (MPCA). If distances between neighbouring cells are smaller than particle diameter ( $\beta < 1$ ), a disk attempting adsorption on a given cell can overlap with a previously adsorbed one belonging to a neighbouring cell, resulting in a failed adsorption attempt. This excluded volume “interaction” between particles during adsorption at *different* cells affects the overall structure of the adsorbed layer and causes a slower asymptotic approach of the coverage fraction  $\theta(t)$  to its jamming limit [45, 83]. Such regime is denoted *interacting cell-cell adsorption* (ICCA). For  $\beta \geq 1$ , disks attempting adsorption cannot overlap other disks in neighbouring cells, yielding the *non-interacting cell-cell adsorption regime* (NICCA). Deposition kinetics in the regime of NICCA is completely determined by the kinetics of adsorption of particles on a finite-size substrate (a single cell) with appropriate boundary conditions [45, 83].

We performed the Monte Carlo simulations on a planar substrate with typically  $256 \times 256$  landing cells. Some cases of landing-cell configurations required more precise measurements and we had to increase the size of the substrate to  $1024 \times 1024$ . We also needed to increase the number of average adsorption attempts per cell, which resulted in a longer simulation execution time.

## 4.2.3 Particle deposition

After the substrate is prepared, we start the RSA process for identical spherical particles of diameter  $d_0$ . Since the adsorption was only possible within the landing cells, we optimized the simulation accordingly. Adsorption attempts were only made within the randomly selected cell. We omit out-of-cell adsorption attempts and therefore testing whether particle fell on the cell becomes redundant. To make up for this omission we have to scale the time step between consecutive attempts by the factor

(total area)/(total cell area). We generate and position particles, one by one, within a randomly chosen landing cell, and then test if they do not overlap previously adsorbed particles. If the condition is met, the test particle becomes a permanent part of the deposit.

The adsorption attempts are repeated until we reach the jammed state, where only gaps too small to accommodate new particles are left on the cells. In some cases, it can take a very long time to fill in every single gap. For practical reasons, we modified the simulation termination condition. The simulation ends when a given total number of attempts is reached or when a number of consecutive failed attempts exceeds the given maximum idle time. These two numbers are given as input parameters to the simulation at run-time, and they differ depending on the system size and parameters. In the case of single-particle per cell, an additional condition is given: simulation can end when every cell in the substrate adsorbs a particle. Note that this condition can never be met for some pattern configurations.

### 4.3 Time scaling and optimizations

The dimensionless adsorption time  $t$  is set to zero at the beginning of the second stage. It is then gradually increased by an increment  $\Delta t$ , given by  $\Delta t = \pi r_0^2 / L^2$ , each time an attempt is made to deposit a disk of radius  $r_0 = d_0/2$  on a square surface (collector) of area  $L^2$ . Consequently, we define dimensionless adsorption time  $t = N_{\text{att}} \pi r_0^2 / L^2$ , where  $N_{\text{att}}$  is the overall number of attempts to place disk particles. By plotting coverage  $\theta(t)$  versus the adsorption time  $t$ , defined above, one can simulate the kinetics of particle adsorption.

To optimize the computing time in the case of a regular pattern, deposition is attempted only inside the cells. We chose a random cell and attempt to deposit a particle at a random position within that cell. This optimization affects time scaling, so that the time increment can be calculated as  $\Delta t = \frac{\pi r_0^2 (\alpha + \beta)^2}{L^2 \alpha^2}$ . In some cases, we wanted to reach very large times which required further optimizations of our calculations. When cells are small enough and can be occupied by one particle at most, we try to achieve the deposition events only in free cells. Then, the time  $t$  is increased after every deposition attempt by an increment  $\Delta t = \frac{\pi r_0^2 (\alpha + \beta)^2}{N_{\text{free}} \alpha^2}$ , where  $N_{\text{free}}$  is the number of free cells. These optimizations do not affect typical jammed state configurations nor the statistically averaged value of  $\theta(t)$ . However, the standard deviation of  $\theta(t)$  is significantly reduced.



---

# Chapter 5

## Randomly patterned substrates

This chapter explores the effect of the presence of randomly patterned substrate on the structural properties of the jammed state of the monolayer deposit. Heterogeneities of a substrate impose further limitations on the positions of adsorbed particles. We consider the irreversible deposition of disks of a fixed diameter  $d_0$  whose centres must fall inside one of the cells arranged at the surface. For simplicity, we will use the length scale in which  $d_0 = 1$  throughout the whole chapter. The cells are positioned in a prior, independent RSA process, conducted until the desired cell density  $\theta_0^{(cell)}$  is reached. Following the rules of RSA, cells do not overlap each other and they are permanently fixed to their spatial positions. A prepared substrate surface stays unaltered throughout the disk deposition process.

In the first part of this chapter, we present and discuss the results of numerical simulation for random deposition of identical disks on pre-patterned substrates covered by randomly positioned squares of arbitrary orientation. We characterize the jammed state in terms of the radial distribution function of the particle centres and the distribution of the Delaunay “free” volumes. In addition, we compare the impact of a regular vs. random pattern on the deposit structure. The second part of this chapter is devoted to the analysis of the adsorption of disks on randomly positioned rectangular cells deposited with arbitrary and fixed orientations.

### 5.1 Square cells

We are interested in the adsorption of disks on substrates prepared by random sequential adsorption of identical square cells of arbitrary orientation. The cell size  $\alpha$  determines how many particles can attach to a cell, provided that the attachment condition is that a particle centre lies inside of the cell. We investigate the cells whose size is comparable with the size of adsorbing particles, and the number of disks adsorbed per cell is a small number (less than five). With  $\alpha_k$  we denote the largest size of a square that can fit at most  $k$  disks. For  $\alpha < \alpha_1 = 1/\sqrt{2}$ , at most one disk can be adsorbed at any given square cell. We denote this case as single-particle per-cell adsorption (SPCA). More than one disk can be placed in the square cell if  $\alpha \geq 1/\sqrt{2}$ , and we denote this as multi-particle per-cell adsorption (MPCA). The cases of up-to-two, -three and -four disks per square cell are obtained, respectively, for



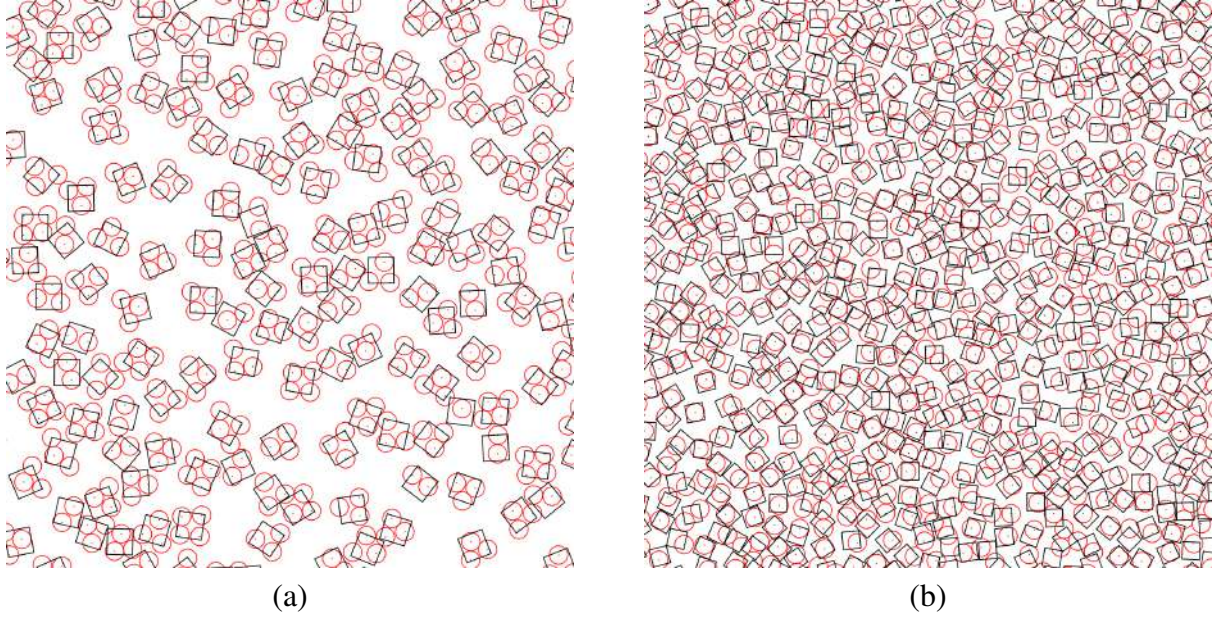


Figure 5.1: Typical jammed-state configuration of a region of size  $30 \times 30$  in units of the disk diameter  $d_0$ , for (a)  $\theta_0^{(\text{cell})} = 0.3$ ,  $\alpha_4 = \sqrt{2} \approx 1.41$ , and (b)  $\theta_0^{(\text{cell})} = 0.5$ ,  $\alpha_2 = (1 + \sqrt{3})/(2\sqrt{2}) \approx 0.966$ .

$\alpha$  smaller than  $\alpha_2 = (1 + \sqrt{3})/(2\sqrt{2}) \approx 0.966$ ,  $\alpha_3 = 1$  and  $\alpha_4 = \sqrt{2}$ .

The effect of density of landing cells  $\theta_0^{(\text{cell})}$  on the adsorption process is illustrated in figure 5.1 by snapshots of the jammed-state coverings for (a)  $\theta_0^{(\text{cell})} = 0.3$  and (b)  $\theta_0^{(\text{cell})} = 0.5$ , for two values of the cell size  $\alpha$ , namely,  $\alpha_4 = \sqrt{2} \approx 1.41$  [figure 5.1(a)] and  $\alpha_2 = (1 + \sqrt{3})/(2\sqrt{2}) \approx 0.966$  [figure 5.1(b)]. For low values of  $\theta_0^{(\text{cell})}$ , adsorption on a given cell is weakly affected by disks previously adsorbed on neighboring cells. Therefore, most of the cells shown in figure 5.1(a) contain at least three discs. However, in the case shown in figure 5.1(b) one can see a significant impact of the cell-cell excluded volume interaction on the cell population. Although each cell has enough area to accommodate up to two disks, only one disk is attached to the majority of the cells.

### 5.1.1 Adsorption on low cell density substrate

In the low limit of cell density  $\theta_0^{(\text{cell})} \rightarrow 0$ , the average distance between two cells is much larger than the diameter of a disk. It is very rare that a particle from one cell can block the available space in another cell. This limit is called the non-interacting mode in which the cell-cell interactions are negligible. The adsorption kinetics is then equivalent to the adsorption kinetics on a single cell if time is appropriately scaled to account for the low cell density. The jamming limit is also dictated by the RSA on a single cell:

$$\theta_J = \frac{\langle n(\alpha) \rangle \pi \theta_0^{(\text{cell})}}{4\alpha^2}, \quad (5.1)$$

where  $\langle n(\alpha) \rangle$  is the average number of disks on a single jammed cell, attached in a RSA process. Equation (5.1) estimates the jamming density well for sufficiently low cell densities  $\theta_0^{(\text{cell})} \lesssim 0.2$ .

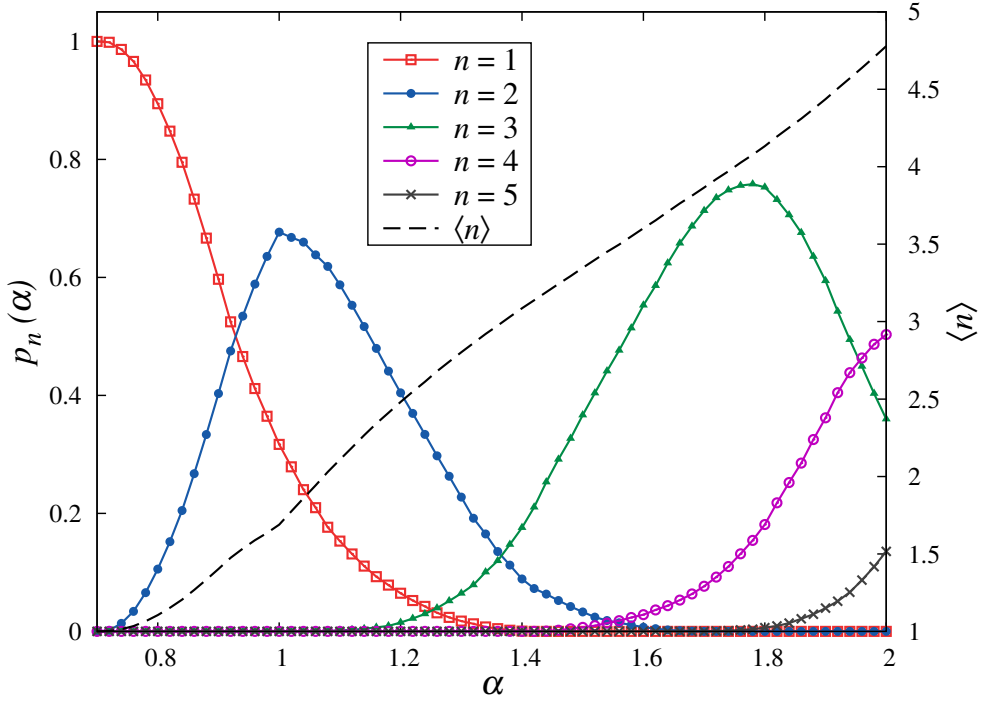


Figure 5.2: Simulation results for the probability that the configurations with  $n = 1, 2, \dots, 5$  disks occur on square cell of size  $\alpha$  in the non-interacting cell-cell adsorption regime (left-hand axis). The dashed line is plotted against the right-hand axis and gives the simulation results for the average number of particles per cell  $\langle n \rangle$  as a function of the cell size  $\alpha$  in the non-interacting cell-cell adsorption regime.

The dashed (black) line in figure 5.2 shows the simulation results for the mean number of particles per cell  $\langle n(\alpha) \rangle$  as a function of cell size  $\alpha$  in the non-interacting cell-cell adsorption regime (i.e., in the case of single-cell on a substrate). In addition, in figure 5.2 we show the probabilities that the jammed square cell of size  $\alpha$  captures  $n = 1, \dots, 5$  disks in the non-interacting cell-cell adsorption regime. If  $\alpha = \alpha_1 \approx 0.707$ , each landing cell (square) can contain no more than one disk. If  $\alpha = \alpha_2 \approx 0.966$ , the number of cells with one and two disks is approximately equal and  $\langle n(\alpha_2) \rangle \lesssim 1.6$ . However, if density  $\theta_0^{(\text{cell})}$  is constant, then the increase of the cell size  $\alpha_1 \rightarrow \alpha_2$  reduces the total number of landing cells on the substrate by a factor  $\approx 2$ . A reduction in the number of adsorbed disks is a consequence of these two effects. In figure 5.2 we see that the growth of  $\langle n(\alpha) \rangle$  only slightly deviates from linear in the shown range of  $\alpha_1 < \alpha < 2$ . Due to the quadratic dampening factor in equation (5.1), which indicates that the jamming density  $\theta_J$  decreases with cell size  $\alpha$  at fixed density  $\theta_0^{(\text{cell})}$ , which is illustrated in figure 5.3. The solid line shows the relative jamming coverage  $\theta_J/\theta_0^{(\text{cell})}$  in the non-interacting mode, while the dashed line represents the case of maximum packing per cell. Although the maximal packing density function is quite jagged with discontinuous jumps at  $\alpha = \alpha_k$ , the randomness in the positioning of particles in an RSA process smooths out the jamming density function.

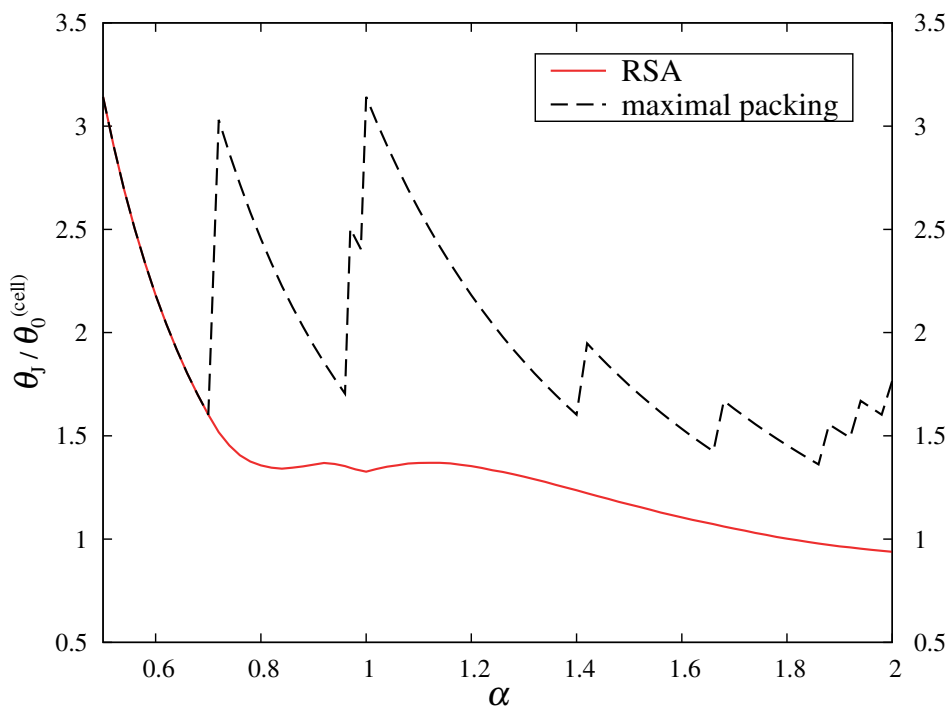


Figure 5.3: RSA jamming density (solid line) vs. maximal packing density (dashed line) relative to the cell density in the non-interacting mode.

### 5.1.2 Densification kinetics

Kinetics of the irreversible deposition of disks is illustrated in figures 5.4(a) – 5.4(e) where the plots of time coverage behavior  $\theta(t)$  are given for the five values of coverage fraction of landing cells,  $\theta_0^{(\text{cell})} = 0.1, 0.2, 0.3, 0.4, 0.5$ . Here the plots of such time-dependence are shown for various values of the cell size,  $\alpha_k$  ( $k = 1, 2, 3, 4$ ). It can be seen that for a fixed density of landing cells  $\theta_0^{(\text{cell})}$ , jamming coverage  $\theta_J = \lim_{t \rightarrow \infty} \theta(t)$  decreases with increasing the cell size  $\alpha_k$ . This effect is clearly visible in the case of the lowest density of the landing cells  $\theta_0^{(\text{cell})} = 0.1$  (figure 5.4(a)), when the average distance between the squares  $\gamma$  (equation (4.2)) is several times larger than the diameter of the disks, as discussed in previous section.

As can be seen from figure 5.4, the time coverage behaviour  $\theta(t)$  is markedly slowed down with the increase of the cell size  $\alpha$  for the fixed density of landing cells  $\theta_0^{(\text{cell})}$ . Indeed, in the MPCA case, large times are needed for filling small isolated vacant targets on landing cells, remaining in the late stages of deposition. Furthermore, in this regime, density curves  $\theta(t)$  show a noticeable slowing down of the deposition process at coverages that are significantly smaller than jamming densities. Coverage growth starts to slow down at the moment when the number of adsorbed disks reaches the number of landing cells. After this initial filling of the landing cells, adsorption events take place on isolated islands of partially occupied cells. This extends the time interval between successful consecutive adsorption events and causes a slowing down of the densification.

The results for the time evolution of the coverage  $\theta(t)$  in the case of up-to-two disks per square cell

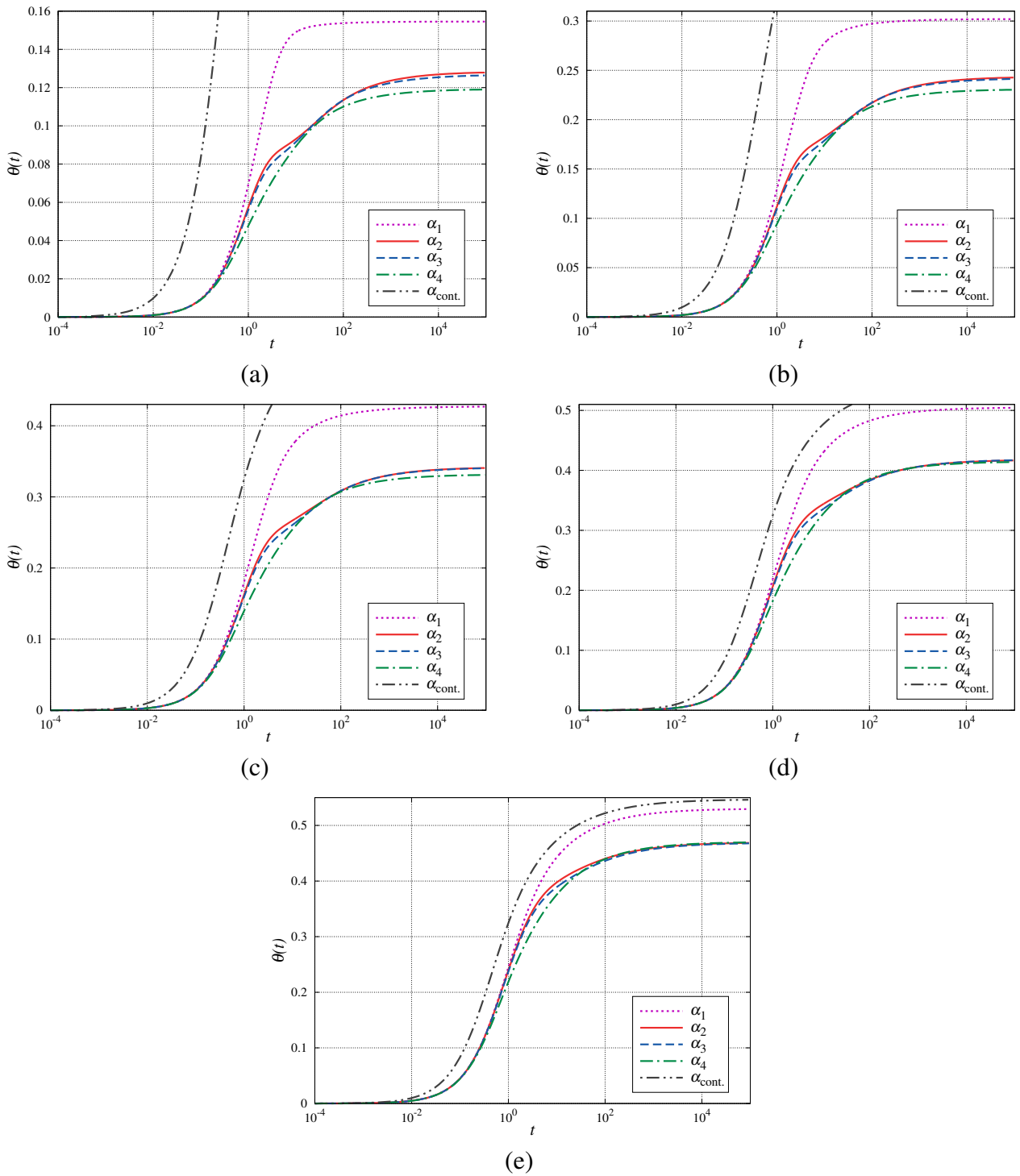


Figure 5.4: Shown here is the time evolution of the coverage fraction  $\theta(t)$  for the five values of density of landing cells,  $\theta_0^{(\text{cell})} = 0.1$  (a), 0.2 (b), 0.3 (c), 0.4 (d), 0.5 (e). The curves in each graph correspond to various values of the cell size,  $\alpha_k$  ( $k = 1, 2, 3, 4$ ), as indicated in the legend. The  $\alpha_{\text{cont}}$  line shows the time dependence of the coverage  $\theta(t)$  for RSA of disks on a continuous substrate. The entire  $\alpha_{\text{cont}}$  curve can be seen in plot (e).

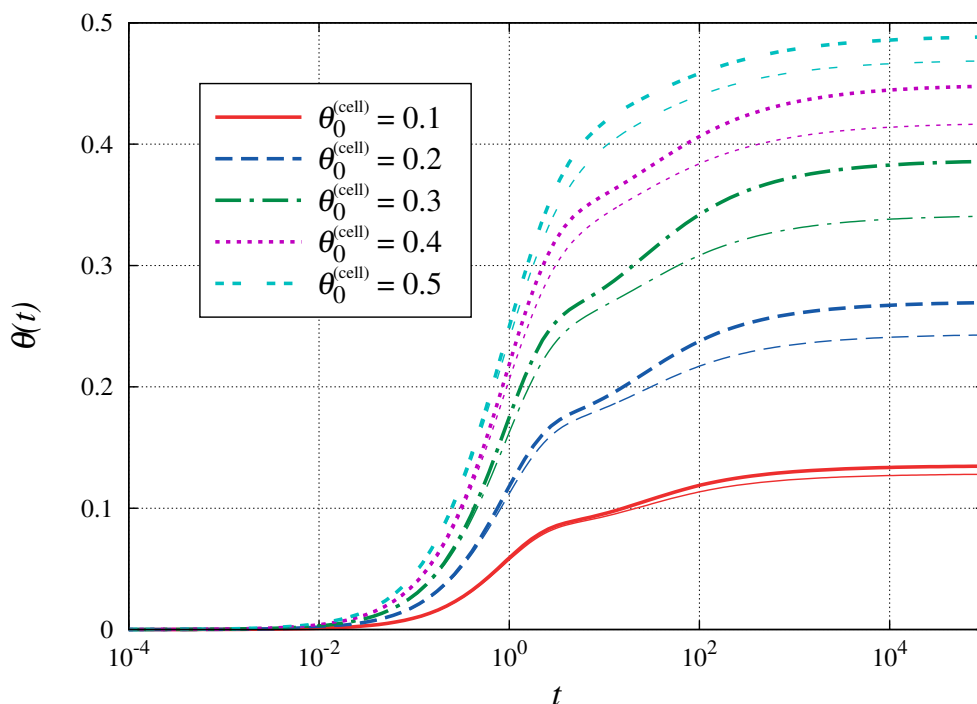


Figure 5.5: Temporal behavior of the coverage  $\theta(t)$  for various values of  $\theta_0^{(\text{cell})}$  in the case of up-to-two disks per square cell (cell size:  $\alpha_2 = (1 + \sqrt{3})/(2\sqrt{2}) \approx 0.966$ ). The curves correspond to various values of density  $\theta_0^{(\text{cell})} = 0.1 - 0.5$ , as indicated in the legend. Thick lines represent results obtained for regular substrate pattern while thin lines are results for random pattern case.

( $\alpha = \alpha_2$ ) are shown in figure 5.5 for various values of  $\theta_0^{(\text{cell})}$ . Qualitatively similar results are obtained with landing cells of other sizes  $\alpha$ . As expected, the jamming density  $\theta_J$  increases with higher coverage fraction of landing cells  $\theta_0^{(\text{cell})}$ . At high values of  $\theta_0^{(\text{cell})} \lesssim 0.5$  when  $\gamma \sim 1$ , a disk attempting adsorption can overlap with a previously adsorbed one belonging to a different cell, resulting in a failed adsorption attempt. This excluded volume interaction between particles during adsorption at *different* cells causes an even slower asymptotic approach of the coverage fraction  $\theta(t)$  to its jamming limit. In addition, the analysis of the time evolution of the coverage  $\theta(t)$  was carried out for deposition on square cells centred at the vertices of a square lattice. Consequently, the temporal evolution of the coverage  $\theta(t)$  obtained for regular substrate pattern is included in figure 5.5. Here, the size  $\alpha$  and density  $\theta_0^{(\text{cell})}$  of landing cells are the same as those used in our previous calculations for the random pattern cases. It can be seen that lower values of the jamming coverage fraction are reached by the deposition process involving randomness in the pattern compared to a deposition process in the presence of a regular substrate pattern, regardless of the value of the density  $\theta_0^{(\text{cell})}$ .

### 5.1.3 Asymptotic behaviour

Below we try to characterize quantitatively the time dependence of the approach to the jammed state at large times. Depending on the system of interest modelled by RSA, the substrate can be continuous (off-lattice) or discrete. The asymptotic approach of the coverage fraction  $\theta(t)$  to its jamming limit,

$\theta_J = \theta(t \rightarrow \infty)$ , is known to be given by an algebraic time dependence for continuous substrates [5, 36, 49, 50, 71]:

$$\theta(t) \sim \theta_J - At^{-1/d}, \quad (5.2)$$

where  $A$  is a constant coefficient and  $d$  is interpreted as substrate dimension [49] in the case of spherical particles adsorption or, more generally, as a number of degrees of freedom [48]. For lattice RSA models, the approach to the jamming coverage is exponential [27, 67–69, 84, 85]:

$$\theta(t) \sim \theta_J - \Delta\theta \exp(-t/\sigma), \quad (5.3)$$

where parameters  $\theta_J$ ,  $\Delta\theta$ , and  $\sigma$  depend on the shape and orientational freedom of depositing objects [68, 69].

Representative examples of the double logarithmic plots of the first derivative of coverage  $\theta(t)$  with respect to time  $t$  are shown in figure 5.6(a), for various values of the cell size,  $\alpha_k$  ( $k = 1, 2, 3, 4$ ), and for high density of landing cells,  $\theta_0^{(\text{cell})} = 0.5$ . The time derivatives of  $\theta(t)$  are calculated numerically from the simulation data. In the case of the algebraic behavior of the coverage fraction  $\theta(t)$  (equation (3.3)), a double logarithmic plot of the first time derivative  $\frac{d\theta}{dt} \propto t^{-\frac{1+d}{d}}$  is a straight line. One can see that the curves shown in figure 5.6(a) are straight lines in the late stage of a deposition process. However, the same is not valid for all values of densities of landing cells  $\theta_0^{(\text{cell})}$ . The double logarithmic plots of the numerically calculated derivatives of  $\theta(t)$  for the data obtained in the case of a low density of landing cell  $\theta_0^{(\text{cell})} = 0.1$  are shown in figure 5.6(b). As it can be seen, at the very late times of the deposition process the plot of the first derivative of coverage fraction  $\theta(t)$  with respect to time  $t$  is not linear on a double logarithmic scale, indicating that the approach to the jamming limit is not consistent with the power-law behaviour given by equation (3.3). The deviation from the power law is particularly pronounced in the case of single-particle per-cell adsorption (SPCA).

Kinetics of the irreversible deposition under SPCA conditions is illustrated in figure 5.7 where a

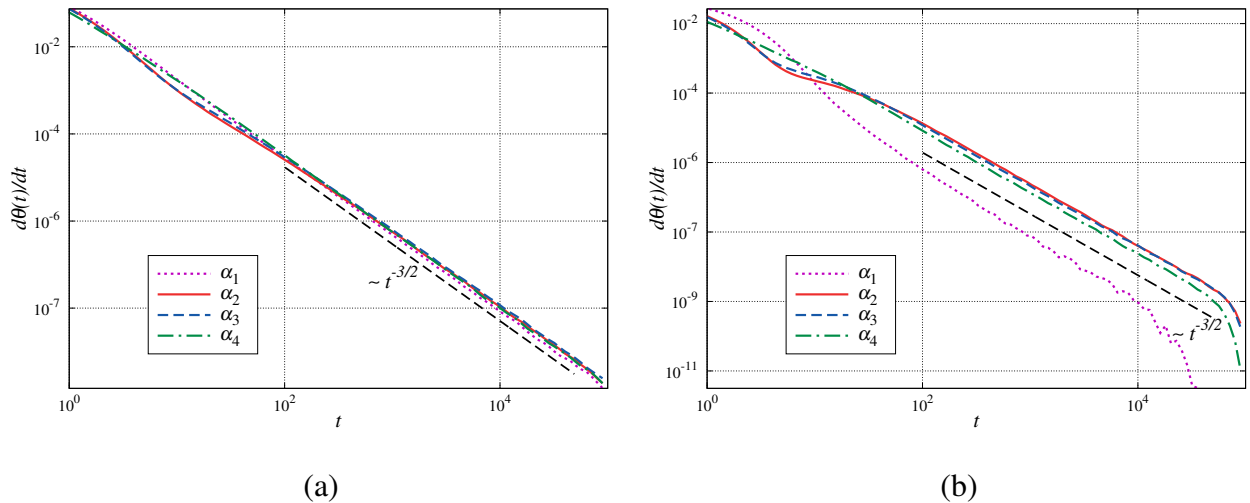


Figure 5.6: Test for the presence of the algebraic law (3.3) in the approach of the coverage  $\theta(t)$  to the jamming limit for different densities of landing cells: (a)  $\theta_0^{(\text{cell})} = 0.5$ , and (b)  $\theta_0^{(\text{cell})} = 0.1$ . The curves in each graph correspond to various values of the cell size,  $\alpha_k$  ( $k = 1, 2, 3, 4$ ), as indicated in the legend. Straight-line sections of the curves show where the law holds. The dashed black line has the slope  $-3/2$  and is a guide for the eye.

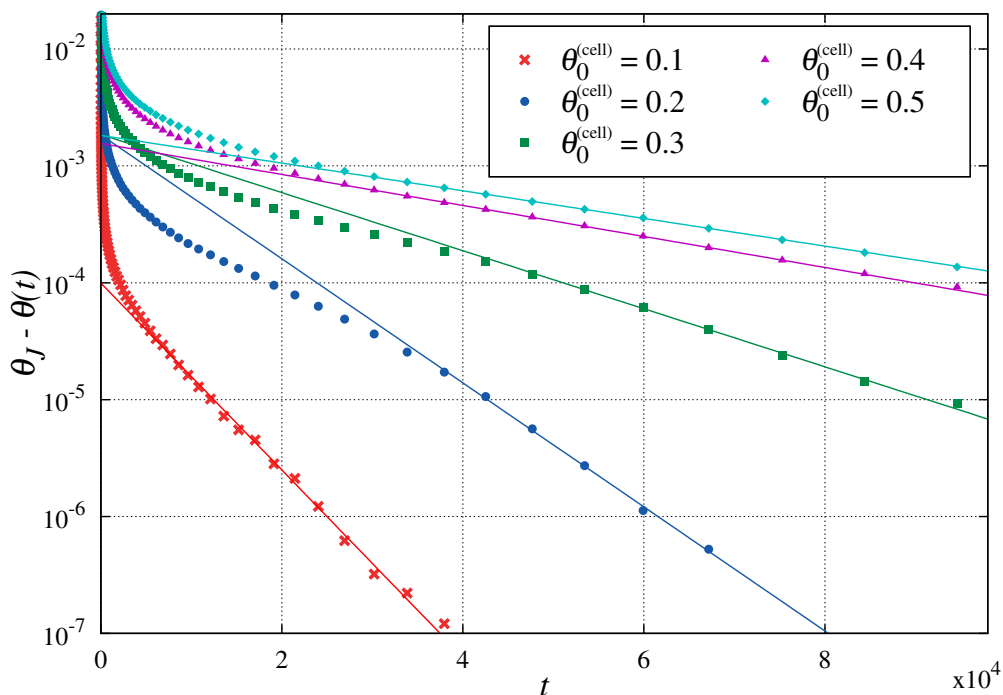


Figure 5.7: Plots of  $\theta_J - \theta(t)$  versus  $t$  in the single particle per-cell adsorption case for various densities of landing cells  $\theta_0^{(\text{cell})} = 0.1 - 0.5$ . The solid lines are the exponential fit of equation (5.3).

logarithmic plots of  $\theta_J - \theta(t)$  vs  $t$  are shown for various densities of landing cells  $\theta_0^{(\text{cell})}$ . These plots are straight lines for the late times of deposition, suggesting that in the case of SPCA the approach to the jamming limit is indeed exponential, as in lattice RSA models. Indeed, the kinetics of deposition in the SPCA case is determined by the kinetics of adsorption processes on finite-size landing cells. The difference relative to the lattice RSA is in the particle positions, which here are uncertain within the order of the size of the cell.

#### 5.1.4 Radial distribution function

Here we compare quantitatively the structural characteristics of jamming coverings corresponding to different values of the cell size  $\alpha$  for various densities  $\theta_0^{(\text{cell})}$ . In order to gain basic insight into the “microstructure” of the jammed state, we first consider the radial distribution function  $g(r)$  (or pair-correlation function) which gives information about the long-range inter-particle correlations and their organization [47]. In absence of external forces, the pair correlation function can be calculated from the expression

$$g(r) = \frac{S \bar{N}_a(r)}{N 2\pi r \Delta r}, \quad (5.4)$$

where  $r$  is the radial coordinate,  $S$  is the surface area,  $N$  is the total number of particles adsorbed over this area, and  $\bar{N}_a$  is the averaged number of particles within the annulus of the radius  $r$  and the thickness  $\Delta r$ . In figure 5.8(a) we compare the radial distribution function  $g(r)$  at various densities  $\theta_0^{(\text{cell})} = 0.1 - 0.5$  in the SPCA case. As expected, the random deposition process never leads to

correlation distances between the deposited particles exceeding two or three particle diameters. The position of the first peak measures typical distances between the closest disks. Decreasing the value of  $\theta_0^{(\text{cell})}$  in the SPCA case increases the uncertainty in the position of the particles which leads to peak broadening. The shape of radial distribution  $g(r)$  is more structured at higher densities, showing higher first and second peaks, because, when the system gets denser, particles will be deposited closer to one another. As can be seen from figure 5.8(a), the minima of  $g(r)$  curves shift to shorter distances ( $\sim \sqrt{3}$ ) when the density  $\theta_0^{(\text{cell})}$  increases. At very low densities, the broad minima are located near the distance  $\sim 2d_0$ . Indeed, since the particles are added at random, the probability that disks are connected as a three-bead chain is negligible.

The results for  $g(r)$  in the MPCA case are shown in figures 5.8(b) – 5.8(d). The shape of the radial distribution function  $g(r)$  is significantly affected by the values of the cell size  $\alpha$ . In the case of up-to-two disks per square cell (figure 5.8(b)) the peak which appears at a unit distance is the most pronounced for low densities of landing cells  $\theta_0^{(\text{cell})}$ . For low values of  $\theta_0^{(\text{cell})}$ , one expects a lower impact of the cell-cell excluded volume interaction on the cell population. However, as

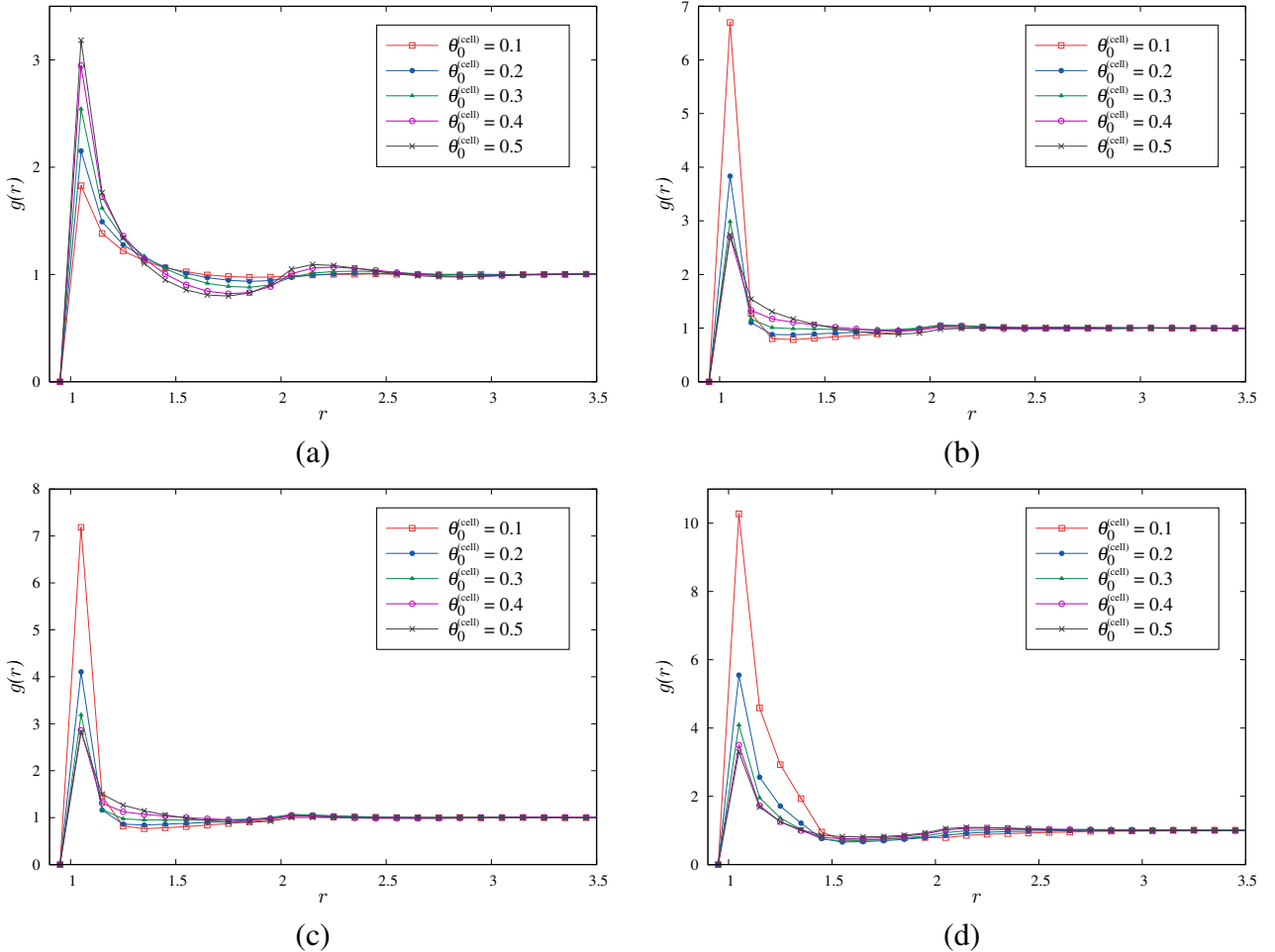


Figure 5.8: Radial distribution function  $g(r)$  for jamming coverings as a function of separation  $r$  (in units of the disk diameter  $d_0$ ) for various values of the cell size  $\alpha$ : (a)  $\alpha_1 = 1/\sqrt{2}$ , (b)  $\alpha_2 = (1 + \sqrt{3})/(2\sqrt{2})$ , (c)  $\alpha_3 = 1$ , (d)  $\alpha_4 = \sqrt{2}$ . The curves in each graph correspond to various values of density  $\theta_0^{(\text{cell})} = 0.1, 0.2, 0.3, 0.4, 0.5$ , as indicated in the legend.



$\theta_0^{(\text{cell})}$  increases, the first peak of  $g(r)$  becomes broader because excluded volume interaction with disks belonging to neighbouring cells reduces the average number of adsorbed disks per cell. This is opposite to what is observed under SPCA conditions (figure 5.8(a)), where the distance to the closest disk, on average, is determined by the distance of the nearest-neighbour landing cells.

The comparison of figures 5.8(b) and 5.8(c) shows that the results for  $g(r)$  in the case of up-to-two and up-to-three disks per square cell are very similar. This arises as a direct consequence of the fact that cells with sizes  $\alpha_2 \approx 0.966$  and  $\alpha_3 = 1$  have very similar population of particles (see figure (5.2)). Figure 5.8(d) shows the radial distribution function  $g(r)$  of jamming coverings at several densities  $\theta_0^{(\text{cell})}$  obtained in simulations carried out with the cell size of  $\alpha_4 = \sqrt{2}$ . For this value of the parameter  $\alpha$ , each cell is of sufficient size to accommodate up to four particles. As can be seen in figures 5.8(b) – 5.8(d), increasing the value of parameter  $\alpha$  in the MPCA case increases the uncertainty in the position of the disk within the cell, i.e., it leads to peak broadening.

### 5.1.5 Volume distribution of pores

The jammed-state coverings are analyzed in terms of volume distributions of the pores. The convenient definition of a pore is based on the Delaunay triangulation (DT), which is a natural way to subdivide a 2D structure of disks into a system of triangles with vertices at the centres of neighbouring disks. Consequently, the circle circumscribing a Delaunay triangle has its centre at the vertex of a Voronoï polygon. In this work, we define the pore as a part of the Delaunay triangle not occupied by the disks (Delaunay “free” volume) [57, 58]. The pore volume  $v$  is normalized by the “volume” of the disks,  $v_0 = d_0^2 \pi / 4$ . In figure 5.9 we show Delaunay triangulation of typical jammed-state covering obtained for the same conditions as in figure 5.1(a) ( $\theta_0^{(\text{cell})} = 0.3$ ,  $\alpha_4 = \sqrt{2} \approx 1.41$ ). Looking at the diagram of figure 5.9, one can observe variations in the area of Delaunay triangles, which indicates the presence of pores of various sizes in the deposit.

Here we consider the probability distribution  $P(v)$  of the Delaunay “free” volume  $v$ . The distribution function  $P(v)$  represents the probability of finding a pore with volume  $v$ . Fluctuations in the measurements of  $P(v)$  are reduced by averaging over 100 different simulations, performed under the same conditions. We compare volume distribution of the pores  $P(v)$  for jamming coverings corresponding to different values of the cell size  $\alpha$  and various densities of landing cells  $\theta_0^{(\text{cell})}$ , as illustrated in figures 5.10(a) – 5.10(e). Here, the pore distributions  $P(v)$  obtained for densities  $\theta_0^{(\text{cell})} = 0.1, 0.2, 0.3, 0.4, 0.5$  have been plotted. At very low value of  $\theta_0^{(\text{cell})} = 0.1$  (figure 5.10(a)), the curves of volume distribution  $P(v)$  are asymmetric with a quite long tail on the right-hand side, which progressively reduces while the cell size  $\alpha$  increases at the fixed density. At the same time, the distribution  $P(v)$  becomes narrower and more localized around the low values of the pore volume  $v$ . This behavior of the distribution  $P(v)$  was not observed for all densities of landing cells  $\theta_0^{(\text{cell})} = 0.1 - 0.5$  (see figures 5.10(a) – 5.10(e)). For densities  $\theta_0^{(\text{cell})} \geq 0.2$ , the pore distributions  $P(v)$  obtained for deposition on square cells of size  $\alpha_2$  and  $\alpha_3$  are broader and shifted to higher values of volumes  $v$  compared to the pore distribution  $P(v)$  corresponding to SPCA case ( $\alpha_1$ ). Qualitative interpretation of this result is given below.

In the case of up-to-four disks per square cell ( $\alpha_4 = \sqrt{2}$ ), we observe the appearance of pronounced peak of  $P(v)$  at low values of  $v$ , approximately at  $v = 0.15 - 0.20$ . It is easy to understand

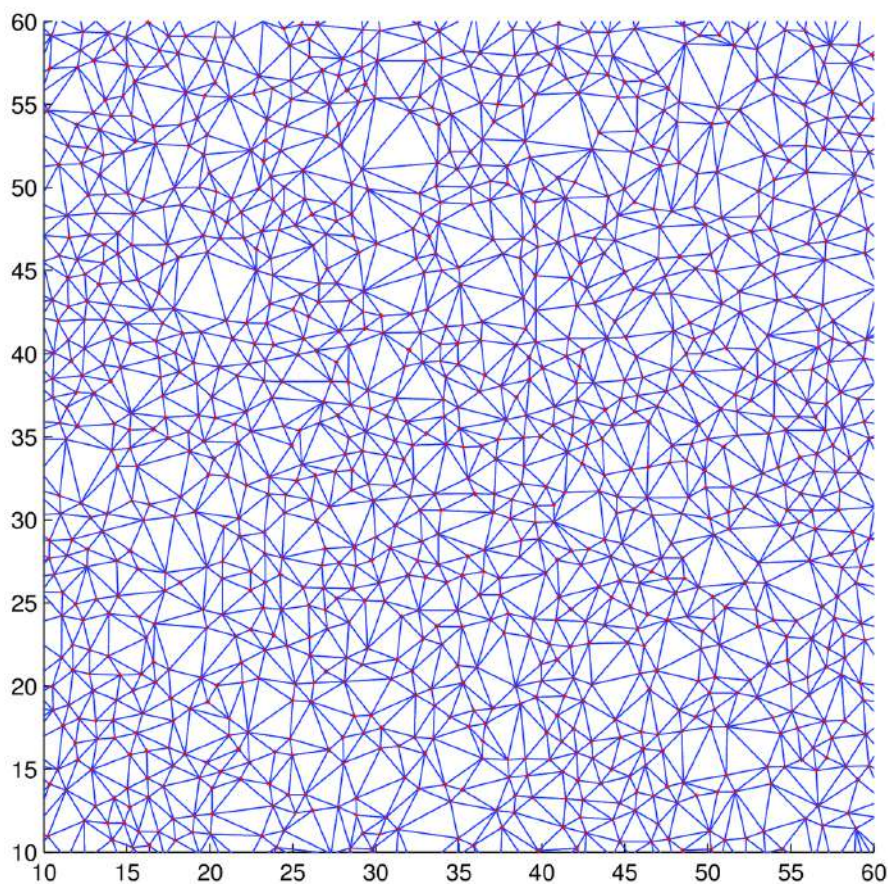


Figure 5.9: Delaunay triangulation of a set of points (centres of disks). Diagram corresponds to jammed-state covering obtained for density of landing cells  $\theta_0^{(\text{cell})} = 0.3$  and cell size  $\alpha_4 = \sqrt{2}$ ; see figure 5.1(a) for a typical configuration. The red dots are the centres of the adsorbed disks. Length is measured in units of the disk diameter  $d_0$ .

which kind of local configuration contributes mostly to this peak of the  $P(v)$ . The Delaunay cells with free dimensionless volume  $v_{\text{hex}} = \sqrt{3}/\pi - 1/2 \approx 0.051$  correspond to the local arrangements of hexagonal symmetry when three disks are all in touch with each other with centres on the vertices of a unilateral triangle. The cells with free volume  $v_{\text{quad}} = 2/\pi - 1/2 \approx 0.13$  correspond to the local configurations of quadratic symmetry when centres of four touching disks are positioned on the vertices of a square. These are minimal values of pore volumes that can be formed with three and four disks deposited on a single landing cell of size  $\alpha_4 = \sqrt{2}$ . However, the probability that the previously described structures of quadratic and hexagonal symmetry arise during the process of random deposition is negligibly small. Therefore, the “free” volumes formed with random deposition of disks into a single cell are larger than the minimal values  $v_{\text{hex}} \approx 0.051$  and  $v_{\text{quad}} \approx 0.13$ , so that observed peak of  $P(v)$  is around  $v \lesssim 0.20$ .

At high values of density of landing cells  $\theta_0^{(\text{cell})} = 0.5$  (figure 5.10(e)), distribution  $P(v)$  obtained under SPCA conditions becomes very similar to pore volume distribution for RSA of disks on a continuous substrate, as expected. The results for the volume distribution of the pores  $P(v)$  obtained in the cases of up-to-two and up-to-three disks per square cell are almost identical at all densities  $\theta_0^{(\text{cell})}$  (see figure 5.10). The similarity of these distributions at small values of pore volumes can be explained by the results shown in figure 5.2. Small pores appear due to the presence of configurations with three

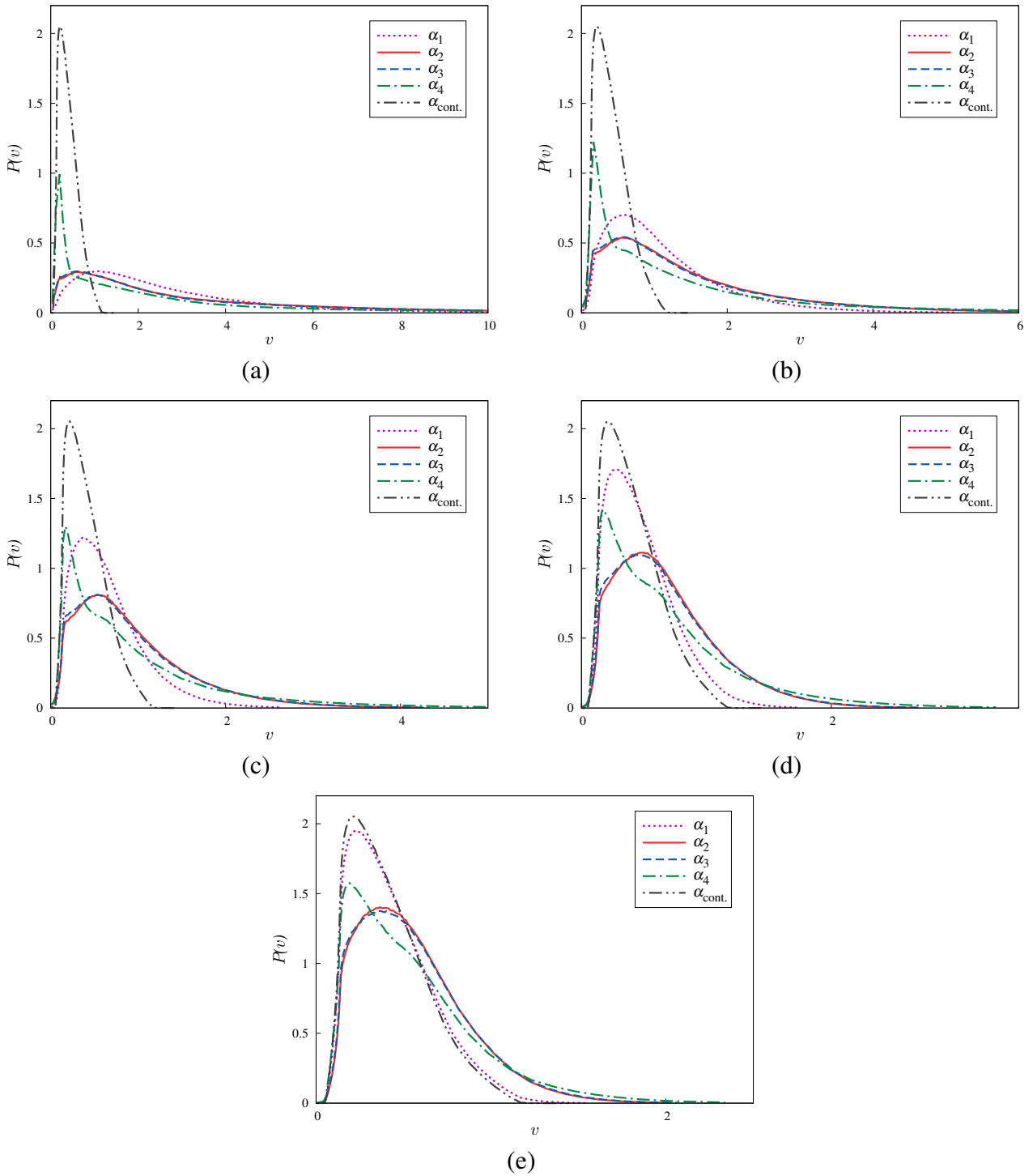


Figure 5.10: Volume distribution of the pores  $P(v)$  in the case of random pattern are shown for jamming coverings at different values of density of the landing cells corresponding to  $\theta_0^{(\text{cell})} = 0.1$  (a), 0.2 (b), 0.3 (c), 0.4 (d), 0.5 (e). The curves in each graph correspond to various values of the cell size,  $\alpha_k$  ( $k = 1, 2, 3, 4$ ), as indicated in the legend. The  $\alpha_{\text{cont}}$  line shows distribution  $P(v)$  for jamming covering in the case of the irreversible disks deposition on a continuous substrate.

or more disks on a single landing cell. But, in the case of up-to-three disks per square cell, the number of in-cell configurations with three disks is considerably smaller than the number of configurations with one or two disks. Consequently, the broad maximum in  $P(v)$ , centred at  $v = 0.4 - 0.6$  is caused by the contribution of large pores formed mostly in the space between the landing cells.

### 5.1.6 Impact of pattern regularity

Further, we study the effect of the presence of a regular substrate pattern of squares on the volume distribution of the pores  $P(v)$ . Distributions  $P(v)$  for jamming coverings corresponding to  $\theta_0^{(\text{cell})} = 0.1 - 0.5$  and different values of the cell size  $\alpha_k$  ( $k = 1, 2, 3, 4$ ) are shown in Figure 5.12. At low density of landing cells  $\theta_0^{(\text{cell})} = 0.1$  and for large cell size  $\alpha \geq \alpha_4 = \sqrt{2}$  (see figure 5.12(a)) we observe the appearance of three peaks of  $P(v)$ . The first peak at  $v \approx 0.2$  is due to Delaunay triangles with their vertices inside a single landing cell (see T1 triangle in figure 5.11). The third peak at  $v \approx 8$  corresponds to Delaunay triangles with vertices located in different landing cells (see T3 triangle in figure 5.11). The central peak at  $v \approx 2$  arises due to Delaunay triangles with two vertices belonging to a single cell, while the third one is located in a neighbouring cell (see T2 triangle in figure 5.11). The first peak at very low values of pore volumes  $v$  does not appear for the smaller landing cells,  $\alpha = \alpha_1, \alpha_2, \alpha_3$ . Indeed, if  $\alpha \leq \alpha_3$ , the Delaunay triangles that lie within a single landing cell are very rare ( $\alpha = \alpha_3$ ) or they can not exist ( $\alpha \leq \alpha_2$ ). In the case of single-particle per-cell adsorption ( $\alpha = \alpha_1$ ) vertices of each Delaunay triangle are located in three different cells, so that distribution  $P(v)$  has only one broad maximum. As can be seen from figure 5.12, the difference between distribution  $P(v)$  for regular substrate pattern of squares and for random pattern case decreases with the increase of the cell density  $\theta_0^{(\text{cell})}$ .

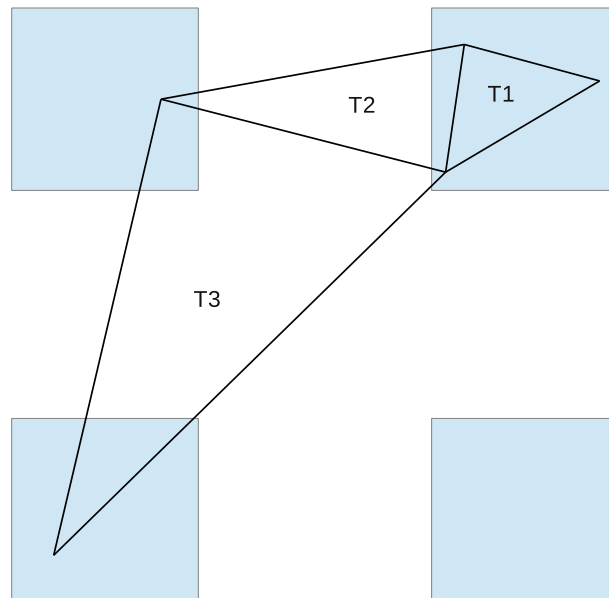


Figure 5.11: Various types of Delaunay triangles (T1, T2, T3) depending on the position of vertices.

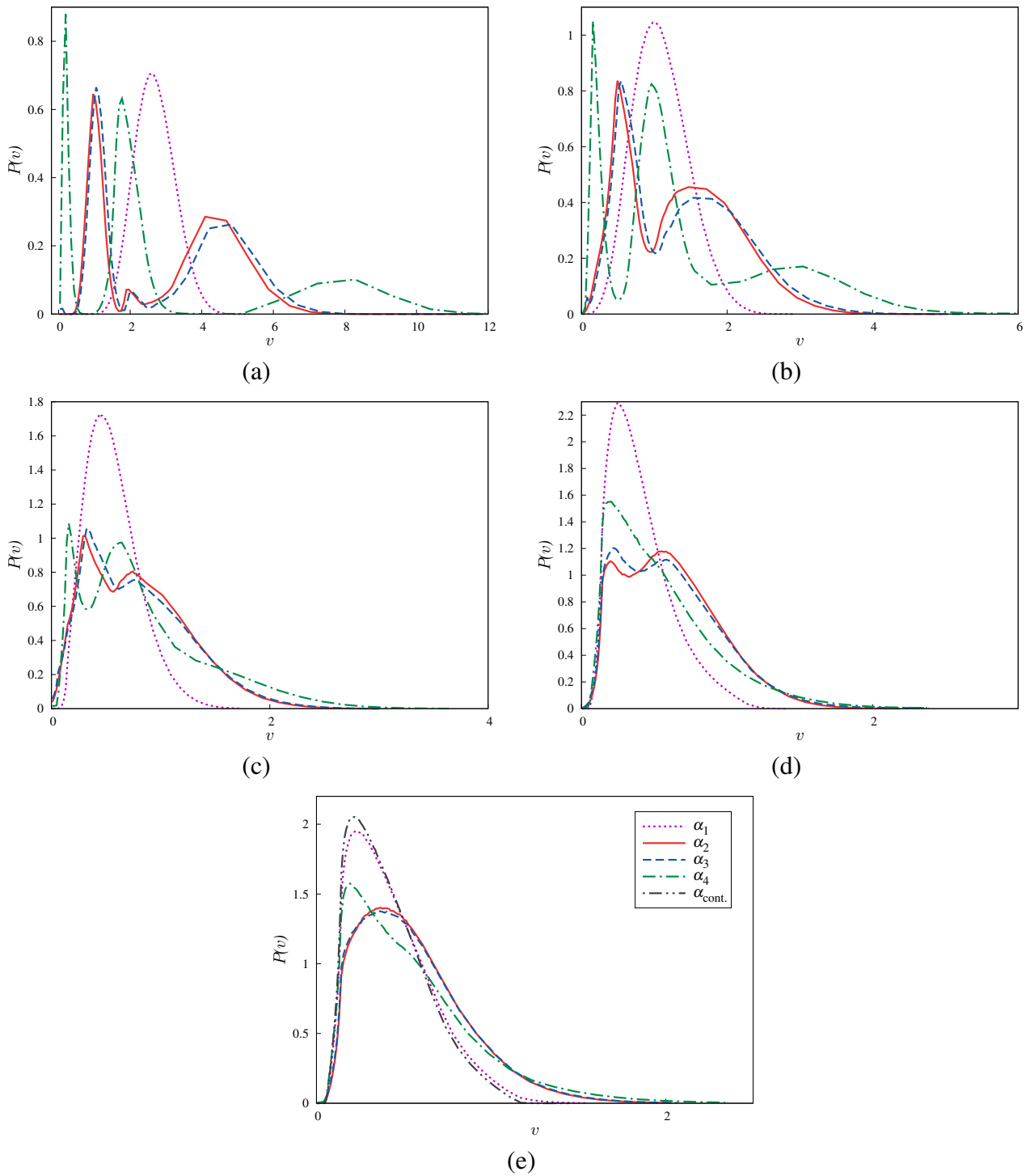


Figure 5.12: Volume distribution of the pores  $P(v)$  in the case of heterogeneous surface covered by square cells centred at the vertices of a square lattice for jamming coverings at different values of density of the landing cells corresponding to  $\theta_0^{(\text{cell})} = 0.1$  (a), 0.2 (b), 0.3 (c), 0.4 (d), 0.5 (e). The curves in each graph correspond to various values of the cell size,  $\alpha_k$  ( $k = 1, 2, 3, 4$ ), as indicated in the legend.

## 5.2 Rectangular cells

We have also performed numerical simulations of random deposition of identical disks on heterogeneous surfaces covered by rectangles of arbitrary orientation. In these simulations, each landing cell is a rectangle with sides  $\alpha = 8$  and  $\alpha/\lambda = 1$  (in units of the disk diameter  $d_0$ ). The choice of the value of aspect ratio  $\lambda$  plays important role in our model. Increasing the aspect ratio of the landing cells (rectangles) leads to the formation of domains of increased regularity. The chosen value of  $\lambda = 8$  is large enough to provide a significantly different patterned substrate compared with the case of the square cells. We have verified that usage of different, but large, aspect ratio values  $\lambda$  gives quantitatively very similar results leading to qualitatively the same phenomenology.

### 5.2.1 Radial distribution function

To characterize the jammed state we studied radial distribution function  $g(r)$  and probability distribution  $P(v)$  of pore volume  $v$  for different values of density of landing cells:  $\theta_0^{(\text{cell})} = 0.1, 0.2, 0.3, 0.4, 0.45$ . Figure 5.13 shows the corresponding results for radial distribution function  $g(r)$ . Comparing the results from figure 5.13 and figures 5.8(b) – 5.8(d), one can see that the first peak near  $r/d_0 = 1$  and local maximum at  $r/d_0 \gtrsim 2$  of  $g(r)$  are more pronounced in the case of elongated rectangular cells than in the case of multi-particle adsorption (MPCA) at squares. This emergence of a better

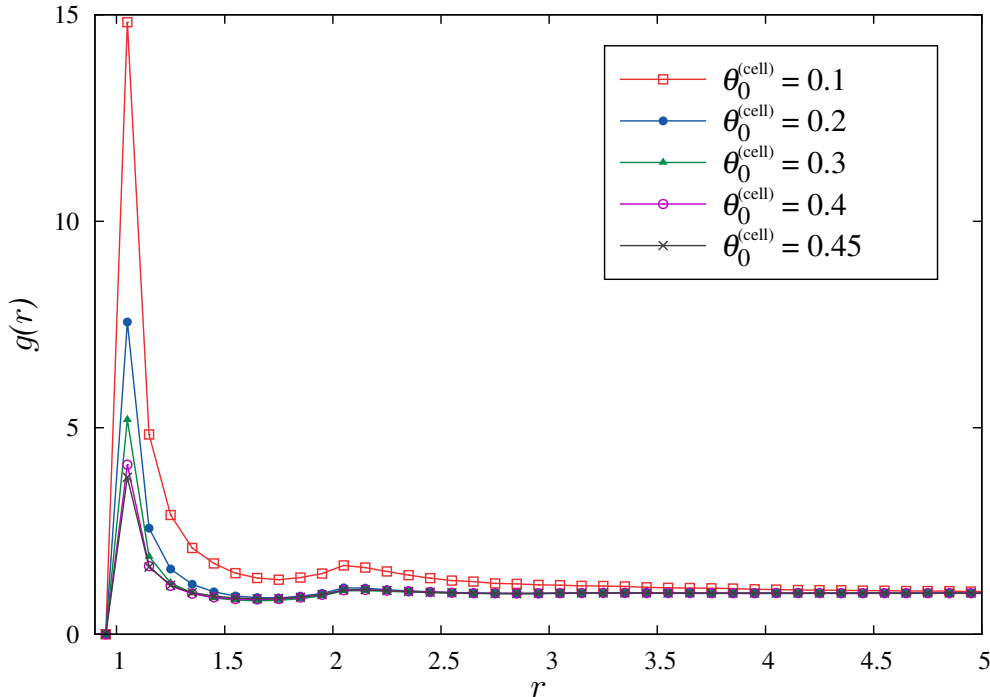


Figure 5.13: Radial distribution function  $g(r)$  for jamming coverings as a function of separation  $r$  (in units of the disk diameter  $d_0$ ) obtained from simulations carried out using the heterogeneous surface covered by rectangles of arbitrary orientation. The curves correspond to various values of density  $\theta_0^{(\text{cell})} = 0.1, 0.2, 0.3, 0.4, 0.45$ , as indicated in the legend.

local order is a correlation effect that develops during the deposition stage due to the formation of arrays of disks within a single elongated rectangular cell.

## 5.2.2 Volume distribution of pores

Figure 5.14 compares volume distribution of the pores  $P(v)$  for jamming coverings corresponding to different densities  $\theta_0^{(\text{cell})}$ . Similar to the case of MPCA on square cells, here we observe the peak of  $P(v)$  at small values of  $v \approx 0.2$ . As previously mentioned, such small pores are a feature of coverings which occurs when three or more particles can be adsorbed on a single cell. The observed peak of the distribution  $P(v)$  broadens when density  $\theta_0^{(\text{cell})}$  increases. Deposition of elongated objects at high densities is characterized by compact domains of parallel objects and large islands of unoccupied substrate area. Figure 5.15(a) shows a typical snapshot of the jammed-state covering obtained for rectangular cells of arbitrary orientation and density  $\theta_0^{(\text{cell})} = 0.45$ . Relatively high local packing of nearly parallel adsorbed rectangles reduces the number of disks effectively adsorbed at a cell. This process is associated with the appearance of larger interstitial voids, which causes peak broadening.

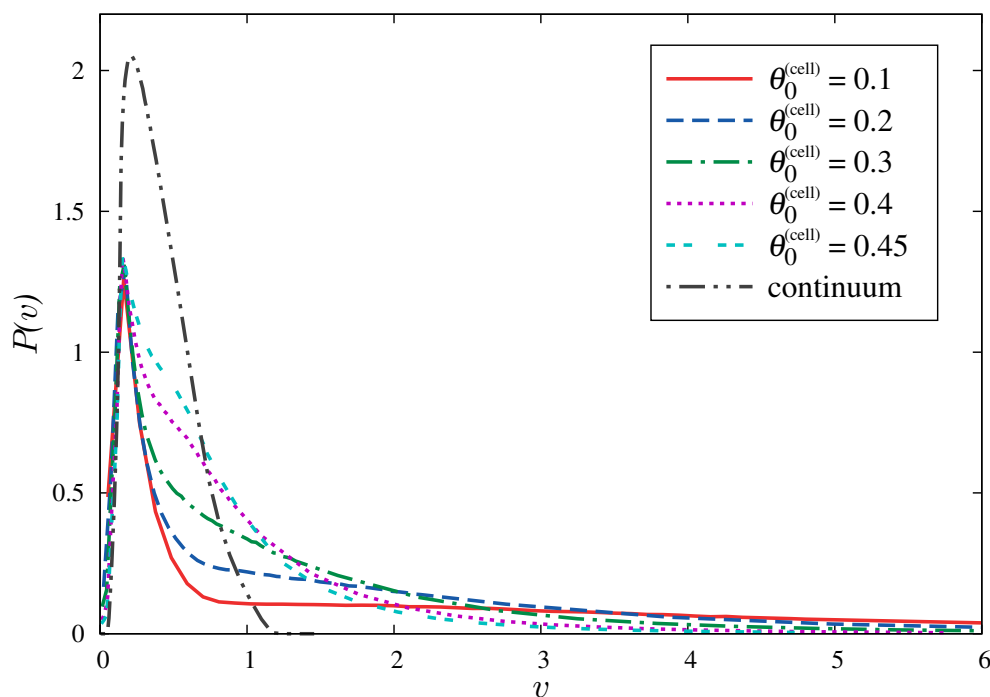


Figure 5.14: obtained from simulations carried out using the heterogeneous surface covered by rectangles of arbitrary orientation. The curves correspond to various values of density  $\theta_0^{(\text{cell})} = 0.1, 0.2, 0.3, 0.4, 0.45$ , as indicated in the legend. Distribution  $P(v)$  for jamming covering in the case of the irreversible disk deposition on a continuous substrate is shown for comparison.

### 5.2.3 Impact of pattern anisotropy

It is now useful to explore the interplay between the anisotropy in the deposition procedure for landing cells and the structural characteristics of jamming coverings. In this case, the orientation of rectangular cells is fixed to the one preferential direction. The configuration formed in the long time regime is made up of a large number of domains; see figure 5.15(b) for a typical configuration. As expected, any such domain contains parallel cells close to each other. This produces better packing of landing cells and a higher impact of the cell-cell excluded volume interaction on the average cell population. Hence, anisotropic deposition of landing cells lowers the average cell population, which enhances the appearance of larger pores, resulting in a peak broadening. Volume distributions of pores  $P(v)$  for jamming coverings of disks corresponding to anisotropic deposition of cells are shown in figure 5.16 with thick lines, while the case of arbitrarily oriented cells from figure 5.14 is drawn with thin lines for comparison. figure 5.16 clearly shows enhanced peak broadening of  $P(v)$  in the case of anisotropic deposition of landing cells, which is consistent with the previous discussion.

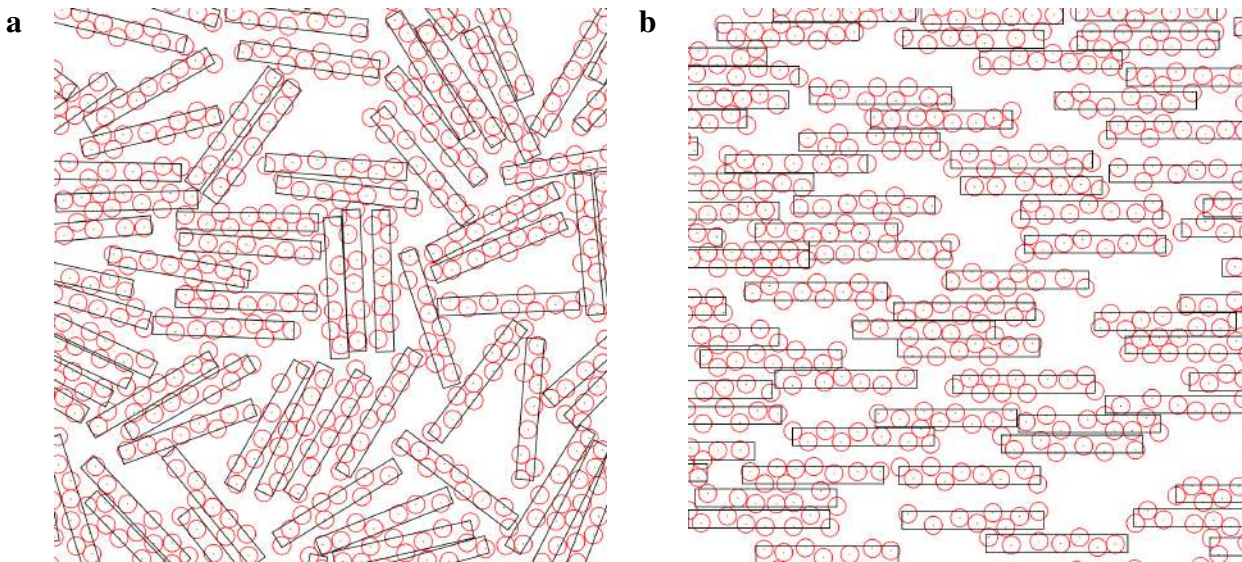


Figure 5.15: Typical jammed-state configuration of a region of size  $30 \times 30$  (in units of the disk diameter  $d_0$ ), for  $\theta_0^{(\text{cell})} = 0.45$ . Orientation of rectangular cells with sides  $\alpha = 8$  and  $\kappa\alpha = 1$  is (a) arbitrary or (b) fixed to the horizontal direction.



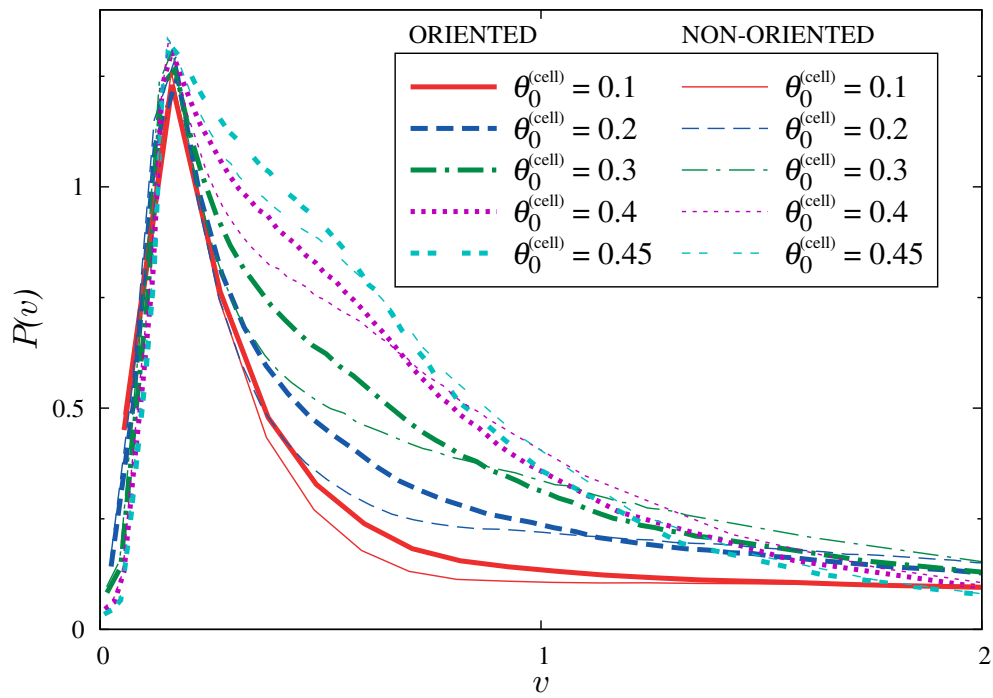


Figure 5.16: Volume distribution of the pores  $P(v)$  obtained from simulations carried out using the heterogeneous surface covered by rectangles of fixed orientation (thick lines) and arbitrary orientations (thin lines). The curves correspond to various values of density  $\theta_0^{(\text{cell})} = 0.1, 0.2, 0.3, 0.4, 0.45$ , as indicated in the legend.

---

## Chapter 6

# Adsorption on imprecise lattice

The difference between deposition on finite-size landing cells and lattice RSA is in the particle positions, which can be uncertain within the order of the size of the cell in the former case. Recently, Privman and Yan [1] have analyzed both numerically and analytically extended model of one-dimensional deposition of segments of length  $a$ , on a lattice of spacing  $\ell$  between its sites, which instead of just being lattice points are symmetrically broadened (about the lattice points) into segments of width  $w$  in which the centres of the depositing objects can land. They reported that even an arbitrarily small imprecision in the lattice-site localization ( $w \gtrsim 0$ ) changes the convergence to jamming from fast, exponential

$$\theta_J - \theta(t) \sim \exp(-t/\sigma), \quad (6.1)$$

to slow, power-law

$$\theta_J - \theta(t) \sim t^{-1/d}. \quad (6.2)$$

In a similar spirit, the study presented in this chapter investigates the rapidity of the approach to the jamming state in the case of *two-dimensional* (2D) pre-patterned substrate. Unlike the models studied in chapter 5, here we analyze deposition on the substrates patterned with a square grid of square-shaped cells onto which the particle can adhere. We consider the process of the irreversible random sequential adsorption (RSA) of fixed size disks. The present chapter focuses on the effect of the presence of a regular substrate pattern on the temporal evolution of the coverage fraction  $\theta(t)$ . We aim to quantify changes in time coverage behaviour  $\theta(t)$  at densities near jamming limit  $\theta_J$ , associated with different cell sizes and densities.

A regular substrate pattern that consists of identical square cells centred at nodes of a regular square lattice is completely defined by two dimensionless parameters: the length of a cell size  $\alpha$  and the length of the smallest gap between two neighbouring cells  $\beta$  (figure. 3.2). These two lengths are measured in the units of the adsorbing particle radius. As described in section 3.3, parameter  $\beta$  determines whether the adsorption is in interacting ( $\beta < 1$ ) or non-interacting mode ( $\beta > 1$ ). Parameter  $\alpha$  distinguishes between single vs. multiple particles per cell mode. The phase diagram as defined by Araújo et al. [45] was discussed earlier in section 3.3 and illustrated in figure. 3.3. In this work, we focus on the interacting cell-cell adsorption (ICCA) regime in the case of single-particle per-cell adsorption (SPCA). The non-interacting regime (NICCA) is equivalent to the low cell density limit case discussed in section 5.1.1. We want to investigate the role of the cell-cell interaction and thus we limit this study to the SPCA case where  $\alpha < \sqrt{2}/2$ , which excludes the interaction of the particles at

the same cell.

## 6.1 Kinetics

### 6.1.1 Effect of varying $\beta$ on the long-time adsorption kinetics

We simulate the adsorption on a substrate with a regular pattern consisting of square cells that are comparable in size to the adsorbing particles and that satisfy the SPCA condition  $\alpha < \sqrt{2}/2$ . We chose the three values of cell size:  $\alpha = 0.3, 0.5,$  and  $0.7$ . Figures 6.1(a) – 6.1(c) illustrate the kinetics of the irreversible deposition of disks. The plots of the time coverage behaviour  $\theta(t)$  are given for the three chosen values of  $\alpha$  and various values of the gap  $\beta$  between the cells, in the range from  $\beta = 0$  (continuous substrate and ICCA regime) to  $\beta = 1$  (upper limit of the parameter  $\beta$ , above which the NICCA occurs). These 2D plots enable us to analyze how the time evolution of the coverage  $\theta(t)$  in

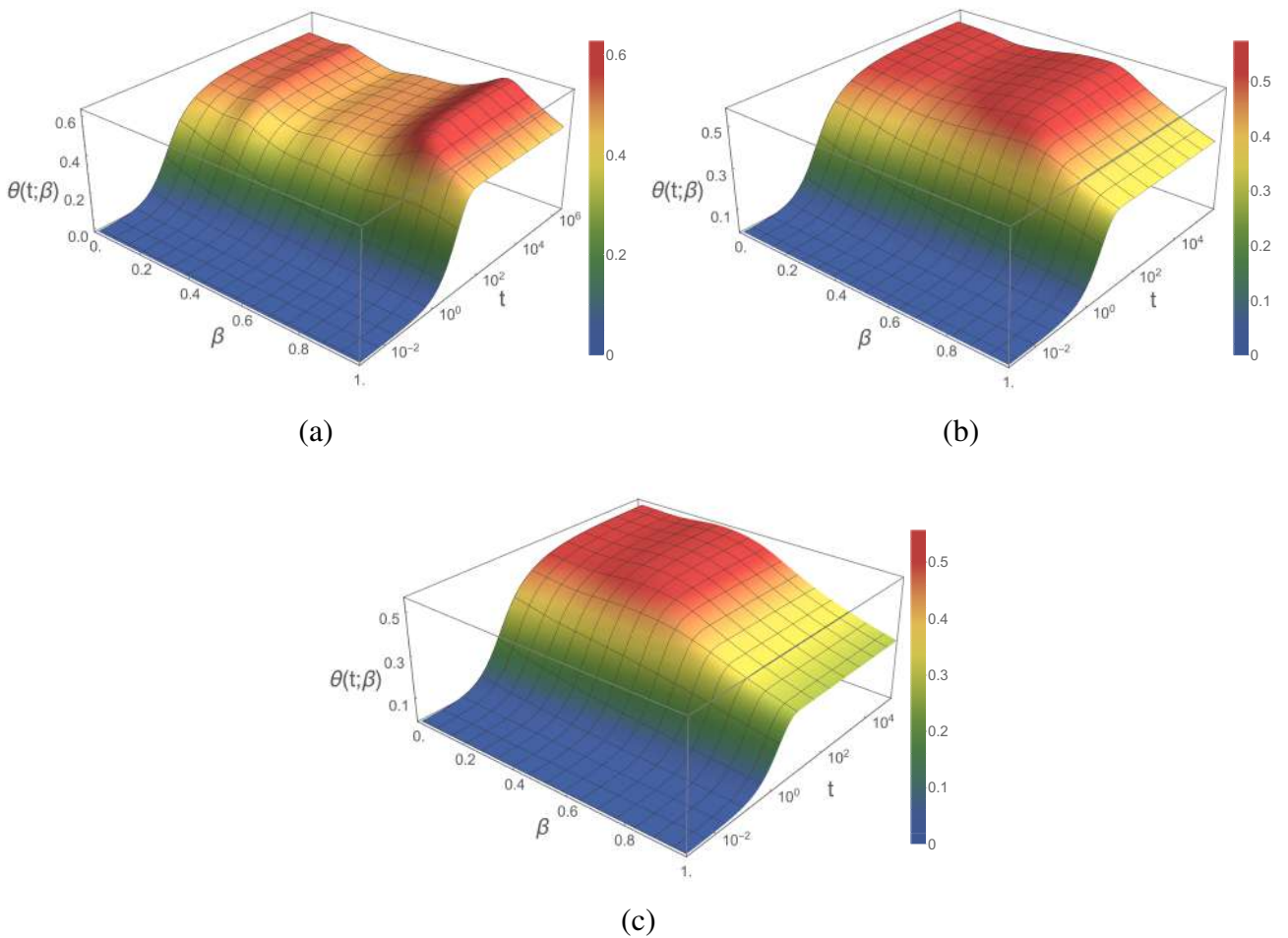


Figure 6.1: Time evolution of the coverage fraction  $\theta(t)$  depending on the gap size  $\beta$  between two neighbouring landing cells (in units of the disk diameter  $d_0$ ), for the three values of cell size,  $\alpha = 0.3$  (a),  $0.5$  (b), and  $0.7$  (c). For each  $\alpha$ , the gap  $\beta$  between cells is varied in the range  $[0, 1]$ , with the step of  $0.02$ .

the case of SPCA depends on the gap size  $\beta$  between the landing cells.

It can be seen that for a fixed size of landing cells  $\alpha$ , coverage  $\theta(t)$  in the early stage of the deposition process increases faster when the gaps between the cells are smaller. Indeed, at very early times of the process, when the coverage fraction  $\theta(t)$  is small, the deposited objects do not “feel” the presence of the other ones, and the coverage grows rapidly in time. Then, the adsorption process has an overall rate proportional to the surface density of landing cells onto which the particles can adhere. Since the flux of incoming particles is fixed, the overall rate at which the coverage  $\theta(t)$  increases is progressively reduced with the increase of the gap between the landing cells.

At a late enough time, when the coverage fraction is sufficiently high and “excluded volumes” of deposited objects begin to overlap, there is a strong dependence of the adsorption rate on the parameter  $\beta$ . The rate of successful adsorption events reduces when the gap size  $\beta$  decreases. This is explained by the larger impact of the cell-cell excluded volume interaction when the cells are closer to each other.

It is interesting to emphasize that the dependence of the jamming coverage  $\theta_j$  is a non-monotonic function of the gap size  $\beta$  (see figure 6.1). It goes from the jamming coverage value for continuum  $\theta_j^{\text{cont}} = 0.5472 \pm 0.0002$  [86] ( $\beta = 0$ ), reaches some local minimum ( $0 < \beta < 1$ ), and tends to a definite value which corresponds to the coverings when each cell is occupied by a single particle. Corresponding explanations of such variations of the jamming coverage  $\theta$  with parameter  $\beta$  are provided later in section 6.3.

## 6.2 Asymptotic behaviour

To gain a better insight into the complex kinetics of SPCA in the ICCA regime, it is useful to analyze in particular the temporal evolution of the first derivative of coverage  $\theta(t)$  with respect to time  $t$ . The time derivatives of  $\theta(t)$  are calculated numerically from the simulation data. Representative examples of double logarithmic plots of the time derivative  $d\theta/dt$  are shown in figures 6.2(a) – 6.2(c), for the three values of cell size,  $\alpha = 0.3$  (a), 0.5 (b), 0.7 (c). For each  $\alpha$ , results are presented for various values of the gap  $\beta$  between the cells in the range  $0.60 \leq \beta \leq 0.98$ . In the case of the algebraic behavior of the coverage fraction  $\theta(t)$  (see equation (6.2)), a double logarithmic plot of the first time derivative  $d\theta/dt \propto t^{-(1+d)/d}$  is a straight line. As seen from figure 6.2, if the values of parameter  $\beta$  for cells of size  $\alpha = 0.3, 0.5, 0.7$  do not exceed, respectively,  $\approx 0.84, 0.74$  and  $0.64$ , the late time kinetics of the deposition process is similar to the one observed for disks with equal size, adsorbing on a clean substrate. Additionally, thin straight lines with the slope  $-3/2$  are shown in figure 6.2, indicating the late time RSA behaviour for clean continuous substrates [5, 36, 49, 50, 71]. However, the same is not valid for large values of the parameter  $\beta$ , regardless of the cell size  $\alpha$  (obviously,  $\alpha < 1/\sqrt{2} \approx 0.707$  in the case of SPCA). As it can be seen, at the late times of the deposition process the plots of  $d\theta/dt$  vs.  $t$  are not linear on a double logarithmic scale for sufficiently large values of the gap  $\beta$ . The deviation from the power-law (6.2) is particularly pronounced for low densities of landing cells, i.e. when  $\beta \lesssim 1$ .

Theoretical arguments supporting Feder’s law (6.2) have been presented by Swendsen [49] and Pomeau [50]. Their analysis is based on the exclusion of the area of radius  $d_0$  around each disc of

radius  $d_0/2$  for selecting the centre of the newly arriving disc. After a certain time, characterizing the beginning of the asymptotic regime, the area that is available to the centre of a new disc consists of small disconnected areas that can be occupied by only one additional disc. When power-law (6.2) holds, a vanishing-small area that is available for the insertion of a new particle can be created with non-zero probability during the deposition process. Arbitrarily small areas are reached with a very small probability for a uniform flux of the arriving disks that attempt deposition. In the case of ICCA-SPCA, since only one particle can fit per cell, the existence of a minimum finite area is related to particles previously adsorbed on neighbouring cells. As seen from figure 6.3(a), particles adsorbed on neighbouring cells can completely overlap the cell when the gap  $\beta$  and cell size  $\alpha$  satisfies the relation [81]:

$$\beta + \alpha/2 < 1. \quad (6.3)$$

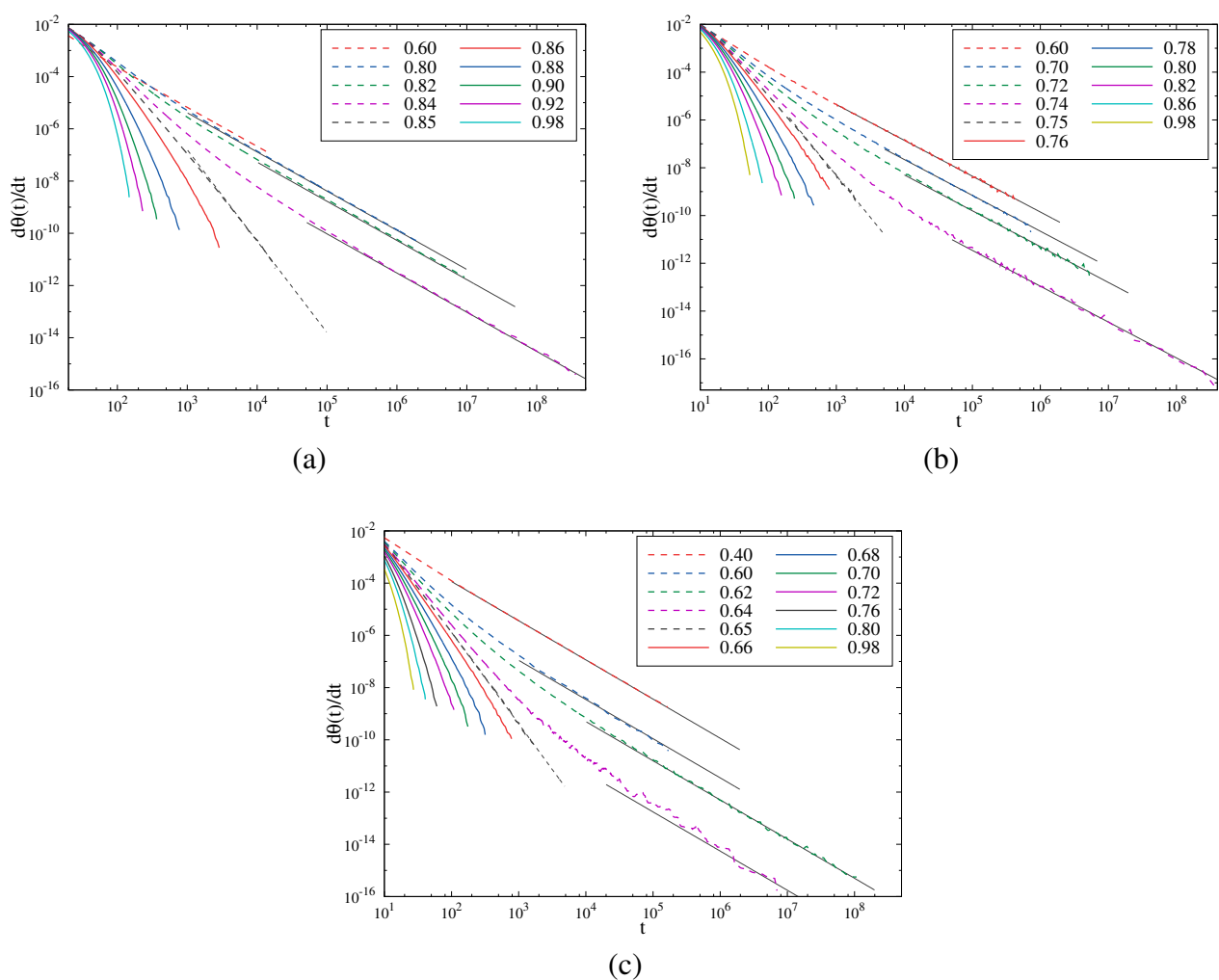


Figure 6.2: Test for the presence of the algebraic law (6.2) in the approach of the coverage  $\theta(t)$  to the jamming limit  $\theta_j$  for different values of cell size,  $\alpha = 0.3$  (a),  $0.5$  (b), and  $0.7$  (c). The curves in each graph correspond to various values of the gap  $\beta$  between the cells, as indicated in the legend. Straight-line sections of the curves show where the law holds. The solid straight lines have the slope  $-3/2$  and are guides for the eye. The dashed straight line has slope  $-5/2$  indicating the late time RSA behaviour of the system for the critical values of the parameter  $\beta$ : (a)  $\beta_c = 0.85$ , (b)  $0.75$ , (c)  $0.65$  (see equation (6.4)).

Hence, below the critical value of the parameter  $\beta$ ,

$$\beta_c = 1 - \alpha/2, \quad (6.4)$$

there is no minimum *finite* area available to accommodate one particle. However, above the critical value  $\beta_c$ , particles adsorbed on neighbouring cells cannot prevent adsorption inside the cell. Then, there exist finite regions where the centre of a disk can land without overlapping a previously adsorbed particle (see figure 6.3(b)). For the critical value of the gap  $\beta_c$ , the approach to the jamming coverage  $\theta_j$  with time is still algebraic (6.2), with the exponent that is approximately equal to  $-3/2$  which does not depend on the cell size  $\alpha$ . A similar anomalous power-law approach was reported in the literature for the case of adsorption on a one-dimensional imprecise substrate [2, 42]. As explained in more detail in section 3.3, in one dimension the reason for this behaviour lies in a different kind of small hole size distribution in the late phase of the process. The distribution of holes available for particle adsorptions in the late phase of the process for adsorption on a two-dimensional imprecise lattice is out of the scope of this thesis.

Our numerical results suggest that for  $\beta_c < \beta < 1$ , the asymptotic approach of the coverage fraction  $\theta(t)$  to its jamming limit  $\theta_j$  is neither algebraic nor exponential. Semi-logarithmic plots of the time derivative  $d\theta/dt$  are shown in figures 6.4(a) – 6.4(c), for three values of the cell size,  $\alpha = 0.3$  (a), 0.5 (b), 0.7 (c). For each  $\alpha$ , results are displayed for various values of the parameter  $\beta$  above the corresponding critical values (see equation (6.4)),  $\beta_c = 0.85$  (a), 0.75 (b), 0.65 (c). One observes that for the fixed value of cell size  $\alpha$ , the time derivatives of  $\theta(t)$  decay at the very late times of the deposition process more quickly for the larger values of the gap  $\beta$  between the cells. Interestingly, in the limit of  $\beta \rightarrow 1$  approach of coverage  $\theta(t)$  to the jamming limit  $\theta_j$  is exponential of the form (6.1). The characteristic timescale  $\sigma$  is found to decrease with the cell size  $\alpha$  according to power-law,

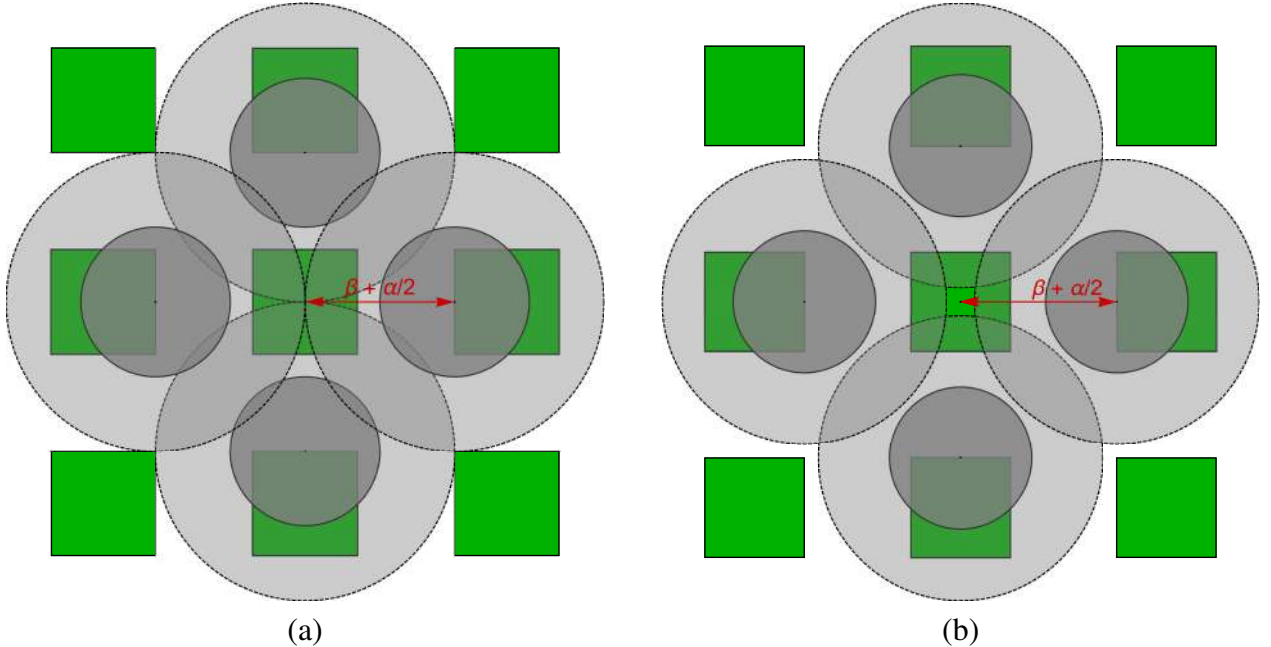


Figure 6.3: Illustration of particles adsorbed in neighbouring cells can prevent adsorption on the central cell: (a) the overlap of the shadowed regions of the four neighbouring particles completely overlap the central cell; (b) particles adsorbed on neighbouring cells cannot prevent adsorption inside the cell.

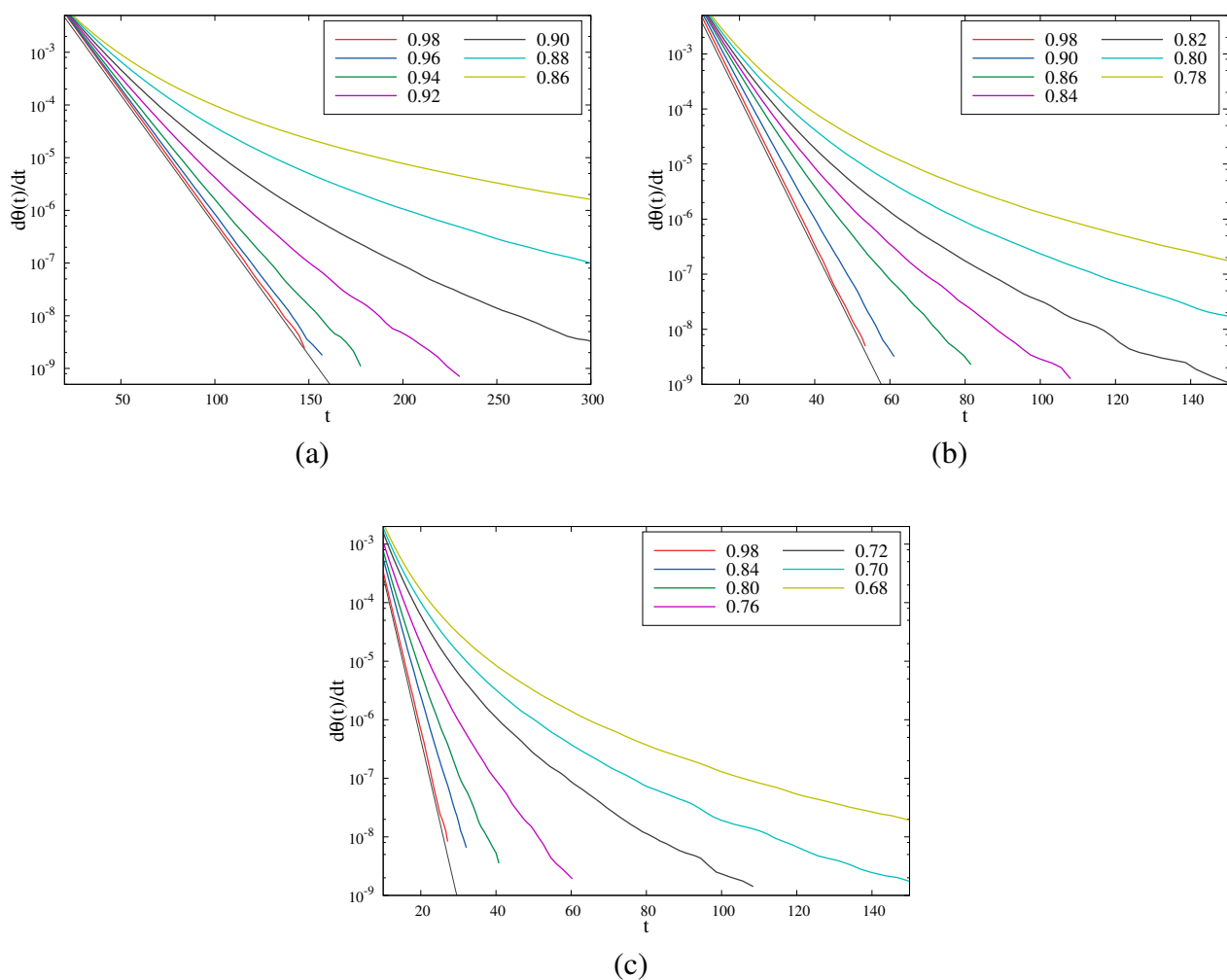


Figure 6.4: Plots of the time derivative of coverage  $d\theta/dt$  for the three values of cell size,  $\alpha = 0.3$  (a), 0.5 (b), 0.7 (c). As indicated in the legend, the results are reported for values of the gap  $\beta$  above the corresponding critical values (equation (6.4)),  $\beta_c = 0.85$  (a), 0.75 (b), 0.65 (c). Additionally, the slanted straight line is shown, indicating the exponential approach to the jamming limit (equation (6.1)), where  $\sigma = 8.80$  (a), 3.15 (b), and 1.56 (c).

$\sigma \propto \alpha^{-2.04 \pm 0.02}$ . In other words, the relaxation time  $\sigma$  in equation (6.1) is inversely proportional to the cell area. It must be stressed that the appearance of even a slight cell-cell excluded volume interaction violates the exponential asymptotic approach (6.1).

## 6.3 Jamming coverage

### 6.3.1 Influence of the pattern on the jamming density $\theta_J$

Let us go back to the analysis of the non-monotonic behaviour of the jamming density  $\theta_J$  as a function of the gap size  $\beta$  between the landing cells observed in figure 6.1. Dependencies of the jamming

coverage  $\theta_j$  on the separation distance  $\alpha + \beta$  between cell centers are presented in figure 6.5 for the three values of cell size,  $\alpha = 0.3, 0.5$  and  $0.7$ . For the case of SPCA, jamming coverage  $\theta_j$  can be exactly calculated for  $\beta$  larger than the critical value  $\beta_c$  (equation (6.4)) [45]. Indeed, since each cell at late enough time contains the centre of a single deposited particle, the jamming coverage is simply

$$\theta_j^c = \frac{r_0^2 \pi}{(\alpha + \beta)^2}. \quad (6.5)$$

The solid black line in figure 6.5 indicates values of the jamming coverages calculated from equation (6.5). The jammed-state value  $\theta_j^{\text{cont}} = 0.5472 \pm 0.0002$  [86] of the coverage in the case of the irreversible disks deposition on continuum substrate is marked on the same figure by the horizontal dashed line. When the gap between the cells  $\beta$  starts to increase, cell-cell excluded volume interaction is still strong, but the substrate area that is available for the insertion of a new particle is reduced, which leads to a decrease in the jamming coverage below the value for continuum  $\theta_j^{\text{cont}}$ . As a gap size  $\beta$  increases further, the cell-cell excluded volume interaction weakens, but one expects a higher impact of patterning of the surface on the local particle arrangements. An increase in the pattern-induced tendency for semi-ordering of the coverings leads to the formation of jammed-state deposits of higher density. Then, for sufficiently large values of parameter  $\beta$ , jamming coverage exceeds the jamming limit  $\theta_j^{\text{cont}}$  for continuum substrate and continues to grow with  $\beta$ . In this case, the theoretical value of the highest possible coverage fraction is equal to  $\pi/4 \approx 0.7854$ . This value corresponds to the local configurations of quadratic symmetry when the disc centres are located at the vertices of a square with a side of  $\alpha + \beta = 1$  [87]. However, in the present model this maximum of the jamming coverage  $\theta_j$  is not reached at  $\alpha + \beta = 1$ . In figure 6.5 we observe the appearance of three pronounced

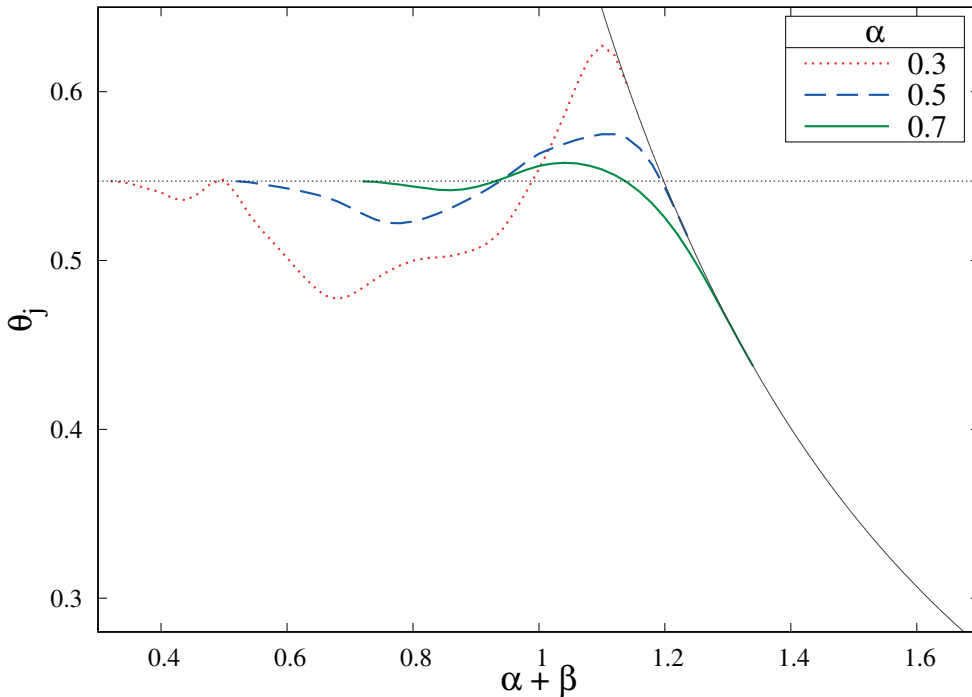


Figure 6.5: Jamming coverage  $\theta_j$  as a function of separation distance  $\alpha + \beta$  (in units of the disk diameter  $d_0$ ) for various values of the cell size  $\alpha$ , as indicated in the legend. The solid black line indicates values of the jamming coverage  $\theta_j^c$  calculated from equation (6.5).



maxima of  $\theta_j$  on shifted positions, approximately at  $\alpha + \beta = 1.04$ ,  $1.12$  and  $1.10$ , for  $\alpha = 0.7$ ,  $0.5$  and  $0.3$ , respectively. These maxima are not positioned at  $\alpha + \beta = 1$  due to the uncertainty in the position of the particle within the cell. Actually, for  $\beta \gtrsim 1 - \alpha$  excluded volume interaction with disks belonging to neighbouring cells still substantially lowers the average number of adsorbed disks per cell. As the parameter  $\beta > 1 - \alpha$  is increased further to the critical value  $\beta_c$  (equation (6.4)), the average cell population rises, and the jamming coverage  $\theta_j$  increases until the appearance of large void space between the cells when it falls to the value given by equation (6.5).

We also study the influence of varying  $\alpha$  on the jamming coverage  $\theta_j$  and on the late time kinetics of deposition process. We carried out a series of simulations at fixed  $\alpha + \beta = 1.0$ ,  $1.1$ , and varied cell size  $\alpha$ . Numerical results regarding the jamming coverages  $\theta_j$  for various  $\alpha$  are shown in figure 6.6. For  $\alpha + \beta = 1.1$ , the criteria (6.3) cannot be satisfied if  $\alpha < 0.2$ . Therefore, for  $\alpha < 0.2$  each cell host exactly one particle in the jamming state so that jamming coverage has the constant value  $\theta_j = 0.6491$  given by equation (6.5). As  $\alpha > 0.2$  increases, the cell-cell exclusion leads to a further reduction of the average cell population, thereby making the jamming coverage lower. However, in the case of  $\alpha + \beta = 1$  the jamming coverage  $\theta_j(\alpha)$  increases first and reaches the wide maximum at  $\alpha \approx 0.5$ , after that the curve  $\theta_j(\alpha)$  is lowered to the jamming value for continuum substrate  $\theta_j^{\text{cont}}$ . For  $\alpha < 1 - \sqrt{2}/2 \approx 0.3$ , a cell can only be blocked by disks deposited at the nearest lateral neighbour cells. In that case, for more cell-cell exclusion effects, it is needed a smaller cell size. But, when cells are larger than  $1 - \sqrt{2}/2$ , a cell can also be blocked by disks deposited at the nearest diagonal neighbour cells, which enhances the cell-cell excluded volume interaction. These two opposite effects that exist when cells increase lead to the formation of the maximum of  $\theta_j(\alpha)$  around  $\alpha \approx 0.5$ . Furthermore, when  $\alpha + \beta = 1$  there is discontinuity of the function  $\theta_j(\alpha)$  at  $\alpha = 0$ , since  $\theta_j(0) = \pi/4 \approx 0.7854$ ,

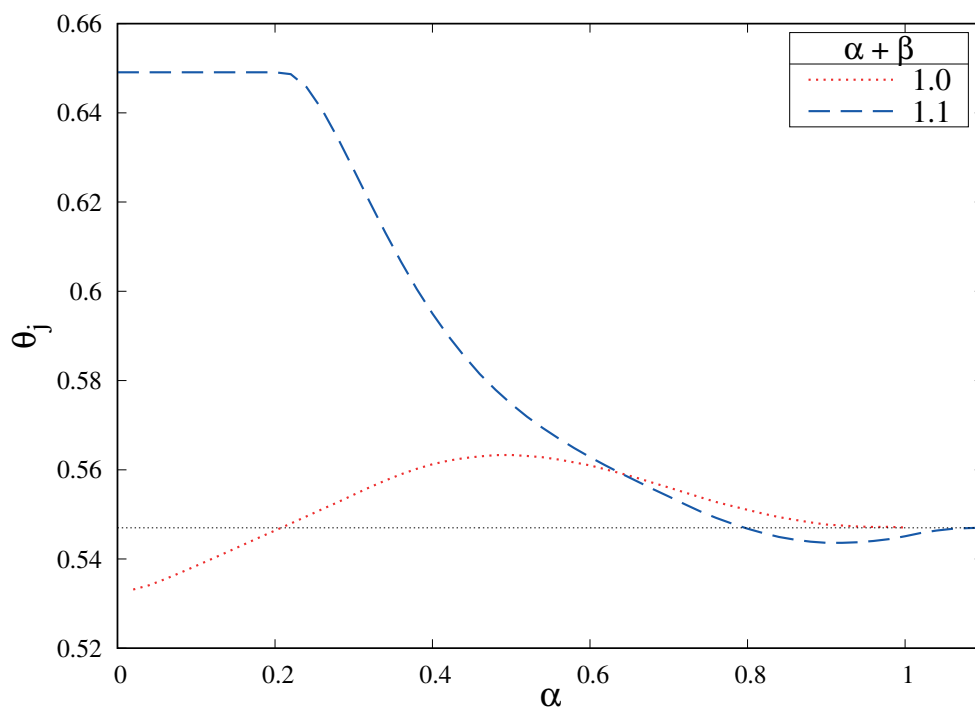


Figure 6.6: Jamming coverage  $\theta_j$  as a function of cell size  $\alpha$  (in units of the disk diameter  $d_0$ ) for two values of separation distance  $\alpha + \beta$ , as indicated in the legend.

but  $\lim_{\alpha \rightarrow 0^+} \theta_J(\alpha) < \theta_J^{\text{cont}} \approx 0.5472$ .

### 6.3.2 Effects of varying $\alpha$ on the long-time adsorption kinetics

It is interesting that in the case when  $\alpha + \beta = 1$ , the approach to the jamming coverage  $\theta_J$  is always algebraic, regardless of the size  $\alpha$  of the landing cells. As can be seen from figure. 6.7, we find that for  $\alpha \geq 0.02$  the coverage  $\theta$  reaches a power-law time-behaviour (6.2) within the length of the simulation. If a cell size  $\alpha$  decreases, the value  $\beta + \alpha/2$  increases and gets closer to unity when the condition (6.3) ceases to be valid. For very small cells ( $\alpha \gtrsim 0$ ), the coverage growth is slowed down by the creation of a smaller fraction of the layer that is available for the insertion of a new particle. Consequently, when cell size  $\alpha$  decreases the onset of long-time power-law behaviour (6.2) shifts to later times (figure 6.7). Generally, this effect occurs when the geometry of the pattern is close to the condition (6.4). In this case, it was necessary to increase the size of the substrate (typically  $1024 \times 1024$  cells) to gain a convincing confirmation of the power-law approach of the coverage fraction  $\theta(t)$  to the jamming limit  $\theta_J$  at the very late times of the deposition process.

When  $\alpha + \beta = 1.1$ , although there is no change of jamming coverage  $\theta_J$  for  $\alpha < 0.2$  (figure 6.6), changes in the dynamics of deposition are obvious (see figure 6.8). The criteria (6.3) is satisfied for  $\alpha > 0.2$  and then the approach to the jamming limit is consistent with the power law behavior given by equation (6.2). As seen from figure (6.8)(a), at the late times of the deposition process the plots of  $d\theta/dt$  vs.  $t$  are linear on a double logarithmic scale with the slope of  $-3/2$  for all  $\alpha > 0.2$ . However, the

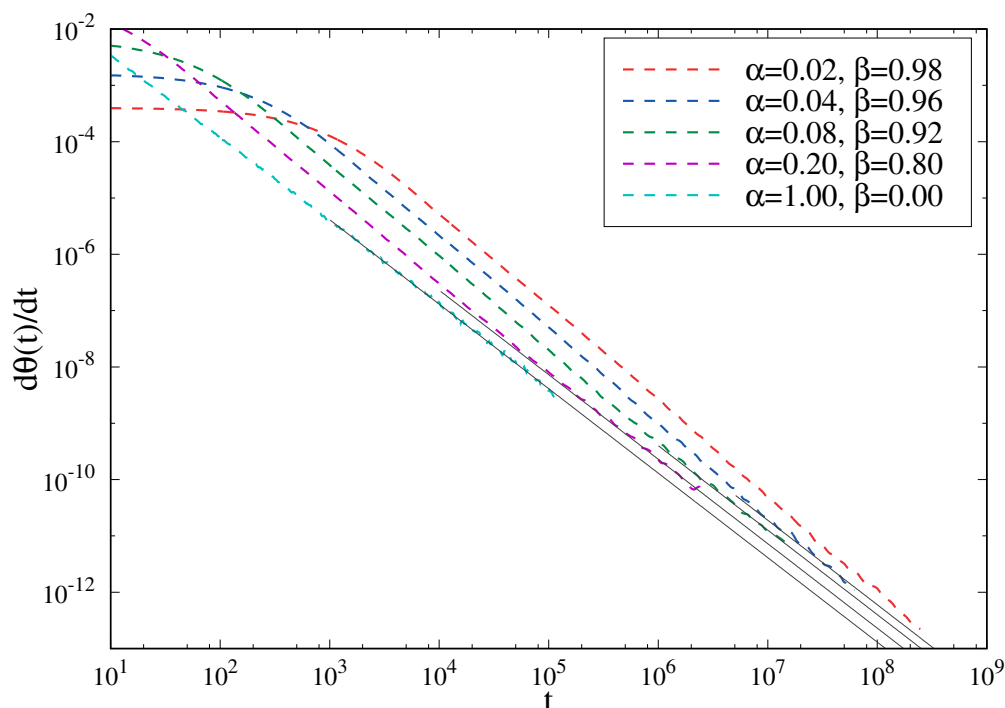


Figure 6.7: Test for the presence of the algebraic law (6.2) in the approach of the coverage  $\theta(t)$  to the jamming limit  $\theta_J$  for different values of parameters  $\alpha$  and  $\beta$  that satisfy the condition  $\alpha + \beta = 1$  (see legend). Straight-line sections of the curves show where the law holds. The solid straight lines have the slope  $-3/2$  and are guides for the eye.

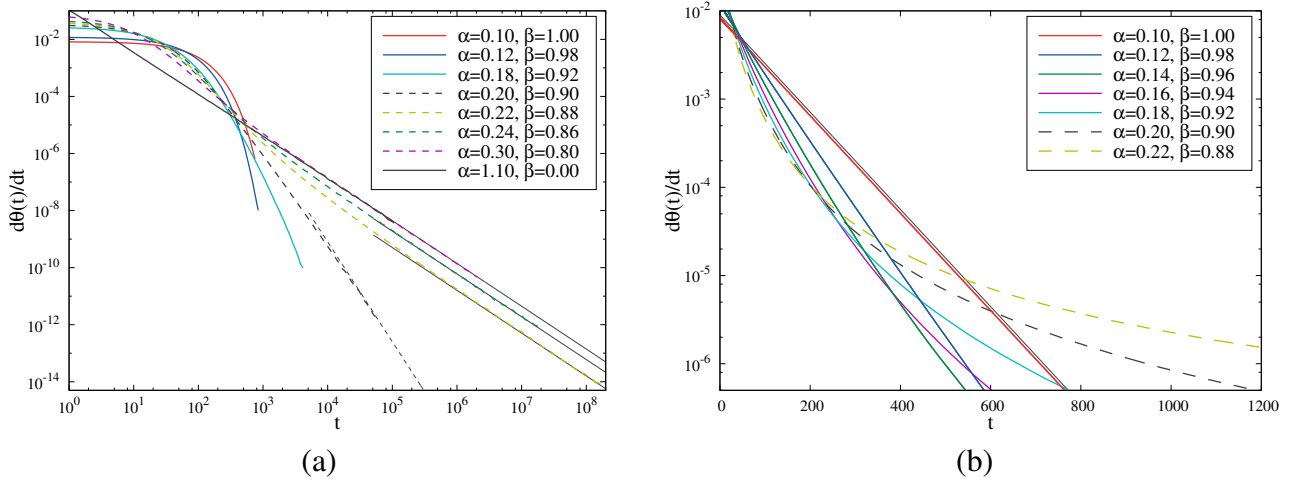


Figure 6.8: Plots of the time derivative of coverage  $d\theta/dt$  for different values of parameters  $\alpha$  and  $\beta$  that satisfy the condition  $\alpha + \beta = 1.1$  (see legends): (a) results are shown on a double logarithmic scale. Solid straight lines have the slope  $-3/2$  and are guides for the eye. Dashed straight line has slope  $-5/2$  indicating the late time RSA behavior of the system for the critical value of parameter  $\beta$ ,  $\beta_c = 0.20$  (see equation (6.4)); (b) results for  $\alpha \leq 0.22$  are shown on a semi-logarithmic scale. Slanted straight line is shown, indicating the exponential approach to the jamming limit (equation (6.1)), where  $\sigma = 78.8$ .

slope of  $d\theta/dt$  abruptly changes to  $\approx -5/2$  when the cell size  $\alpha$  reaches the critical value of  $\alpha = 0.2$  (see equation (6.4)). By reducing the size of cells below the critical value  $\alpha = 0.2$ , algebraic approach disappears. Under conditions when the cell size  $\alpha$  decreases towards non-interacting condition ( $\alpha \rightarrow 0.10^+$ ,  $\beta \rightarrow 1.0^-$ ), asymptotic approach of the coverage fraction  $\theta(t)$  to its jamming limit  $\theta_j$  becomes closer to the exponential law (6.1) (see figure 6.8(b)).

## 6.4 Structural properties of the jammed state

To gain additional insight into the late time kinetics of the deposition process onto a nonuniform substrate, it is useful to analyze in particular the spatial distribution of particles inside the cells. In figures 6.9, 6.10, and 6.11 we show the spatial distribution of particles inside the cell at the jammed state, for  $\alpha = 0.3, 0.5$  and  $0.7$ , respectively, and the twelve different values of parameter  $\beta \in [0.02, 0.98]$ . To calculate these probability distributions, we divided cell space in mesh with  $40 \times 40$  bins and counted the number of particles falling into bins. The data are averaged over 100 independent runs for each of the investigated substrate patterns with  $256 \times 256$  landing cells. Spatial distribution of particles shown in figures 6.9 – 6.11 are accompanied by corresponding radial distribution functions  $g(r)$  (or pair-correlation functions) defined as

$$g(r) = \frac{S}{N^2} \left\langle \sum_{i=1}^N \sum_{j=1}^N \delta[\vec{r} - (\vec{r}_j - \vec{r}_i)] \right\rangle, \quad (6.6)$$

where  $\vec{r}$  is the position vector of a point over the adsorption plane (measured from the centre of an adsorbed particle),  $\delta$  is the Dirac delta function,  $\vec{r}_i$  and  $\vec{r}_j$  are the position vectors of the particles  $i$

and  $j$ , respectively, and angle brackets mean the ensemble average. Here,  $S$  is the surface area, and  $N$  is the total number of particles adsorbed over this area. Radial distribution  $g(r)$  gives information about the long-range inter-particle correlations and their organization [15, 47]. This function can be interpreted as an averaged probability of finding a particle at the distance  $r$  from another particle, with the centre located at  $r = 0$ . For sake of convenience, the distance  $r$  is usually normalized by using the particle radius  $d_0/2$  as a scaling variable. In the absence of external forces, when the system can be considered isotropic, the vector  $\vec{r}$  can be replaced with the radial coordinate  $r$  and the pair correlation function may be calculated more directly by converting equation (6.6) to the form

$$g(r) = \frac{S \bar{N}_a(r)}{N 2\pi r \Delta r}, \quad (6.7)$$

where  $\bar{N}_a$  is the averaged number of particles within the annulus of the radius  $r$  and the thickness  $\Delta r$ .

To discuss the effect of the parameter  $\beta$  on the spatial distribution of particles inside the cell at the jammed state, let us first consider the fixed value  $\alpha = 0.3$ , with varying  $\beta = 0.02 - 0.98$ , as shown in figure 6.9. In the case of the ICCA regime, the temporal evolution of the coverage  $\theta(t)$  towards its jamming state value  $\theta_j$  is a two-stage process. At very early times of the process, when the coverage fraction is small, the coverage grows rapidly in time. Particles adsorbed during this stage are homogeneously distributed in the cells. At a late enough time, when the coverage fraction is sufficient to make the geometry of the unoccupied substrate complex, the growth of the coverage fraction  $\theta(t)$  requires the filling of holes that are large enough for the insertion of an additional particle. Consequently, the structure of the spatial distribution of particles inside the cell is determined by the late stage of the deposition process. For  $\beta \leq 0.02$ , particles are distributed uniformly throughout the whole substrate and the shape of radial distribution  $g(r)$  is the same as in the case of RSA of disks on a continuous substrate. Since the cell-cell excluded volume interaction is changing with  $\beta$ , the spatial distribution of particles inside the cell reveals various preferential regions. From the probability distribution plots in figure 6.9, we can identify various regions such as corners (f), sides (g), interior ring (h), central square (i), central peak (j), etc., that are predominantly populated with particles. For  $\beta$  below the critical value  $\beta_c$  (equation (6.4)) particles adsorb preferentially at the cell edges. Approaching the critical value of  $\beta_c = 0.85$  ( $\alpha = 0.30$ ), the probability of deposition in the centre of a cell increases. Close to the critical value, we observe the appearance of a pronounced peak of probability distribution in the centre of the cell. In addition, as parameter  $\beta$  is increased, one observes that the radial distribution functions  $g(r)$  become more detailed with peaks becoming sharper. There is also peak splitting, related to a weaker excluded volume interaction between particles deposited into different cells. For the large  $\beta = 0.98$ , since adsorption on an empty cell is weakly constrained by particles previously adsorbed on a neighbouring one, adsorption can occur, with almost equal probability all over the cell (figure 6.9(l)). The radial distribution function now shows a series of well-developed peaks which correspond to the various cell-defined distances in the square lattice matrix. Finally, in the NICCA regime ( $\beta > 1$ ), the adsorption inside cells is entirely uniform and the shape of the radial distribution function  $g(r)$  is no longer changing (not shown here).

Numerical simulations for the other cell sizes,  $\alpha = 0.5, 0.7$ , produce qualitatively similar results for the spatial distribution of particles inside the cell leading to qualitatively the same phenomenology (see figures 6.10 and 6.11). However, increasing the value of  $\alpha$  in the NICCA-SPCA regime increases the uncertainty in the position of the particle within the cell, i.e., it leads to peak broadening of the radial distribution function  $g(r)$ .

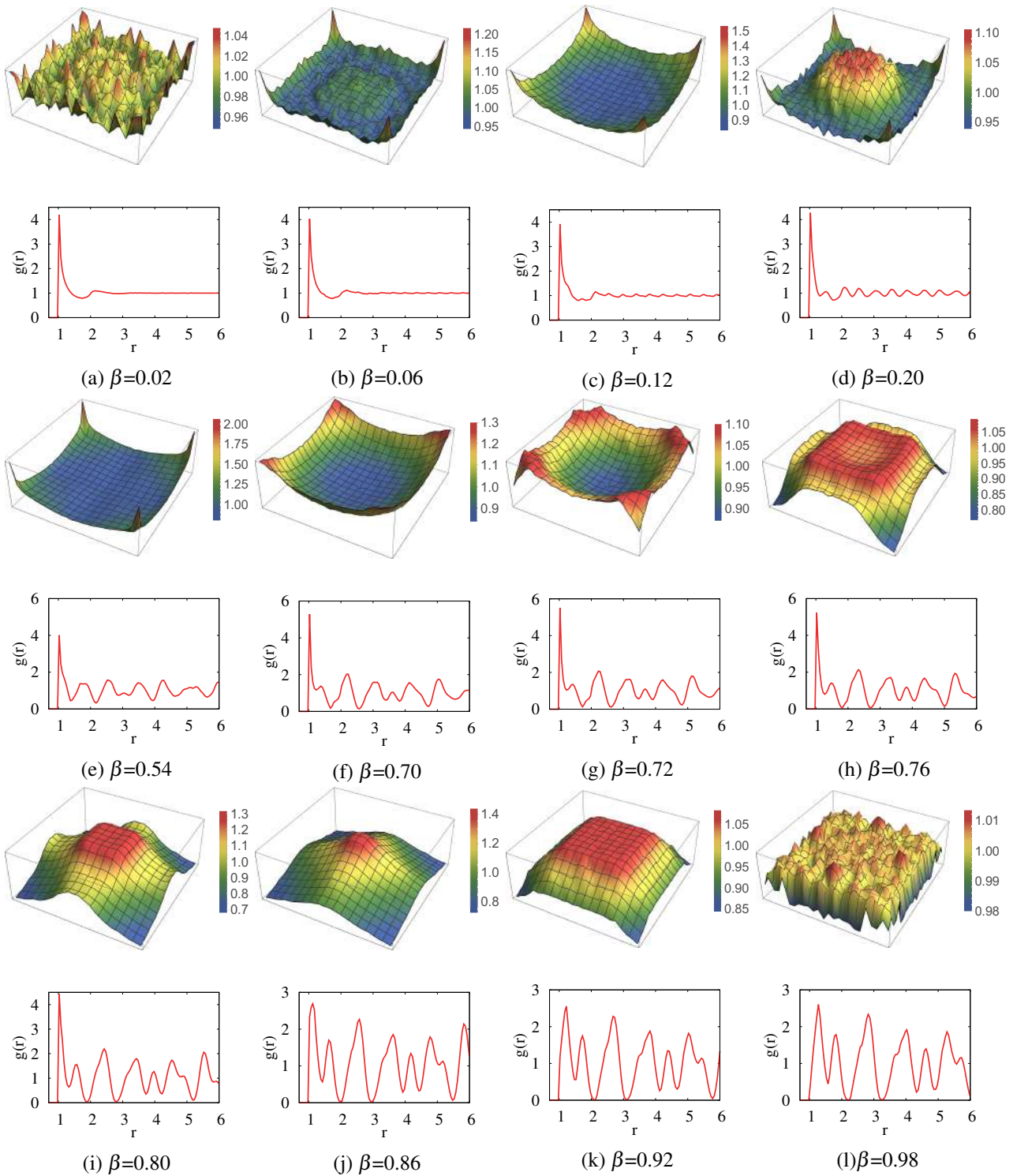


Figure 6.9: Spatial distribution of particles inside the cell and radial distribution function  $g(r)$  at the jammed state, for the fixed value of cell size  $\alpha = 0.3$  and different values of parameter  $\beta$ .

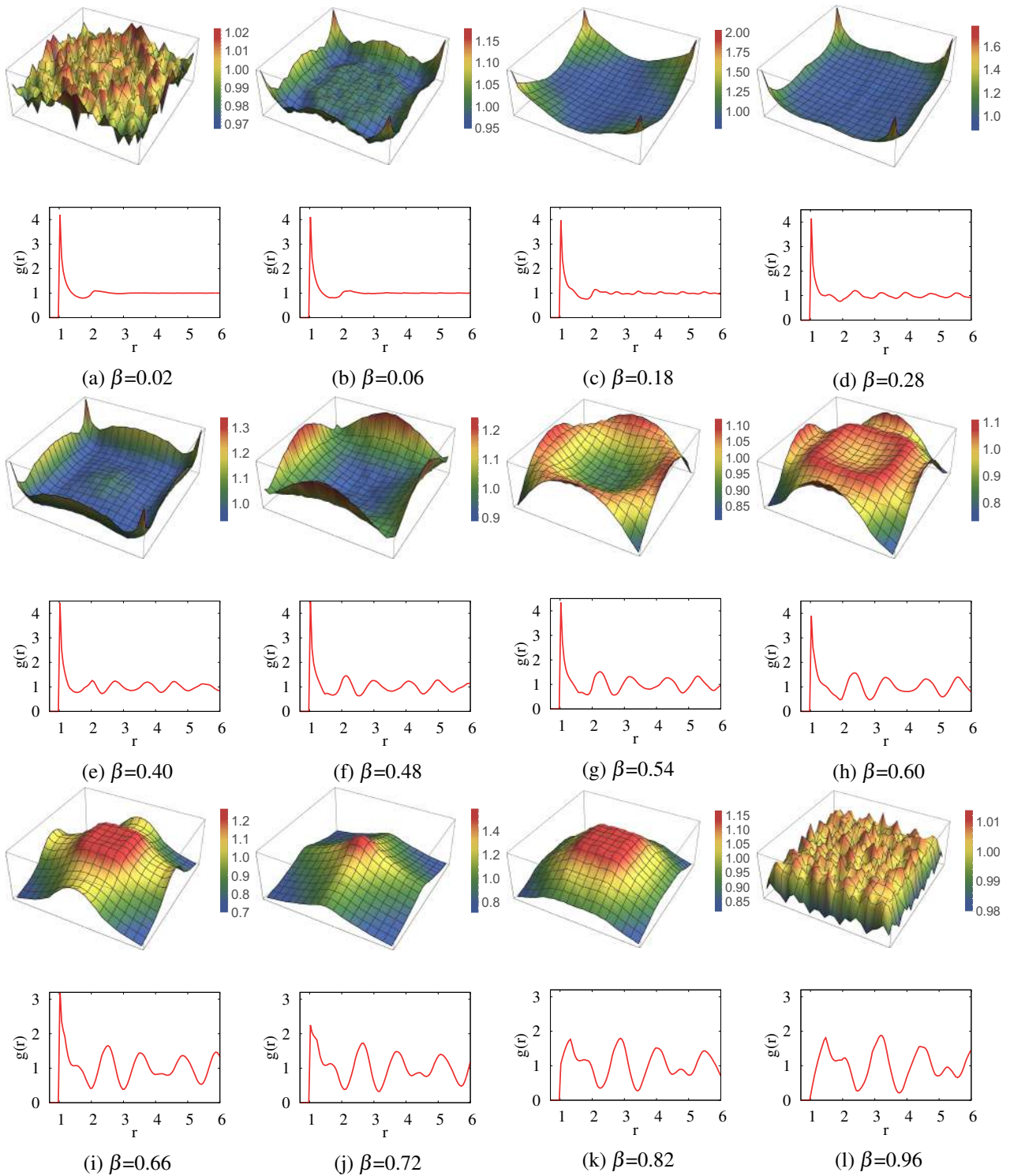


Figure 6.10: Spatial distribution of particles inside the cell and radial distribution function  $g(r)$  at the jammed state, for the fixed value of cell size  $\alpha = 0.5$  and different values of parameter  $\beta$ .

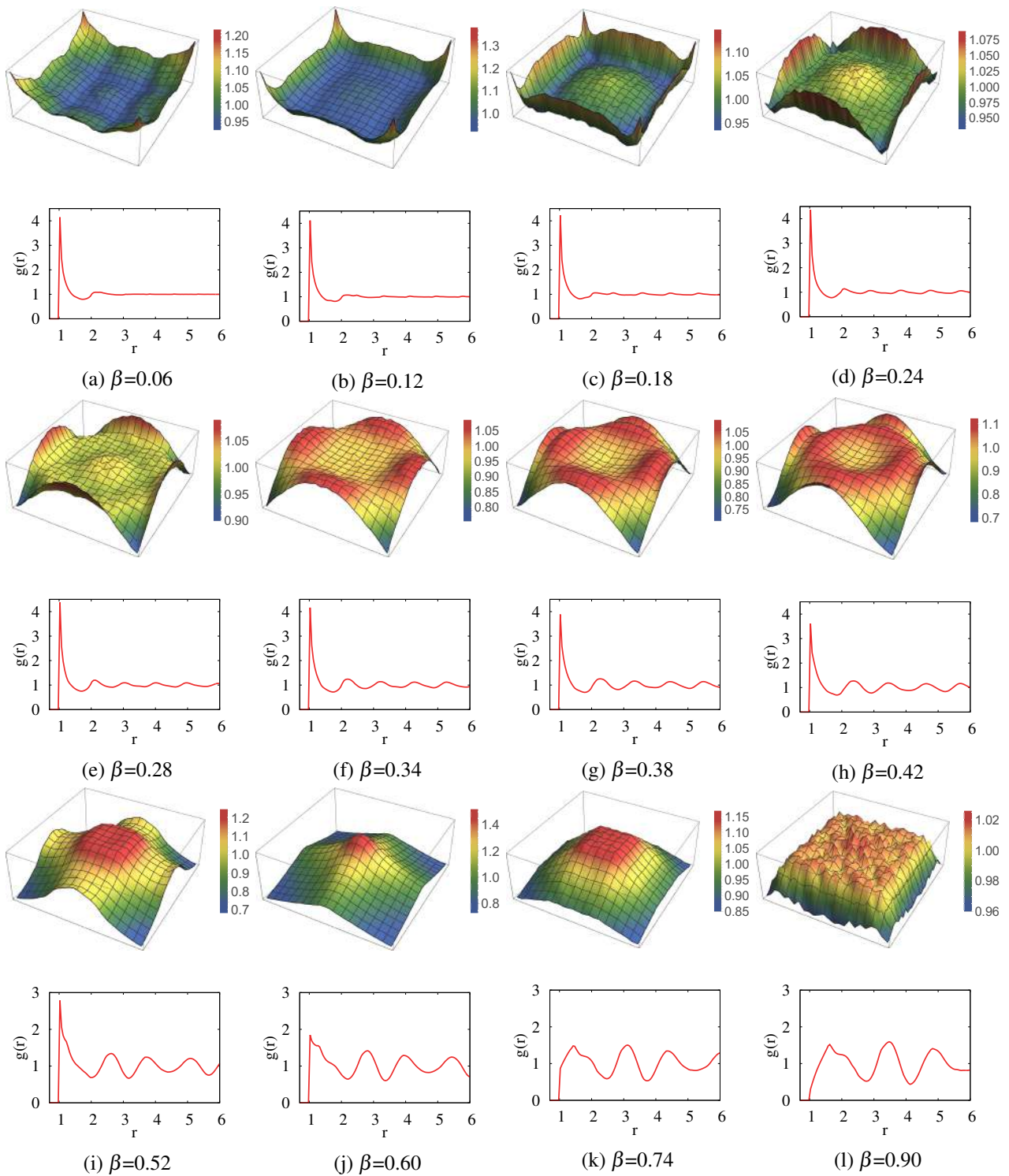


Figure 6.11: Spatial distribution of particles inside the cell and radial distribution function  $g(r)$  at the jammed state, for the fixed value of cell size  $\alpha = 0.7$  and different values of parameter  $\beta$ .

---

# Chapter 7

## Conclusions

In this thesis, we have used the Random Sequential Adsorption model to numerically investigate the deposition of identical spherical particles of fixed radius onto a flat heterogeneous substrate. A surface heterogeneities consisted of square or elongated rectangle adsorption cells with the typical geometrical cell length comparable with the size of the particles. A particle is irreversibly adsorbed at a random position on the substrate if it does not overlap any of previously adsorbed particles and if it touches one of the cells on the substrate. The equivalent model is the adsorption of two-dimensional disks (sphere projections), without overlapping already adsorbed disks and with a condition that the disk centres lie in the adsorption cells. We studied the influence of the cell size, density and arrangement of the landing cells and emphasized the influence of substrate inhomogeneities on the coverage growth rate and the geometry of the final (jammed) state. It was shown that manipulation of the substrate pattern can yield monolayer deposits with desired properties.

In the first part of this thesis research, we presented the results of numerical simulations of RSA deposition on randomly patterned substrates, with a focus on the jammed-state properties. We found that for a given density of landing cells, the highest jamming coverage and the fastest kinetics of the deposition process can be achieved in the single-particle per-cell adsorption (SPCA) case. Because the densification kinetics is dictated by geometric exclusion effects, the coverage kinetics is severely slowed down in the multiple-particles per-cell adsorption (MPCA) case.

To examine the short scale structure in the jammed-state coverings, we evaluated the radial correlation function  $g(r)$  which measures the particle density-density correlation at distance  $r$  for various shapes and sizes of the landing cells. The oscillation of  $g(r)$  quickly decays for all densities of landing cells  $\theta_0^{(\text{cell})}$ , which means that long-range order does not exist in the system. In the MPCA case, the peak of  $g(r)$  which appears at a unit distance is the most pronounced for low densities of landing cells  $\theta_0^{(\text{cell})}$ . This is opposite to what is observed under SPCA conditions when the shape of radial distribution  $g(r)$  is more structured at higher adsorption cell densities  $\theta_0^{(\text{cell})}$ .

The morphology of deposited disks has been analyzed through the distribution of pore volumes. The pore is defined as the free area of a Delaunay triangle. Its volume distribution is sensitive to small structural changes in the covering and it, therefore, describes the degree to which the cell size and cell density affect the deposit morphology. We have found that pore volumes have a distribution



with a long tail, particularly at low densities of adsorption cells  $\theta_0^{(\text{cell})}$ . The distribution  $P(v)$  becomes narrower and more localized around the low values of volumes  $v$  with the increase of cell density  $\theta_0^{(\text{cell})}$ . In the case of the largest cells that we examined ( $\alpha_4 = \sqrt{2}$ ), we observed the pronounced peak of distribution  $P(v)$  at low values of volume  $v = 0.15 - 0.20$ , which appears due to the presence of configurations with three or more disks on a single landing cell. We have also studied the influence of a regular substrate pattern on the volume distribution of the pores  $P(v)$ . At low cell densities,  $\theta_0^{(\text{cell})}$ , distribution function  $P(v)$  shows well-developed peaks which correspond to the various types of Delaunay triangles. A triangle can have three or two vertices in the same cell or all three vertices in three different cells. Cell-cell excluded volume interaction increases with the cell density  $\theta_0^{(\text{cell})}$  so that distribution  $P(v)$  for regular substrate pattern of squares becomes similar to distribution  $P(v)$  for random pattern case at densities near the jamming limit of adsorption cells.

Numerical simulations of Random Sequential Adsorption on heterogeneous substrates composed of elongated rectangular adsorption cells have shown that the shape of the pore distribution function  $P(v)$  is affected by the anisotropy in the deposition procedure for landing cells. It is shown that anisotropic deposition of landing cells lowers the average cell population and reduces the number of small pores. Our results suggest that the porosity of deposit (pore volumes) can be controlled by the size and shape of landing cells, and by the anisotropy of the cell deposition procedure. The radial correlation function  $g(r)$  for jamming coverings of disks corresponding to anisotropic deposition of rectangles is quite similar to  $g(r)$  for the case of the isotropic landing-cell pattern.

The second part of this thesis research considered a pattern with the equal square cells, positioned in a square-lattice matrix. Analysis of numerical simulation of RSA of disk-shaped particles is focused on the kinetics of the deposition process in the interacting cell-cell adsorption (ICCA) regime. An efficient numerical algorithm was implemented to simulate the disk deposition in the case of single-particle per-cell adsorption (SPCA).

It was demonstrated that the two geometrical parameters, the cell size  $\alpha$  and the cell-cell separation  $\beta$ , have a striking influence on the kinetic properties of a deposition process, as well as on the in-cell particle population. By studying the temporal evolution of the first derivative of coverage  $\theta(t)$  we have found that the asymptotic approach of the coverage fraction  $\theta(t)$  to its jamming limit  $\theta_J$  is algebraic if the parameters  $\alpha$  and  $\beta$  satisfy the simple condition  $\beta + \alpha/2 < 1$ . If this relation is valid, particles adsorbed on neighbouring cells can block adsorption inside the central cell, so that there is no minimum finite area available for adsorption. A vanishing-small area can be created with non-zero probability and an asymptotic approach to the jamming limit in the late stage of the deposition process obeys the power law.

If the geometry of the pattern does not satisfy the criteria  $\beta + \alpha/2 < 1$ , the approach of the coverage fraction  $\theta(t)$  to the jamming limit is not consistent with the power-law behaviour. The existence of the minimum finite area where the centre of a disk can land without overlapping a previously adsorbed particle is a sufficient condition for deviation from the algebraic asymptotic approach. When the geometry of the pattern approaches towards non-interacting condition ( $\beta \rightarrow 1.0^-$ ), the asymptotic approach of the coverage fraction  $\theta(t)$  to its jamming limit  $\theta_J$  becomes closer to the exponential law. It must be stressed that the appearance of even a slight cell-cell excluded volume interaction violates the exponential asymptotic approach. Consequently, changing the pattern in our numerical model allows interpolating the deposition kinetics between the continuum limit and the lattice-like behaviour.

We found that the asymptotic approach obeys a power-law  $t^{-p}$  with a different exponent  $p = 3/2$  on the critical line in the parameter phase space  $(\alpha, \beta)$ , determined by equation  $\beta + \alpha/2 = 1$ . This line is the boundary of the standard power-law asymptotic behaviour phase with  $p = 1/2$ . A similar anomalous power-law approach was reported in the literature for the case of adsorption on a one-dimensional imprecise substrate [2, 42]. We are the first to observe and document this kind of behaviour in two-dimensional RSA systems. In one dimension, this behaviour is explained by a different kind of small hole size distribution in the late phase of the process. For the normal power-law approach, this distribution is constant in the limit of the hole size zero, while for the anomalous power-law approach the small hole distribution vanishes linearly in the same limit. The distribution of holes available for particle adsorptions in the late phase of the process for adsorption on a two-dimensional imprecise lattice is out of the scope of this thesis and this topic could be addressed in further research.

To examine the short scale structure in the jammed-state coverings, we evaluated the spatial distribution of particles inside the cell and the radial distribution function  $g(r)$ . Interesting, non-trivial spatial distributions are observed, with local order resulting not only from the constraint of the pattern but also due to steric effects that make certain insertions of particles impossible owing to an effective high local density. Close to the critical values of parameter  $\beta$  determined with  $\beta_c = 1 - \alpha/2$ , we observe the appearance of the pronounced peak of probability distribution in the centre of the cell. Hence, by tuning the pattern parameters on the critical values, it is possible to obtain jammed-state covering with a highly ordered structure.

In the available literature, various models of thin-film formation were used to investigate the impact of particle properties on the kinetics of adsorption and the structure of the jammed state. With technological advances and the development of methods to modify substrate surfaces, more studies are devoted to the influence of the substrate on the deposition process. This direction of research is largely unexplored and leaves a lot of space for further research. For example, our research can be extended to different particle and cell shapes, as well as to different substrate patterns. The relaxation processes in the deposit formation with weaker particle-cell interaction play a more important role and can not be neglected. Inter-particle interactions, hydrodynamic interactions, and external forces like gravitation and electromagnetic forces can also be incorporated into an extended model. The experimental measurements of monolayer deposit formations are extremely difficult to realize, especially when it comes to kinetics. This makes numerical simulations an indispensable tool for advancing our understanding of the adsorption process.



---

## Appendix A

### Dense packing of equal disks in a square

In this work, we investigated the adsorption of equal hard disks on square cells of different sizes and arrangements. But what is the maximal number of disks that can fit into a square cell of a given size? Or stated differently, what is the minimal square cell that can contain centres of  $n$  non-overlapping disks? Finding and proving the most optimal configuration might be easy for up to 5 disks, but the cases of 6 and more disks require more creativity and more profound mathematical knowledge.

This appendix lists the sizes of minimal squares that contain the centres of up to ten disks, along with the coordinates of disk centres in the optimal configuration (see figures A.1 - A.9). Next to each figure, we give the exact values [88–91], except for the case of 10 disks where we cite approximate numerical values proposed and proved by Groot et al. [92]. It is interesting that the optimal solution for  $n = 10$  is not symmetric and the side of the minimal square is calculated as the smallest real root of the polynomial of degree 18.

Rigorous mathematical proofs exist for  $n = 2$  to 30, and for  $n = 36$ . Best known solutions for up to  $\approx 10^4$  disks are summarized in a web page maintained by Eckard Specht [93], most of which found numerically.

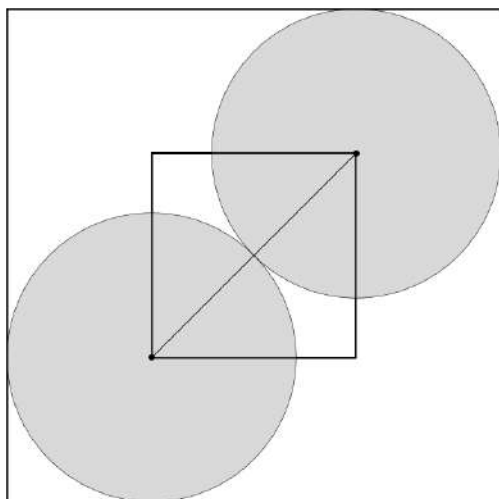


Figure A.1: Dense packing of  $n = 2$  disks in a square

$$\begin{aligned} a_2 &= \sqrt{2}/2 \\ P_1 &= (0, 0) \\ P_2 &= (\sqrt{2}/2, \sqrt{2}/2) \end{aligned}$$

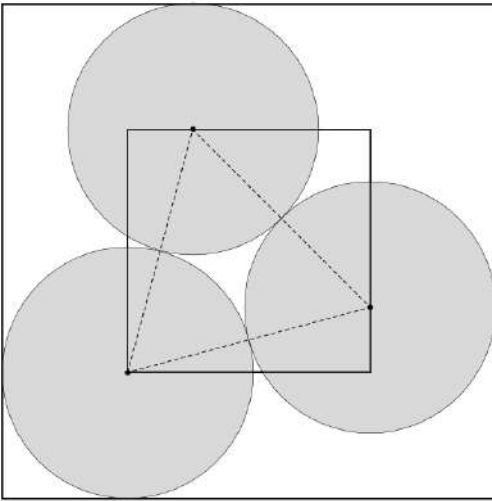


Figure A.2: Dense packing of  $n = 3$  disks in a square

$$a_3 = (\sqrt{6} + \sqrt{2})/4$$

$$P_1 = (0, 0)$$

$$P_2 = ((\sqrt{6} - \sqrt{2})/4, (\sqrt{6} + \sqrt{2})/4)$$

$$P_3 = ((\sqrt{6} + \sqrt{2})/4, (\sqrt{6} - \sqrt{2})/4)$$

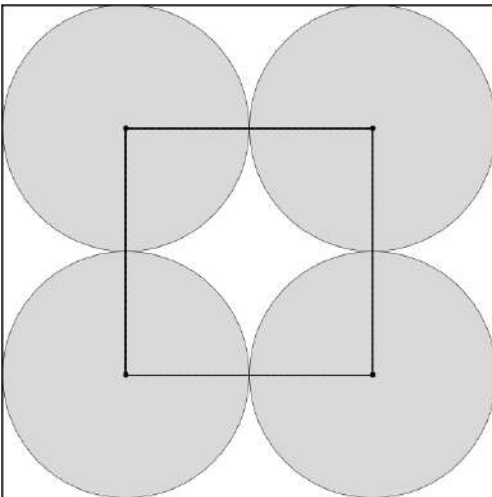


Figure A.3: Dense packing of  $n = 4$  disks in a square

$$a_4 = 1$$

$$P_1 = (0, 0)$$

$$P_2 = (0, 1)$$

$$P_3 = (1, 0)$$

$$P_4 = (1, 1)$$

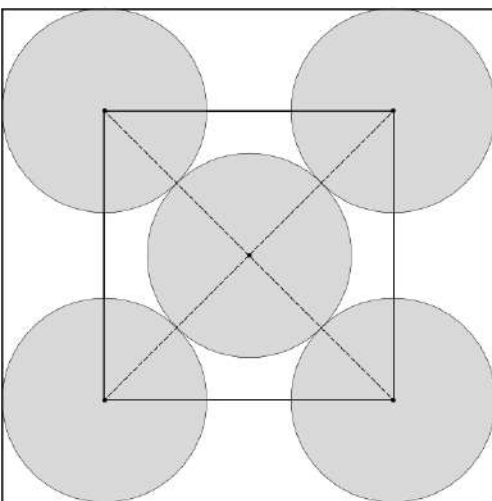


Figure A.4: Dense packing of  $n = 5$  disks in a square

$$a_5 = \sqrt{2}$$

$$P_1 = (0, 0)$$

$$P_2 = (\sqrt{2}, \sqrt{2})$$

$$P_3 = (0, \sqrt{2})$$

$$P_4 = (\sqrt{2}, 0)$$

$$P_5 = (\sqrt{2}/2, \sqrt{2}/2)$$

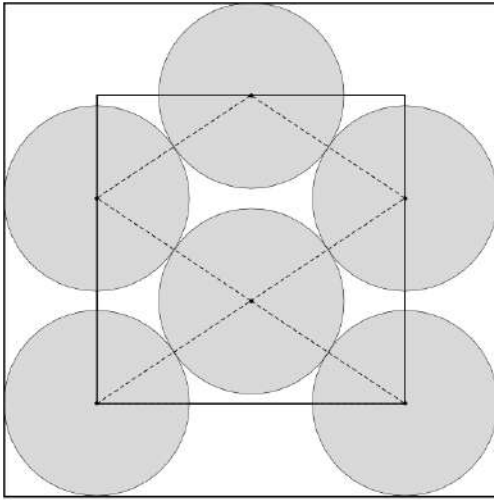


Figure A.5: Dense packing of  $n = 6$  disks in a square

$$\begin{aligned}
 a_6 &= \frac{6}{\sqrt{13}} \\
 P_1 &= (0, 0) \\
 P_2 &= \left(\frac{6}{\sqrt{13}}, 0\right) \\
 P_3 &= \left(\frac{3}{\sqrt{13}}, \frac{2}{\sqrt{13}}\right) \\
 P_4 &= \left(0, \frac{4}{\sqrt{13}}\right) \\
 P_5 &= \left(\frac{6}{\sqrt{13}}, \frac{4}{\sqrt{13}}\right) \\
 P_6 &= \left(\frac{3}{\sqrt{13}}, \frac{6}{\sqrt{13}}\right)
 \end{aligned}$$

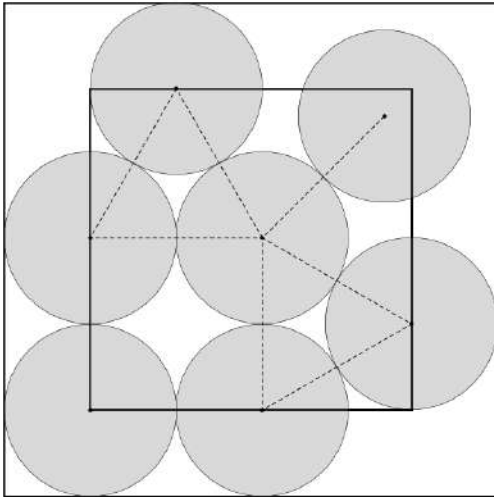


Figure A.6: Dense packing of  $n = 7$  disks in a square

$$\begin{aligned}
 a_7 &= 1 + \sqrt{3}/2 \\
 P_1 &= (0, 0) \\
 P_2 &= (1, 0) \\
 P_3 &= (1, 1) \\
 P_4 &= (0, 1) \\
 P_5 &= (1 + \sqrt{3}/2, 1/2) \\
 P_6 &= (1/2, 1 + \sqrt{3}/2) \\
 P_7 &= (1 + \sqrt{2}/2, 1 + \sqrt{2}/2)
 \end{aligned}$$

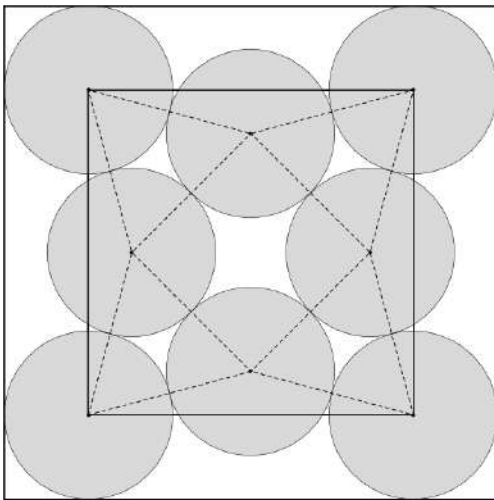


Figure A.7: Dense packing of  $n = 8$  disks in a square

$$\begin{aligned}
 a_8 &= (\sqrt{6} + \sqrt{2})/2 \\
 P_1 &= (0, 0) \\
 P_2 &= ((\sqrt{6} + \sqrt{2})/2, 0) \\
 P_3 &= ((\sqrt{6} + \sqrt{2})/2, (\sqrt{6} + \sqrt{2})/2) \\
 P_4 &= (0, (\sqrt{6} + \sqrt{2})/2) \\
 P_5 &= ((\sqrt{6} + \sqrt{2})/4, (\sqrt{6} - \sqrt{2})/4) \\
 P_6 &= ((\sqrt{6} + \sqrt{2})/4, (\sqrt{6} + 3\sqrt{2})/4) \\
 P_7 &= ((\sqrt{6} - \sqrt{2})/4, (\sqrt{2} + \sqrt{6})/4) \\
 P_8 &= ((\sqrt{6} + 3\sqrt{2})/4, (\sqrt{6} + \sqrt{2})/4)
 \end{aligned}$$

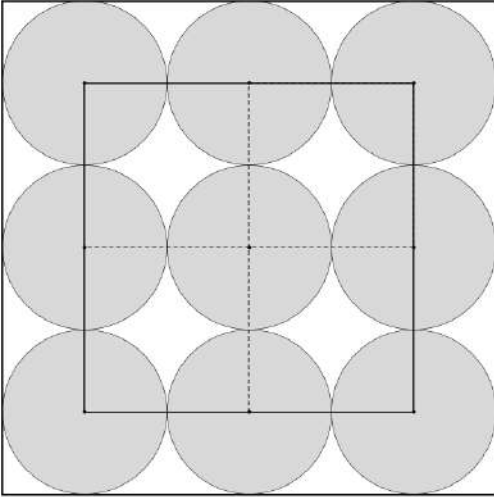


Figure A.8: Dense packing of  $n = 9$  disks in a square

$$a_9 = 2$$

$$P_1 = (0, 0)$$

$$P_2 = (0, 1)$$

$$P_3 = (0, 2)$$

$$P_4 = (1, 0)$$

$$P_5 = (1, 1)$$

$$P_6 = (1, 2)$$

$$P_7 = (2, 0)$$

$$P_8 = (2, 1)$$

$$P_9 = (2, 2)$$

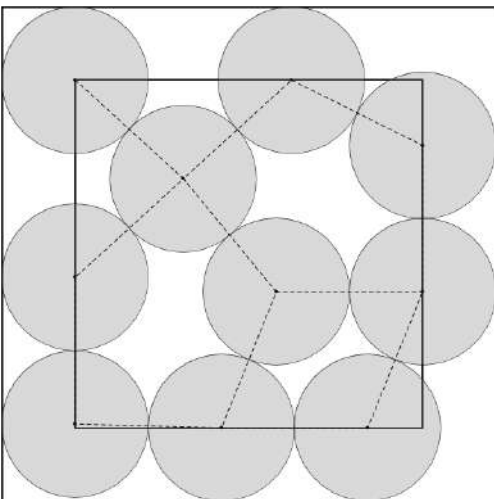


Figure A.9: Dense packing of  $n = 10$  disks in a square

$$a_{10} = 2.87372076161906$$

$$P_1 = (0, 0.027244965467)$$

$$P_2 = (0.999628787029, 0)$$

$$P_3 = (1.999628787029, 0)$$

$$P_4 = (1.373720761619, 0.927391607978)$$

$$P_5 = (2.373720761619, 0.927391607978)$$

$$P_6 = (0, 1.027244965467)$$

$$P_7 = (0.739425948012, 1.700482863543)$$

$$P_8 = (2.373720761619, 1.927391607977)$$

$$P_9 = (0, 2.373720761619)$$

$$P_{10} = (1.478851896025, 2.373720761619)$$

---

## References

- [1] V. Privman and H. Yan, *Random sequential adsorption on imprecise lattice*, [The Journal of Chemical Physics](#) **144**, 244704, (2016).
- [2] A. Verma and V. Privman, *Nonstandard convergence to jamming in random sequential adsorption: The case of patterned one-dimensional substrates*, [Physica A: Statistical Mechanics and its Applications](#) **491**, 560–573, (2018).
- [3] I. R. Epstein, *Kinetics of large-ligand binding to one-dimensional lattices: theory of irreversible binding*, [Biopolymers](#) **18**, 765–788, (1979).
- [4] P. R. Van Tassel, P. Viot, and G. Tarjus, *A kinetic model of partially reversible protein adsorption*, [The Journal of Chemical Physics](#) **106**, 761–770, (1997).
- [5] J. Feder, *Random sequential adsorption*, [J. Theoret. Biol.](#) **87**, 237–254, (1980).
- [6] S. Ravichandran and J. Talbot, *Mobility of Adsorbed Proteins: A Brownian Dynamics Study*, [Biophysical Journal](#) **78**, 110–120, (2000).
- [7] V. Privman, *Recent Theoretical Results for Nonequilibrium Deposition of Submicron Particles*, [The Journal of Adhesion](#) **74**, 421–440, (2000).
- [8] J. A. Liddle, Y. Cui, and P. Alivisatos, *Lithographically directed self-assembly of nanostructures*, [Journal of Vacuum Science & Technology B: Microelectronics and Nanometer Structures Processing, Measurement, and Phenomena](#) **22**, 3409–3414, (2004).
- [9] A. V. Subashiev and S. Luryi, *Random sequential adsorption of shrinking or expanding particles*, [Phys. Rev. E](#) **75**, 011123, (2007).
- [10] O. Gromenko and V. Privman, *Random sequential adsorption of objects of decreasing size*, [Phys. Rev. E](#) **79**, 011104, (2009).
- [11] R. D. Deshmukh, G. A. Buxton, N. Clarke, and R. J. Composto, *Nanoscale Block Copolymer Templates Decorated by Nanoparticle Arrays*, [Macromolecules](#) **40**, 6316–6324, (2007).
- [12] J. W. Evans and D. R. Burgess, *Irreversible reaction on a polymer chain with range two cooperative effects*, [The Journal of Chemical Physics](#) **79**, 5023–5028, (1983).
- [13] J. F. Marques, A. B. Lima, N. A. M. Araújo, and A. Cadilhe, *Effect of particle polydispersity on the irreversible adsorption of fine particles on patterned substrates*, [Phys. Rev. E](#) **85**, 061122, (2012).



- 
- [14] O. Gromenko, V. Privman, and M. L. Glasser, *Random Sequential Adsorption Model of Damage and Crack Accumulation: Exact One-Dimensional Results*, [Journal of Computational and Theoretical Nanoscience](#) **5**, 2119–2123, (2008).
- [15] J. W. Evans, *Random and cooperative sequential adsorption*, [Rev. Mod. Phys.](#) **65**, 1281 – 1329, (1993).
- [16] V. Privman (Ed.), *Nonequilibrium Statistical Mechanics in One Dimension*, Cambridge University Press, Cambridge, UK, 1997.
- [17] P. J. Flory, *Intramolecular Reaction between Neighboring Substituents of Vinyl Polymers*, [J. Am. Chem. Soc.](#) **61**, 1518, (1939).
- [18] A. Rényi, *On a One-Dimensional Problem Concerning Random Space-Filling*, [Publ. Math. Inst. Hung. Acad. Sci.](#) **3**, 109–127, (1958).
- [19] B. Widom, *Random Sequential Addition of Hard Spheres to a Volume*, [The Journal of Chemical Physics](#) **44**, 3888–3894, (1966).
- [20] R. D. Vigil and R. M. Ziff, *Random sequential adsorption of unoriented rectangles onto a plane*, [The Journal of Chemical Physics](#) **91**, 2599–2602, (1989).
- [21] J. Talbot, G. Tarjus, and P. Schaaf, *Unexpected asymptotic behavior in random sequential adsorption of nonspherical particles*, [Phys. Rev. A](#) **40**, 4808–4811, (1989).
- [22] P. Viot and G. Tarjus, *Random Sequential Addition of Unoriented Squares: Breakdown of Swendsen’s Conjecture*, [Europhysics Letters \(EPL\)](#) **13**, 295–300, (1990).
- [23] J. D. Sherwood, *Random sequential adsorption of lines and ellipses*, [Journal of Physics A: Mathematical and General](#) **23**, 2827–2833, (1990).
- [24] R. M. Ziff and R. D. Vigil, *Kinetics and fractal properties of the random sequential adsorption of line segments*, [J. Phys. A: Math. Gen.](#) **23**, 5103 – 5108, (1990).
- [25] R. D. Vigil and R. M. Ziff, *Kinetics of random sequential adsorption of rectangles and line segments*, [The Journal of Chemical Physics](#) **93**, 8270–8272, (1990).
- [26] B. J. Brosilow, R. M. Ziff, and R. D. Vigil, *Random sequential adsorption of parallel squares*, [Phys. Rev. A](#) **43**, 631–638, (1991).
- [27] S. S. Manna and N. M. Švrakić, *Random sequential adsorption: line segments on the square lattice*, [J. Phys. A: Math. Gen.](#) **24**, L671 – L676, (1991).
- [28] N. M. Švrakić and M. Henkel, *Kinetics of irreversible deposition of mixtures*, [J. Phys. I France](#) **1**, 791–795, (1991).
- [29] P. Viot, G. Tarjus, S. M. Ricci, and J. Talbot, *Random sequential adsorption of anisotropic particles. I. Jamming limit and asymptotic behavior*, [J. Chem. Phys.](#) **97**, 5212, (1992).
- [30] P. Meakin and R. Jullien, *Random-sequential adsorption of disks of different sizes*, [Phys. Rev. A](#) **46**, 2029–2038, (1992).
-

- [31] B. Bonnier, Y. Leroyer, and E. Pommiers, *Random sequential adsorption of line segments: universal properties of mixtures in 1, 2 and 3D lattices*, *J. Phys. I France* **2**, 379–384, (1992).
- [32] Z. Adamczyk, B. Siwek, M. Zembala, and P. Weroński, *Influence of Polydispersity on Random Sequential Adsorption of Spherical Particles*, *Journal of Colloid and Interface Science* **185**, 236–244, (1997).
- [33] Z. Adamczyk, B. Siwek, and P. Weroński, *NOTE: Adsorption of colloid particles at partially covered surface*, *Journal of Colloid and Interface Science* **195**, 261–263, (1997).
- [34] Z. Adamczyk and P. Weroński, *Random sequential adsorption on partially covered surfaces*, *The Journal of Chemical Physics* **108**, 9851–9858, (1998).
- [35] J. W. Lee, *Irreversible random sequential adsorption of mixtures*, *Colloids Surf. A* **165**, 363 – 372, (2000).
- [36] B. Bonnier, *Random sequential adsorption of binary mixtures on a line*, *Phys. Rev. E* **64**, 066111, (2001).
- [37] G. Kondrat, *The effect of impurities on jamming in random sequential adsorption of elongated objects*, *The Journal of Chemical Physics* **124**, 054713, (2006).
- [38] P. B. Shelke, M. D. Khandkar, A. G. Banpurkar, S. B. Ogale, and A. V. Limaye, *Universality of the power-law approach to the jamming limit in random sequential adsorption dynamics*, *Phys. Rev. E* **75**, 060601, (2007).
- [39] M. Cieśla, G. Pająk, and R. M. Ziff, *Shapes for maximal coverage for two dimensional random sequential adsorption*, *Phys. Chem. Chem. Phys.* **17**, 24376–24381, (2015).
- [40] L. Reeve and J. Wattis, *Random sequential adsorption with two components: Asymptotic analysis and finite size effects*, *Journal of Physics A: Mathematical and Theoretical* **48**, (2015).
- [41] X. Jin, N. H. L. Wang, G. Tarjus, and J. Talbot, *Irreversible adsorption on non-uniform surfaces: the random site model*, *J. Chem. Phys.* **97**, 4256, (1993).
- [42] B. Bonnier, Y. Leroyer, and E. Pommiers, *Random sequential adsorption on a dashed line*, *Journal of Physics A: Mathematical and General* **28**, 1847–1860, (1995).
- [43] Z. Adamczyk, P. Weroński, and E. Musiał, *Irreversible adsorption of hard spheres at random site (heterogeneous) surfaces*, *J. Chem. Phys.* **116**, 4665, (2002).
- [44] Z. Adamczyk, P. Weroński, and E. Musiał, *Colloid Particle Adsorption at Random Site (Heterogeneous) Surfaces*, *Journal of Colloid and Interface Science* **248**, 67–75, (2002).
- [45] N. A. M. Araújo, A. Cadilhe, and V. Privman, *Morphology of fine-particle monolayers deposited on nanopatterned substrates*, *Phys. Rev. E* **77**, 031603, (2008).
- [46] Z. Adamczyk, *Particles at Interfaces: Interactions, Deposition, Structure*, *Interface Science and Technology* 9. Elsevier, Academic Press, 2006, ISBN 9780123705419.
- [47] T. M. Truskett, S. Torquato, S. Sastry, P. G. Debenedetti, and F. H. Stillinger, *Structural precursor to freezing in the hard-disk and hard-sphere systems*, *Phys. Rev. E* **58**, 3083–3088, (1998).

- 
- [48] E. L. Hinrichsen, J. Feder, and T. Jøssang, *Geometry of random sequential adsorption*, *J. Stat. Phys.* **44**, 793–827, (1986).
- [49] R. H. Swendsen, *Erratum: Dynamics of random sequential adsorption*, *Phys. Rev. A* **24**, 3285–3285, (1981).
- [50] Y. Pomeau, *Some asymptotic estimates in the random parking problem*, *J. Phys. A: Math. Gen.* **13**, L193–L196, (1980).
- [51] F. Downton, *A Note on Vacancies on a Line*, *Journal of the Royal Statistical Society. Series B (Methodological)* **23**, 207–214, (1961).
- [52] E. S. Page, *The Distribution of Vacancies on a Line*, *Journal of the Royal Statistical Society. Series B (Methodological)* **21**, 364–374, (1959).
- [53] N. A. M. Araújo and A. Cadilhe, *Gap-size distribution functions of a random sequential adsorption model of segments on a line*, *Phys. Rev. E* **73**, 051602, (2006).
- [54] N. A. M. Araújo and A. Cadilhe, *Jammed state characterization of the random sequential adsorption of segments of two lengths on a line*, *Journal of Statistical Mechanics: Theory and Experiment* **2010**, P02019, (2010).
- [55] P. Philippe and D. Bideau, *Numerical model for granular compaction under vertical tapping*, *Phys. Rev. E* **63**, 051304, (2001).
- [56] P. Richard, P. Philippe, F. Barbe, S. Bourles, X. Thibault, and D. Bideau, *Analysis by x-ray microtomography of a granular packing undergoing compaction*, *Phys. Rev. E* **68**, 020301(R), (2003).
- [57] T. Aste, *Variations around disordered close packing*, *J. Phys.: Condens. Matter* **17**, S2361 – S2390, (2005).
- [58] T. Aste, *Volume fluctuations and geometrical constraints in granular packs*, *Phys. Rev. Lett.* **96**, 018002, (2006).
- [59] D. Arsenović, S. B. Vrhovac, Z. M. Jakšić, L. Budinski-Petković, and A. Belić, *Simulation Study of Granular Compaction Dynamics under vertical tapping*, *Phys. Rev. E* **74**, 061302, (2006).
- [60] P. Su and R. L. Scot Drysdale, *A comparison of sequential Delaunay triangulation algorithms*, *Computational Geometry* **7**, 361–385, (1997).
- [61] C. B. Barber, D. P. Dobkin, and H. Huhdanpaa, *The quickhull algorithm for convex hulls*, *ACM Trans. Math. Softw.* **22**, 469, (1996).
- [62] Wikipedia contributors, *Delaunay triangulation*, *Wikipedia, The Free Encyclopedia*, (2021).
- [63] F. Aurenhammer, *Voronoi diagrams – A survey of a fundamental geometric data structure*, *ACM Comput. Surv.* **23**, 345, (1991).
- [64] R. S. Nord and J. W. Evans, *Irreversible immobile random adsorption of dimers, trimers, ... on 2D lattices*, *The Journal of Chemical Physics* **82**, 2795–2810, (1985).
-

- [65] R. Nord, *Irreversible random sequential filling of lattices by monte carlo simulation*, [Journal of Statistical Computation and Simulation](#) **39**, 231–240, (1991).
- [66] K. J. Vette, T. W. Orent, D. K. Hoffman, and R. S. Hansen, *Kinetic model for dissociative adsorption of a diatomic gas*, [The Journal of Chemical Physics](#) **60**, 4854–4861, (1974).
- [67] M. C. Bartelt and V. Privman, *Kinetics of irreversible multilayer adsorption: One-dimensional models*, [J. Chem. Phys.](#) **93**, 6820, (1990).
- [68] Lj. Budinski-Petković and U. Kozmidis-Luburić, *Random sequential adsorption on a triangular lattice*, [Phys. Rev. E](#) **56**, 6904, (1997).
- [69] Lj. Budinski-Petković, S. B. Vrhovac, and I. Lončarević, *Random sequential adsorption of polydisperse mixtures on discrete substrates*, [Phys. Rev. E](#) **78**, 061603, (2008).
- [70] B. Bonnier, D. Boyer, and P. Viot, *Pair correlation function in random sequential adsorption processes*, [Journal of Physics A: Mathematical and General](#) **27**, 3671–3682, (1994).
- [71] D. J. Burridge and Y. Mao, *Recursive approach to random sequential adsorption*, [Phys. Rev. E](#) **69**, 037102, (2004).
- [72] P. Parisse, D. Luciani, A. D’Angelo, S. Santucci, P. Zuppella, P. Tucceri, A. Reale, and L. Ottaviano, *Patterning at the nanoscale: Atomic force microscopy and extreme ultraviolet interference lithography*, [Mater. Sci. Eng. B](#) **165**, 227–230, (2009).
- [73] T. Kraus, L. Malaquin, H. Schmid, W. Riess, N. D. Spencer, and H. Wolf, *Nanoparticle printing with single-particle resolution*, [Nat. Nanotechnol.](#) **2**, 570–576, (2007).
- [74] R. J. Kershner, L. D. Bozano, C. M. Micheel, A. M. Hung, A. R. Fornof, J. N. Cha, C. T. Rettner, M. Bersani, J. Frommer, P. W. K. Rothmund, and G. M. Wallraff, *Placement and orientation of individual DNA shapes on lithographically patterned surfaces*, [Nat. Nanotechnol.](#) **4**, 557–561, (2009).
- [75] A. del Campo, C. Greiner, I. Alvarez, and E. Arzt, *Patterned Surfaces with Pillars with Controlled 3D Tip Geometry Mimicking Bioattachment Devices*, [Adv. Mater.](#) **19**, 1973–1977, (2007).
- [76] X. Jin, J. Talbot, and N. H. L. Wang, *Analysis of steric hindrance effects on adsorption kinetics and equilibria*, [AIChE J.](#) **40**, 1685, (1994).
- [77] C. Oleyar and J. Talbot, *Reversible adsorption on random site surface*, [Physica A](#) **376**, 27 – 37, (2007).
- [78] Z. Adamczyk, B. Siwek, P. Weronki, and E. Musial, *Irreversible adsorption of colloid particles at heterogeneous surfaces*, [Appl. Surf. Sci.](#) **196**, 250, (2002).
- [79] Z. Adamczyk, K. Jaszczólt, A. Michna, B. Siwek, L. Szyk-Warszyńska, and M. Zembala, *Irreversible adsorption of particles on heterogeneous surfaces*, [Adv. Colloid Interface Sci.](#) **118**, 25–42, (2005).
- [80] A. Cadilhe, N. A. M. Araújo, and V. Privman, *Random sequential adsorption: from continuum to lattice and pre-patterned substrates*, [J. Phys.: Condens. Matter](#) **19**, 065124, (2007).

- 
- [81] N. Araújo, *Nonequilibrium thin-film growth: kinetics of deposition and post evolution relaxation*, LAP LAMBERT Academic Publishing, 2010, ISBN 9783838369419.
- [82] M. Mascagni and A. Srinivasan, *Algorithm 806: SPRNG: a scalable library for pseudorandom number generation*, *ACM Transactions on Mathematical Software* **26**, 436–461, (2000).
- [83] D. Stojiljković, J. R. Šćepanović, S. B. Vrhovac, and N. M. Švrakić, *Structural properties of particle deposits at heterogeneous surfaces*, *Journal of Statistical Mechanics: Theory and Experiment* **2015**, P06032, (2015).
- [84] P. Nielaba, V. Privman, and J. S. Wang, *Journal of Physics A: Mathematical and General Kinetics of multilayer adsorption: Monte Carlo studies of models without screening*, *J. Phys. A: Math. Gen.* **23**, L1187, (1990).
- [85] Lj. Budinski-Petković and U. Kozmidis-Luburić, *Jamming configurations for irreversible deposition on a square lattice*, *Physica A* **236**, 211 – 219, (1997).
- [86] E. L. Hinrichsen, J. Feder, and T. Jøssang, *Random packing of disks in two dimensions*, *Physical Review A* **41**, 4199–4209, (1990).
- [87] P. G. Szabó, M. C. Markót, T. Csendes, E. Specht, L. G. Casado, and I. García, *New approaches to circle packing in a square: with program codes*, volume 6, Springer Science & Business Media, 2007.
- [88] B. Schwartz, *Separating points in a square*, *J. of Recreational Mathematics* **3**, 195–204, (1970).
- [89] K. J. Nurmela and P. R. J. Östergård, *More Optimal Packings of Equal Circles in a Square*, *Discrete & Computational Geometry* **22**, 439–457, (1999).
- [90] J. Schaer and A. Meir, *On a Geometric Extremum Problem*, *Canadian Mathematical Bulletin* **8**, 21–27, (1965).
- [91] J. Schaer, *The Densest Packing of 9 Circles in a Square*, *Canadian Mathematical Bulletin* **8**, 273–277, (1965).
- [92] C. Groot, R. Peikert, and D. Würtz, *The Optimal Packing of Ten Equal Circles in a Square*, *IPS Research Report* **90-12**, (1990).
- [93] Eckard Specht, *The best known packings of equal circles in a square (up to  $N = 10000$ )*, 2018, <http://hydra.nat.uni-magdeburg.de/packing/csq/>.
-

---

## Biography of the author

Danica Stojiljković was born on August 19th, 1981 in Kruševac, Serbia. She went to Mathematical high school in Belgrade, and subsequently, in 2000, started studies of Theoretical and experimental physics at the Faculty of Physics, University of Belgrade. She wrote her diploma thesis entitled “The method of efficient calculation of energy spectra in functional formalism”, conducted under the mentorship of Dr. Aleksandar Bogojević and graduated in 2005 (GPA 9.93/10). In 2005 Danica Stojiljković started undergraduate studies in the department of “Theoretical physics of the condensed state of matter” at the Faculty of Physics, UoB. Under guidance of Dr. Aleksandar Bogojević she worked on the subjects of the functional formalism applications and development of Monte Carlo simulations. She started PhD studies in 2016 in the department of “Physics of condensed matter and statistical physics” at the Faculty of Physics, UoB, under the supervision of Dr. Slobodan Vrhovac. So far, Danica Stojiljković have published 5 research papers in peer-review international journals:

1. D. Stojiljkovic and S. B. Vrhovac, *Kinetics of Particle Deposition at Heterogeneous Surfaces*, Physica A 488, 16-29 (2017)
2. J. R. Scepanovic, D. Stojiljkovic, Z. M. Jaksic, Lj. Budinski-Petkovic, and S. B. Vrhovac, *Response Properties in the Adsorption-desorption Model on a Triangular Lattice*, Physica A 451, 213 (2016)
3. D. Stojiljkovic, J. R. Scepanovic, S. B. Vrhovac, and N. M. Svrakic, *Structural Properties of Particle Deposits at Heterogeneous Surfaces*, J. Stat. Mech.-Theory Exp. 2015, P06032 (2015)
4. A. Balaz, I. Vidanovic, D. Stojiljkovic, D. Vudragovic, A. Belic, and A. Bogojevic, *SPEEDUP Code for Calculation of Transition Amplitudes Via the Effective Action Approach*, Commun. Comput. Phys. 11, 739 (2012)
5. D. Stojiljkovic, A. Bogojevic, and A. Balaz, *Efficient Calculation of Energy Spectra Using Path Integrals*, Phys. Lett. A 360, 205 (2006).

Two of these papers (1. and 3.) are directly related to the research presented in this thesis. She presented her research at 3 international and one national conference, and edited one book of proceedings of an international conference.

Danica Stojiljković is employed at the Institute of Physics in Belgrade since 2007. Her scientific work was supported by the national research project ON171017 “Modeling and Numerical Simulations of Complex Many-Particle Systems” and integrated project III43007, funded by the Ministry of Education, Science, and Technological Development of the Republic of Serbia. From 2008 till 2010 she was engaged as liason officer for FP7 projects SEE-GRID-SCI and EGEE-III, the position that was based at CERN, Geneva, Switzerland. From 2012-2017 she was a member of the European Particle Physics Communication Network. She was engaged on several other FP7 projects such as HP-SEE, PRACE-1IP, PRACE-2IP and PRACE-3IP.



## **Изјава о ауторству**

Име и презиме аутора – **Даница Стојиљковић**

Број индекса – **2016/8021**

### **Изјављујем**

да је докторска дисертација под насловом

**Kinetics and Morphology of Particle Deposition at Heterogeneous Surfaces**

**(Кинетика и морфологија депозиције честица на хетерогеним површинама)**

- резултат сопственог истраживачког рада;
- да дисертација у целини ни у деловима није била предложена за стицање друге дипломе према студијским програмима других високошколских установа;
- да су резултати коректно наведени и
- да нисам кршила ауторска права и користила интелектуалну својину других лица.

У Београду, 2022

**Потпис аутора**

---





# **Изјава о истоветности штампане и електронске верзије докторског рада**

Име и презиме аутора – **Даница Стојиљковић**

Број индекса – **2016/8021**

Студијски програм – **Физика кондензоване материје и статистичка физика**

Наслов рада – **Kinetics and Morphology of Particle Deposition at Heterogeneous Surfaces**

**(Кинетика и морфологија депозиције честица на хетерогеним површинама)**

Ментор – **др Слободан Врховац**

Изјављујем да је штампана верзија мог докторског рада истоветна електронској верзији коју сам предала ради похрањивања у **Дигиталном репозиторијуму Универзитета у Београду**.

Дозвољавам да се објаве моји лични подаци везани за добијање академског назива доктора наука, као што су име и презиме, година и место рођења и датум одбране рада.

Ови лични подаци могу се објавити на мрежним страницама дигиталне библиотеке, у електронском каталогу и у публикацијама Универзитета у Београду.

У Београду, 2022

**Потпис аутора**

---



## Изјава о коришћењу

Овлашћујем Универзитетску библиотеку „Светозар Марковић“ да у Дигитални репозиторијум Универзитета у Београду унесе моју докторску дисертацију под насловом:

### **Kinetics and Morphology of Particle Deposition at Heterogeneous Surfaces**

**(Кинетика и морфологија депозиције честица на хетерогеним површинама)**

која је моје ауторско дело.

Дисертацију са свим прилозима предала сам у електронском формату погодном за трајно архивирање.

Моју докторску дисертацију похрањену у Дигиталном репозиторијуму Универзитета у Београду и доступну у отвореном приступу могу да користе сви који поштују одредбе садржане у одабраном типу лиценце Креативне заједнице (Creative Commons) за коју сам се одлучила.

1. Ауторство (CC BY)
2. Ауторство – некомерцијално (CC BY-NC)
3. Ауторство – некомерцијално – без прерада (CC BY-NC-ND)
4. Ауторство – некомерцијално – делити под истим условима (CC BY-NC-SA)
5. Ауторство – без прерада (CC BY-ND)
6. Ауторство – делити под истим условима (CC BY-SA)

(Молимо да заокружите само једну од шест понуђених лиценци. Кратак опис лиценци је саставни део ове изјаве).

У Београду, 2022

Потпис аутора

---

1. **Ауторство.** Дозвољаваате умножавање, дистрибуцију и јавно саопштавање дела, и прераде, ако се наведе име аутора на начин одређен од стране аутора или даваоца лиценце, чак и у комерцијалне сврхе. Ово је најслободнија од свих лиценци.
2. **Ауторство – некомерцијално.** Дозвољаваате умножавање, дистрибуцију и јавно саопштавање дела, и прераде, ако се наведе име аутора на начин одређен од стране аутора или даваоца лиценце. Ова лиценца не дозвољава комерцијалну употребу дела.
3. **Ауторство – некомерцијално – без прерада.** Дозвољаваате умножавање, дистрибуцију и јавно саопштавање дела, без промена, преобликовања или употребе дела у свом делу, ако се наведе име аутора на начин одређен од стране аутора или даваоца лиценце. Ова лиценца не дозвољава комерцијалну употребу дела. У односу на све остале лиценце, овом лиценцом се ограничава највећи обим права коришћења дела.
4. **Ауторство – некомерцијално – делити под истим условима.** Дозвољаваате умножавање, дистрибуцију и јавно саопштавање дела, и прераде, ако се наведе име аутора на начин одређен од стране аутора или даваоца лиценце и ако се прерада дистрибуира под истом или сличном лиценцом. Ова лиценца не дозвољава комерцијалну употребу дела и прерада.
5. **Ауторство – без прерада.** Дозвољаваате умножавање, дистрибуцију и јавно саопштавање дела, без промена, преобликовања или употребе дела у свом делу, ако се наведе име аутора на начин одређен од стране аутора или даваоца лиценце. Ова лиценца дозвољава комерцијалну употребу дела.
6. **Ауторство – делити под истим условима.** Дозвољаваате умножавање, дистрибуцију и јавно саопштавање дела, и прераде, ако се наведе име аутора на начин одређен од стране аутора или даваоца лиценце и ако се прерада дистрибуира под истом или сличном лиценцом. Ова лиценца дозвољава комерцијалну употребу дела и прерада. Слична је софтверским лиценцама, односно лиценцама отвореног кода.